Hans Irschik
Michael Krommer
Kazumi Watanabe
Toshio Furukawa
Editors

Mechanics and Model-Based Control of Smart Materials and Structures

SpringerWienNewYork

SpringerWienNewYork

Hans Irschik • Michael Krommer • Kazumi Watanabe
Toshio Furukawa (Eds.)

Mechanics and Model-Based Control of Smart Materials and Structures

SpringerWienNewYork

Editors
Hans Irschik
Universität Linz
Institut für Technische Mechanik
Altenbergstr. 69
4040 Linz
Austria
hans.irschik@jku.at

Michael Krommer
Universität Linz
Institut für Technische Mechanik
Altenbergerstraße 69
4040 Linz
Austria
michael.krommer@jku.at

Kazumi Watanabe
Graduate School of Science & Engineering
Yamagata University (Yonezawa Campus)
Yonezawa, Yamagata 992-8510
Japan
kazy@yz.yamagata-u.ac.jp

Toshio Furukawa
Department of Mechanical
Systems Engineering
University of the Ryukyus
Senbaru 1, Nishihara
Okinawa 903-0213
Japan
furukawa@teada.tec.u-ryukyu.ac.jp

Printed in Germany

SpringerWienNewYork is part of Springer Science+Business Media
springer.at

Typesetting: Camera-ready by authors

Printed on acid-free and chlorine-free bleached paper

SPIN: 12581207

With 118 Figures

Library of Congress Control Number: 2009936787

ISBN 978-3-211-99483-2 e-ISBN 978-3-211-99484-9
DOI: 10.1007/978-3-211-99484-9
SpringerWienNewYork

Foreword

The Workshop revived a long-lasting and fruitful cooperation between Japanese and Austrian researchers in mechanical sciences, particularly concerning thermal stresses and related fields. The close relationship between the two groups of researchers was initiated at the *First International Conference on Thermal Stresses* in Hamamatsu, Japan in 1995, with Professor NAOTAKE NODA, the conference chair. The cooperation deepened in the course of the following bi-annual series of Conferences on Thermal Stresses, the fourth, chaired by Professor YOSHINOBU TANIGAWA, took place in Osaka in 2001, and the sixth in Vienna in 2005 was co-chaired by RUDOLF HEUER and FRANZ ZIEGLER. For obvious reasons, the researchers interest has shifted towards the emerging related field of smart materials and structures. In 2002, Professors KAZUMI WATANABE and FRANZ ZIEGLER co-chaired the *IUTAM Symposium on Dynamics of Advanced Materials and Smart Structures* in Yamagata, Japan. The recently founded *Austrian Center of Competence in Mechatronics*, ACCM in Linz, Austria, provided us with the opportunity to pursue the intense mutual exchange of know-how in this high-tech area of research. The undersigned greatly enjoyed the reunion with distinguished colleagues at this 1st *Japan-Austria Joint Workshop on Mechanics and Model Based Control of Smart Materials and Structures*, which took place at the Johannes Kepler University in Linz, September 2008. Distinguished researchers from Germany and Italy were invited to complete the Austrian research group. The Proceedings of this Workshop will make available up-to-date results to the international community and therefore will stimulate further developments and successful international co-operations in the field of Mechatronics.

Vienna, June 2009 *Franz Ziegler*

Preface

The 1^{st} *Japan-Austria Joint Workshop on Mechanics and Model Based Control of Smart Materials and Structures* aimed at bringing together scientists from Japan and Austria with an outstanding expertise in mechanics and control, with emphasis on the application of smart materials for the control of structures.

The workshop was intended as a scientific kick-off event for the Area *Mechanics and Model Based Control* within the newly founded *Austrian Center of Competence in Mechatronics (ACCM)*, which served as the Steering Organisation for the workshop. Mechanics and model based Control are both rapidly expanding scientific fields and fundamental disciplines of engineering. They share demanding mathematical and/or system-theoretic formulations and methods. One challenge in Mechanics and Model based Control is to use the ever increasing computer power with respect to both, the simulation of complex physical phenomena in mechanics, and the design and real-time implementation of novel control systems. Further challenges follow from the availability of efficient multi-functional materials, so-called smart materials, allowing the design and implementation of new types of actuator/sensor fields and networks. The latter topics were the goals of the present workshop.
The main topics of the workshop are:

- Laminated, composite and functionally graded materials.
- Thermal as well as piezoelectric actuation.
- Active and passive damping.
- Vibrations and waves.

We believe that the workshop will finally result into the creation of research teams with participation not only from Japan and Austria, but also from other European countries; the latter was enabled by the participation of widely renowned scientists from Europe. Such teams should push the frontiers of mechanics and control of smart materials and structures to new dimensions, resulting into the advanced design of future intelligent structures.

The key objectives of the workshop were:

- Enabling the interchange of ideas from advanced mechanics of structures and from control theory.
- Clarification of expectations of researches in the field of mechanics from advanced control theory and vice versa.
- Development of joint Japan and Austria research proposals and teams with participation from other countries.
- Encouragement of collaborations among industry and universities across the borders of the participating countries.

The undersigned editors are happy to present in the following full length papers of presentations from Japan, from Austria, 2 from Italy and 1 from Germany. It is hoped that these contributions will further stimulate the international research and cooperation in the field. The present book is aimed as a first volume of a future *Series in Research on Advanced Methods of Mechatronics*

Linz, Okinawa, Yamagata
June 2009

Hans Irschik
Michael Krommer
Kazumi Watanabe
Toshio Furukawa

Acknowledgements

Support of the 1st *Japan-Austria Joint Workshop on Mechanics and Model Based Control of Smart Materials and Structures* in the framework of the *COMET K2 Austrian Center of Competence in Mechatronics (ACCM)* is gratefully acknowledged. The ACCM is a Research and Innovation Centre for collaborative research between science and industry in the field of mechatronics at an international level with the goal of achieving scientific knowledge and results. ACCM executes an ambitious research program in collaboration with researchers, scientific partners and companies worldwide, and served as steering organisation of the workshop. ACCM is jointly run by the following organisations:

- *Johannes Kepler University of Linz (JKU)*
- *Linz Center of Mechatronics GmbH (LCM)*
- *vatron gmbh*

The help of these organisations is highly appreciated. In particular, the editors wish to thank the Johannes Kepler University for serving as host of the workshop. The workshop had not been possible without the sponsoring of:

- *City of Linz*
- *Wirtschaftsregion Donaustädte*
- *Magna Powertrain, Engineering Center Steyr GmbH & Co KG*
- *Salvagnini Maschinenbau GmbH*
- *SpringerWienNewYork*

Contents

Energy Absorption of Axially-Impacted Column Controlled by Transverse Impact

Tadaharu Adachi

Abstract Energy absorption of a column under an axial impact was controlled by a transverse impact which attributed instantaneous reduction of the structural stiffness. It was found that the absorption of the axial impact energy increased due to the post-buckling deformation being enlarged by transverse impact, though the axial impact load decreased. The experiment showed that the time elapsed from the beginning of the axial impact to the transverse impact significantly influenced the energy absorption. A transverse impact applied simultaneously with an axial impact produced the highest energy absorption. The method suggested in this paper could increase the energy absorption without loosing any stiffness and static strength.

1 Introduction

Safety is becoming a vital issue in the design of modern transportation means such a vehicle, train, helicopter and airplane. In recent years, impact energy absorption during structural crash becomes very important and is excessively investigated. Generally, in a collision, the structure collapses within the crushable zone to absorb the impact energy for safety of the passenger [1-3]. The most common method to easily collapse a structure is reducing its structural stiffness by adding imperfections such as dents and bents [4,5].

However, this method has a consequence of reducing the stiffness which is very important for a better operation performance, minimizing vibration and noise. Therefore, it is important to maintain high stiffness while improving the energy absorption using alternative ways. To achieve this purpose, system of impact energy absorption must be developed based on principle of smart

---

Tadaharu Adachi
Department of Mechanical Engineering, Toyohashi University of Technology, Toyohashi, Japan, e-mail: adachi@mech.tut.ac.jp

structure. The main concept of the smart structure is an active control of absorption and reducing structure stiffness only when an impact occurs.

In a previous studies, the author has investigated the effect of a transverse impact on static post-buckling [6, 7] and dynamic post-buckling [8, 9] of a column to control energy absorption by experiment and finite element method (FEM). In this paper, the effect of transverse impact on the dynamic post-buckling of a column under axial impact loading was summarized. Especially effect of transverse-impact timing on energy absorption was discussed. Generating column buckling by applying an axial impact and generating beam bending by applying a transverse impact have been reported in several studies [10-13]. However, energy absorption of axially-impacted beam controlled by transverse impact has not been investigated except the author.

2 Concept of Energy-Absorption Control

The principle idea of this study is illustrated in Fig. 1. In the conventional method as shown in Fig. 1(a), the stiffness of a column is reduced beforehand by adding imperfections such as a dent. When impactor M collides with the column, the structure collapses easily due to the dent, and the impact energy absorption increases. In this study, a transverse impact load $Q(t)$ is applied to a column without an imperfection during an axial impact load $P_2(t)$ caused by the collision of impactor M, as shown in Fig. 1(b). The transverse impact load $Q(t)$ leads to dynamic buckling of the column and energy absorption of the column is improved without reduction of static stiffness and strength caused by imperfection.

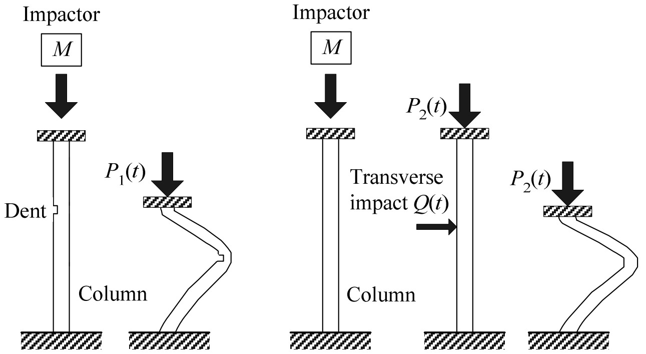

(a) Conventional method (b) Present method

Fig. 1 Concept of absorption by applying transverse impact

3 Experiment

Based on the concept, the experimental apparatus was set up as shown in Fig. 2. First, an axial impactor was dropped onto a specimen. The axial impactor was a steel bar with a diameter of $40mm$ and a length of $750mm$. During the axial impact, a transverse impactor launched from an air gun collided with the specimen. The transverse impactor was an acrylic bar with a diameter of $10mm$ and a length of $600mm$. The specimen was clamped $30mm$ from both ends by steel vices. The crosshead could slide smoothly in vertical direction along four guide bars to compress the specimen axially. A rubber plate of $20mm$ in thickness was set on the crosshead to prevent the axial impactor from rebounding.

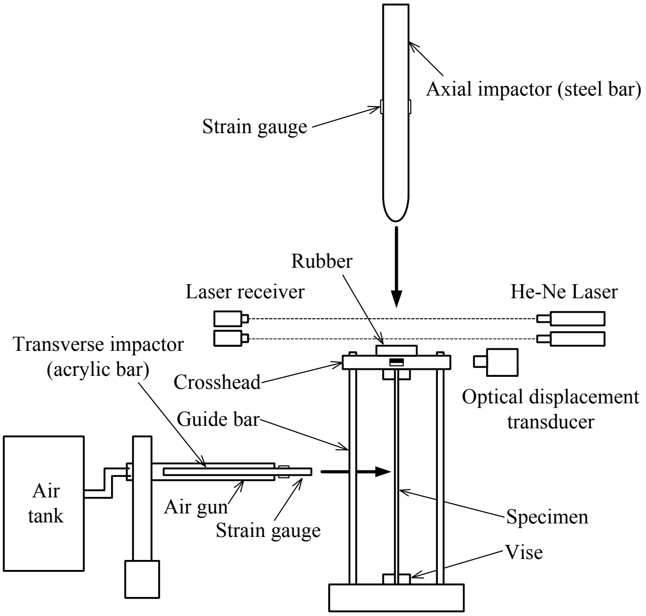

Fig. 2 Experimental apparatus

The axial impact load $P(t)$ applied to the specimen by collision with the steel bar on the crosshead can be calculated from the longitudinal strain history at the middle point of the steel bar based on the one-dimensional elastodynamics theory [14]. The strain history was measured with semiconductor gauges (Kyowa, KSP-2-120-E4). The displacement of the crosshead measured by an optical displacement transducer (Zimmer, Model 100B) was assumed to be equal to the axial displacement $u(t)$ at the top end of the specimen.

The transverse impact load $Q(t)$ was measured with strain gauges (Kyowa, KFG-2-120-C1-23) located at 50 mm from the impacted tip of the transverse impactor. The axial impact velocity v_A and transverse impact velocity v_T were evaluated from the passing time interval between two He-Ne laser beams just before the collision with the specimen.

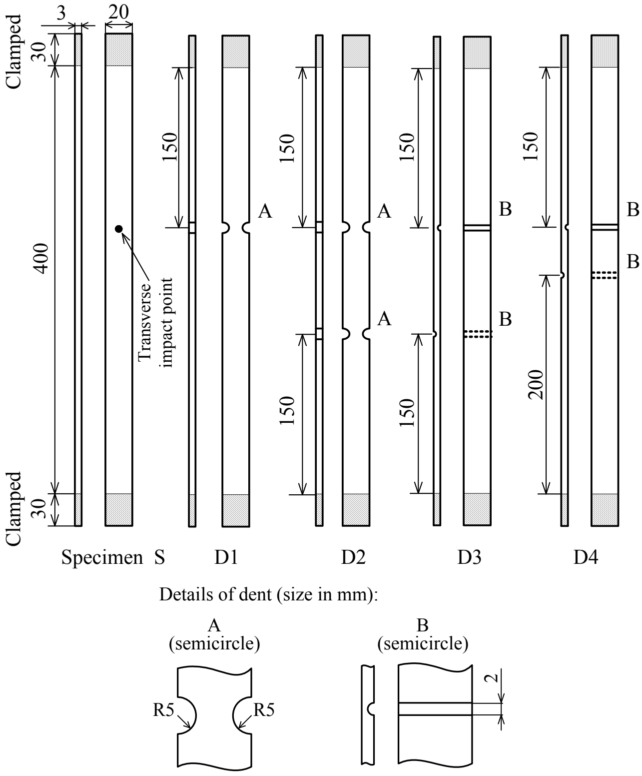

Fig. 3 Specimens

The specimens and the experimental conditions related to the transverse impact are shown in Fig. 3 and Table 1. Specimen S was a straight column with a length of $400mm$ and a thickness of $3mm$. Specimen S was subjected to a transverse impact during an axial impact as shown in Fig. 1(b). Another test where specimen S was only applied with an axial impact was also conducted. The two tests with and without a transverse impact was distinguished as test $S-T$ and test $S-0$. Tests of the conventional method shown in Fig. 1(a) were also carried out using specimens with dents. Specimens D_1 to D_4 were straight columns with one or two semi-cylindrical dents, which were $2mm$ and $10mm$ in diameter, to easily generate buckling when applied by an axial impact only. The dents were located such that the column would buckle easily. All specimens were made of aluminum alloy (JIS A6063). The Young's modulus and the yield stress were $70GPa$ and $180MPa$, respectively. The combinations of the specimens and the experimental conditions are called the test types given in Table 1 hereafter. The axial impact velocities v_A were $1.7m/s$, $2.6m/s$, and $3.5m/s$, while the transverse impact velocities v_T were $4.8m/s$, $5.3m/s$, and $6.3m/s$. The transverse impactor collided at $250mm$ from the bottom end of specimen S.

Specimen	Test type	Transverse impact
S	$S-0$	No
S	$S-T$	Applied
D_1	D_1-0	No
D_2	D_2-0	No
D_3	D_3-0	No
D_4	D_4-0	No

Table 1 Specimens and test types

4 Experimental Results

Figure 4 shows the experimental results of test type $S-T$ with $v_A = 3.5m/s$ and $v_T = 5.3m/s$. In the figures, the transverse impact time t_T is defined as the time elapsed between the collision of the axial impactor and that of the transverse impactor. Here, the results with different transverse impact times are denoted. The history of the axial impact load for test $S-0$ was an approximate half-sine curve with a period of $8ms$ as shown in Fig. 4(a), while the duration of the transverse load in Fig. 4(c) was much shorter and the maximum value was smaller. The transverse impact at $t_T = 0.4ms$ reduced the axial load more significantly compared to that with other transverse impacts and that with no transverse impact ($S-0$), as shown in Fig. 4(a). As t_T became longer, the axial load histories converged to the result of type $S-0$. On the other hand, the axial displacement at the top of the specimen for the transverse impact at $t_T = 0.4ms$ was the largest out of the results in Fig. 4(b).

From Figs. 4(a) and 4(c), the axial load-displacement curves were evaluated as shown in Fig. 4(d). The curves stood rapidly just after the axial impact, although the curves of $S-T(t_T = 0.4ms)$ has a flatter slope due to the short t_T. After the buckling, the curve decreased gradually during the post-buckling process as the displacement increased. The transverse impact was confirmed to cause lower peaks and horizontally longer curves, which were irreversible. This means external work by the axial impact was lost by the post-buckling behavior of the specimen, that is, the energy absorption. Therefore, the absorbed energy E_{ab} of a specimen defined as the lost exter-

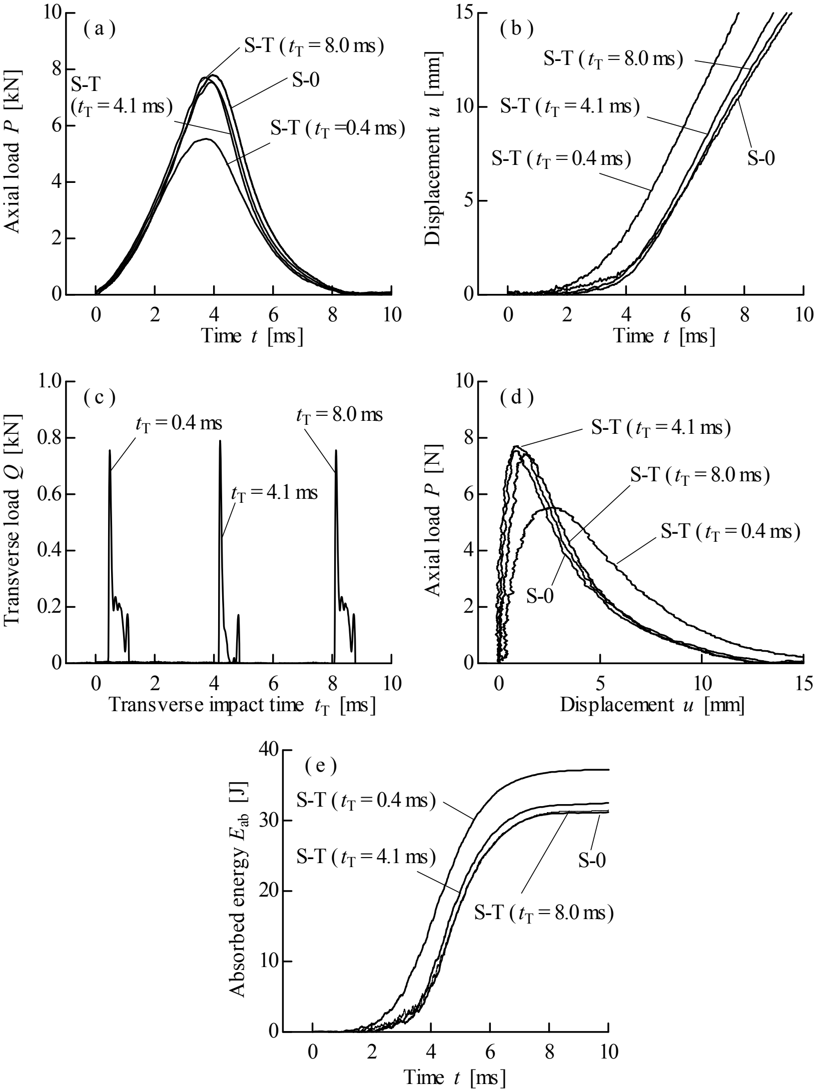

Fig. 4 Experimental results for test type $S-T$: Axial impact velocity $v_A = 3.5m/s$; transverse impact velocity $v_T = 5.3m/s$

nal work by the axial impact, can be evaluated from the envelope area of the $P-u$ curve.

Figure 4(e) shows the histories of energy absorption E_{ab}. All tests show different E_{ab} histories after buckling. The total E_{ab} for $t_T = 0.4ms$ had the highest value. The transverse impact contributes to improving the energy absorption significantly. The transverse impact instantaneously reduced the column stiffness and made the specimen more ready to absorb higher energy. The effect was observed to be strongly dependent on the transverse impact time regardless of the transverse impact velocity.

Figure 5 shows the experimental results of tests $S-0$, D_1, D_2, D_3 and D_4 (with no transverse impact) to clarify the effect of the dent on the specimen. In Fig. 5(a), each axial load was applied for approximately $8ms$. The axial impact loads reached the highest values for tests $S-0$ and D_1-0 and the lowest one for test D_4-0. As shown in Fig. 5(b), the axial displacement for test type D_3-0 was the largest. The $P-u$ curves are shown in Fig. 5(c). Different from the $P-u$ curve of the tests with a transverse impact, the $P-u$ curves for the dented specimens had the same shape as the one of test $S-0$, even though the peaks were lower and the displacements were horizontally longer. Figure 5(d) shows that the total energy absorption of test D_3-0 was the largest compared to the other tests. As expected, these

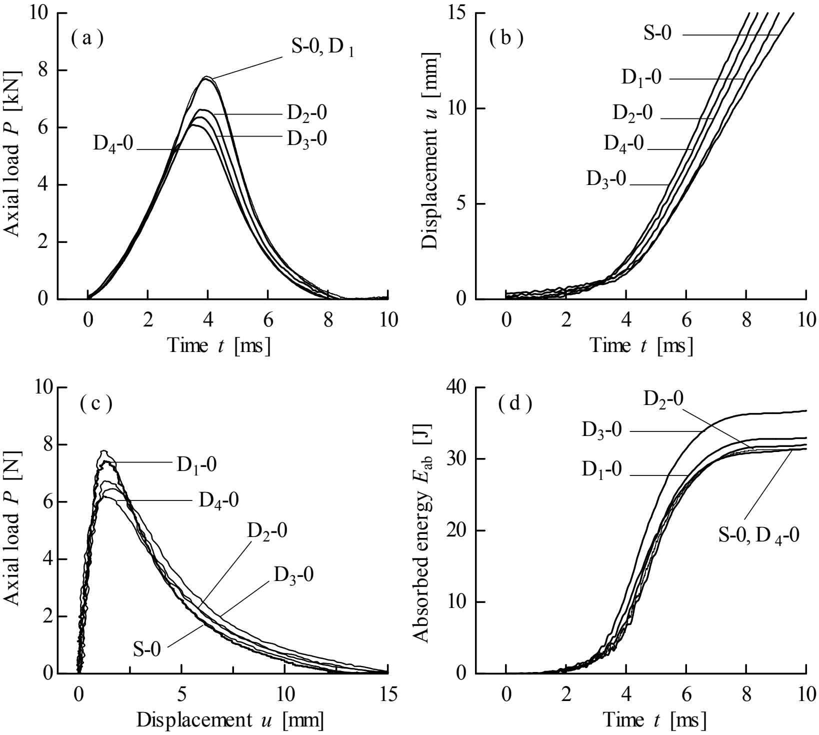

Fig. 5 Experimental results for test types D_1-0 to D_4-0: Axial impact velocity $v_A = 3.5m/s$

results denoted that the existence of dents on the specimen affects increasing the energy absorption.

5 Discussion

In the previous section, it is described that the transverse impact time t_T strongly influenced the energy absorption. Here, the effect of t_T on absorbed energy E_{ab} and maximum value of the axial load P_{max} were considered in detail. The results for the axial impact velocity v_A at $3.5 m/s$ are shown in Fig. 6. In this figure, the efficiency of E_{ab} is defined as the ratio of E_{ab} to the impact energy, which is the kinetic energy of the axial impactor just before collision. In the bottom graph of Fig. 6, the history of axial load for test $S - 0$ is shown to help understanding t_T. The E_{ab} are independent of

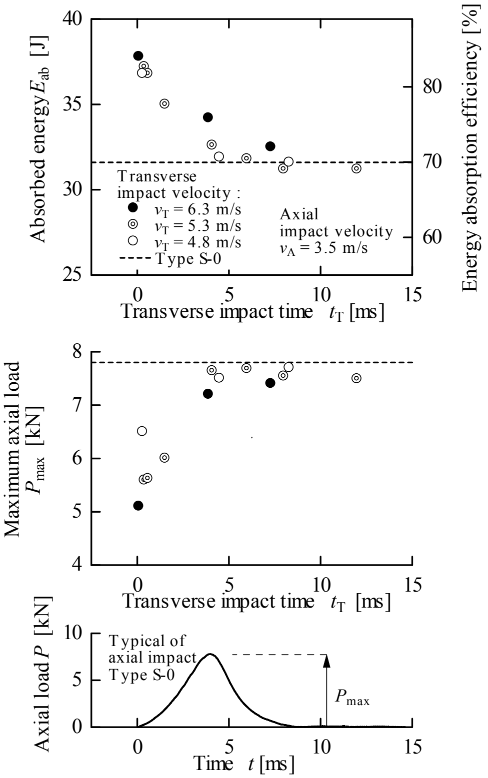

Fig. 6 Effect of transverse impact time and transverse impact velocity

the transverse impact velocity v_T within the region of these experiments but they are strongly dependent on t_T. When the transverse and axial impacts were applied to the specimen simultaneously (e.g., $t_T \cong 0$), the efficiency of E_{ab} was improved by up to 18% and P_{max} was the lowest compared to the results for tests without a transverse impact. As the transverse impact time t_T became longer, P_{max} increased and E_{ab} decreased. The transverse impact had no influence on the improvement of energy absorption when it was applied after the axial impact load reached its maximum value. This was because at that time the specimen had already buckled and deformed largely. It is considered that the instantaneous imperfection of the specimen caused by the transverse impact is more effective to induce buckling at the stage of small specimen deformation. Therefore, the energy absorption was improved much more efficiently when the transverse impact was applied simultaneously with the axial impact. Similar results were obtained for different v_A and v_T.

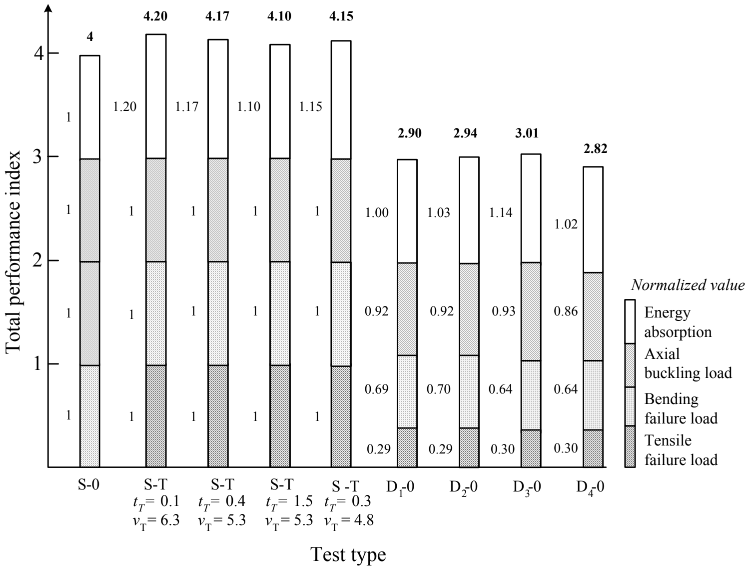

Fig. 7 Summary of energy absorption and static properties for each method

6 Summary

An overall comparison between the present method using a transverse impact and the conventional method using dents is summarized as a bar graph in Fig. 7. In this figure, the performance indexes are the structural properties normalized by the values of specimen $S-0$ as the standards. The energy absorption for the transversely impacted specimens $(S-T)$ were a little larger than that of the dented specimens $(D_1-0$ to $D_4-0)$ and much larger than those of test type $S-0$. The transverse impact and the dent methods effectively increased the capabilities of the energy absorption. The dented specimens $(D_1-0$ to $D_4-0)$ had lower buckling and failure loads than the straight specimen $S-0$. Since these static properties are dependent on the shape of the specimen, the structural properties for the transversely impacted specimens $(S-T)$ are naturally the same as those for the straight ones $(S-0)$. The present method proved to preserve the highly static properties and improve the energy absorption more effectively than the method using dents.

References

1. Ezra AA, Fay RJ (1972) An assessment of energy absorption devices for prospective use in aircraft impact. In: Herrman G, Perrone N (ed) Dynamic response of structures. Pergamon, New York.
2. Macaulay M (1987) Introduction of impact engineering. Chapman and Hall, London.
3. Jones N (1989) Structural impact. Cambridge, Cambridge.
4. Alghamdi AAA (2001) Collapsible impact energy absorbers: an overview. Thin-Walled Struct 39:189-213.
5. Lee S, Hahn C, Rhee M, Oh JE (1993) Effect of triggering on the energy absorption capacity of axially compressed aluminum tubes. Mater & Design 20:31-40.
6. Adachi T, Tanaka T, Sastranegara A, Yamaji A, Kim SK, Yang JJ (2004) Effect of transverse impact on buckling behavior of a column under static axial force. Int J Impact Eng 30:465-475.
7. Sastranegara A, Adachi T, Yamaji A (2006) Effect of Transverse Impact on Buckling Behavior of Compressed Column. Thin-Walled Struct 44:701-707.
8. Sastranegara A, Adachi T, Yamaji A (2005) Improvement of Energy Absorption of Impacted Column due to Transverse Impact. Int J Impact Eng 31:483-496.
9. Sastranegara A, Adachi T, Yamaji A (2005) Improving Energy Absorption of Impacted Column due to Transverse Impact: Finite Element Analysis. Int J Impact Eng 32:444-460.
10. Cost TL, Jones HW (1979) Dynamic response of blast loaded prestressed flat plates. J Sound Vibration 62:111-120.
11. Zeinoddini M, Harding JE, Parke GAR (1999) Dynamic behavior of axially preloaded tubular steel members of offshore structures subjected to impact damage. Ocean Eng 26:963-978.
12. Chen FL, Yu XL (2000) Influence of axial preload on plastic failure of beams subjected to transverse dynamic load. Key Eng Mater 177-180:255-260.
13. Zeinoddini M, Parke GAR, Harding JE (2002) Axially preloaded steel tubes subjected to lateral impacts: an experimental study. Int J Impact Eng 27:669-690.
14. Adachi T, Sakanoue K, Ujihashi S, Matsumoto H (1991) Damage Evaluation of CFRP Laminates Due to Iterative Impact. Trans JSME (Series A) 57:569-575 (in Japanese).

Seismic Performance of Tuned Mass Dampers

Christoph Adam and Thomas Furtmüller

Abstract In a fundamental parametric study the seismic performance of Tuned Mass Dampers (TMDs) is investigated. Earthquake excited vibration-prone structures are modeled as elastic single-degree-of-freedom oscillators and they are equipped with a single TMD. The TMD performance is assessed by means of response reduction coefficients, which are generated from the ratio of the structural response with and without TMD attached. It is found that TMDs are effective in reducing the dynamic response of seismic excited structures with light structural damping. The results of the presented study are based on a set of 40 recorded ordinary ground motions.

1 Introduction

New technologies and refined methods of analysis permit the design and construction of more slender, and hence, in many cases more vibration-prone structures with rather light damping. One effective measure to protect buildings against excessive large vibration amplitudes is the installation of Tuned Mass Dampers (TMDs). A TMD is a control device with a single-degree-of-freedom (SDOF) of either mass-spring-dashpot type, or a pendulum-dashpot system. The Tuned Liquid Column Damper (TLCD) is a variety of the TMD, which is based on the same mode of operation [1].

The natural frequency of the TMD is tuned closely to the dominant mode of the vibration-prone structure. Thus, the kinetic energy is transferred from

---

Christoph Adam
University of Innsbruck, Faculty of Civil Engineering, 6020 Innsbruck, Austria, e-mail: christoph.adam@uibk.ac.at

Thomas Furtmüller
University of Innsbruck, Faculty of Civil Engineering, 6020 Innsbruck, Austria, e-mail: thomas.furtmueller@uibk.ac.at

the vibrating main structure to the TMD, where it is subsequently dissipated by its viscous element. Optimal design of TMDs is discussed in various papers, e.g. [2 - 6].

TMDs have been proven to be effective in reducing the dynamic response of structures induced by narrow-band periodic excitation such as wind and traffic loads. However, the effectiveness of TMDs to mitigate earthquake induced vibrations is still a topic of controversial discussion. For example, [7] reports about weak seismic performance of TMDs with very small mass ratios. On the other hand, in [6] it is shown that for a large mass ratio TMDs become very effective in minimizing the structural response.

In this paper the seismic performance of TMDs, i.e. their effectiveness and robustness, is assessed. The presented parametric study of SDOF structures covers a wide range of structural periods between $0.05s$ and $5.0s$, and mass ratios between 2% and 8%. The results are based on a set of recorded ordinary ground motions.

2 Applied Procedure

2.1 Mechanical Model

A SDOF oscillator with mass M, stiffness K and viscous damping coefficient R (or expressed alternatively by the non-dimensional damping coefficient ζ_S) is utilized to represent a vibration-prone structure. The base acceleration $\ddot{x}_g$ induces structural vibrations, which are characterized by the displacement X of mass M with respect to the base. To this SDOF system a TMD is attached, which is itself a SDOF oscillator with mass m, stiffness k, and damping r (or ζ_T, alternatively). The relative displacement x of mass m is related to the base. Together, structure and TMD form a non-classically damped system with two-degrees-of-freedom (displacements X and x). An example of a structure-TMD system is shown in Figure 1.

2.2 Seismic Excitation

For this study a set of "real" earthquake records is employed to excite the structural model. This set of ordinary ground motion records, denoted as LMSR-N, contains 40 ground motions recorded in Californian earthquakes of moment magnitude between 6.5 and 7 and closest distance to the fault rupture between 13 km and 40 km on NEHRP site class D according to FEMA 368, 2000, [8]. This set of ordinary records has strong motion duration characteristics, which are not sensitive to magnitude and distance. A statistical

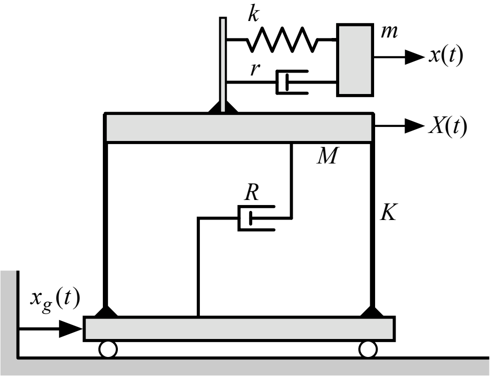

Fig. 1 Mechanical model of structure-TMD system subjected to seismic excitation

evaluation of this bin of records and its detailed description are provided in [8].

2.3 Applied Tuning Procedures

The effectivity of TMDs to mitigate the dynamic structural response depends on appropriate, or better, "optimal" tuning of its parameters, i.e. the natural frequency ω of the decoupled TMD expressed by the frequency ratio δ

$$\delta = \frac{\omega}{\Omega} \quad , \quad \omega = \sqrt{\frac{k}{m}} \quad , \quad \Omega = \sqrt{\frac{K}{M}} \tag{1}$$

and the damping ratio ζ_T [2]. In Eq. (1) Ω denotes the natural frequency of the structure without TMD. Assuming that ordinary earthquake excitation can be approximated with sufficient accuracy by a stationary white noise random process the appropriate structural response quantity to be minimized is the variance σ_x^2 of the structural displacement X. The variance σ_x^2 is related to the constant white noise spectral density S_0 by [3]

$$\sigma_x^2 = E\left[x^2(t)\right] = S_0 \int\limits_{-\infty}^{\infty} |H(\nu)|^2 \, d\nu \tag{2}$$

$H(\nu)$ is the complex frequency response function [9],

$$H(\nu) = \frac{\mu + Z(\nu)}{\mu\left(1 - \alpha^2 + 2i\zeta_S\alpha\right)}\alpha^2\nu^2 \quad , \quad Z(\nu) = \frac{\delta^2 + 2i\zeta_T\alpha\delta}{\delta^2 - \alpha^2 + 2i\zeta_T\alpha\delta} \tag{3}$$

where μ is the mass ratio and α an excitation frequency ratio,

$$\mu = \frac{m}{M} \quad , \quad \alpha = \frac{\nu}{\Omega} \tag{4}$$

Mathematically, the optimization of the TMD parameters requires a performance index J_0, which complies with σ_x^2 [4],

$$J_0 = S_0 \int_{-\infty}^{\infty} |H(\nu)|^2 \, d\nu \tag{5}$$

Subsequently, J_0 is minimized with respect to δ and ζ_T. For an undamped main structure ($\zeta_S = 0$) the optimization procedure leads to analytical expressions for the TMD parameters [3], which depend on the mass ratio μ only,

$$\delta_{opt} = \frac{\sqrt{1 - \mu/2}}{1 + \mu} \quad , \quad \zeta_{Topt} = \sqrt{\frac{\mu \, (1 - \mu/4)}{4 \, (1 + \mu) \, (1 - \mu/2)}} \tag{6}$$

In this study the parameters of the TMDs are optimized also utilizing recorded earthquake motion records. Since ordinary ground motions are random processes with in general wide-banded frequency content the performance index according to white noise excitation is utilized for the optimization procedure. However, the actual spectral density $S_i(\nu)$ of the considered record, which is a function of frequency ν, must be employed. Thus, the performance index reads [6]

$$J_i = \int_{-\infty}^{\infty} |H(\nu)|^2 \, S_i(\nu) d\nu \tag{7}$$

For a given structure, and a given ground motion record this performance index is used to determine the optimal tuning frequency and optimal viscous damping coefficient of the TMD. The procedure is repeated for all 40 records. Subsequently, the median TMD parameters of the 40 individual optimized TMD parameters are employed to derive the structural response.

2.4 Representation of Outcomes

The effectiveness of the optimized TMD is presented by means of so-called response reduction coefficients. Two types of response reduction coefficients are defined: The response reduction coefficient $R_{m,i}$ is the ratio of the structural peak displacement with attached TMD to the structural peak displacement without TMD induced by the ith earthquake record, while $R_{\sigma,i}$ is generated from the ratio of the displacement standard deviation with TMD to the displacement standard deviation without TMD,

$$R_{m,i} = \frac{\max|X_i|_{TMD}}{\max|X_i|_{NOTMD}} \quad , \quad R_{\sigma,i} = \frac{\sqrt{\int X_i^2 dt}\Big|_{TMD}}{\sqrt{\int X_i^2 dt}\Big|_{NOTMD}} \tag{8}$$

The response reduction coefficients for all 40 records are evaluated statistically. In particular, their medians R_m and R_σ are utilized to assess the TMD performance.

3 Assessment of the Seismic TMD Performance

In the following the results of parametric studies involving a series of structure-TMD systems are discussed. Thereby, each system is characterized by the natural period T_S of the stand-alone main structure, $T_S = 2\pi/\Omega$, and the mass ratio μ. After finishing all simulations for a particular structure another system with different T_S and μ is examined. The period T_S is changed stepwise with increments of $0.05s$, starting from $0.05s$ up to $5.0s$: $0.05s \leq T_S \leq 5.0s$. I.e. very stiff to soft structures are covered by the considered periods. The range of mass ratios, $0.02 \leq \mu \leq 0.08$, correlates to the mass ratios of practically applied TMDs.

In Figure 2 the response reduction coefficients R_m and R_σ are depicted as a function of structural period T_S and mass ratio μ. Viscous damping of the main structure is selected to be 1% ($\zeta_S = 0.01$). TMDs of this parametric study are tuned according to the assumption of white-noise ground acceleration, compare with Eq. (5). The median response reduction coefficients R_m shown in Figure 2(a) reveal that the median peak displacements are reduced for all combinations of T_S and μ, since R_m is always smaller than 1. A reduction from 10% to 40% can be observed. As expected the response diminishes with increasing mass ratio. Furthermore it can be seen that the effectiveness of TMDs is better for short period structures than for long period systems.

The response reduction coefficients R_σ of displacement standard deviations are plotted in Figure 2(b). They exhibit values between 0.35 and 0.65. These results demonstrate that for this set of earthquake records TMDs are capable to reduce the vibration amplitudes of seismic excited structures.

Figure 3 shows the distribution of response reduction coefficients R_m and R_σ for the same set of main structures. However, tuning of the attached TMDs is based on the optimization procedure including the actual earthquake records, see Eq. (7). Comparison of these outcomes with the results of Figure 2 reveals that the influence of the applied tuning procedure on the performance of TMDs is of negligible magnitude, since the median TMD parameters instead of the individual optimized TMD parameters are employed. Thus, for this study simplified tuning of the TMD parameters for stationary white noise base acceleration is justified, although real recorded ordinary ground motions induce structural vibrations. Subsequently, the control effectiveness of TMDs for structures with heavier damping is discussed. Viscous structural damping of the main structure is increased to 3% ($\zeta_S = 0.03$). TMD parameters are optimally tuned for white noise ground acceleration. Figure 4 verifies that the effectiveness of TMDs declines for main structures with heavier structural damping. For the considered mass ratios and structural periods the peak displacements can be reduced at most up to 30% (i.e. a R_m of 0.70), but in average not more than 15% to 20%, compare with Figure 4(a). For the standard deviation of displacements a reduction of up to 45% can be achieved (i.e. a R_σ of 0.55). Eventually, the robustness of the seismic TMD performance to uncertainty in its parameters is studied. Exemplarily, a structure-TMD system with the following properties is considered: Mass

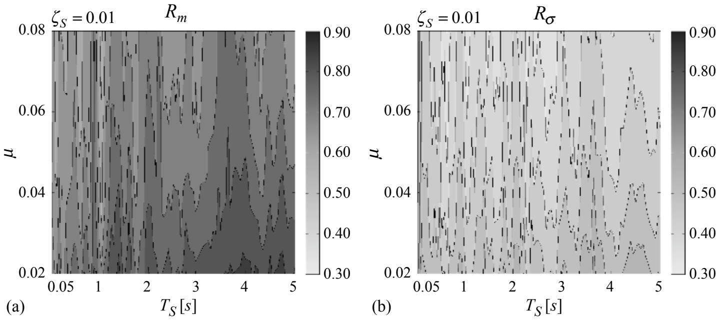

Fig. 2 Response reduction coefficients, optimal TMD tuning assuming white noise base excitation: (a) peak displacement, (b) standard deviation of displacement

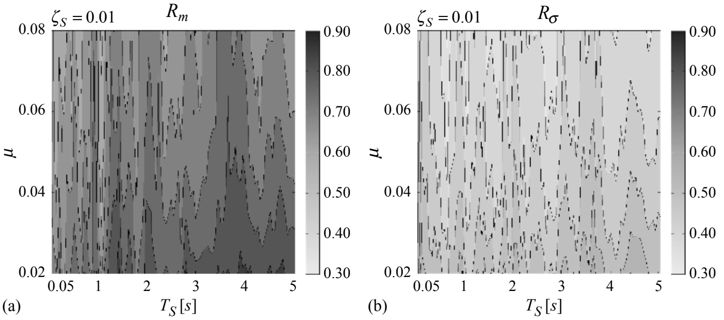

Fig. 3 Response reduction coefficients, optimal TMD using actual seismic ground motions records: (a) peak displacement, (b) standard deviation of displacement

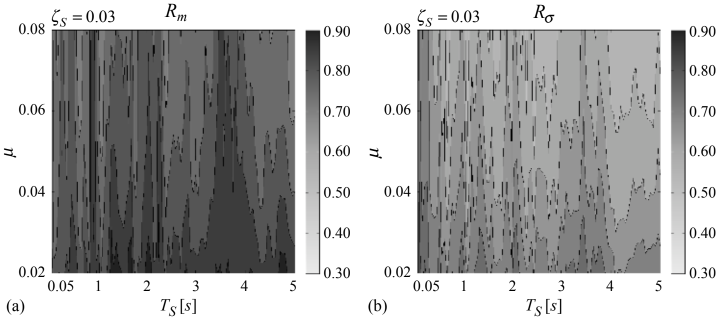

Fig. 4 Response reduction coefficients, optimal TMD tuning assuming white noise base excitation: (a) peak displacement, (b) standard deviation of displacement

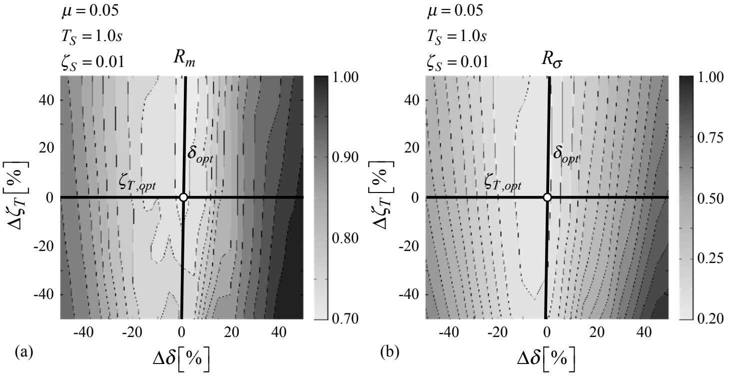

Fig. 5 Response reduction coefficients, effect of mistuned TMD parameters: (a) peak displacement, (b) standard deviation of displacement

ratio $\mu = 0.05$, period of the decoupled main structure $T = 1.0s$, damping of the main structure $\zeta_S = 0.01$. Tuning of the TMD utilizing the performance index J_0, Eq. (5), leads to the following optimal TMD parameters: $\delta_{opt} = 0.935$, $\zeta_{T,opt} = 0.110$. The response reduction coefficients R_m and R_σ are determined for this optimal TMD configuration. Subsequently, the frequency ratio and the damping coefficient are stepwise mistuned from -50% to 50% compared to the corresponding optimal value. For each mistuned system the response reduction coefficients are plotted as a function of the deviation from optimal conditions. The results are visualized in Figure 5, where a horizontal black line refers to results based on the optimal damping coefficient $\zeta_{T,opt}$, and the vertical black line highlights response reduction coefficients derived utilizing the optimal frequency ratio δ_{opt}. The intersection point of both lines identifies results for optimal tuning parameters. Both, R_m (Figure 5(a)) and R_σ (Figure 5(b)) reveal that the seismic TMD performance is robust with respect to mistuning of the TMD damping coefficient ζ_T as long as δ is optimal. However, mistuning of δ has a grave effect on the TMD effectiveness. In particular, if δ is much larger than δ_{opt} the TMD is not able to function properly. However, mistuning of δ less than 3% can be accepted for this particular system and set of ground motions.

4 Conclusion

The results presented in this study suggest that the application of Tuned Mass Dampers (TMDs) with mass ratios between 2% and 8% is an appropriate measure to mitigate the dynamic response of structures subjected to ordinary seismic ground motions. This statement applies both for stiff and soft structures. The seismic effectiveness of an optimally tuned TMD decreases with increasing initial structural damping of the vibrating structure. Reviewing the results obtained in this study reveals that optimal tuning of the TMD parameters under the assumption of white noise base acceleration is sufficiently accurate. The seismic performance of the TMD is robust against mistuning of the viscous element in the TMD. However, accurate tuning of the TMD natural frequency is essential for its effectiveness.

References

1. Ziegler F (2008) Special design of tuned liquid column-gas dampers for the control of spatial structural vibrations. Acta Mechanica 201: 249-267
2. Den Hartog JP (1956) Mechanical Vibrations. 4^{th} ed. McGraw-Hill, New York
3. Ayorinde EO, Warburton GB (1980) Minimizing structural vibrations with absorbers. Earthquake Engineering and Structural Dynamics 8: 219-236
4. Hoang N, Warnitchai P (2005) Design of multiple tuned mass dampers by using a numerical optimizer. Earthquake Engineering and Structural Dynamics 34: 125-144
5. Lee C-L, Chen Y-T, Chung L-L, Wang Y-P (2006) Optimal design theories and applications of tuned mass dampers. Engineering Structures 28: 43-53
6. Hoang N, Fujino Y, Warnitchai P (2008) Optimal tuned mass damper for seismic applications and practical design formulas. Engineering Structures 30: 707-715
7. Casciati F, Giulani F (accepted for publication) Performance of multi-TMD in the towers of suspension bridges. Journal of Vibration and Control
8. Medina RA, Krawinkler H (2003) Seismic demands for nondeteriorating frame structures and their dependence on ground motions. Report no. 144. The John A. Blume Earthquake Engineering Center, Stanford University
9. Igusa T, Xu K (1994) Vibration control using multiple tuned mass dampers. Journal of Sound and Vibration 175: 491-503

Problems in Fast Moving Non-Holonomic Elastic Systems

Hartmut Bremer

Abstract The Central Equation of Dynamics allows a unified view on existing methods and reveals them as a specific view on one and the same classical mechanics. Thereby, the particular methods exhibit special advantages and disadvantages according to the aim of investigation. For the derivation of the motion equations, the analytical methods display some drawbacks: the use of non-holonomic velocities needs an enormous effort and non-holonomic constraints can not à-priori be considered. Due to the directional derivatives w.r.t. the angular velocities, the obtained linearized equations do not represent the motions w.r.t. the co-rotational frame (and any orthogonal frame, resp.) as usually requested. This fact may lead to severe misinterpretations. In elastic multi body systems, the calculation effort increases dramatically. All these drawbacks are removed when using the Projection Equation.

1 Basics: The Central Equation of Dynamics

The principle of virtual work in dynamics,

$$\int_{(S)} (dm\ddot{\mathbf{r}} - d\mathbf{f}^e)^T \delta\mathbf{r} = 0, \tag{1}$$

was established by J.L. de Lagrange in 1764. Two years before he explained "I have to emphasize that I introduced a new characteristic δ; here, $\delta\mathbf{r}$[1] shall express a differential w.r.t. $\mathbf{r}$ which is not the same as $d\mathbf{r}$ but which is nevertheless built with the same rules". This statement obviously misled many people, in the past as well as in the present, ["obscure" (L.Poinsot,

---

Hartmut Bremer
Institut für Robotik, Johannes Kepler Universität Linz, e-mail: hartmut.bremer@jku.at

[1] Z from his original contribution is replaced here with $\mathbf{r}$.

1837); "black magic" (Th. Kane (1986)]. However, considering $d\mathbf{r}/dt$ instead of $d\mathbf{r}$ sheds light on the brilliant background of LAGRANGE's concept: $d\mathbf{r}/dt = \dot{\mathbf{r}}$ and $\delta\mathbf{r}$ are tangent vectors w.r.t. the constraint plane $\boldsymbol{\Phi}(\mathbf{r}) = 0 : (\partial\boldsymbol{\Phi}/\partial\mathbf{r})\dot{\mathbf{r}} = 0 \bigwedge (\partial\boldsymbol{\Phi}/\partial\mathbf{r})\delta\mathbf{r} = 0$. (LAGRANGE himself calls $\delta\mathbf{r}$ virtual *velocities*). Hence, $\delta\mathbf{r}$ is kept arbitrary (in direction and in magnitude) while $\dot{\mathbf{r}}$ represents the real solution. Adopting this intepretation leads with a few steps of calculation to the Central Equation of Dynamics

$$\frac{d}{dt}\left[\left(\frac{\partial T}{\partial \dot{\mathbf{s}}}\right)\delta\mathbf{s}\right] - \delta T - \delta W = 0, \quad \begin{cases} T : \text{kinetic energy} \\ \dot{\mathbf{s}} = \mathbf{H}(\mathbf{q})\dot{\mathbf{q}} : \text{minimal velocities,} \\ \qquad\qquad \text{non-holonomic} \\ \mathbf{q} \in \mathbb{R}^f : \text{minimal coordinates} \\ \mathbf{H} \in \mathbb{R}^{f,f} : \text{regular,} \end{cases} \tag{2}$$

from which a considerable body of methods in dynamics is derived (HELMHOLTZ, GIBBS, APPELL, HAMILTON, LAGRANGE, TZENOFF, NIELSEN, MAGGI, HAMEL $\cdots$ and the Projection Equation). The Central Equations thereby states that all these methods represent one and the same (classical) mechanics but looked at from different view-points. The Central Equation allows thus a fair comparison of methods.

2 Non-Holonomicity

The motion of a (fast moving) elastic system is composed of "rigid body coordinates" and of superimposed "elastic coordinates" (the combination of which has been introduced as "hybrid coordinates" by P.W. LIKINS in the 1970ies). The corresponding "elastic velocities" are assumed to move with small amplitudes and are therefore integrable. Thus, non-holonomicity can only arise from the rigid body motion. It is essential to emphasize that non-holonomic velocities have à-priori nothing in common with non-holonomic constraints while, the other way round, non-holonomic constraints need non-holonomic velocities for description.

2.1 Analytical Methods

One of the most common procedures for the treatment of non-holonomic systems is due to G. HAMEL. His (explicit form of) equations read

$$\frac{d}{dt}\frac{\partial T}{\partial \dot{s}_n} - \frac{\partial T}{\partial s_n} - Q_n + \sum_{\nu,\mu}\frac{\partial T}{\partial \dot{s}_\nu}\dot{s}_\mu\beta_\nu^{\mu,n} = 0\,; \quad n = 1\cdots f, \tag{3}$$

$$\beta_\nu^{\mu,n} = \sum_{i,k} \frac{\partial \dot{q}_k}{\partial \dot{s}_\mu} \frac{\partial \dot{q}_i}{\partial \dot{s}_n} \left(\frac{\partial^2 s_\nu}{\partial q_i \partial q_k} - \frac{\partial^2 s_\nu}{\partial q_k \partial q_i} \right) = -\beta_\nu^{n,\mu} \, , \quad i,k = 1 \cdots f, \tag{4}$$

where $\beta_\nu^{\mu,n}$ represent his famous coefficients; as can be seen from Eq.(4), they are zero for s_ν being holonomic (fulfillment of H. SCHWARZ's rule). For nonholonomic s_ν, the term in parentheses vanishes for $i = k$, thus $2f(f-1)$ summation terms remain for each $\beta_\nu^{\mu,n}$.

Let us consider a simplified model of a (rigid) car neglecting the wheel masses. It moves in the (inertial) x-y-plane with velocities v_x, v_y, γ. The front wheel is a suspension wheel with arbitrary motion while the rear wheels are not allowed to slide, i.e. $v_y = 0$ w.r.t. the body-fixed frame (index B). This is a non-holonomic constraint. It is, however, not allowed to set $v_y = 0$ in advance, since then T would not more depend on v_y yielding wrong results. Thus, the calculation has first to be done for the whole set of variables:

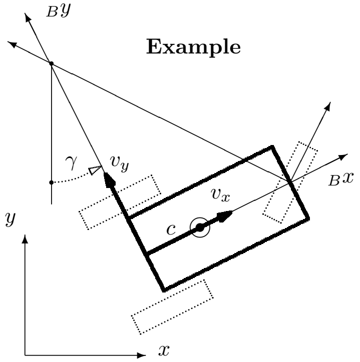

$$T = \frac{1}{2} \dot{\mathbf{s}}^T \begin{bmatrix} m & 0 & 0 \\ 0 & m & mc \\ 0 & mc & C^o \end{bmatrix} \dot{\mathbf{s}},$$

$$\dot{\mathbf{s}} = \begin{pmatrix} v_x \\ v_y \\ \omega_z \end{pmatrix} \, , \quad \mathbf{q} = \begin{pmatrix} x \\ y \\ \gamma \end{pmatrix} \, , \tag{5}$$

$$\begin{pmatrix} \dot{s}_1 \\ \dot{s}_2 \\ \dot{s}_3 \end{pmatrix} = \begin{bmatrix} \cos\gamma & \sin\gamma & 0 \\ -\sin\gamma & \cos\gamma & 0 \\ 0 & 0 & 1 \end{bmatrix} \begin{pmatrix} \dot{q}_1 \\ \dot{q}_2 \\ \dot{q}_3 \end{pmatrix} \Rightarrow \begin{pmatrix} \dot{q}_1 \\ \dot{q}_2 \\ \dot{q}_3 \end{pmatrix} = \begin{bmatrix} \cos\gamma & -\sin\gamma & 0 \\ \sin\gamma & \cos\gamma & 0 \\ 0 & 0 & 1 \end{bmatrix} \begin{pmatrix} \dot{s}_1 \\ \dot{s}_2 \\ \dot{s}_3 \end{pmatrix} \, , \tag{6}$$

(m: mass, c: mass center distance, C^o: moment of inertia w.r.t. the B-frame origin). The determination of the β's is tedious[2] even for this simple example. They turn out $+1, -1, 0$, e.g.

$$\beta_1^{1,3} = -\frac{\partial q_1}{\partial s_1} \frac{\partial^2 s_1}{\partial q_1 \partial q_3} - \frac{\partial q_2}{\partial s_1} \frac{\partial^2 s_1}{\partial q_2 \partial q_3} = (-\cos\gamma)(-\sin\gamma) - (\sin\gamma)(\cos\gamma) = 0 \tag{7}$$

etc. From Eq.(3) one obtains the equations

---

[2] For practical purposes, HAMEL himself prefers a direct calculation of $d\delta\mathbf{s} - \delta d\mathbf{s}$: "it is perhaps not always convenient to calculate the table of the β's . . . but in fact easier to look for the δs_μ from the expression $\delta d s_\rho - d\delta s_\rho$" [Hamel 1949], p. 483. (Hamel's original ϑ is replaced here with s).

$$
\begin{aligned}
&(\frac{d}{dt}\frac{\partial T}{\partial v_x} + \underbrace{\beta_2^{3,1}}_{-1}\omega_z\frac{\partial T}{\partial v_y} - Q_1)\delta s_1 = \big[m\dot{v}_x - mc\omega_z^2 - m\omega_z v_y - f_x\big]\,\delta s_1 = 0,\\
&(\frac{d}{dt}\frac{\partial T}{\partial v_y} + \underbrace{\beta_1^{3,2}}_{+1}\omega_z\frac{\partial T}{\partial v_x} - Q_2]\delta s_2 = [m\dot{v}_y + mc\dot{\omega}_z + m\omega_z v_x - f_y)\,\delta s_2 = 0,\\
&\qquad(\frac{d}{dt}\frac{\partial T}{\partial \omega_z} + \underbrace{\beta_1^{2,3}}_{-1}v_y\frac{\partial T}{\partial v_x} + \underbrace{\beta_2^{1,3}}_{+1}v_x\frac{\partial T}{\partial v_y} - Q_3)\delta s_3\\
&\qquad\quad = [C^o\dot{\omega}_z + mc\dot{v}_y + mcv_x\omega_z - M_z]\,\delta s_3 = 0, \qquad (8)
\end{aligned}
$$

which, after inserting the non-holonomic constraint $v_y = 0$, yields the equations of motion

$$
\begin{bmatrix} m & 0 \\ 0 & C^o \end{bmatrix}\begin{pmatrix} \dot{v}_x \\ \dot{\omega}_z \end{pmatrix} + \begin{bmatrix} 0 & -mc\omega_z \\ mc\omega_z & 0 \end{bmatrix}\begin{pmatrix} v_x \\ \omega_z \end{pmatrix} - \begin{pmatrix} f_x \\ M_z \end{pmatrix} = \begin{pmatrix} 0 \\ 0 \end{pmatrix}. \qquad (9)
$$

2.2 Projection Equation

On the other hand, applying the Projection Equation

$$
\sum_{i=1}^{N}\left\{\left[\left(\frac{\partial \mathbf{v}_c}{\partial \dot{\mathbf{s}}}\right)^T \left(\frac{\partial \boldsymbol{\omega}_c}{\partial \dot{\mathbf{s}}}\right)^T\right]\begin{bmatrix} \dot{\mathbf{p}} + \widetilde{\boldsymbol{\omega}}_{IR}\mathbf{p} - \mathbf{f}^e \\ \dot{\mathbf{L}} + \widetilde{\boldsymbol{\omega}}_{IR}\mathbf{L} - \mathbf{M}^e \end{bmatrix}\right\}_i = 0 \qquad (10)
$$

(index c: mass center, index IR: reference frame R w.r.t. inertial frame I; $\mathbf{v}, \boldsymbol{\omega}$: velocity and angular velocity.; $\mathbf{p}, \mathbf{L}$: momentum and momentum of momentum; $\mathbf{f}^e, \mathbf{M}^e$: impressed force and torque; $\widetilde{(\;)}$: spin tensor; all terms represented in the reference coordinate system R) leads directly to the desired results. Once the cartesian velocities are calculated, all the remainder is known. Especially, the functional matrix $[(\partial \mathbf{v}_c/\partial \dot{\mathbf{s}})^T(\partial \boldsymbol{\omega}_c/\partial \dot{\mathbf{s}})^T]$ is nothing but the coefficient matrix of the cartesian velocities w.r.t. the (chosen or calculated) minimal velocities $\dot{\mathbf{s}}$. For the car model we have

$$
\begin{pmatrix} v_{cx} \\ v_{cy} \\ \omega_{cz} \end{pmatrix} = \begin{bmatrix} 1 & 0 \\ 0 & c \\ 0 & 1 \end{bmatrix}\dot{\mathbf{s}}\,, \quad \dot{\mathbf{s}} = \begin{pmatrix} v_x \\ \omega_z \end{pmatrix}. \qquad (11)
$$

The chosen reference frame is the body-fixed one and the non-holonomic constraint $v_y = 0$ is already inserted. The matrix in square brackets represents the requested functional matrix $[(\partial v_{cx}/\partial \dot{\mathbf{s}})^T(\partial v_{cy}/\partial \dot{\mathbf{s}})^T(\partial \omega_{cz}/\partial \dot{\mathbf{s}})^T]^T$. The momenta are obtained by multiplication with m (mass) and C^c (moment of inertia w.r.t. the mass center c), respectively. These ingredients are combined according to Eq.(10) by simple matrix multiplications to obtain the motion equations without any detour,

$$\begin{bmatrix} 1 & 0 & 0 \\ 0 & c & 1 \end{bmatrix} \left\{ \begin{bmatrix} m & 0 \\ 0 & mc \\ 0 & C^c \end{bmatrix} \ddot{\mathbf{s}} + \begin{bmatrix} 0 & -\omega_z & 0 \\ \omega_z & 0 & 0 \\ 0 & 0 & 0 \end{bmatrix} \begin{bmatrix} m & 0 \\ 0 & mc \\ 0 & C^c \end{bmatrix} \dot{\mathbf{s}} - \begin{pmatrix} f_x \\ f_y \\ M_z \end{pmatrix} \right\} = 0, \qquad (12)$$

yielding Eq.(9) directly.

As a conclusion one may state that for non-holonomic systems the use of the Projection Equation is preferable to the use of any of the analytical methods which come into question. The calculation requirements are simple and the non-holonomic constraints may be inserted already at the beginning. This is because directional derivations are not requested. The required effort is minimal.

3 Rigid Multibody Systems (MBS)

For a later comparison with fast moving elastic systems we may stay for a short while with MBS. The over all sum in Eq.(10) may be split into a double sum where the first one denotes a number of considered subsystems to be chosen. The second one then characterizes the number of bodies N_n within the actual subsystem n. Along with the chain rule of differentiation one obtains

$$\sum_{n=1}^{N_{sub}} \left(\frac{\partial \dot{\mathbf{y}}_n}{\partial \dot{\mathbf{s}}}\right)^T \sum_{i=1}^{N_n} \left\{ \left[\left(\frac{\partial \mathbf{v}_c}{\partial \dot{\mathbf{y}}_n}\right)^T \left(\frac{\partial \boldsymbol{\omega}_c}{\partial \dot{\mathbf{y}}_n}\right)^T \right] \begin{bmatrix} \dot{\mathbf{p}} + \widetilde{\boldsymbol{\omega}}_{IR}\mathbf{p} - \mathbf{f}^e \\ \dot{\mathbf{L}} + \widetilde{\boldsymbol{\omega}}_{IR}\mathbf{L} - \mathbf{M}^e \end{bmatrix} \right\}_i = 0 \qquad (13)$$

in terms of describing velocities $\dot{\mathbf{y}}_n$ for each subsystem. Carrying out the calculation for the second sum, from 1 to N_n, leads to the typical structure of mechanical systems in the form $[\mathbf{M}_n\ddot{\mathbf{y}}_n + \mathbf{G}_n\dot{\mathbf{y}}_n - \mathbf{Q}_n]$. In matrix notation one has then for Eq.(13)

$$\left[\left(\frac{\partial \dot{\mathbf{y}}_1}{\partial \dot{\mathbf{s}}}\right)^T \left(\frac{\partial \dot{\mathbf{y}}_2}{\partial \dot{\mathbf{s}}}\right)^T \cdots \left(\frac{\partial \dot{\mathbf{y}}_N}{\partial \dot{\mathbf{s}}}\right)^T \right] \begin{bmatrix} \mathbf{M}_1\ddot{\mathbf{y}}_1 + \mathbf{G}_1\dot{\mathbf{y}}_1 - \mathbf{Q}_1 \\ \mathbf{M}_2\ddot{\mathbf{y}}_2 + \mathbf{G}_2\dot{\mathbf{y}}_2 - \mathbf{Q}_2 \\ \vdots \\ \mathbf{M}_N\ddot{\mathbf{y}}_N + \mathbf{G}_N\dot{\mathbf{y}}_N - \mathbf{Q}_N \end{bmatrix} = 0 \qquad (14)$$

where N_{sub} is abbreviated N for brevity. The describing velocities follow from the kinematic chain $\dot{\mathbf{y}}_n = \mathbf{T}_{np}\dot{\mathbf{y}}_p + \mathbf{F}_n\dot{\mathbf{s}}_n$ (index p: predecessor). Starting with the first subsystem which does not have a predecessor yields $\dot{\mathbf{y}}_1 = \mathbf{F}_1\dot{\mathbf{s}}_1$. Insertion into $\dot{\mathbf{y}}_2$ then yields $\dot{\mathbf{y}}_2 = \mathbf{T}_{21}\mathbf{F}_1\dot{\mathbf{s}}_1 + \mathbf{F}_2\dot{\mathbf{s}}_2$, hence $\dot{\mathbf{y}}_3 = \mathbf{T}_{31}\mathbf{F}_1\dot{\mathbf{s}}_1 + \mathbf{T}_{32}\mathbf{F}_2\dot{\mathbf{s}}_2 + \mathbf{F}_2\dot{\mathbf{s}}_3$ where $\mathbf{T}_{31} = \mathbf{T}_{32}\mathbf{T}_{21}$ etc. Using $\dot{\mathbf{s}} = (\dot{\mathbf{s}}_1^T \dot{\mathbf{s}}_2^T \cdots \dot{\mathbf{s}}_N^T)^T$ for minimal velocities leads Eq.(14) to

$$\begin{bmatrix} \mathbf{F}_1^T & \mathbf{F}_1^T\mathbf{T}_{21}^T & \cdots & \mathbf{F}_1^T\mathbf{T}_{\mathrm{N}1}^T \\ & \mathbf{F}_2^T & \cdots & \mathbf{F}_2^T\mathbf{T}_{\mathrm{N}2}^T \\ & & \ddots & \vdots \\ & & & \mathbf{F}_{\mathrm{N}}^T \end{bmatrix} \begin{bmatrix} \mathbf{M}_1\ddot{\mathbf{y}}_1 + \mathbf{G}_1\dot{\mathbf{y}}_1 - \mathbf{Q}_1 \\ \mathbf{M}_2\ddot{\mathbf{y}}_2 + \mathbf{G}_2\dot{\mathbf{y}}_2 - \mathbf{Q}_2 \\ \vdots \\ \mathbf{M}_{\mathrm{N}}\ddot{\mathbf{y}}_{\mathrm{N}} + \mathbf{G}_{\mathrm{N}}\dot{\mathbf{y}}_{\mathrm{N}} - \mathbf{Q}_{\mathrm{N}} \end{bmatrix} = 0 \qquad (15)$$

which gives access to either a minimal representation (by inserting $\dot{\mathbf{y}}_n, \ddot{\mathbf{y}}_n$ explicitly) or to a recursive alorithm in the sense of a GAUSSian elimination procedure. Obviously, the use of the Projection Equation once more leads to minimum effort when compared to the analytical procedures.

4 Orthogonality

4.1 Hamilton's Principle

One of the most popular procedures in the field of elastic body oscillations is the use of HAMILTON's Principle to derive the equations of motion. Its direct use in fast moving elastic systems, however, may cause problems. This is demonstrated by a simple example: consider an elastic beam [two bending variables $v(x,t)$ and $w(x,t)$] which rotates quickly around its x-axis with $\dot{\alpha}$. HAMILTON's Principle requires the variation of the kinetic energy T and of the elastic potential V,

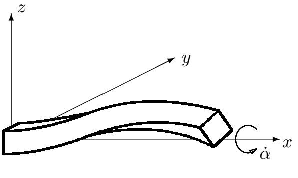

$$\delta T = \int_0^L \left(\mathbf{v}_c^T \rho A \delta \mathbf{v}_c + \boldsymbol{\omega}_c^T \rho \mathbf{I} \delta \boldsymbol{\omega}_c\right) dx,$$

$$\delta V = \int_0^L \left(EI_z v''\delta v'' + EI_y w''\delta w''\right) dx,$$

$$\delta W = M_x \delta\alpha \quad (16)$$

where: ρ: mass density, A: cross sectional area, $\mathbf{I} = diag\{I_x, I_y, I_z\}$: tensor of area moments of inertia, E: YOUNG's modulus, M_x: driving torque. The mass center velocities of an element are

$$\mathbf{v}_c = \begin{pmatrix} 0 \\ \dot{v} - \dot{\alpha} w \\ \dot{w} + \dot{\alpha} v \end{pmatrix}, \quad \omega_c = \begin{bmatrix} \left(1 - \frac{v'^2}{2} - \frac{w'^2}{2}\right) & v' & 0 \\ -v' & \left(1 - \frac{v'^2}{2}\right) & 0 \\ -w' & 0 & 1 \end{bmatrix} \begin{pmatrix} \dot{\alpha} \\ -\dot{w}' \\ \dot{v}' \end{pmatrix} \qquad (17)$$

where a CARDAN–sequence $-w', v'$ has been chosen for transformation from the reference frame (rotating with $\dot{\alpha}$) to the element-fixed frame (sometimes referred to as TAIT-BRYAN-sequence in the english speaking area). The prime denotes spatial derivation, $(\,)' = \partial(\,)/\partial x$. Without going into the details of (the tedious) calculations, one obtains, after carrying out the required integrations by parts, a result in the form $\int_0^L\{\delta\alpha[\cdots]+\delta v[\cdots]+\delta w[\cdots]\}$ plus boundary terms. This is correct. However, usually one takes the square brackets as motion equations, setting these individually equal to zero. Then, in the present case, one obtains a rather strange result. Considering a circular cross sectional area ($I_x = 2I_y = 2I_z := 2I$) yields

$$\begin{aligned}\int_0^L (\rho I_x\ddot{\alpha} - M_x)dx = 0 \quad (\Rightarrow \alpha(t) \text{ known function}),\\ \rho A(\ddot{v} - 2\dot{\alpha}\dot{w}\underline{-\ddot{\alpha}w} - \dot{\alpha}^2 v) - \rho I(\ddot{v}'' + v''\dot{\alpha}^2\underline{\underline{-w''\ddot{\alpha}}}) + (EIv'')'' = 0,\\ \rho A(\ddot{w} + 2\dot{\alpha}\dot{v}\underline{+\ddot{\alpha}v} - \dot{\alpha}^2 w) - \rho I(\ddot{w}'' + w''\dot{\alpha}^2\underline{\underline{-v''\ddot{\alpha}}}) + (EI_y w'')'' = 0.\end{aligned} \tag{18}$$

Here, the (generalized) circulatory forces due to the angular acceleration $\ddot{\alpha}$ are, as expected, skew-symmetric for the translational part (ρA), but they are symmetric for the rotational part (ρI). The reason is, that the rotation axes which are assigned to the Cardan angular velocities ($\dot{\alpha}, -\dot{w}', \dot{v}'$ in the present example) are not orthogonal. Because the analytical methods require directional derivatives w.r.t. these, Eq.(18) represents the motion equations in a non-orthogonal coordinate system which depends on the choice of the sequence of deformations even in the case of small deformations. An interpretation as motion equations w.r.t. the co-rotating reference frame, as usually requested, is wrong.

4.2 The Projection Equation

The same as in the case of non-holonomic systems, the Projection Equation does not need directional derivations and will therefore avoid such difficulties. Considering elastic multibody systems (EMBS), the number of bodies of a subsystem (e.g. beam slices) goes to infinity and the summation is replaced with an integral, yielding the same equation structure as in the rigid body case:

$$\sum_{n=1}^{N_{sub}} \int_{B_n} \left(\frac{\partial \dot{\mathbf{y}}_n}{\partial \dot{\mathbf{s}}}\right)^T \underbrace{\left\{\left[\left(\frac{\partial \mathbf{v}_c}{\partial \dot{\mathbf{y}}_n}\right)^T \left(\frac{\partial \boldsymbol{\omega}_c}{\partial \dot{\mathbf{y}}_n}\right)^T\right] \begin{bmatrix} d\dot{\mathbf{p}} + \widetilde{\boldsymbol{\omega}}_{IR} d\mathbf{p} - d\mathbf{f}^e \\ d\dot{\mathbf{L}} + \widetilde{\boldsymbol{\omega}}_{IR} d\mathbf{L} - d\mathbf{M}^e \end{bmatrix}\right\}_n}_{[d\mathbf{M}_n \ddot{\mathbf{y}}_n + d\mathbf{G}_n \dot{\mathbf{y}}_n - d\mathbf{Q}_n]} = 0 \tag{19}$$

However, since the describing velocities now require the consideration of partial derivatives w.r.t. the spatial variables (arising from bending angles and curvatures), the functional matrix $(\partial \dot{\mathbf{y}}_n/\partial \dot{\mathbf{s}})$ can not directly be calculated. We therefore pass to the corresponding virtual work expression,

$$\sum_{n=1}^{N_{sub}} \int\limits_{B_n} \delta \mathbf{y}_n^T \left[d\mathbf{M}_n \ddot{\mathbf{y}}_n + d\mathbf{G}_n \dot{\mathbf{y}}_n - d\mathbf{Q}_n \right] = 0. \tag{20}$$

The solution steps are as follows: Consider $N_{sub} = 1$ for simplicity. Then $\dot{\mathbf{y}}$ is calculated with the aid of a differential operator, $\dot{\mathbf{y}} = \overline{\mathcal{D}} \circ \dot{\mathbf{s}}$, yielding $\delta \mathbf{y} = \overline{\mathcal{D}} \circ \delta \mathbf{s}$. Integration by parts yields

$$\int\limits_{B_n} \delta \mathbf{s}^T \mathcal{D}^T \circ \left[d\mathbf{M}_n \ddot{\mathbf{y}}_n + d\mathbf{G}_n \dot{\mathbf{y}}_n - d\mathbf{Q}_n \right] + \delta W_{bound} = 0 \tag{21}$$

with a new differential operator $\mathcal{D}$. This seemingly costly procedure results extremely simple: The operator $\overline{\mathcal{D}}$ follows from $\dot{\mathbf{y}}$ which contains the deviations, the bending angles and the curvatures,

$$\dot{\mathbf{y}} = \begin{pmatrix} \dot{\alpha} \\ \dot{v} \\ \dot{w} \\ -\dot{w}' \\ \dot{v}' \\ \dot{v}'' \\ \dot{w}'' \end{pmatrix} = \begin{bmatrix} 1 & 0 & 0 \\ 0 & 1 & 0 \\ 0 & 0 & 1 \\ 0 & 0 & -\frac{\partial}{\partial x} \\ 0 & \frac{\partial}{\partial x} & 0 \\ 0 & \frac{\partial^2}{\partial x^2} & 0 \\ 0 & 0 & \frac{\partial^2}{\partial x^2} \end{bmatrix} \circ \begin{pmatrix} \dot{\alpha} \\ \dot{v} \\ \dot{w} \end{pmatrix} = \bar{\mathcal{D}} \circ \dot{\mathbf{s}}. \tag{22}$$

The requested operator $\mathcal{D}$ is the same as $\overline{\mathcal{D}}$ with the only difference that odd derivatives change their sign. (Simultaneously one obtains the operators $\mathcal{B}_0$ and $\mathcal{B}_1$ for the (kinetic) boundary conditions by successive degeneration of the differentiation grade with once more changing sign – this reflects the consecutive integrations by parts with its sign changes). Applying $\mathcal{D}^T$ to $d\mathbf{M}\ddot{\mathbf{y}} + d\mathbf{G}\dot{\mathbf{y}} - d\mathbf{Q}$ yields, for the present example,

$$\begin{bmatrix} 1 & 0 & 0 & 0 & 0 & 0 & 0 \\ 0 & 1 & 0 & 0 & -\frac{\partial}{\partial x} & \frac{\partial^2}{\partial x^2} & 0 \\ 0 & 0 & 1 & \frac{\partial}{\partial x} & 0 & 0 & \frac{\partial^2}{\partial x^2} \end{bmatrix} \circ \begin{pmatrix} \rho I \ddot{\alpha} \\ \rho A(-\ddot{\alpha} w + \ddot{v} - \dot{\alpha}^2 v - 2\dot{\alpha}\dot{w}) \\ \rho A(+\ddot{\alpha} v + \ddot{w} - \dot{\alpha}^2 w + 2\dot{\alpha}\dot{v}) \\ \rho I(v'\ddot{\alpha} - \ddot{w}' - \dot{\alpha}^2 w') \\ \rho I(w'\ddot{\alpha} + \ddot{v}' + \dot{\alpha}^2 v') \\ EIv'' \\ EIw'' \end{pmatrix} dx =$$

$$\begin{pmatrix} \rho I \ddot{\alpha} \\ \rho A(\ddot{v} - 2\dot{\alpha}\dot{w} \underline{- \ddot{\alpha} w} - \dot{\alpha}^2 v) - \rho I(\ddot{v}'' + \dot{\alpha}^2 v'' \underline{\underline{+ w''\ddot{\alpha}}}) + (EIv'')'' \\ \rho A(\ddot{w} + 2\dot{\alpha}\dot{v} \underline{+ \ddot{\alpha} v} - \dot{\alpha}^2 w) - \rho I(\ddot{w}'' + \dot{\alpha}^2 w'' \underline{\underline{- v''\ddot{\alpha}}}) + (EIw'')'' \end{pmatrix} = 0. \tag{23}$$

As expected, one obtains automatically the correct signs for a representation in the co-rotating frame, along with much less effort in calculation.

5 Elastic Multibody System (EMBS)

5.1 Partial Differential Equations

Clearly, one might proceed this way to generate the partial differential equations (along with the corresponding boundary conditions) for an elastic multi body system. The result is a Gauss form for the rigid body variables and a set of differential operators for the elastic variables, and a combination of these for the boundary conditions (in detail reported in [1]). However, such a foregoing seems to lead to a dead end, because an analytical solution is virtually impossible to achieve.

5.2 Approximative Solution

When looking for an approximative solution, it is not advisable to expand the equations into partial differential equations and the corresponding boundary conditions. This is simply because one will obviously never find admissible shape functions which fulfill all the boundary conditions as requested by Galerkin's (original) method, for instance. With an interpretation of Galerkin's method as a result from the virtual work one might think of adding the work which is accomplished by the boundary forces and torques, thus reducing the requirements for the shape functions to pure geometrical ones. But formulating the boundary terms explicitly is, for the approximative motion equations, unnecessary because the spatial coordinates do not appear as independent variables any more. Therefore, we go back to Eq.(20) along with $\dot{\mathbf{y}}_n = \overline{\mathcal{D}}_n \circ \dot{\mathbf{s}}_n$ [see Eq.(22)]. A Ritz series expansion $\dot{\mathbf{s}}_n = \mathbf{\Phi}_n(\mathbf{x})^T \dot{\mathbf{y}}_{n\mathrm{Ritz}}(t)$ yields $\dot{\mathbf{y}}_n = [\overline{\mathcal{D}} \circ \mathbf{\Phi}(\mathbf{x})^T]_n \dot{\mathbf{y}}_{n\mathrm{Ritz}}(t) := [\mathbf{\Psi}(\mathbf{x})^T]_n \dot{\mathbf{y}}_{n\mathrm{Ritz}}(t)$ where $\mathbf{\Psi}(\mathbf{x})$ comprises the shape functions along with their spatial derivatives as far as they are needed. The virtual displacements are then $\delta\mathbf{y}_n = [\mathbf{\Psi}]_n^T (\partial \dot{\mathbf{y}}_{n\mathrm{Ritz}}/\dot{\mathbf{s}})\delta\mathbf{s}$. Since $\delta\mathbf{s}$ is arbitrary, one obtains from Eq.20)

$$\begin{bmatrix} \mathbf{F}_1^T & \mathbf{F}_1^T \mathbf{T}_{21}^T & \cdots & \mathbf{F}_1^T \mathbf{T}_{\mathrm{N}1}^T \\ & \mathbf{F}_2^T & \cdots & \mathbf{F}_2^T \mathbf{T}_{\mathrm{N}2}^T \\ & & \ddots & \vdots \\ & & & \mathbf{F}_{\mathrm{N}}^T \end{bmatrix} \begin{bmatrix} \mathbf{M}_1 \ddot{\mathbf{y}}_{1\mathrm{Ritz}} + \mathbf{G}_1 \dot{\mathbf{y}}_{1\mathrm{Ritz}} - \mathbf{Q}_1 \\ \mathbf{M}_2 \ddot{\mathbf{y}}_{2\mathrm{Ritz}} + \mathbf{G}_2 \dot{\mathbf{y}}_{2\mathrm{Ritz}} - \mathbf{Q}_2 \\ \vdots \\ \mathbf{M}_{\mathrm{N}} \ddot{\mathbf{y}}_{N\mathrm{Ritz}} + \mathbf{G}_{\mathrm{N}} \dot{\mathbf{y}}_{N\mathrm{Ritz}} - \mathbf{Q}_{\mathrm{N}} \end{bmatrix} = 0 \tag{24}$$

where

$$\mathbf{M}_n = \int\limits_{B_n} \left[\mathbf{\Psi} d\mathbf{M} \mathbf{\Psi}^T\right]_n , \quad \mathbf{G}_n = \int\limits_{B_n} \left[\mathbf{\Psi} d\mathbf{G} \mathbf{\Psi}^T\right]_n , \quad \mathbf{Q}_n = \int\limits_{B_n} \left[\mathbf{\Psi} d\mathbf{Q}\right]_n . \tag{25}$$

One has thus once more the same Gauss form as in Eq.(15).

6 Conclusions

When non-holonomic constraints come into play, then the analytical methods require at first a calculation for the f ull set of variables. The non-holonomic constraint may be inserted afterward. This is because the analytical methods need directional derivations of the kinetic energy w.r.t. the minimal velocities. Inserting the non-holonomic constraint in advance would lead to a loss of information and yields wrong results. This is avoided with the Projection Equation which does not require directional derivatives. Here, the constraints may be inserted in advance. This goes along with a considerable reduction of calculation effort.

Directional derivations are also the reason that fast moving (accelerated) systems have to be considered with care. At least when using CARDAN-like transformations, the resulting rotational axes which refer to the generalized angular velocities are not orthogonal. As a consequence, the resulting equations are not independent when seen from the co-rotating coordinate system, for instance. This difficulty is avoided with the Projection Equation. Its use once more goes along with considerable effort savings.

Considering elastic *multi* body systems, the use of the analytical methods requires an enormous effort in calculation. Here, one really runs into problems. Once more, the Projection Equation reduces this effort to a minimum. Along with a direct RITZ approach one obtains the afore mentioned GAUSS form for approximative solution. Its evaluation leads to an order-n-formalism which seems the only reasonable way to come around with such challenging systems.

It should not remain unnoticed that in case of fast moving elastic systems the corresponding zero order reaction forces (as well as zero order impressed forces) need the consideration of second order displacement fields. These lead to the so-called "dynamical stiffening effects". They are, in the present context, assumed to be taken into account with $d\boldsymbol{Q}$.

Acknowledgements This contribution has been supported by the AUSTRIAN CENTER OF COMPETENCE IN MECHATROMICS (ACCM).

For space requirements, we refer to only one (recently published) reference which contains nearer explanations as well as a literature overview.

References

1. H.Bremer: Elastic Multibody Dynamics – A Direct Ritz Approach. Springer, ISBN 978-1-4020-8679-3, August 2008.

Using GPS sensors in Structural Mechanics

Fabio Casciati and Zhicong Chen

Abstract Distributed sensor networks are conceived for a simple installation all around the free boundary of deformable media. The impact on current structural engineering technology depends on some requisites which are preliminarily discussed in this chapter: wireless communication between sensors and storage unit(s), reliability of the acquisition, low power consumption. Within this framework, non contact displacement sensors should be preferred in view of reconstructing the stress and strain fields inside the medium. GPS (Global Positioning System) sensors would be adequate, but they suffer some drawbacks which suggest the study of land GPS configurations. Assuming that the milestones listed above have all been reached, the design of the sensors dislocation is identified as the core structural-mechanics optimization problem.

1 Introduction

Within structural mechanics, the recent development of smart technologies also resulted in adding to methods of numerical simulation (toward analysis and design) a follow up of the structural system managed on experimental bases. This is mainly achieved by the adoption of distributed sensor networks [1-6].

The use of dense sensor networks was promoted by significant cost reductions and by the implementation of wireless technologies [7-9], which be-

---

Fabio Casciati
Department of Structural Mechanics, University of Pavia, Pavia, Italy, e-mail: fabio@dipmec.unipv.it

Zhicong Chen
Department of Structural Mechanics, University of Pavia, Pavia, Italy, e-mail: zhicong.chen@unipv.it

come a must when hundreds (or thousands) of acquisition channels must be managed. The characterization of the wireless channel, the reliability of the acquisition and the aspect associated with power consumption [10] are preliminarily discussed in next section.

The goal of the dense sensor network is an accurate sensing of structural entities with a well-posed physical meaning, such as relative displacements between members of a structural system, or slopes of displacement fields, to mention only two examples. Even if the desired structural output in some special cases might be accessible to a targeted single sensor, results obtained by a dense network of sensors are advantageous from the viewpoint of accuracy and sensitivity to measurement errors. Moreover, multiple tunings of the sensor weights will yield as many different desired outputs as may be needed, such that redundant measurements become possible.

In view of reconstructing the stress and strain fields inside the medium [11], non contact displacement sensors should be preferred. GPS (Global Positioning System) sensors would be adequate [12], but they suffer some drawbacks which suggest the study of land GPS configurations. However there remains a lack concerning the proper structural interpretation of the measured network output. Research should therefore be focused on feasible spatial distributions of properly located and weighted dense sensor networks, designed to make the reconstruction of the internal stress and strain distribution feasible.

2 Wireless Communication Systems

2.1 Signal-Channel Characteristic

Unlike wired signal channels, a wireless signal channel is random, unpredictable and time-varying. In order to achieve robust wireless digital communication, the characteristic of wireless signal-channel should be understood and then be matched by the frequency band and baseband processing approach whose key points are modulation and coding [13].

1. Multipath: as illustrated in Figure 1, multipath originates from the fact that the signal will arrive at the receiver through multiple paths. The composition of the same signals from different paths with different phase will result in the signal distortion. It will lead to significant negative influence when the obstacle size is large enough as compared to the wave length.

2. Interference and noise: nowadays, many kinds of wireless systems are in use in many different frequency bands [14]. Moreover, automotive ignition interference, industrial EM (Electro-Magnetic) pollution, various electronic equipments and natural EM noise, are also commonplace. Therefore, the actual EM environment all around is quite different from the ideal free

space, and full of various interferences and noises. Furthermore, the signal power is usually limited, so that the matched modulation and coding technology is necessary to achieve robust communication in the environment of low SNR (Signal to Noise Ratio) [15].

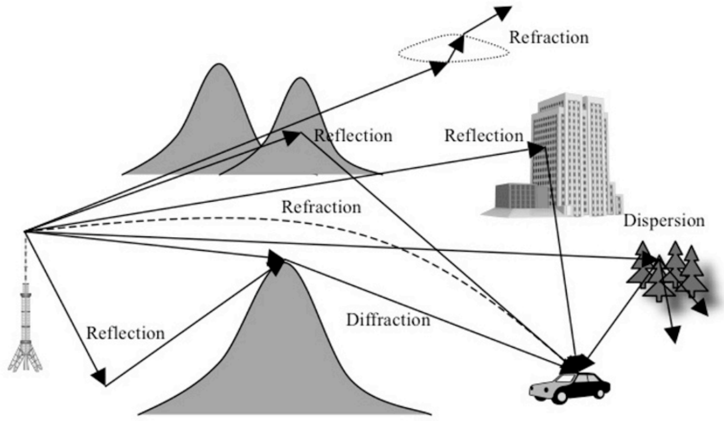

Fig. 1 Propagation of electromagnetic waves

2.2 Implementation Approaches

The physical layer of a wireless digital communication system is usually complex, and mainly consists of modulation, demodulation, encoding, decoding, and other baseband processing. But thank to the development of the IC (Integrated Circuit) technology, the whole physical layer hardware is usually integrated in single chip or chip groups which facilitate the implementation very much. For example, the physical layer of ZigBee 802.15.4 is realized by TI (Texas Instruments) in a single chip CC2420/CC2430 (the System on Chip, SoC, includes a 8051 core compared to CC2420), and many non standard ISM (Industrial, Scientific, Medical) frequency band transceivers(CC1101, nRF24L01, IA4432 and so on) also exist. However, if the wireless communication system comes without the support of those off-the-shelf RF (Radio Frequency) single-chips or chip-groups, it is supposed to be constructed by frequency band modules with monolithic IC (Low Noise Amplifier, Mixer, Frequency Synthesizer, Modulator, Demodulator, Filter, and so on), and baseband modules with DSP (Digital Signal Processor) or FPGA (Field Programmable Gate Array).[16-18]

2.3 Key Points for Wireless Sensor Networks

1. Network topology and reliability: nowadays, the wireless sensor network (WSN) is often expected to be a distributed computation sensing network, i.e., it is not only conceived just to collect sensing data, but also to perform some computations [19]. Therefore, the network topology should be well considered, not just as simple as the traditional centralized star structure. Usually, the network topologies for WSN can be categorized into the following basic types: star, tree and mesh, and then more complex network can be built as hybrid of the above basic topologies. The mesh topology is the most flexible, since it allows the communication between any two nodes in the network. But it is more difficult to be built and costs much more resources than those strictly necessary. Therefore, the kind of hierarchical topology which is regarded as more promising is the hybrid one, made of the above basic topologies. Of course the optimal result depends on the specific application. In addition, the network topology also corresponds to the communication protocol. Since the undesired errors and conflicts of communication are unavoidable, the protocol should be able to perform an error control in order to achieve high reliability. It usually adopts the mechanisms of CRC (Cyclic Redundancy Check) and acknowledgement.

2. Delay and synchronization: as the mentioned communication reliability, sensing synchronization is another very important aspect in the wireless sensing network. If every node of the WSN possesses a high accuracy and stability clock, just like the GPS satellite, to realize sensing synchronization is an easy task. But this generally is not the case. Currently, digital system extensively adopts the crystal oscillator which possesses relatively high accuracy and stability. Although its accuracy is up to 1ppm (points per million) level, it is still not enough, because it will still produce significant asynchronies after running some time. Therefore, to estimate the communication delay seems to be a better way to realize synchronization among nodes. Clock synchronization is not only for sensing synchronization, but also for coordinating the power-saving sleep mode and the ability of communication, because the node in sleep mode can not be accessed by other nodes. Two nodes can only communicate each with the other when they are all in active mode. So in addition to the basic sensing synchronization, one should also pursue a way to get a good balance between the low power consumption and accessibility.

3. Low power and power supply: many WSN systems are powered by battery and impractical to be all powered by commercial power. Therefore, in order to extend the operating time, low power characteristic should be taken into account. Usually, this problem can be approached from two sides: reducing the power consumption and/or harvesting power through any convenient way. Sleeping is the main way to reduce power consumption, and the low

power characteristic should be carefully emphasized in the selection of IC. Rechargeable batteries combined with solar panels are in use for many low power systems. But the climate and sunshine conditions should be carefully considered to determine first the applicability and then the capacity of the rechargeable battery. In addition, harvesting power from mechanical energy, such as wind and vibration, is a promising field of research [10].

3 Potential of Land GPS

Nowadays, the radio positioning system is becoming more and more important, and the most famous among the available one is the United States GPS (Global Positioning System) in which the receiver get the related time and position information from at least four visual (i.e., in open sky) satellites to determine its global position. In many applications, the GPS is adequate and suitable, but the open sky satellite visibility requisite prevents one from the many applications where the presence of a roof cannot be avoided. Moreover, when operating on urban buildings, inside them the GPS signal will be too weak and, even outside them, there will be a negative influence of the multipath effect. One should also remark that often the relative, rather than the absolute, position in a small local area is required and that the cost of the devices becomes soon rather high when high precision is nee pursued.

Therefore, as a complement to GPS, the local positioning system is emerging. The local positioning system (or Land GPS, LGPS) utilizes several fixed position-determined base stations as reference coordinates, just like GPS uses the satellites. The similarity of the concepts of GPS and LGPS is illustrated in Figure 2. If the distances of the target from each base station are determined, the position is obtained of consequence.

In this section, the principles of several existing positioning approach will first be reviewed. Then the different concepts will be introduced with reference to the prototype realized (or in construction) by some research bodies.

3.1 State-of-the art

Basically, from the positioning point of view, the local positioning system approaches can be divided into two classes: remote-positioning and self-positioning. The remote-positioning utilizes the base station to determine the position of a moving unit, whereas this moving unit is directly enabled to determine its position in the self-positioning system. Of course, in the self-positioning scheme, the moving unit can send the obtained information on its position back to the base stations. The selection of one of the two

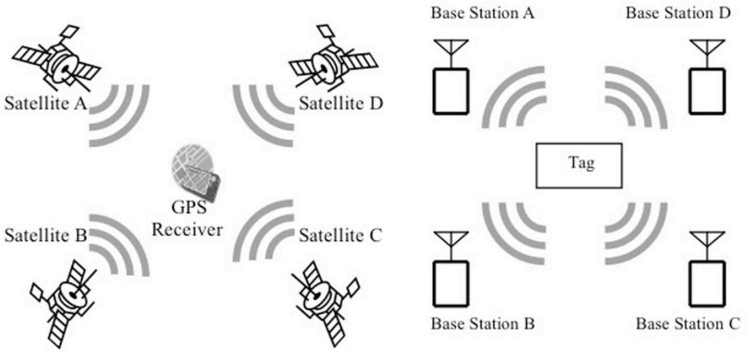

Fig. 2 Comparison between satellite GPS and "Land GPS"

schemes mainly depends on the specific application. Another way to classify the proposed schemes is based on the positioning principle. Here the local positioning system methods can mainly be divided into three classes, the concepts of which are simply illustrated in Figure 3 [20]:

1. Angle Of Arrival (AOA)
2. Received Signal Strength (RSS)
3. propagation time which can further be divided into three different subclasses:
    - Time Of Arrival (TOA)
    - Roundtrip Time Of Flight (RTOF)
    - Time Difference Of Arrival (TDOA).

3.2 RSS

The RSS positioning approach is implemented on the ZigBee SoC CC2431 of TI (Texas Instruments) which has a location engine hardware capable of calculating a two dimensional position of the blind node from the RSSI (Received Signal Strength Indicator) and the known coordinates of the base nodes [16]. This approach works on the relation between the distance and RSSI, assuming the antenna has the isotropic radiation characteristic, which can be expressed by the formula

$$RSSI = -\left(10\log_{10} d + A\right)^{n} \tag{1}$$

where

- n is the signal propagation constant, also named propagation exponent;

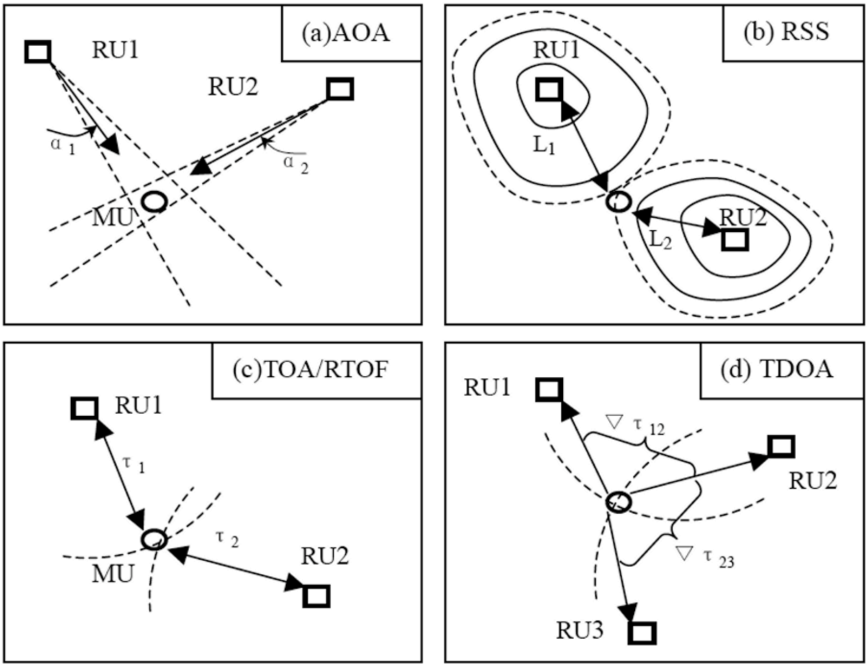

Fig. 3 Measuring principles for a Local Positioning System: (a) angle-of-arrival AOA, where RU and MU denote remote and mobile unit, α_1 and α_2, are the measured direction angles; (b) received signal strength RSS, where L_1 and L_2 denote the measured path loss; (c) time-of-arrival (TOA) and roundtrip time-of-flight (RTOF), where, τ_1 and τ_2 denote the measured one-way or roundtrip signal propagation time; the spatial position is given by the intersection of circles centered at the RUs; (d) time difference of arrival (TDOA), where $\nabla\tau_{12}$ and $\nabla\tau_{23}$ denote the measured propagation time difference from a signal traveling from the MU to two different RUs and the position is given by the intersection of hyperbola with foci at the RUs.

- d is distance from the sender;
- A is received signal strength at the distance of one meter.

The location engine of the blind node implements a distributed computation algorithm that uses RSSI values from known reference nodes, such as mobile neighbor nodes with the same Location Engine, or fixed infrastructure nodes. The location error depends on signal environment, deployment pattern of the reference nodes and the density of the reference nodes in the area of interest. In general, having more reference nodes available, one improves the accuracy of the location estimation. This approach just calculates the position on the basis of the available RSSI without extra hardware and with little computation. Its cost therefore is very low but the accuracy of the target position is at the level of the meter. Therefore, for such a low resolution, the RSS positioning approach is the most cost-effective.

3.3 RTOF

The RTOF positioning approach is prototyped by Berkeley for the location in sensor networks [21]. This approach achieves positioning through directly measuring TOF (Time Of Flight) by sampling in time domain. Therefore, the accuracy is limited by the time quantization which depends on the sampling period and on the corresponding signal bandwidth. In addition, an OFDM (Orthogonal Frequency Division Multiplexing) wideband signal is selected for implementation, due to its flexibility and its low computational complexity.

To achieve TOF measurements, the RX (Receiver) must be synchronized with the TX (Transmitter), i.e. the RX needs to be aware of the clock offset between the two. Unsynchronized TOF measurement results include the clock offset as an additive (subtractive) term. If the same measurement was carried out in the reverse direction, then the same clock offset would appear as a subtractive (additive) term. Averaging the forward and reverse measurement results, one cancels the contribution of the clock offset. Also, halving the difference of the forward and reverse TOF measurements, one obtains the clock offset between the TX and RX.

Two important points should be noted regarding the round trip time transfer method. First, the clock offset needs to remain constant during the forward and reverse transmissions. Typically this implies that the measurements should be carried out in rapid succession. Second, there is the need of an additional, reliable communication mechanism for exchanging, transmitting and receiving times. The prototype measurement error is within 0.5m to 2m, when operating at 100Msps sampling rate and using a 50MHz signal in the 2.4 GHz ISM band. The system accuracy is limited by the sampling rate and can be linearly improved with increasing rates.

3.4 TDOA-FWMW

The TDOA positioning approach prototyped by ICIE (Institute for Communications and Information Engineering, University of Linz, Austria) mainly relies on FMCW (Frequency-Modulated Continuous-Wave) radar principle which utilizes the frequency difference obtained from a mixer to represent the round trip time of electromagnetic wave propagation [22]. The prototype at least consists of four position-known BSs (Base Station), one position-unknown MT (Measurement Transponder), one position-known RT (Reference Transponder), and one MPU (Master Processing Unit).

Since the distances to be determined between the MT and BSs are short, which corresponds to a TOF (Time of Flight) in the range from nanoseconds to micro-seconds (which is difficult to be directly measured), an indirect measurement in the frequency domain based on linear chirps is adopted. In contrast to the TOF approach, which requires a common and highly accurate time base between transponders and BSs, the TDOA just need to achieve synchronization among the BSs, which is realized by the RT instead of expensive atomic clock or high-speed optical fibers. From the operational aspect, the RT operates continuously to keep the BSs synchronized, whereas the individual MTs are activated by means of a trigger telegram to avoid mutual interference among them. In this prototype, the accuracy of a few centimeters can be achieved. From the aspect of system implementation, the devices to be used, for both RF and digital modules, are available on the markets and of common use. Although it is expensive compared to the above RSS approach, this approach is able to achieve high precision, so that it results to be cost-effective for high precision application. An alternative implementation can be found in ref. [23].

4 Conclusions

The chapter is devoted to an obvious computational need that is to be resolved before dense sensor networks can be applied to structures of civil and mechanical engineering in a more advantageous manner. The goal is to develop design methodologies for the spatial distribution of networks of properly weighted sensors such that the computed combination of their outputs can be interpreted as an entity with a well-posed physical meaning. In particular new methodologies for measuring an output with a meaning in the context of structural mechanics and strength of materials are emphasized.

Potential applications of such dense sensor networks shall be studied concerning structural systems of civil and mechanical engineering, robotics and environmental processes. Implications of the new design methodologies for sensor networks upon control and health monitoring shall also be worked out.

Acknowledgements The research summarized in this paper was supported by an Athenaeum Research Fund (FAR 2008), with Professor L. Faravelli serving as responsible.

References

1. D.K Miu: Mechatronics. Electromechanics and Contromechanics. Springer-Verlag 1993.
2. A. Preumont: Vibration Control of Active Structures. An Introduction, 2.nd ed., Kluwer 2002.
3. F. Casciati, ed.: Proc. of the Third World Conf. on Structural Control, Wiley & Sons, 2003.
4. L. Faravelli, B. F. Spencer jr., eds., Proceedings of the US Europe (ESF-NSF) Workshop on Sensors and Smart Structures Technology, Como and Somma Lombardo, Italy, Wiley 2003.

5. R. Flesch, H.Irschik and M. Krommer, eds.: Proc. of the Third European Conf. on Structural Control, Vienna, Austria 2004, Schriftenreihe der Technischen Universitt Wien 2005.
6. B.F. Spencer jr., Tomizuka M., Yun C.B., Chen W.M., Chen R.W. eds, World Forum on Smart Materials and Smart Structures Technology, Taylor & Francis, London, 2008.
7. B.F. Spencer, jr. M.E. Ruiz-Sandoval, N. Kurata: Smart Sensing Technology: Opportunities and challenges. Structural Control and Health Monitoring **11** , 2004, 349-368.
8. F. Casciati, R. Rossi, Fuzzy Chip Controllers and Wireless Links in Smart Structures, in J. Holnicki-Szulc and C.A. Mota-Soares eds. Advances in Smart Technologies in Structural Engineering, Springer-Verlag, Berlin, 2004, 1-24.
9. Lynch J.P. , Loh K. A Summary Review of Wireless Sensors and Sensors Networks for Structural Health Monitoring, Shock and Vibration Digest, 2006, **38**(2), 91-128.
10. F. Casciati, R. Rossi, A Power Harvester for Wireless Sensing Applications, Structural Control and Health Monitoring **14**(4) , 2007, 649-659.
11. H. Irschik, K. Schlacher, eds. Advanced Dynamics and Control of Structures and Machines. CISM Vol. 444. Springer-Verlag, Berlin, 2004
12. F. Casciati, C. Fuggini. Monitoring an Industrial Steel Building by GPS receivers, Proceedings 4th Europ. Workshop on Structural Health Monitoring, DEStech, Lancaster, US, 219-226
13. A. Goldsmith. Wireless Communications, Cambridge Univ. Press, Cambridge, UK, 2005.
14. R. Prasad, M. Ruggieri. Technology Trends in Wireless Communications. John Wiley & Sons, Chichester, UK , 2006.
15. R. H. Morelos-Zaragoza. The Art of Error Correcting Coding. Wiley & Sons, UK , 2006.
16. www.ti.com
17. www.anolog.com
18. www.nordicsemi.com
19. A. Swami, Q. Zhao, Y-W. Hong, L. Tong. Wireless Sensor Networks Signal Processing and Communications Perspectives. John Wiley & Sons, Chichester, UK, 2007.
20. M. Vossiek, L. Wiebking, P. Gulden, J. Wieghardt, and C. Hoffmann. Wireless local positioning-Concepts, solutions, applications. Proc. Radio Wireless Conf., 2003, 219-224.
21. T. Karalar, J. Rabaey. An RF ToF Based Ranging Implementation for Sensor Networks. IEEE International Communications Conference, Istanbul, Turkey, June 11-15, 2006,.
22. A. Stelzer, K. Pourvoyeur, A. Fischer. Concept and Application of LPMA Novel 3-D Local Position Measurement System. IEEE Transactions on Microwave Theory and Techniques, Vol. 52, n. 12, 2004
23. M. R. Mahfouz, C. Zhang, B. C. Merkl , M. J. Kuhn, A. E. Fathy. Investigation of High-Accuracy Indoor 3-D Positioning Using UWB Technology IEEE Transactions on Microwave Theory and Techniques, Vol. 56, n. 6, 2008.

Hybrid Control Procedures in Mitigating Cable Vibrations

Lucia Faravelli, Clemente Fuggini and Filippo Ubertini

Abstract Cable vibration control is an active research field in the technical literature. Yet, a robust and effective control strategy for cable dynamics is still missing. Indeed, cables exhibit a complex behavior, mainly due to internal resonances and nonlinear couplings. Moreover, most of the control solutions already known in the literature are affected by damper/actuator localization, which significantly impairs their overall control effectiveness. To overcome these drawbacks, the authors have recently proposed a hybrid solution combining wrapped shape memory alloy (SMA) wires and an open-loop actuation. These control solutions have shown promising vibration mitigation capabilities when the motion was essentially dominated by the first in-plane mode. Here, a particular attention is posed to controlling the second in-plane modal amplitude which is known to entail serious control difficulties and proved to be considerably relevant in technical situations. To this end, the effectiveness of the passive (SMA wires), open-loop active and hybrid control solutions are investigated by means of a campaign of laboratory tests. The results extend the previous theoretical/experimental study and confirm the potentialities of the proposed hybrid approach.

Lucia Faravelli
Department of Structural Mechanics, University of Pavia, Via Ferrata 1, 27100 Pavia, Italy, e-mail: lucia@dipmec.unipv.it

Clemente Fuggini
Department of Structural Mechanics, University of Pavia, Via Ferrata 1, 27100 Pavia, Italy, e-mail: clemente.fuggini@unipv.it

Filippo Ubertini
Department of Civil and Environmental Engineering, University of Perugia, Via G. Duranti 93, 06125 Perugia, Italy, e-mail: filippo.ubertini@unipv.it

1 Introduction

Cable vibration mitigation is a well-established research field due to the broad diffusion of cables in bridge design. Among the different types of stay cables, longer ones are those which suffer the most from vibration problems. As a consequence of these undesired levels of vibrations, fatigue ruptures may appear in the cables [1].

Steel cables are characterized by a complex nonlinear dynamic with a large variety of internal resonance conditions [2-3]. When structural control solutions are concerned, such a complexity is even enhanced [4]. Within this field, dampers mounted transversally to the cable are usually employed as passive devices [5]. Unfortunately, the localisation of the dampers close to the cable support often limits their control capability. Alternatively, to overcome the localization drawback, a pre-stressed shape memory alloy wire can be added to the cable. Indeed, this passive solution was seen able to increase the damping of the system by exploiting the hysteretic stress-strain relations of the SMA [6]. The best vibration mitigation capabilities are however guaranteed by more expensive active or semi-active strategies as well-known from the theory of structural control [7].

The authors recently proposed a hybrid control strategy [8-9] obtained by combining an open loop actuation and the distributed passive one utilizing wrapped SMA wires. The open loop control law was designed to enhance the energy exchanges between modes produced by nonlinear couplings. The hybrid solution was seen able to combine the added damping provided by the SMA wire with the additional mitigation capability provided by the open loop actuation. However, the experimental results presented in [9] were essentially limited to the mitigation of the response when the motion was dominated by the first in-plane mode. Here, a campaign of experimental tests is presented to better investigate the capability of the said control strategies in mitigating the vibrations of the second in-plane mode. Indeed, such a mode is already known in the literature to entail serious control difficulties and it is usually activated in large amplitude vibrations observed in stay cables.

2 Physical cable model

A heavy suspended cable is considered (see Figure 1) with span length L and sag d. With the aim of mitigating the vibrations of the cable, three control strategies are here considered [9]: distributed passive solution using wrapped SMA wire (DP-SMA), open loop control solution (OP-LOOP) and hybrid control solution (HYB).

In the OP-LOOP case a transversal vertical control actuator, represented by a linear motor, is placed in the vicinity of one of the cable ends (at a distance x_c) and exerts the control force F_c (see Figure 1). On the opposite side,

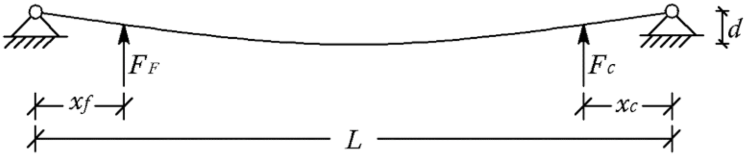

Fig. 1 Sketch of the cable and of the control architecture

Fig. 2 Physical cable model

at a distance x_f from the cable end, the external excitation F_F is provided by a second linear motor. Both dynamic forces F_c and F_F are applied to the cable without a fixed contact. Thus, the two linear motors do not modify the physical system and excite the cable by simply impacting on it.

The control effectiveness is analyzed through experimental tests on a physical cable model (see Figure 2). The cable has a span length $L = 2.36m$ and is supported at its ends by means of spherical joints fixed to rigid supports placed at the same height. One of the two anchorages allows to vary the tension in the cable and, consequently, to vary its sag. The system is instrumented with two tri-axial accelerometers placed at one-fourth and one-fifth of the span. The sensors record the accelerations in the in-plane direction and in the out-of-plane one of the two application points. The cable is made by a steel wire of diameter $2mm$ and with an elastic modulus $E = 135000MPa$. Six equally-spaced spherical masses are mounted on the cable such that the total weight per unit length is equal to $3.805N/m$. The initial configuration chosen for the cable has a sag $d = 2.0cm$.

The output-only system identification of the cable model was carried out elsewhere [9] and led to the results summarized in Table 1. In such a table f_i denotes the frequency of the i-th in-plane or out-of-plane mode while ξ_i denotes the corresponding damping ratio. The cable revealed to be close to the $2:1$ internal resonance between the third and the first in-plane modes ($f_3/f_1 = 1.96$) and to be detuned from the $1:1$ resonance between the first and the second in-plane modes ($f_2/f_1 = 1.39$).

In-plane modes		Out-of-plane modes	
Frequency $[Hz]$	Damping ratio	Frequency $[Hz]$	Damping ratio
$f_1 = 5.25$	$\xi_1 = 0.0198$	$f_1 = 4.03$	$\xi_1 = 0.096$
$f_2 = 7.30$	$\xi_2 = 0.092$	$f_2 = 7.63$	$\xi_2 = 0.0196$
$f_3 = 10.31$	$\xi_3 = 0.011$	$f_3 = 11.05$	$\xi_3 = 0.0098$

Table 1 Identified modal frequencies and damping ratios

3 Hybrid control strategy

The DP-SMA approach aims at increasing the modal damping of the structural system by wrapping a SMA wire [10] along the cable. This allows to achieve a mitigation solution which is distributed along the cable and, hence, it is not affected by the device localisation. The SMA wire (in austenite phase) of diameter 1 mm is wrapped around the steel cable several times, anchored to the same vertical point of the cable and fixed at one end by a device that allows to assign a pre-tension force H to the wire but not to the cable. An optimal configuration for the union between the steel cable and the SMA wire was investigated [6] and the optimal pre-tension in the SMA wire was found [9]. Particularly, the pretension force that produce a 2% of strain (which corresponds to the so-called plateau of the stress-strain diagram for the considered SMA) into the wire was found to be the value that maximizes the control effectiveness.

The idea of the OP-LOOP control strategy is to exploit nonlinear coupling phenomena for control purposes. The aim is to make the vibration energy flow from low order modes (controlled modes) to some higher order one (excited mode). The results presented in [9] have shown that choosing a simple sinusoidal control law allows to reduce the nonlinear response of the cable. To activate this mechanism, the frequency f_c of the control action must be chosen in such a way to activate the nonlinear vibrations of the excited mode. In [9], the value $f_c \approx 2f_3$ was chosen ($f_c = 18Hz$) in order to excite the third in-plane mode (excited mode) nonlinearly (approximately in a $2:1$ ratio). This approach made the harmonic component with frequency f_c dominate the response of the third mode without significantly exciting any others modes.

It is clear that the OP-LOOP approach is a non-conventional control strategy in the sense that it is meant to mitigate the nonlinear response of the cable by introducing energy into the system instead of taking energy out of it. A possible way for controlling the response of the system in both linear and nonlinear cases is to combine the DP-SMA and the OP-LOOP control solutions in a hybrid strategy (HYB), as proposed in reference [9].

4 Experimental results

The capability of DP-SMA, OP-LOOP and HYB control solutions to mitigate the cable vibrations was demonstrated both theoretically and experimentally in [9]. Here, the results of a second campaign of experimental tests are presented by devoting a special care to the mitigation of the cable response when the second (anti-symmetric) in-plane mode is significantly excited. For the seek of clarity, the effectiveness of HYB control solution is studied after dealing with DP-SMA and OP-LOOP cases, separately. To this end, the forced oscillations of the cable under harmonic in-plane excitation F_F are considered. For every test, the recorded signals have a sampling frequency of $250Hz$.

4.1 DP-SMA case

In the first stage of experimental tests the DP-SMA control solution is concerned. First of all, the modal identification of the cable-SMA wire system has been realized to evaluate the change in the natural frequencies of the cable produced by the SMA wire. The results have been obtained as described in reference [9] and are summarized in Table 2 where f_i^{SMA} denotes the frequency of the i-th in-plane or out-of-plane mode of the cable-SMA wire system. The SMA wire was seen able to strongly reduce the harmonic response of the cable in the vicinity of the primary resonance with the first in-plane mode [9]. Here, the experimental frequency response curves ($frcs$) of the system in the vicinity of the resonance with the second in-plane mode are presented. The $frcs$ represent the amplitudes of the steady uncontrolled and controlled responses, as functions of the frequency of the external load F_F. The results, shown in Figure 3, emphasize that the passive strategy reduces the response at one-fifth of the cable span, while being substantially ineffective in mitigating the vibration of the second in-plane mode (maximum response at one-fourth of the cable span). It is worth noting that, in Figure 3, there is a frequency shift between uncontrolled and DP-SMA controlled $frcs$ due to the difference between the frequencies of the second in-plane modes in the two cases.

In-plane modes		Out-of-plane modes	
Frequency $[Hz]$	f_i^{SMA}/f_i	Frequency $[Hz]$	f_i^{SMA}/f_i
$f_i^{\text{SMA}} = 6.66$	1.27	$f_i^{\text{SMA}} = 6.03$	1.50
$f_i^{\text{SMA}} = 10.95$	1.50	$f_i^{\text{SMA}} = 9.93$	1.30
$f_i^{\text{SMA}} = 17.77$	1.72	$f_i^{\text{SMA}} = 9.04$	1.45

Table 2 Identified modal frequencies of cable-SMA wire system

Thus, a complementary approach is needed in order to configure a control

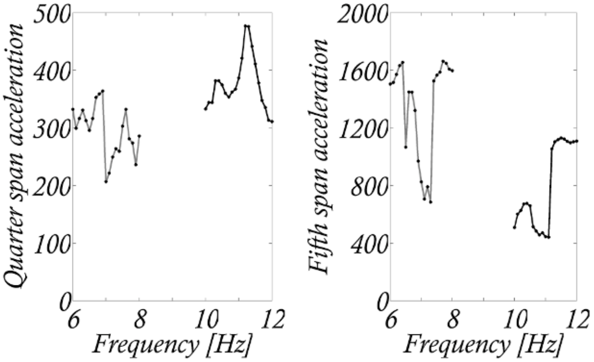

Fig. 3 Experimental normalized $frcs$ under in-plane excitation in the region of the resonance with the second in-plane mode: cable with the SMA wire (black lines) vs. cable without the SMA wire (grey lines)

strategy which is able to overcome the drawbacks of the DP-SMA solution.

4.2 OP-LOOP case

In the second stage of experimental tests, the effectiveness of the open loop control action in mitigating the response of the second in-plane mode is investigated. The control frequency $f_c = 18Hz$ is chosen.

To analyze the forced response of the system close to the resonance with the second in-plane mode, the frequency f_f of the harmonic forcing load F_F is tuned to the value of $7.0Hz$. At this given frequency the open loop controlled response is compared to the uncontrolled one. The recorded time history of the in-plane acceleration components is shown in Figure 4. The presented results confirm that the control action is capable to reduce the resonant response of the second in-plane mode. In order to investigate the effectiveness of the open loop controller in different regions of the external excitation, the $frcs$ to in-plane excitation are also considered. The results are presented in Figure 5 and evidence that the open loop controller is able to reduce the response of the system for a wide range of frequency values close to f_2.

4.3 HYB case

After investigating the effectiveness of DP-SMA and OP-LOPP control solution separately, the HYB control strategy is worth considering. In principle, since the SMA wire modifies the natural frequencies and the internal detun-

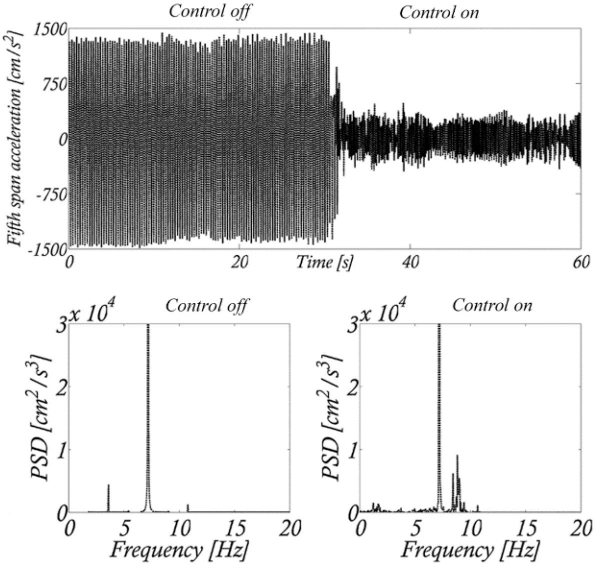

Fig. 4 Cable without the SMA wire: experimental time history of in-plane mid-span acceleration record under forced in-plane excitation in resonance with the second in-plane mode ($f_f = 7.0Hz$) before and after the application of the open loop control input (top); power spectral density (PSD) of in-plane acceleration (bottom) in both uncontrolled and open loop controlled cases

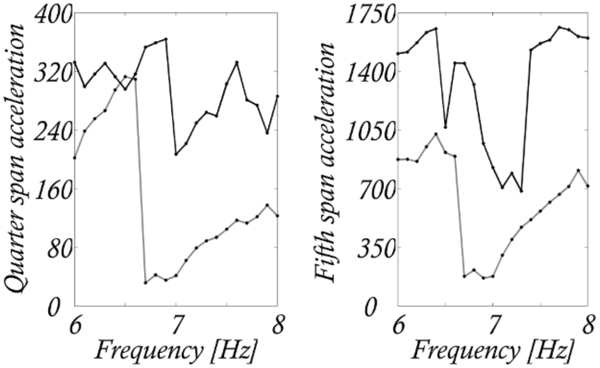

Fig. 5 Cable without the SMA wire: experimental normalized $frcs$ under in-plane excitation for uncontrolled (black lines) and open loop controlled (grey lines) cases in the region of the resonance with the second in-plane mode

ings of the cable, the control frequency f_c adopted in the HYB case should be different from that adopted in the OP-LOOP case. Here, however, the value $f_c = 18Hz$ is kept also in the HYB case for reasons that will be explained below.

First of all the forced solution in resonance with the second in-plane mode is investigated. To this end, the frequency f_f of the harmonic forcing load F_F is tuned to the value of $10.9Hz$ which corresponds to the frequency of the second in-plane mode of the cable-SMA wire system. At this given frequency the HYB controlled response is compared to the DP-SMA controlled one. The recorded time history of the in-plane acceleration components is shown in Figure 6. The presented results confirm that, as expected, the open loop control action is capable to reduce the resonant response of the second in-plane mode of the cable-SMA wire system. The PSD analysis reveals that the passively controlled solution is quasiperiodic since it posses incommesurate frequencies.

The effectiveness of the HYB solution is then investigated by varying the frequency of the external load in the vicinity of the resonance with the second in-plane mode. To this end, the $frcs$ of the cable-SMA wire system, with and without the open loop controller, are shown in Figure 7. The results outline that the additional control capability provided by the open loop controller is not limited to the resonant case with the second in-plane mode but it extends to all the considered frequency spectrum.

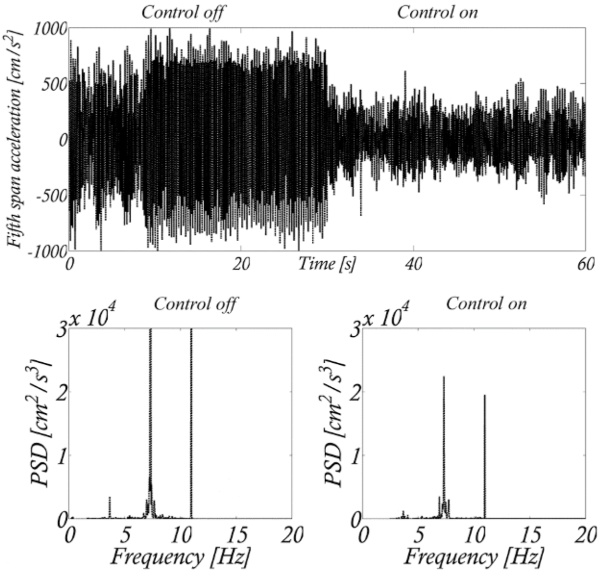

Fig. 6 Cable without wrapped SMA wire: experimental time history of in-plane mid-span acceleration record under forced in-plane excitation in resonance with the second in-plane mode ($f_f = 10.9Hz$) before and after the application of the open loop control input (top); power spectral density (PSD) of in-plane acceleration (bottom) in both passively controlled and hybrid controlled cases

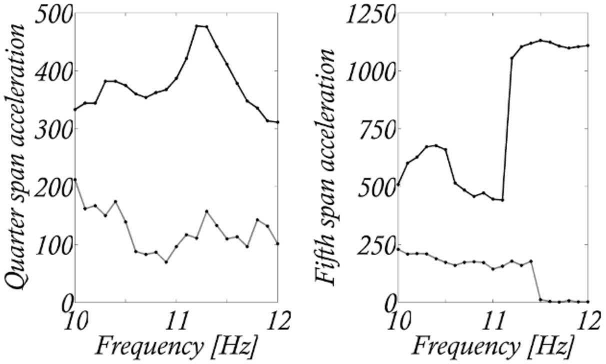

Fig. 7 Experimental normalized $frcs$ under in-plane excitation for passively controlled utilizing wrapped SMA wire (black lines) and hybrid controlled (grey lines) cases in the region of the resonance with the second in-plane mode

5 Conclusions

The experimental results presented in this paper extend a previous theoretical-experimental study by the authors. The effectiveness of a hybrid control strategy in reducing the vibrations of the second in-plane mode is investigated here through a campaign of laboratory tests. The hybrid strategy is obtained by combining a distributed passive solution utilizing wrapped SMA wires with an open loop actuation. The experimental results show that the SMA wire, which provides the system with significant vibration mitigation capabilities in the case of symmetric in-plane motions, is substantially ineffective in reducing the vibrations of antisymmetric modes. On the contrary, the experimental results outline that the open loop controller guarantees a significant reduction of the nonlinear response of the second in-plane mode.

Thanks to the control capability of the open loop controller, the hybrid solution is seen able to guarantee a significant mitigation of the cable response for a wide range of frequency values in the region of the resonance with the second in-plane mode. The frequency analysis of the experimental resonant response reveals that the hybrid solution reduces both the leading harmonic peak and the subharmonic one.

In summary, the proposed hybrid approach confirms its potentialities for controlling both symmetric and antisymmetric cable vibrations, with low energy consumptions, large control robustness and with no actuator/damper localization drawbacks.

Acknowledgements This paper was supported by a grant from the University of Pavia (FAR) for which the first author is serving as coordinator.

References

1. Cluni F., Gusella V., Ubertini F. A parametric investigation of wind-induced cable fatigue. Engineering Structures 2007; **29**(11) : 3094-3105
2. Rega G. Nonlinear vibrations of suspended cables, part I: modelling and analysis. Appl. Mech. Rev. 2004; **57** : 443-478
3. Rega G. Nonlinear vibrations of suspended cables, part II: deterministic phenomena. Appl. Mech. Rev. 2004; **57** : 479-514
4. Ubertini F. Active feedback control for cable vibrations. Smart Structures and Systems 2008; **4**(4) : 407-428
5. Li H., Liu M, Ou J. Vibration mitigation of a stay cable with one shape memory alloy damper. Structural Control and Health Monitoring 2004; **11**(1) : 21-36
6. Casciati F., Faravelli L., Fuggini C. Cable vibration mitigation by added SMA wires. Acta Mechanica 2008; **195** : 141-95
7. Casciati F., Magonette G., Marazzi F. Technology of semiactive devices and applications in vibration mitigation Wiley: Chichester, 2006
8. Faravelli L., Fuggini C., Ubertini F. Adaptive solution for intelligent cable vibration mitigation. Advances in Science and Technology 2008; **56**, 137-146
9. Faravelli L., Fuggini C., Ubertini F. Toward a hybrid control solution for cable dynamics: theoretical prediction and experimental validation. Structural Control and Health Monitoring 2009, in press, DOI: 10.1002/stc.313
10. Auricchio F., Faravelli L., Magonette G., Torra V. Shape Memory Alloys: Advances in Modelling and Applications Cimne: Barcelona, 2001

Thermal Stress Analysis in a Functionally Graded Material Considering Finite Thermal Wave Speed

Toshio Furukawa

Abstract Three-dimensional generalized thermoelasticity based on the Lord and Shulman's theory and the Green and Lindsay's theory is analyzed by use of the state space approach and integral transform techniques (Laplace and Fourier transforms). The functionally graded material is approximated to a multi-layered medium. Each layer is homogeneous and isotropic. The surfaces are traction free and subjected to a partial heating. The numerical calculations for temperature and thermal stresses are carried out.

1 Introduction

The dynamical coupled theory [1], which takes into account the coupling between temperature and strain fields, involves the contradiction that thermal wave propagates at an infinite velocity. The theory of generalized thermoelasticity has been developed in an attempt to eliminate this paradox. There are two different theories of the generalized thermoelasticity. The first is proposed by Lord and Shulman [2] (L-S theory) and the second is proposed by Green and Lindsay [3] (G-L theory). Recently, another some generalized theories [4-7] have been proposed. Hetnarski and Ignaczak [8] reviewed the recent progress on the generalized thermoelasticity. We used the basic equations of generalized thermoelasticity introduced by Noda et al. [9], which include the L-S theory and G-L theory, and analyzed a solid cylinder and layered medium [10-12], etc.

This paper deals with the three-dimensional generalized thermoelasticity for a functionally graded material, which is approximated to a multi-layered medium, based on the L-S and G-L theories. The state space approach [13]

Toshio Furukawa
Department of Mechanical Systems Engineering, University of the Ryukyus, Okinawa, Japan, e-mail: furukawa@teada.tec.u-ryukyu.ac.jp

is utilized for this problem. It is assumed that the medium is initially natural state. The surfaces of the medium are traction free and subjected to a partial heating. The temperature, displacements and stresses are obtained by means of the Laplace and Fourier transforms. The inversions of these transforms are carried out numerically.

2 Analysis

We consider three-dimensional generalized thermoelasticity for a multi-layered medium composed of homogeneous and isotropic n layers, and total thickness is l as shown in Fig. 1. The basic equations, which include the L-S and G-L theories, consist of three equations, that is, the heat conduction equation

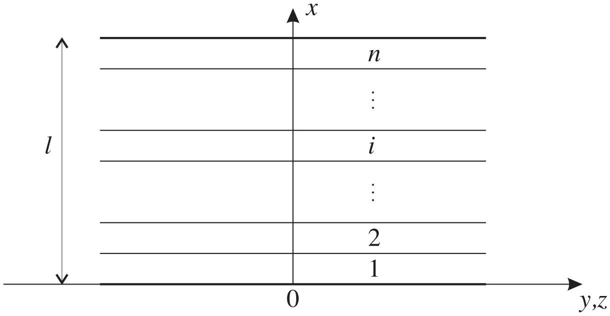

Fig. 1 Multi-layered medium

$$\kappa_i(T_{,xx}+T_{,yy}+T_{,zz})-(T-T_0+t_{0i}T_{,t}\,)_{,t}=(\lambda_i+2\mu_i)\frac{\delta_i}{\gamma_i}(e+\delta_{1k}t_{0i}e_{,t})_{,t}, \quad (1)$$

the equations of motion represented by displacement components

$$\begin{aligned}\mu_i(u_{x,xx}+u_{x,yy}+u_{x,zz})+(\lambda_i+\mu_i)e_{,x}-\gamma_i(T-T_0+\delta_{2k}t_{1i}T_{,t})_{,x}&=\rho_i u_{x,tt},\\ \mu_i(u_{y,xx}+u_{y,yy}+u_{y,zz})+(\lambda_i+\mu_i)e_{,y}-\gamma_i(T-T_0+\delta_{2k}t_{1i}T_{,t})_{,y}&=\rho_i u_{y,tt},\\ \mu_i(u_{z,xx}+u_{z,yy}+u_{z,zz})+(\lambda_i+\mu_i)e_{,z}-\gamma_i(T-T_0+\delta_{2k}t_{1i}T_{,t})_{,z}&=\rho_i u_{z,tt},\end{aligned} \quad (2)$$

and the stress-strain-temperature relations

$$\begin{gathered}
\sigma_{xx} = 2\mu_i u_{x,x} + \lambda_i e - \gamma_i (T - T_0 + \delta_{2k} t_{1i} T_{,t}), \\
\sigma_{yy} = 2\mu_i u_{y,y} + \lambda_i e - \gamma_i (T - T_0 + \delta_{2k} t_{1i} T_{,t}), \\
\sigma_{zz} = 2\mu_i u_{z,z} + \lambda_i e - \gamma_i (T - T_0 + \delta_{2k} t_{1i} T_{,t}), \\
\sigma_{xy} = \mu_i (u_{x,y} + u_{y,x}) \ , \quad \sigma_{yz} = \mu_i (u_{y,z} + u_{z,y}) \ , \quad \sigma_{zx} = \mu_i (u_{z,x} + u_{x,z}),
\end{gathered} \tag{3}$$

where

$$\gamma_i = (3\lambda_i + 2\mu_i)\alpha_i \ , \quad e = u_{x,x} + u_{y,y} + u_{z,z}. \tag{4}$$

Here, T: temperature, u_x, u_y and u_z: displacement components in the x, y and z directions respectively, σ_{ij}: stress component, t: time, T_0: initial temperature, κ: thermal diffusivity, α: coefficient of linear thermal expansion, δ: thermomechanical coupling parameter, ρ: density, λ and μ: Lame's constants, t_0 and t_1: relaxation times, δ_{jk}: Kronecker's delta whose subscript k denotes the number of relaxation times. The subscript i of each symbol denotes the referred layer number. The comma denotes the differentiation with following variable.

We introduce the dimensionless quantities:

$$\begin{gathered}
(\bar{x}, \bar{y}, \bar{z}) = \frac{1}{l}(x, y, z) \ , \quad (\tau, \tau_0, \tau_1) = \frac{c_i}{l}(t, t_0, t_1) \ , \quad \theta = \frac{T - T_0}{T_1 - T_0}, \\
(\bar{u}_x, \bar{u}_y, \bar{u}_z) = \frac{(u_x, u_y, u_z)}{l\alpha_i (T_1 - T_0)} \ , \quad \bar{\sigma}_{ij} = \frac{\sigma_{ij}}{\mu_i \alpha_i (T_1 - T_0)}, \\
\xi_i = \frac{c_i l}{\kappa_i} \ , \quad \beta_{0i} = \frac{\lambda_i + 2\mu_i}{\mu_i} \ , \quad \beta_{1i} = \frac{3\lambda_i + 2\mu_i}{\mu_i},
\end{gathered} \tag{5}$$

where c_i is the velocity of longitudinal wave and T_1 is a prescribed temperature. Substituting Eq.(5) into Eqs.(1) and (2) and applying the Laplace and Fourier transforms, we have

$$\hat{\theta}^*_{,\bar{x}\bar{x}} - [\xi_i s(1 + \tau_{0i} s) + \eta^2 + \zeta^2]\hat{\theta}^* = \frac{\beta_{0i}}{\beta_{1i}} \xi_i \delta_i s(1 + \delta_{1k}\tau_{0i} s)(\hat{\bar{u}}^*_{x,\bar{x}} + i\eta\hat{\bar{u}}^*_y + i\zeta\hat{\bar{u}}^*_z), \tag{6}$$

$$\begin{aligned}
\beta_{0i}\hat{\bar{u}}^*_{x,\bar{x}\bar{x}} - (\eta^2 + \zeta^2 + \beta_{0i}s^2)\hat{\bar{u}}^*_x + i(\beta_{0i} - 1)(\eta\hat{\bar{u}}^*_y + \zeta\hat{\bar{u}}^*_z)_{,\bar{x}} - & \\
-\beta_{1i}(1 + \delta_{2k}\tau_{1i}s)\hat{\theta}^*_{,\bar{x}} = 0&, \\
\hat{\bar{u}}^*_{y,\bar{x}\bar{x}} - [\beta_{0i}(\eta^2 + s^2) + \zeta^2]\hat{\bar{u}}^*_y + (\beta_{0i} - 1)\eta(i\hat{\bar{u}}_{x,\bar{x}} - \zeta\hat{\bar{u}}^*_z) - & \\
-i\eta\beta_{1i}(1 + \delta_{2k}\tau_{1i}s)\hat{\theta}^* = 0&, \\
\hat{\bar{u}}^*_{z,\bar{x}\bar{x}} - [\beta_{0i}(\zeta^2 + s^2) + \eta^2]\hat{\bar{u}}^*_z + (\beta_{0i} - 1)\zeta(i\hat{\bar{u}}^*_{x,\bar{x}} - \hat{\eta}\bar{u}^*_y) - & \\
-i\zeta\beta_{1i}(1 + \delta_{2k}\tau_{1i}s)\hat{\theta}^* = 0&,
\end{aligned} \tag{7}$$

where Laplace transform and Fourier transform are denoted by the asterisk (*) and the hat (ˆ), and the transform parameters are s, η and ζ, respectively.

Equations (6) and (7) are represented as the following matrix form

$$\frac{d\mathbf{V}(\bar{x},\eta,\zeta,s)}{d\bar{x}} = \mathbf{A}_i(\eta,\zeta,s)\mathbf{V}(\bar{x},\eta,\zeta,s), \tag{8}$$

where

$$\mathbf{V}(\bar{x},\eta,\zeta,s) = \{\hat{\bar{u}}_x^*, \hat{\bar{u}}_y^*, \hat{\bar{u}}_z^*, \hat{\theta}^*, D\hat{\bar{u}}_x^*, D\hat{\bar{u}}_y^*, D\hat{\bar{u}}_z^*, D\hat{\theta}^*\}^T,$$

$$\mathbf{A}_i(\eta,\zeta,s) = \begin{bmatrix} 0 & 0 & 0 & 0 & 1 & 0 & 0 & 0 \\ 0 & 0 & 0 & 0 & 0 & 1 & 0 & 0 \\ 0 & 0 & 0 & 0 & 0 & 0 & 1 & 0 \\ 0 & 0 & 0 & 0 & 0 & 0 & 0 & 1 \\ a_{51i} & 0 & 0 & 0 & 0 & a_{56i} & a_{57i} & a_{58i} \\ 0 & a_{62i} & a_{63i} & a_{64i} & a_{65i} & 0 & 0 & 0 \\ 0 & a_{72i} & a_{73i} & a_{74i} & a_{75i} & 0 & 0 & 0 \\ 0 & a_{82i} & a_{83i} & a_{84i} & a_{85i} & 0 & 0 & 0 \end{bmatrix},$$

$$a_{51i} = \frac{1}{\beta_{0i}}(\eta^2+\zeta^2)+s^2\ , \quad a_{56i} = -\frac{\beta_{0i}-1}{\beta_{0i}}i\eta\ , \quad a_{57i} = -\frac{\beta_{0i}-1}{\beta_{0i}}i\zeta,$$

$$a_{58i} = \frac{\beta_{1i}}{\beta_{0i}}(1+\delta_{2k}\tau_1 s)\ , \quad a_{62i} = \beta_{0i}(\eta^2+\zeta^2)+s^2\ , \quad a_{63i} = (\beta_{0i}-1)\eta\zeta,$$

$$a_{64i} = i\beta_{1i}\eta(1+\delta_{2k}\tau_{1i}s)\ , \quad a_{65i} = -i(\beta_{0i}-1)\eta\ , \quad a_{72i} = a_{63i}\ ,$$

$$a_{73i} = \eta^2+\beta_{0i}(\zeta^2+s^2)\ , \quad a_{74i} = \frac{\beta_{1i}}{\beta_{0i}}i\zeta a_{58i}\ , \quad a_{75i} = \beta_{0i}a_{57i}\ ,$$

$$a_{82i} = i\eta a_{85i}\ , \quad a_{83i} = i\zeta a_{85i}\ , \quad a_{84i} = \eta^2+\zeta^2+\xi_i(1+\tau_{0i}s)s,$$

$$a_{85i} = \frac{\beta_{0i}}{\beta_{1i}}\xi_i\delta_i s(1+\delta_{1k}\tau_{0i}s),$$

and $D = d/d\bar{x}$. The differential equation (8) can be directly solved and we obtain

$$\mathbf{V}(\bar{x},\eta,\zeta,s) = \exp[\mathbf{A}_i(\bar{x}-\bar{x}_{i-1})]\mathbf{V}(\bar{x}_{i-1},\eta,\zeta,s), \tag{9}$$

where $\bar{x}_{i-1}$ is the lower side of i-th layer and $\bar{x}_0 = 0$

The characteristic equation is represented by

$$\det|\mathbf{A}_i - p_i\mathbf{I}| = p_i^8 + b_{1i}p_i^6 + b_{2i}p_i^4 + b_{3i}p_i^2 + b_{4i} = 0, \tag{10}$$

where $\mathbf{I}$ is the identity matrix composed of 8 rows and 8 columns, p_i is eigenvalue and the all odd orders are eliminated from manual calculation, and the explicit representations of coefficient b_{ij} are omitted here.

Cayley-Hamiltons theorem leads

$$\mathbf{A}_i^8 + b_{1i}\mathbf{A}_i^6 + b_{2i}\mathbf{A}_i^4 + b_{3i}\mathbf{A}_i^2 + b_{4i}\mathbf{I} = \mathbf{0}. \tag{11}$$

From Eq.(11), the matrix exponential is represented by finite matrix polynomial with no approximation as

$$\exp[\mathbf{A}_i(\bar{x}-\bar{x}_{i-1})] = c_{0i}\mathbf{I}+c_{1i}\mathbf{A}_i+c_{2i}\mathbf{A}_i^2+c_{3i}\mathbf{A}_i^3+c_{4i}\mathbf{A}_i^4+c_{5i}\mathbf{A}_i^5+c_{6i}\mathbf{A}_i^6+c_{7i}\mathbf{A}_i^7, \tag{12}$$

where the explicit representations of coefficient c_{ij} are omitted, too.

When we put

$$\mathbf{F}_i(\bar{x},\eta,\zeta,s) = \exp[\mathbf{A}_i(\bar{x}-\bar{x}_{i-1})], \tag{13}$$

equation (9) is rewritten as

$$\mathbf{V}(\bar{x},\eta,\zeta,s) = \mathbf{F}_i(\bar{x},\eta,\zeta,s)\mathbf{V}(\bar{x}_{i-1},\eta,\zeta,s). \tag{14}$$

The physical quantities that must be matched at the interface of each layer consist of temperature T, displacements u_x, u_y and u_z, heat flux q_t, normal stress σ_{xx}, and shear stresses σ_{xy} and σ_{zx}. The dimensionless transformed stress components are expressed as

$$\begin{aligned}\hat{\bar{\sigma}}^*_{xx} &= \beta_{0i}\hat{\bar{u}}^*_{x,\bar{x}} + i(\beta_{0i}-2)(\eta\hat{\bar{u}}^*_y + \zeta\hat{\bar{u}}^*_z) - \beta_{1i}(1+\delta_{2k}\tau_{1i}s)\hat{\theta}^*,\\ \hat{\bar{\sigma}}^*_{xy} &= i\eta\hat{\bar{u}}^*_x + \hat{\bar{u}}^*_{y,\bar{x}}\ ,\quad \hat{\bar{\sigma}}^*_{zx} = \hat{\bar{u}}^*_{z,\bar{x}} + i\zeta\hat{\bar{u}}_x.\end{aligned} \tag{15}$$

The matrix-type relation at the interface of the i-th layer and $(i-1)$-th layer is

$$\mathbf{V}(\bar{x}^+_{i-1},\eta,\zeta,s) = \mathbf{P}_{i-1}(\eta,\zeta,s)\mathbf{V}(\bar{x}^-_{i-1},\eta,\zeta,s), \tag{16}$$

where

$$\mathbf{P}_{i-1} = \begin{bmatrix} 1 & 0 & 0 & 0 & 0 & 0 & 0 & 0\\ 0 & 1 & 0 & 0 & 0 & 0 & 0 & 0\\ 0 & 0 & 1 & 0 & 0 & 0 & 0 & 0\\ 0 & 0 & 0 & 1 & 0 & 0 & 0 & 0\\ 0 & d_{52i} & d_{53i} & d_{54i} & d_{55i} & 0 & 0 & 0\\ 0 & 0 & 0 & 0 & 0 & 1 & 0 & 0\\ 0 & 0 & 0 & 0 & 0 & 0 & 1 & 0\\ 0 & 0 & 0 & 0 & 0 & 0 & 0 & d_{88i} \end{bmatrix},$$

$$d_{52i} = \frac{\beta_{0(i-1)}-\beta_{0i}}{\beta_{0i}}i\eta\ ,\ d_{53i} = \frac{\beta_{0(i-1)}-\beta_{0i}}{\beta_{0i}}i\zeta\ ,\ d_{88i} = \frac{\bar{k}_{(i-1)}(1+\delta_{1k}\tau_{0i}s)}{\bar{k}_i(1+\delta_{1k}\tau_{0(i-1)}s)},$$

$$d_{54i} = -\frac{1}{\beta_{0i}}[\beta_{1(i-1)}(1+\delta_{2k}\tau_{1(i-1)})s - \beta_{1i}(1+\delta_{2k}\tau_{1i}s)]\ ,\ d_{55i} = \frac{\beta_{0(i-1)}}{\beta_{0i}},$$

and $\bar{k}_i = k_i/k_1$ is a dimensionless thermal conductivity.

This procedure is repeated to the first layer. The final form is represented by

$$\mathbf{V}(\bar{x},\eta,\zeta,s) = \mathbf{G}(\bar{x},\eta,\zeta,s)\mathbf{V}(0,\eta,\zeta,s), \tag{17}$$

where

$$\mathbf{G}(\bar{x},\eta,\zeta,s) = \mathbf{F}_i(\bar{x}_i-\bar{x}_{i-1},\eta,\zeta,s)\prod_{j=1}^{i-1}\mathbf{P}_j(\eta,\zeta,s)\mathbf{F}_j(\bar{x}_j-\bar{x}_{j-1},\eta,\zeta,s). \tag{18}$$

The initial state vector $\mathbf{V}(0,\eta,\zeta,s)$ is determined from the boundary conditions. The both surfaces of the medium are stress-free, so that the next dimensionless mechanical boundary conditions are obtained

$$\begin{aligned} \bar{x}=0 \ &; \quad \hat{\bar{\sigma}}^*_{xx}=\hat{\bar{\sigma}}^*_{xy}=\hat{\bar{\sigma}}^*_{zx}=0, \\ \bar{x}=1 \ &; \quad \hat{\bar{\sigma}}^*_{xx}=\hat{\bar{\sigma}}^*_{xy}=\hat{\bar{\sigma}}^*_{zx}=0. \end{aligned} \tag{19}$$

We consider that the partial heat, whose profile is $f(y,z,t)$, is applied to the upper surface $x=l$. The dimensionless thermal boundary conditions are

$$\begin{aligned} \bar{x}=0 \ &; \quad -\hat{\theta}^*_{,\bar{x}}+H_a(1+\tau_{01}s)\theta^*=0, \\ \bar{x}=1 \ &; \quad \hat{\theta}^*_{,\bar{x}}+H_b(1+\tau_{0n}s)(\hat{\theta}^*-\hat{\bar{f}}^*)=0, \end{aligned} \tag{20}$$

where H_a and H_b are Biot's numbers of lower and upper surfaces, respectively. From these eight equations, the initial state vector can be determined. So that, the solutions for temperature, displacements and thermal stresses are obtained in the Laplace and Fourier transformed domains. Because the analytical inversions are much difficult, so the inversions are carried out numerically.

3 Numerical Results and Discussion

Numerical calculations are carried out for multi-layers up to 10 layers based on the generalized theories. The calculation conditions are shown below:

1. Materials
   (a) 1 layer: mild steel (JIS S15C)
   (b) 2 layers:
      layer 1: $\bar{l}_1=0.5$, mild steel (JIS S15C)
      layer 2: $\bar{l}_2=0.5$, ceramics (SiO_2)
   (3) 3-10 layers:
      Each layer has same thickness and mixture of two materials.

2. Biot's numbers (dimensionless relative heat transfer coefficients)
   $H_b=1$, $H_a=\bar{k}_nH_b$

3. Dimensionless relaxation time
   $\tau_{0i}=\tau_{1i}=0.01$

4. Dimensionless heat profile
   $\bar{f}(\bar{y},\bar{z},\tau)=H(1-\bar{y})H(1-\bar{z})H(\tau)$,
   where $H(\cdot)$ is Heavisides unit step function.

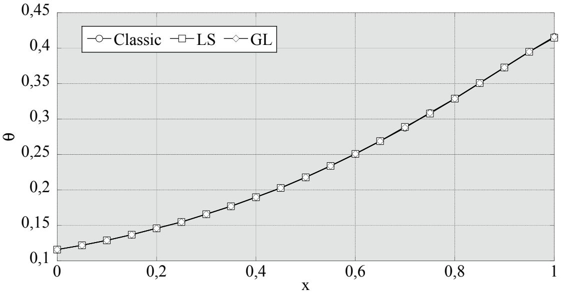

Fig. 2 Temperature distributions θ at the position $\bar{y} = \bar{z} = 0(\tau = 0.6\ ,\ 1\ layer)$

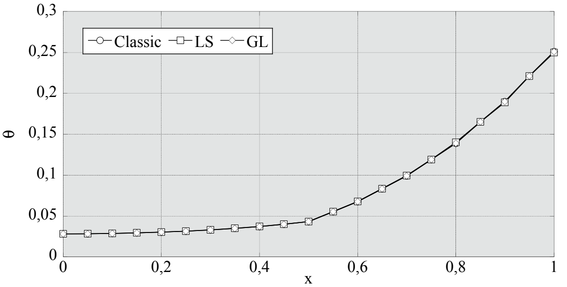

Fig. 3 Temperature distributions θ at the position $\bar{y} = \bar{z} = 0(\tau = 0.6\ ,\ 10\ layers)$

5. Dynamical coefficient and initial temperature
   $\xi_i = 1.0\ ,\quad T_0 = 293\text{K}$

The mechanical and thermal properties for mild steel (JIS S15C) and ceramics (SiO_2) are

$$\nu_s = 0.3\ ,\ \nu_c = 0.31\ ,\ E_s = 206\text{GPa}\ ,\ E_c = 220\text{GPa}\ ,\ \alpha_s = 11.8 \times 10^{-6}\text{K}^{-1},$$
$$\alpha_c = 10.8 \times 10^{-6}\text{K}^{-1}\ ,\ c_{vs} = 473\text{J/(kgK)}\ ,\ c_{vc} = 460\text{J/(kgK)},$$
$$k_s = 51.6\text{W/(mK)}\ ,\ k_c = 3.0\text{W/(mK)}\ ,\ \rho_s = 7860\text{kg/m}^3\ ,\ \rho_c = 6000\text{kg/m}^3,$$

where subscripts s and c mean the mild steel and ceramics, respectively. The mixture rule of particle dispersion reinforcements [14,15] is used for inner layers.

Figures 2 and 3 show the temperature distributions θ in $\bar{x}$ direction of 1 layer and 10 layers at the position $\bar{y} = \bar{z} = 0$ and dimensionless time $\tau = 0.6$, respectively.,The temperature distribution of 10 layers is lower than that of 1 layer. The differences between classical and generalized theories are not cleared here.

Figure 4 shows the comparison of layer numbers for generalized theory (L-S) at the position $\bar{y} = \bar{z} = 0$ and dimensionless time $\tau = 0.6$. The reduction effects of temperature are occurred at the case of large layers.

Figures 5 and 6 show the thermal stress distributions $\bar{\sigma}_{xx}$ in $\bar{x}$ direction of 1 layer and 10 layers at the position $\bar{x} = \bar{z} = 0$ and dimensionless time $\tau = 0.6$,

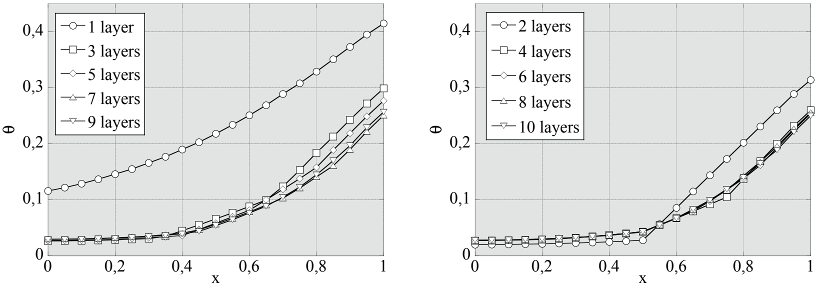

Fig. 4 Temperature distributions θ at the position $\bar{y} = \bar{z} = 0 (\tau = 0.6\ ,\ L - S)$

respectively. The compressive maximum thermal stress of 10 layers is lower than that of 1 layer. The stresses for generalized theories are slightly larger than that of classical one. Figure 7 shows the comparison of layer numbers for L-S theory at the position $\bar{x} = \bar{z} = 0$ and dimensionless time $\tau = 0.6$. The reduction effects of stresses are occurred at the case of large layers.

Fig. 5 Stress distributions $\bar{\sigma}_{xx}$ at the position $\bar{x} = \bar{z} = 0\ ,\ (\tau = 0.6\ ,\ 1\ layer)$

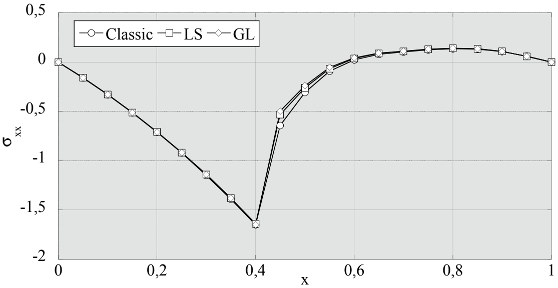

Fig. 6 Stress distributions $\bar{\sigma}_{xx}$ at the position $\bar{x} = \bar{z} = 0\ ,\ (\tau = 0.6\ ,\ 10\ layers)$

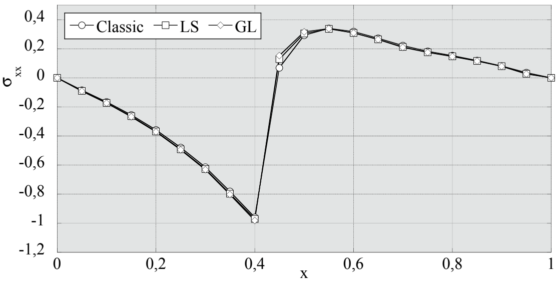

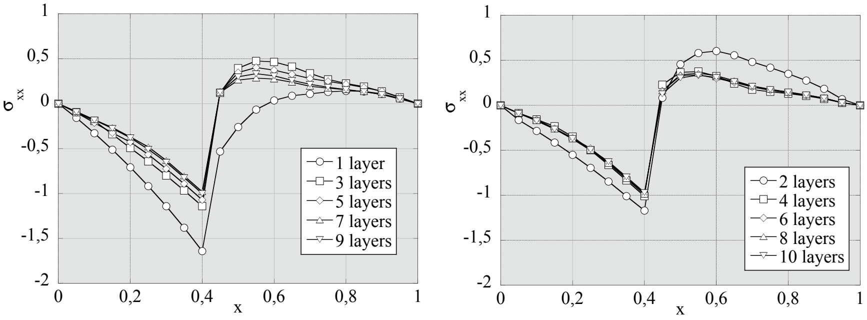

Fig. 7 Stress distributions $\bar{\sigma}_{xx}$ at the position $\bar{x} = \bar{z} = 0$, $(\tau = 0.6\ ,\ L - S)$

4 Conclusions

Three-dimensional generalized thermoelasticity based on L-S and G-L theories is analyzed by use of the state space approach and integral transform techniques. The functionally graded material is approximated to a multi-layered medium and each layer is homogeneous and isotropic. The surfaces are traction free and subjected to a partial heating. The following facts can be found.

1. The state space approach can be applicable to replace the functionally graded material to a multi-layered medium and the numerical calculation of multi-layered medium has been performed up to 10 layers.
2. The global tendency of reduction effects of temperature and thermal stresses by increasing layer number has been examined.
3. The difference between classical and generalized theories is not cleared under this calculation condition. However, the maximum stress of the generalized theories is larger than that of classical one.

References

1. Furukawa T, Irschik H (2005) Body-force analogy for one-dimensional coupled dynamic problems of thermoelasticity. J Therm Stresses 28: 455-464.
2. Lord HW, Shulman Y (1967) A generalized dynamical theory of thermoelasticity. J Mech Phys Solids 15: 299-309.
3. Green AE, Lindsay KA (1972) Thermoelasticity. J Elast 2: 1-7.
4. Hetnarski RB, Ignaczak J (1996) Soliton-like waves in a low-temperature nonlinear thermoelastic solid. Int J Eng Sci 34: 1767-1787.
5. Green AE, Naghdi PM (1993) Thermoelasticity without energy dissipation. J Elast 31: 189-208.
6. Chandrasekharaiah DS (1998) Hyperbolic thermoelasticity; A review of recent literature. Appl Mech Rev 51: 705-729.

7. Tzou DY (1995) A unified approach for heat conduction from macro to micro-scales. J Heat Transf 117: 8-16.
8. Hetnarski RB, Ignaczak J (1999) Generalized thermoelasticity. J Therm Stresses 22: 451-476.
9. Noda N, Furukawa T, Ashida F (1989) Generalized thermoelasticity in an infinite solid with a hole. J Therm Stresses 12: 385-402.
10. Furukawa T, Noda N, Ashida F (1991) Generalized thermoelasticity for an infinite solid cylinder. JSME Int J Ser I 34: 281-286.
11. Furukawa T, Nakanishi H, Uneyama H (1999) State space approach to generalized thermoelasticity of layered medium subjected to partial heating. Proc 3rd Int Congr Therm Stresses. Thermal Stresses 99:111-114.
12. Furukawa T (2001) State space approach to generalized thermoelasticity of layered medium subjected to axisymmetric heating. Proc 4th Int Congr Therm Stresses. Thermal Stresses 2001: 297-300.
13. Baher LY, Hetnarski RB (1980) Coupled thermoelasticity of a layered medium. J Therm Stresses 3: 141-152.
14. Kerner EH (1956) The electrical conductivity of composite media. Proc Phys Soc B 69: 802-807.
15. Kerner EH (1956) The elastic and thermo-elastic properties of composite media. Proc Phys Soc B 69: 808-813.

Numerical homogenization and optimization of smart composite materials

Ulrich Gabbert, Sreedhar Kari, Niels Bohn and Harald Berger

Abstract The paper presents a numerical homogenisation approach to calculate the effective properties of fibre and particle reinforced materials including smart and multifunctional materials with a focus on piezoelectric fibre composites applied to control vibration and noise radiation of structures. This finite element based homogenisation is used to optimise the material distribution at the micro-scale by applying an evolutionary approach to receive a desired global behaviour of a structure at the macro-scale.

1 Introduction

Composite materials play a major role in meeting the increasing demand of the industry for lightweight and low-cost structures. Compared to classical monolithic engineering materials, composites offer higher specific strength and specific stiffness values.

Smart piezoelectric fiber and particle reinforced composites are a new class of materials, which are increasingly used to actively influence structures to reduce, e.g., the vibration and the noise radiation [10]. Recently, composite piezoelectric materials have been developed by combining piezoceramic fibers with passive non-piezoelectric polymers, such receiving active fibrous composites.

A number of methods have been developed to predict the homogenized material properties of composites, which are required to perform static and dynamic structural analysis. Analytical approaches ([1], [17]) are not capable of predicting the response to general loadings, i.e., they do not give the full set of overall material parameters. Semi analytical, Hashin/Shtrikman-type

---

Ulrich Gabbert, Sreedhar Kari, Niels Bohn and Harald Berger
Institute of Mechanics, Otto von Guericke University of Magdeburg, Universitätsplatz 2, D-391106 Magdeburg, Germany, e-mail: ulrich.gabbert@mb.uni-magdeburg.de

and other bounds for describing the complete overall behavior (i.e., providing all elements of the material tensors) have been developed (see [4], [7], [15], [16]), which are useful tools for theoretical considerations. However, the range between the bounds can be very wide for certain effective moduli. Mechanical mean field type methods have been extended to include electro-elastic and thermal effects based on an Eshelby-type solution [9], [14], [18]. The restrictions of the methods can be overcome by employing periodic micro field approaches where the fields are typically solved numerically with high resolution, e.g., by the finite element method [11]. Most of these methods are restricted to regular packings of fibers (rectangular and hexagonal). However, in practical situations the fibers are aligned in their longitudinal direction, while their arrangement in the matrix in transverse cross-section is usually distributed randomly. To the knowledge of the authors, there is not much development to handle the problem of transversely randomly distributed multi-field fiber composites properly. The aim of the present paper is to present a numerical finite element based approach to predict the full set of piezoelectric, dielectric, and mechanical effective material coefficients of such composites with complex geometrical reinforcements (for details see [5], [13]). This approach is used to optimize the microstructure (fiber distribution, fiber orientation, fiber-volume fraction etc.) with respect to an objective function defined at the macrostructure.

2 Numerical homogenization

Numerical finite element based micromechanical methods provide a powerful general tool to calculate the homogenized properties of fiber and particle reinforced and multi-field composite materials, such as piezoelectric fiber composites, through an analysis of a periodic representative volume element (RVE).

In piezoelectric fiber composites an electric potential gradient causes deformations (converse piezoelectric effect), while strains cause an electric potential gradient in the material (direct piezoelectric effect). The behavior of a piezoelectric medium in low electric and mechanical applications can be described by the following linear piezoelectric constitutive equations, which correlate stresses T, strains S, electric fields E, and electrical displacements D as follows (the superscript t for transpose)

$$\begin{bmatrix} T \\ D \end{bmatrix} = \begin{bmatrix} C & -e^t \\ e & \varepsilon \end{bmatrix} \begin{bmatrix} S \\ E \end{bmatrix}, \tag{1}$$

where C is the elasticity matrix, ε is the permittivity matrix, and e is the piezoelectric strain coupling matrix.

The numerical finite element based calculation of the mean values of a

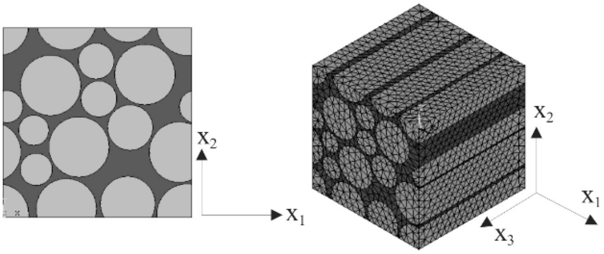

Fig. 1 Representative unit cell (left) and corresponding finite element mesh (right)

piezoelectric fiber composite is based on a representative volume element (RVE), which captures the global behaviour of the composite. If the fibers are randomly distributed the size of the RVE with respect to the diameter of the fibers is an important criterion. Our approach applies the random sequential absorption algorithm (RSA) [19] modified to provide a minimum distance between any two fibers and for periodicity between opposite boundary surfaces. In this algorithm the coordinates of the center of the fibers are generated randomly step by step. A new generated midpoint coordinate is checked for non-overlapping conditions with previously placed fibers. If there is no overlapping and the periodicity is satisfied, then the fiber will be placed on the plane. If a fiber cuts the boundary of the unite cell, then on the opposite site also a fiber has to be placed to grantee the periodicity. This process will be terminated when the desired volume fraction is achieved or when no more fibers can be added because of the jamming limit, which can occur at a volume fraction higher than 55%. For higher volume fractions, different diameters of fibers are used, and these are placed on the x_1-x_2 plane in a descending manner. With this approach the volume fraction achieved is about 80% with an adequate finite element meshing. Figure 1 shows an example of such a generated RVE with variable diameters of fibers, and their corresponding 3D finite element mesh.

Composite materials can be represented as a periodical array of the RVEs, where each RVE has the same deformation mode, and there is no separation or overlap between the neighboring RVEs after deformation. These periodic boundary conditions described in Cartesian coordinates are given by [17]

$$u_i = \bar{S}_{ij} x_j + v_i \tag{2}$$

$\bar{S}_{ij}$ denotes the average strains, and v_i is the periodic part of the displacement components (local fluctuation) on the boundary surfaces. The difference of the displacements of a pair of opposite boundary surfaces points (with their normal along the x_i axis) is

$$u_i^{K^+} - u_i^{K^-} = \bar{S}_{ij} \left(x_j^{K^+} - x_j^{K^-} \right), \tag{3}$$

where the index 'K^+' means along the positive x_i direction, and 'K^-' means along the negative x_i direction on the corresponding surfaces of the 3D RVE. The local fluctuations are identical on two opposing faces and disappear in the difference. Similarly, the periodic boundary conditions for the electrical potential are given as

$$\Phi^{K^+} - \Phi^{K^-} = \bar{E}_i \left(x_i^{K^+} - x_i^{K^-} \right) , \tag{4}$$

where Φ represents the voltage and $\bar{E}_i$ represents the average electric field.

The average mechanical and electrical properties of a unit cell, calculated by

$$\begin{aligned} \bar{S}_{ij} &= \frac{1}{V} \int_V S_{ij} dV \quad , \quad \bar{T}_{ij} = \frac{1}{V} \int_V T_{ij} dV , \\ \bar{E}_i &= \frac{1}{V} \int_V E_i dV \quad , \quad \bar{D}_i = \frac{1}{V} \int_V D_i dV , \end{aligned} \tag{5}$$

are finally used to calculate the mean values of the material tensor with help of equation (1) (for details see [13]).

All finite element calculations are made with the commercial FE package ANSYS for fully coupled electromechanical analyses. An APDL-script allows performing all required calculations to evaluate finally the effective material properties automatically in a batch processing, which provides a powerful tool for a fast calculation of homogenized material properties for composites with a great variety of inclusion geometries.

3 Optimization of fiber reinforced composites

The optimization goal is the minimization of an appropriate objective function

$$\min_{\mathbf{x} \in S} f(\mathbf{x}) \; , \quad S = \left\{ \mathbf{x} \in \Re^N \, | h_i(\mathbf{x}) = 0 \, , \; g_j(\mathbf{x}) \leqslant 0 \right\} , \tag{6}$$

where $\mathbf{x}$ is the N-dimensional vector of design variables, $h_i(\mathbf{x}) \, , \; i = 1, ..., n$ and $g_j(\mathbf{x}) \, , \; j = 1, ..., m$ are the equality constraints and the inequality constraints, respectively. To solve the optimization problem various methods have been developed [12], which require the computation of gradients. Their operability can only be guaranteed if the objective function is continuously differentiable and uni-modal. When composite materials are considered, the objective functions are more likely to be non-smooth, non-differentiable and multimodal [20]. In such cases we suggest direct methods, which apply principles of natural evolution (recombination, mutation and selection) to a set μ of feasible solutions, the individuals

$$\mathbf{w} = [x_1,\ x_2,\ \cdots\ x_N,\ \sigma_1,\ \sigma_2,\ \cdots\ \sigma_{N_\sigma}]\ , \quad k = 1, ..., \mu \tag{7}$$

N stands for the problem dimension, x_i represent the design variables of the optimisation problem, and σ_i are the step-sizes for the mutation process. The generation of new solutions starts with recombination, where a number of $\lambda \geq \mu$ offspring individuals are created by exchanging or averaging the properties of randomly selected parents

$$w'_{ki} = \begin{cases} w_{pi} \text{ or } w_{qi} \\ (w_{pi} + w_{qi})/2 \end{cases} \quad k = 1, ..., \lambda, \quad i = 1, ..., N, \quad p, q \sim U(1, \mu). \tag{8}$$

For more recombination variants see [3]. A mutation is carried out by the application of small random changes in each component of an individual. The process starts with the variation of the mutation step-sizes as

$$\sigma''_{ki} = \sigma'_{ki} \cdot h\left(\bar{z}_k,\ \tau_1,\ \cdots\ \tau_r\right). \tag{9}$$

The function h depends on the standard normal distributed random variants $\bar{z} \sim N(1, 0)$ as well as on r heuristic factors τ_j, $j = 1, ..., r$ (see [2], [3], [6]). The object variables are then mutated according to

$$x''_{ki} = x'_{ki} + z_{ki}\ , \quad k = 1, ..., \lambda, \tag{10}$$

where $z_{ki} \sim N(0, \sigma''_{ki})$ is a normal distributed random variant which depends on the individual mutation step-sizes. The population consists finally of λ offsprings

$$\mathbf{w}'' = \left[x''_1,\ x''_2,\ \cdots\ x''_N,\ \sigma''_1,\ \sigma''_2,\ \cdots\ \sigma''_{N_\sigma}\right]\ , \quad k = 1, ..., \lambda. \tag{11}$$

After the evaluation of the objective function is performed for each individual, the μ best individuals are selected to become the parents for the next iteration.

The generation loop is repeated until a termination criterion, such as a lower limit for the mutation step-sizes, is fulfilled. A general software tool has been developed on the basis of evolution strategies with an interface to the commercial finite element code ANSYS. Our software possesses a modular structure, allowing for the implementation of various intermediate steps in the optimization process.

4 Results and Discussion

For the calculation of effective coefficients we consider a composite with circular piezoelectric (PZT-5) fibers uniformly polarized along the x_3 direction

	C_{11}	C_{12}	C_{13}	C_{33}	C_{44}	C_{66}	e_{15}	e_{13}	e_{33}	ε_{11}	ε_{33}
PZT-5	12.1	7.54	7.52	11.1	2.11	2.28	12.3	5.4	15.8	8.11	7.35
Polymer	0.386	0.257	0.257	0.386	0.064	0.064	-	-	-	0.07965	0.07965

Table 1 Material properties of the composite constituents fiber (PZT-5) and matrix, (Polymer) ($C_{ij}\,[GPa]\,;\ e_{ij}\,[C/m^2]\,;\ \varepsilon_{ij}\,[nF/m]$)

50% volume fraction	C_{11}	C_{12}	C_{22}	C_{23}	C_{33}	C_{13}	C_{66}	C_{44}
Same diameter	9.40	4.93	9.07	5.47	31.96	5.58	1.87	1.99
Random diameter	9.23	4.93	9.13	5.49	31.91	5.52	1.87	2.0

50% volume fraction	e_{15}	e_{13}	e_{33}	ε_{11}	ε_{33}
Same diameter	0.0021	-0.224	9.81	0.273	3.86
Random diameter	0.0021	-0.219	9.80	0.266	3.85

Table 2 Comparison of piezoelectric fibers, ($C_{ij}\,[GPa]\,;\ e_{ij}\,[C/m^2]\,;\ \varepsilon_{ij}\,[nF/m]$)

and embedded randomly in a soft non-piezoelectric material (polymer) in the transverse cross section (Table 1).

4.1 Effect of the Fiber Diameter on Effective Material Properties

Investigations are performed to study the influence of the diameter of piezoelectric fibers on the effective material properties of these composites. The fluctuations (error) of effective material properties around the mean value, which are obtained from the ensemble averages of the effective material properties of five RVE samples, are negligible.

The numerical homogenization techniques are also applied to two different types of the RVE models, one with an identical diameter of all piezoelectric fibers and another with a random diameter of fibers between 0.32mm and 0.12mm at 50% volume fraction. In both cases, also five different RVE samples are considered, and the effective material properties are obtained from the ensemble average of the effective material properties. It is observed that the differences in the effective material properties are again negligible, and the differences between the random and identical diameter of piezoelectric fibers are at most 2% (see Table 2).

4.2 Influence of the fiber arrangement

The effective electrical and mechanical properties of transversely randomly distributed uni-directional piezoelectric fiber composites are evaluated for different volume fractions up to 80%. The effective material properties, which

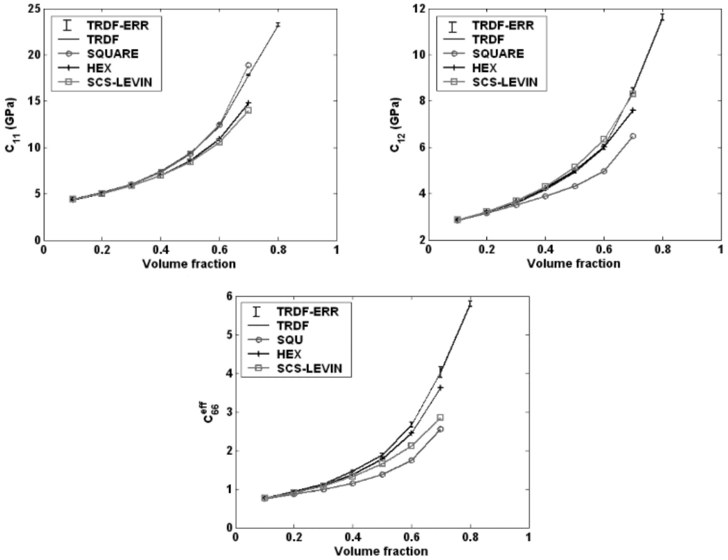

Fig. 2 Comparison of effective mechanical properties of transversely randomly distributed piezoelectric fiber composites (TRDF) with square (SQUARE) and hexagonal (HEX) array with the analytical self-consistent scheme by Levin [14] (SCS-Levin).

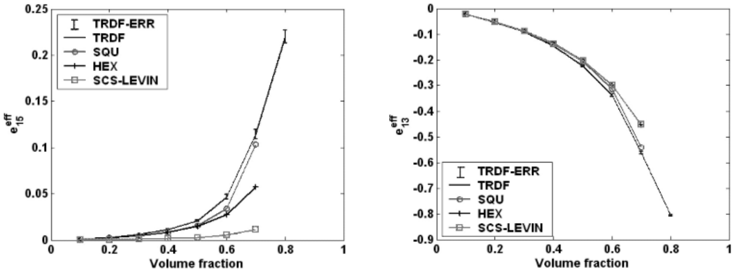

Fig. 3 Comparison of effective piezoelectric properties of transversely randomly distributed fiber composites (TRDF) with square (SQUARE) and hexagonal (HEX) array with the analytical self-consistent scheme by Levin [14] (SCS-Levin).

are obtained for these cases, are compared with a square arrangement and a hexagonal arrangement of the piezoelectric fibers. For the square arrangement the maximum theoretically achievable volume fraction is 78.54%. Due to the meshing limits with our finite element approach a maximum volume fraction of 70% can be generated only. Figs. 2 and 3 represent the effective mechanical and piezoelectric properties, respectively, calculated for different fiber arrangements in the composite. The figures compare the numerically calculated results based on different fiber arrangements, such as the transversely randomly distributed arrangement (TRDF), the square arrangement (SQUARE) and the hexagonal arrangement (HEX) with the results calculated by the self consistent schema (SCS-LEVIN) [14]. From Fig 2 it can be observed that the transverse mechanical properties are tending to increase for transversely randomly distributed composites when compared with regular array composites, especially for the hexagonal array, but not in all other cases. As a comparison between the square array and the hexagonal array, the hexagonal array has a 6-fold axis of symmetry along fiber direction, and results in a transverse isotropic behavior, i.e., $C_{11}^{\text{eff}} - C_{22}^{\text{eff}} = 2C_{66}^{\text{eff}}$, whereas for the case of the square array, it has only 4-fold axis of symmetry, and it will give rise to a tetragonal behavior resulting in a higher transverse stiffness. For the transverse shear modulus C_{66}^{eff}, it is observed that the square array composite has a lower transverse shear modulus, and the hexagonal array composite has a higher value and satisfies the transverse isotropy.

In general, from our analysis it can be observed that the assumption of a transversely randomly distributed fiber composites results in higher transverse material properties when compared with a regular array of fiber arrangement. The longitudinal material properties are almost the same like for a regular array of composites. Also the numerical results of the effective material coefficients like C_{11}^{eff}, $\varepsilon_{11}^{\text{eff}}$ along the transverse direction of a transversely randomly distributed fiber composites match well with the results of SCS at lower volume fractions in the considered fraction range between 10% and 40%. Beyond this volume fraction range, the effective coefficients of SCS are underestimated.

The transverse isotropy was checked for all generated RVE samples and for all effective material coefficients.

4.3 Optimization of a short fiber composite

We consider a quadratic plate with a hole in the middle consisting form a polysulfon matrix being reinforced by short aramid fibers and loaded in x-direction by a distributed load (for details see [8]). The amount of fibers in the plate is limited to a prescribed average fiber density. The purpose of the optimization is to distribute a fixed amount of fibres in the matrix material in such a way, that a maximal structural stiffness is obtained under restrictions concerning the maximal principal stress and the average fibre density in the plate. A (10, 70)-ES with discrete recombination and Schwefels mutation type is applied [6].

Fig. 4 shows the optimal fiber orientations and the directions of the principal stresses. The fibres concentrate in regions close to the upper side of the hole, where the maximal stresses occur. A similar result is published in [8]. The optimization algorithm converges after about 80 generations leading to

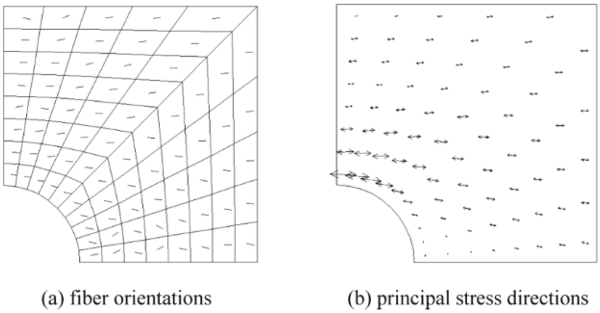
(a) fiber orientations (b) principal stress directions

Fig. 4 Optimal short fibre orientations and principal stress directions

a decrease of 49% in the objective function when compared to the random initial design.

5 Conclusion

A finite element based numerical homogenization approach to evaluate the effective material properties of active piezoelectric fiber composites is presented. A generalized procedure has been developed to calculate all effective coefficients automatically for all volume fractions based on the ANSYS Parametric Design Language. It reduces the manual work and time and can be used as a template to evaluate the effective coefficients of piezoelectric fiber composites with arbitrary arrangement of fibers. It is shown that evolution strategies are a reliable and efficient method for the optimization of composite structures. The algorithm operates on a set of feasible solutions and requires no derivatives of the objective function. It has superior global search qualities and can be used even for non-differentiable, non-smooth and multimodal problems, which arise frequently in the context of the optimization of composite structures. The test example underlines the good research properties of evolution strategies.

Acknowledgements This work has been supported by German Research Foundation (DFG), *Graduate College 828*, as well as the German State of Saxony-Anhalt and the European Commission in the frame of the research project *COmpetence in MObility COMO*. These supports are gratefully acknowledged.

References

1. Bakhvalov, N., Panasenko, G., 1989. Homogenization: Averaging Processes in Periodic Media-Mathematical Problems in the Mechanics of Composite Materials, Kluwer, Dordrecht.
2. Bäck, T.: Evolutionary algorithms in theory and practice: evolution strategies, evolutionary programming, genetic algorithms. Oxford University Press, Oxford, UK, 1996.
3. Bäck, T., Schwefel, H.P.: Evolution Strategies I: Variants and their Computational Implementation. In: Winter, G., Periaux, J., Galan, M., Cuesta, P. (eds.) Genetic Algorithms in Engineering and Computer Science, Wiley & Sons Ltd., chap. 6, pp. 111-126, 1995.
4. Benveniste, Y., 1993. Universal relations in piezoelectric composites with eigenstress and polarization fields. Part I: Binary media-local fields and effective behavior, J. Appl. Mech., 60 (2): 265-269.
5. Berger, H., Kari, S., Gabbert, U., Rodriguez-Ramos, R., Guinovart-Diaz, R., Otero, J. A., Bravo-Castillero, J., 2005. An analytical and numerical approach for calculating effective material coefficients of piezoelectric fiber composites, Int. J. Sol. Struct., Vol. 42, pp. 5692-5714.
6. Beyer, H.G., Schwefel, H.P.: Evolution strategies - a comprehensive introduction. Natural Computing 1(1):3-52, 2002.
7. Bisegna, P., Luciano, R., 1997. On methods for bounding the overall properties of periodic piezoelectric fibrous composites, J. Mech. Phys. Solids, 45 (8): 1329-1356.
8. Brighenti, R.: Fibre distribution optimisation in fibre-reinforced composites by a genetic algorithm. Composite Structures 71:1-15, 2005.
9. Dunn, M.L., Wienecke, H.A., 1997. Inclusions and inhomogeneities in transversely isotropic piezoelectric solids, Int. J. Sol. Struct., 34 (27): 3571-3582.
10. Gabbert, U., Nestorović, T., Wuchatsch, J.: Methods and possibilities of a virtual design for actively controlled smart structures, Computers and Structures, Vol. 86, 2008, pp. 240-250.
11. Gaudenzi, P., 1997. On the electromechanical response of active composite materials with piezoelectric inclusions, Comput. Struct., 65 (2): 157-168.
12. Haftka, R., Grdal, Z.: Elements of Structural Optimization. Kluwer, Dordrecht, 1992.
13. Kari, S., Berger, H., Rodriguez-Ramos, R., Gabbert, U.: Numerical evaluation of effective material properties of transversely randomly distributed uni-directional piezoelectric fiber composites, Journal of Intelligent Material Systems and Structures, Vol. 18, 2007, pp. 361-372.
14. Levin V. M., Rakovskaja M. I., Kreher W. S., 1999. The effective thermoelectroelastic properties of microinhomogeneous materials, Int. J. Solids Struct., 36: 2683-2705.
15. Rodriguez-Ramos, R., Guinovart-Diaz, R., Bravo-Castillero, J., Sabina ,F.J. , Berger, H., Kari, S., Gabbert, U.: Variational bounds for anisotropic elastic multiphase composites with different shapes of inclusions. Archive of Applied Mechanics, online available.
16. Schulgasser, K., 1992. Relationships between the effective properties of transversely isotropic piezoelectric composites, J. Mech. Phys. Solids, 40: 473-479.
17. Suquet, P., 1987. Elements of homogenization theory for inelastic solid mechanics, in: Sanchez-Palencia, E., Zaoui, A. (Eds.), Homogenization Techniques for Composite Media, Springer-Verlag, Berlin: pp.194-275.
18. Wang, B., 1992. Three-dimensional analysis of an ellipsoidal inclusion in a piezoelectric material, Int. J. Sol. Struct., 29: 293-308.
19. Wang J.S., 1998. Random sequential adsorption, series expansion and monte carlo simulation, Physics A, 254: 179-184.
20. Zohdi, T.: Genetic design of solids possessing a random-particulate microstructure. Phil. Trans. R. Soc. Lond. A. 361:1021-1043, 2003.

Hybride Bell Tower Like Structures in Earthquake Environment

Rudolf Heuer and S. Mehdi Yousefi

Abstract Dynamic actions of bell movement are characteristic aspects in bell towers and thus show significant influences on the response of the main structure. In case of strong motions the oscillation of the bell exhibits (moderately) large rotations and nonlinear analysis becomes essential to understand the nature of the system and its dynamic process. The bell is modeled as rigid pendulum and the equations of motion of the hybrid structure follow from the formulation according to Lagrange equations. A coupled 2DOF system is used to study the dominant geometrically nonlinear influence of the bells rotation in frequency domain. Numerical nonlinear computer simulations are performed for MDOFs studying the influence of the higher modes of the main structure on the behavior of the pendulum. Parameter studies are performed for two different types of support excitations, i.e., time-harmonic, stationary random process.

1 Introduction

A Bell Tower (BT) can be considered as a structure consisting of two substructures, namely the tower and the bell. The bell ringing action is modeled as a simple pendulum that is suspended near the towers upper part by a hinge bearing. The mechanical model of a tower is represented by a continuous structure and it is idealized as a Multi-Degree-of-Freedom (MDOF) system.

Rudolf Heuer
Vienna University of Technology, Vienna A-1040/E2063, Vienna, Austria, e-mail: rudolf.heuer@tuwien.ac.at

S. Mehdi Yousefi
Vienna University of Technology, Vienna A-1040/E2063, Vienna, Austria,e-mail: s.mehdiyousefi@gmail.com

In the following research the tower structure coupled with a bell is studied under dynamic loading, particularly against support excitation. The complete structure is modeled as extended MDOF system [1], discrete bell and continuous tower, in order to give insight into its complex nonlinear dynamic behavior. Both linear and nonlinear behavior of the coupled system are analyzed. The formulation of the equation of motion is based on Lagrange equations that are applicable to systems in both linear and nonlinear conditions. After applying appropriate analytical methods, parametric studies for forced vibrations are performed by means of computer simulations. The nonlinear dynamic analysis of the forced vibrations are chosen in time domain by using numerical investigation with emphasize on the nonlinear interaction between the excited tower and movement of the bell.

As shown in Figure 1, the mechanical model of a tower is represented by a continuous slender structure, and the bell is modeled as a rigid pendulum, that can also be interpreted as passive tuned pendulum mass damper to improve the response of the entire structure under dynamic loads.

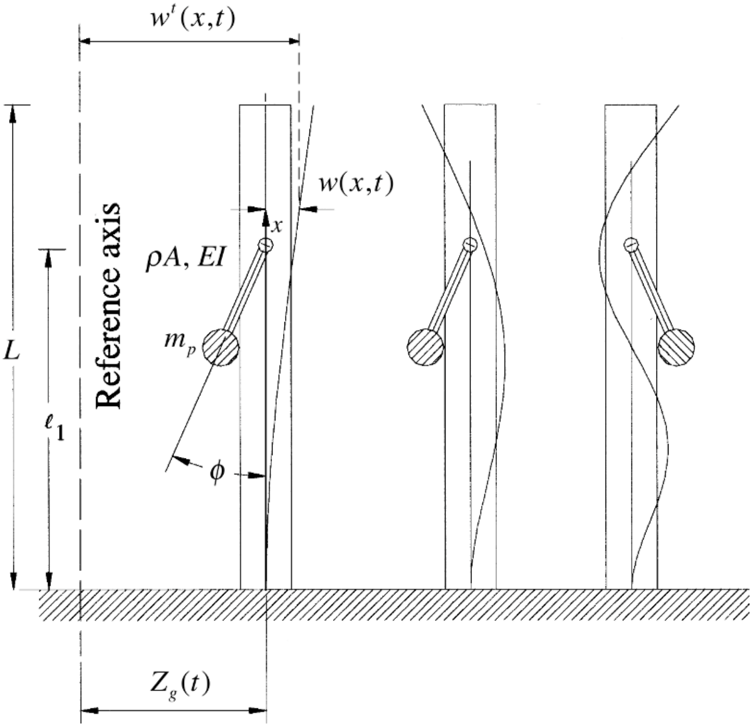

Fig. 1 Mechanical model of the bell tower like structure and its first 3 mode shapes

2 The generalized MDOF system

The tower is mechanically idealized as a MDOF system and the bell is idealized as a "mathematical pendulum". The nonlinearity in this system is due to large rotation of pendulum. In order to approximate the motion of the tower, several mode shapes $\psi_i(x)$ are assumed for the deflection. The amplitudes of the motion are represented in form of generalized coordinates $Z_i(t)$, compare [2],

$$w(x,t) = \sum_{i=1}^{n} \psi_i(x) Z_i(t). \tag{1}$$

The total displacement of the tower at point x is

$$w^t(x,t) = Z_g(t) + w(x,t). \tag{2}$$

The structure is subjected to base excitation $\ddot{Z}_g(t)$ or/and to an external moment due to the bell-ringing action $M(t)$. The generalized coordinates are selected as the modal displacements of some convenient point of the tower such as its tip. By using the expressions for the kinetic and potential energy,

$$T = \frac{1}{2}\left(\int_0^L \rho A \left[\dot{w}^t(x,t)\right]^2 dx + m_p v_p^2\right), \tag{3}$$

$$V = \frac{1}{2}\int_0^L EI\left[w''(x,t)\right]^2 dx - m_p g s cos\phi - M\phi, \tag{4}$$

and applying Lagrange equations of motion [3],

$$\frac{d}{dt}\left(\frac{\partial T}{\partial \dot{Z}_i}\right) - \frac{\partial T}{\partial Z_i} + \frac{\partial V}{\partial Z_i} = Q_i, \tag{5}$$

where

$$Q_i = -r_i \sum_{j=1}^{n} \dot{Z}_j \int_0^L \psi_i \psi_j dx, \tag{6}$$

the system equations, exemplarily, for the first two modes of the tower, and pendulum are expressed as follows [4]

$$(m_1 + m_p)\ddot{Z}_1(t) + m_p \ddot{Z}_2(t) + c_1 \dot{Z}_1(t) + k_1 Z_1(t) + m_p s\left(\ddot{\phi} cos\phi - \dot{\phi}^2 sin\phi\right) = -\left(m_1^* + m_p\right)\ddot{Z}_g(t) \tag{7}$$

$$\begin{aligned}(m_2 + m_p)\ddot{Z}_2(t) + m_p\ddot{Z}_1(t) + c_2\dot{Z}_2(t) + k_2 Z_2(t) + \\ + m_p s(\ddot{\phi}\cos\phi - \dot{\phi}^2\sin\phi) = -(m_2^* + m_p)\ddot{Z}_g(t),\end{aligned} \tag{8}$$

$$m_p s\cos\phi \ddot{Z}_1(t) + m_p s\cos\phi \ddot{Z}_2(t) + m_p s^2\ddot{\phi} + 2m_p s^2\omega_p\zeta_p\dot{\phi} + \\ + m_p s g\sin\phi = -m_p s\cos\phi \ddot{Z}_g(t) + M(t). \qquad (9)$$

The damping parameter of the pendulum reads

$$c_p = 2s^2\zeta_p m_p\omega_p. \qquad (10)$$

Definition of the generalized mass, stiffness and damping are introduced as

$$m_i = \int_0^L \rho A\,\psi_i^2(x)\,dx\ , \quad k_i = \int_0^L EI\,[\psi_i''(x)]^2 dx,$$

$$c_i = r_i\int_0^L \psi_i^2(x)\,dx\ , \quad m_i^* = \int_0^L \rho A\,\psi_i(x)dx\ , \quad i = 1, 2. \qquad (11)$$

where ρA is the mass per unit length of the tower, and m_p is the mass of the idealized (mathematical) pendulum. EI stands for the flexural stiffness of the tower and s is the length of the pendulum. Considering proportional Rayleigh Damping the coefficients c_i are expressed as linear combination of the modal mass and stiffness coefficients m_i and k_i as

$$c_i = a_0 m_i + a_1 k_i, \qquad (12)$$

where a_0 and a_1 have to be determined experimentally.

By means of time-integration the solution of these three equations leads to the displacements of the tower for the first and second mode and the rotation angle of the pendulum in each time step.

3 Geometrical nonlinear influence of the bell (pendulum)

In order to study the geometrical influence of the bell rotation on the response of the total structure, initially, the tower is discretized only by means of its dominant basic mode, thus the two coupled equations of motion read

$$(1+\mu)\ddot{Z} + \frac{r}{m_1}\dot{Z} + \omega^2 Z + \mu s\,\ddot{(\sin\phi)} = -(1+\mu)\ddot{Z}_g\ , \quad \mu = m_p/m_1, \qquad (13)$$

$$\ddot{\phi} + \frac{r_p}{m_p s^2}\dot{\phi} + \omega_p^2\sin\phi = -\frac{\cos\phi}{s}\underbrace{\left(\ddot{Z}_g + \ddot{Z}\right)}_{\ddot{Z}^t} + \frac{M}{m_p s^2}. \qquad (14)$$

Expansion of both the system an excitation parameters leads to

$$\sin\phi \approx \phi - \frac{1}{6}\phi^3 \ , \quad \cos\phi \approx 1 - \frac{1}{2}\phi^2. \tag{15}$$

Consequantly, the movement of the rigid pendulum (bell) is described as

$$D\left\{\phi\right\} = \ddot{\phi} + \omega_p^2\left(\phi - \frac{1}{6}\phi^3\right) + \frac{1}{s}\left(1 - \frac{1}{2}\phi^2\right)\ddot{Z}^t - \frac{M}{m_p s^2} = 0. \tag{16}$$

Furthermore, in case of a time-harmonic excitation,

$$\ddot{Z}^t = sb\cos\nu t \quad or \quad \frac{M}{m_p s^2} = d\cos\nu t. \tag{17}$$

Galerkin's procedure can be applied to find an approximate frequency-domain solution for the response in the neighborhood of the primary resonance,

$$\int\limits_0^{2\pi/\nu} D\left\{\phi^*\right\}\cos\nu t\ dt = 0, \ , \quad \phi^* = a\cos\nu t, \tag{18}$$

$$-\frac{1}{8}a^3 - \frac{3}{8}\frac{b}{\omega_p^2}a^2 + \left[1 - \left(\frac{\nu}{\omega_p}\right)^2\right]a + \frac{b-d}{\omega_p^2} = 0. \tag{19}$$

It can be proved that the cubic as well as the quadratic terms produce a nonlinear oscillator showing the behavior of a softening spring, [5].

4 Time-harmonic excitation

When a linear system is time-harmonically excited, the steady state response expresses the same frequency as the input excitation. In the nonlinear case the system's natural frequency is changed and additional subharmonic and superharmonic parts can be detected. Figure 2 shows a 3-D plot of response function of the tower $|Z/A|$, where Z is displacement amplitude of the tower tip point and A is the amplitude of the harmonic base excitation, which is of the form

$$\ddot{Z}_g(t) = A\cos\nu t. \tag{20}$$

Results for linear response of the tower are chosen under the assumption of interpreting the bell tower like structure as slender cantilever beam with passive pendulum absorber. Initially, the pendulum absorber's optimum parameters are set in front of the plot series, see [4]. Comparison due to the increase of amplitude A shows an unstable maximum frequency of the tower. It also shows that when $A < 0.5 m/s^2$ and $\phi_{max} \leq 0.4 rad$, the maximum optimal values of tuning mass is almost constant and it obeys the linear theory. Pendulum rotation angle ϕ_{max} increases with increasing amplitude A.

For $A \geq 1.65m/s^2$ and $\phi_{max} > 0.9rad$ the pendulum starts to rotate. The increase of the rotation angle of the pendulum increases the pendulum tuning values because of the systems nonlinearity. Figure 3 shows the change of the pendulum optimum parameters according to the increase of the excitation amplitude. Note that for larger pendulum amplitudes, the absorption efficiency decreases and two peaks finally merge and form one peak only.

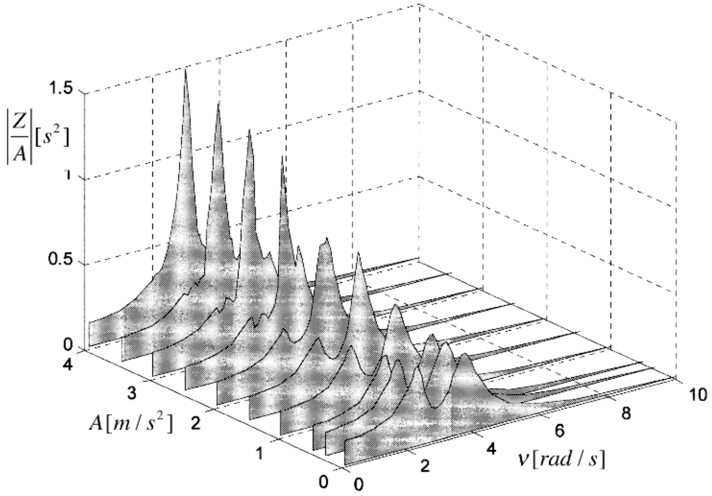

Fig. 2 $|Z/A|$ (Z: displacement amplitude of the tower top point, A: amplitude of base excitation) versus ν (circular frequency) and A

5 Stationary random base excitation

The artificial sample function for support excitation are generated by Simulink software, where the stationary power density function $S(\nu)$ and base random excitation $\ddot{Z}_g(t)$ can be expressed according to [6]

$$\ddot{Z}_g(t) = \sum_{n=1}^{N} \sqrt{4S(\nu)\Delta\nu} \times \cos(n\Delta\nu t - \varphi). \tag{21}$$

Numerical parameters are chosen as follows

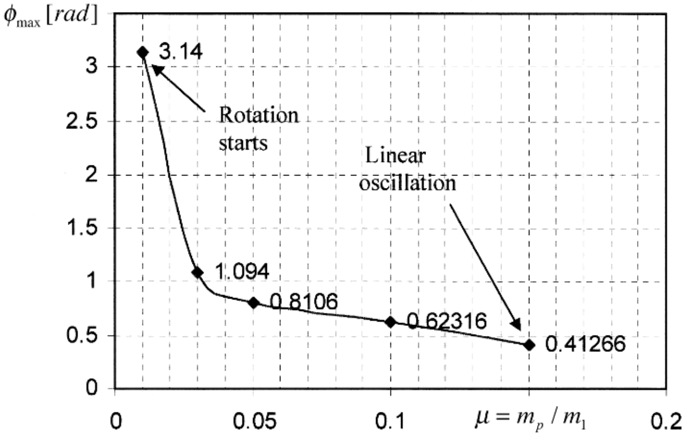

Fig. 3 Maximum rotation angle of pendulum ϕ_{max}versus pendulum mass ratio ν

$$S(\nu) = const.\ \left[m^2/s^3\right]\ ,\quad T = 100s\ ,\quad \Delta\nu = \frac{2\pi}{100} = 0.0628rad/s,$$
$$N = 100\ ,\quad A = \sqrt{4S(\nu)\Delta\nu}\ ,\quad 0 \le \varphi(random) \le 2\pi. \quad (22)$$

Due to the excitation in time domain, the response of the tower and the pendulum are computed (built by Simulink). By increasing the amplitude of excitation, the nonlinearity effect appears and changes the pendulum optimum parameters.

Figure 3 shows the maximum rotation angle of pendulum with mass ratio ν for constant values of amplitude A. When pendulum mass increases to 15% of total mass of the tower, rotation angle of the pendulum decreases and system yields to behave linearly. While the pendulum mass decreases to 1% of total mass of the tower, it begins to rotate.

6 Conclusions

This paper studies the dynamic behavior of bell tower like structures excited by various sources. Governing equations for the dynamic response of the tower coupled with pendulum motion are derived based on Lagrange equations of motion. A coupled 2DOF system is used to study the dominant geometrically nonlinear influence of the bells rotation in frequency domain. Furthermore, this system is extended to a discretized MDOF model of the tower coupled with a mathematical pendulum. Comparison is made between the characteristics in linear and nonlinear analysis. In order to evaluate nonlinear system, time-step analysis of numerical example by means of computer programming is performed. When the rotation angle of pendulum increases, the effects of nonlinearity appear. The nonlinear effects due to large motion of pendulum changes the linear natural frequency of the pendulum and adds subharmonic resonate frequencies to the coupled system. For numerical investigations the forcing types time-harmonic and stationary random support excitations are selected. While the excitation frequency is smaller than the bells eigenfrequency, nonstationary happens in the responses of the structure considered.

References

1. Chopra A.K.: Dynamics of Structures. 2ed. Prentice Hall, 2001
2. Weaver W. Jr., Timoshenko S.P., Young D.H.: Vibration problems in engineering. 5ed. John Wiley & Sons, 1989
3. Ziegler, F.: Mechanics of Solids and Fluids. Repr. 2ed. Springer, 1998
4. Yousefi, S.M.: Dynamic Behavior of Bell Tower Like Structures in Earthquake Environment, Dissertation, Vienna University of Technology, Center of Mechanics and Structural Dynamics, 2008.
5. Nayfeh A.H., Mook D.T.: Nonlinear Oscillations. John Wiley & Sons, 1998.
6. Yang, C.Y.: Random Vibration of Structures. John Wiley & Sons, New York, 1985.

Tracking of Stresses: A Further Step Towards Ageless Structures

Hans Irschik, Michael Krommer and Markus Gusenbauer

Abstract The present paper deals with the derivation of distributions of smart actuators, which enforce a structure to follow a desired stress trajectory everywhere and at all times. A particular case is the complete cancellation of force-induced stresses, a topic of particular interest in the context of ageless structures. Our formulation is derived within the framework of the linear dynamic theory of elasticity, and is based on the characterization of the initial boundary value problem of elasticity in terms of stresses. Smart actuation is represented by actuation stresses. We derive conditions, under which the desired stresses can be tracked exactly by the actuation stresses, and we present an easy to solve initial value problem for computing the actuation stresses.

1 Introduction

Smart structure technology has become a key technology in the design of modern structures. Smart or intelligent structures are capable to react to disturbances similar to human beings by mimicking their sensing, actuation and control capabilities. The design of smart structures thus is a highly multidisciplinary task, which involves multi-field modeling and structure-control interaction by means of suitable sensing and actuation. There is an agreement

---

Hans Irschik
Institute for Technical Mechanics, Johannes Kepler University Linz, Altenbergerstr. 69, A-4040 Linz, Austria, e-mail: hans.irschik@jku.at

Michael Krommer
Institute for Technical Mechanics, Johannes Kepler University Linz, Altenbergerstr. 69, A-4040 Linz, Austria, e-mail: michael.krommer@jku.at

Markus Gusenbauer
Magna Powertrain, St. Valentin, Austria

in the international engineering science community that smart sensor and actuator systems have the potential to change fundamentally the way structural systems are monitored and controlled. So far, a main field of smart structure technology has been the control of structural displacements, see Refs. [1]-[6]. During the last decade, more and more attention has been paid in the literature to control the behavior of structures with the goal of enhancing their lifetime, in the long term of designing even ageless structures, see Ref. [7]. In the literature, these goals are often connected to a controlled self-repair by utilizing chemical agencies that are incorporated into the structure and are activated in a controlled manner. Notwithstanding the need for developing such self-repair technologies, the vision of ageless structures from the mechanics point of view also brings into the play the necessity to study the complex problem of controlling stresses in structures. Control of vibrations and control of stresses are not equivalent, since the actuating effects in smart structure technology, such as heat or piezoelectricity, produce stresses that in general do not cancel out the stresses produced by imposed forces responsible for the vibrations to be controlled. So far, our group has been particularly interested in providing general solutions for finding smart actuator distributions, which theoretically can cancel out stresses completely, see Refs. [8] and [9]. A converse to these findings in the form of a body-force analogy has been presented in Ref. [10] for the case of thermal actuation. References [8]-[10] on the control of stresses represent results that are complementary to the research of our group on the so-called shape control of structures, i.e. the complete suppression of force-induced structural displacements by smart actuation, see Refs. [11]-[14].

The present paper is concerned with an extension of Ref. [8]-[10] on the cancellation of stresses: We present a methodology to derive distributions of smart actuations, which can theoretically enforce the structure to follow a desired stress trajectory everywhere (in every point of the structure) and at all times (during a certain observation period). Our formulation is derived within the framework of the dynamic linear theory of elasticity, see Gurtin [15], and is based on the characterization of the initial boundary value problem of elasticity in terms of stresses by Ignaczak [16]. In our formulation, the smart actuation is represented by actuation stresses, and we derive conditions, under which the desired stresses can be tracked exactly by the actuation stresses, where we present an easy method to solve the initial boundary value problem for computing the latter. The present contribution should be not only of interest in the context of smart structures technology with an emphasis on the development of ageless structures, but it represents a novel solution of the linear theory of elasticity in its own right. Due to limitations in space, in the following we restrict to theoretical aspects, leaving practical applications to a future contribution.

2 Initial boundary value problem

Subsequently, we use a direct tensor notation, similar to the one introduced in the Handbuchartikel by Gurtin [15]. The initial boundary value problem of linear elasticity in the presence of actuation stresses S_A reads as follows:

$$divS + b = \rho\ddot{u}, \tag{1}$$

$$S = S^T, \tag{2}$$

$$S - S_A = C\left[E\right], \tag{3}$$

$$E = sym\nabla u, \tag{4}$$

$$\partial B_U \ : \quad u = \hat{u}, \tag{5}$$

$$\partial B_S \ : \quad Sn = \hat{s}, \tag{6}$$

$$t = 0 \ : \quad u = r\ ; \quad \dot{u} = v \tag{7}$$

Here, S denotes the (second order) stress tensor, E is the symmetric strain tensor, u is the displacement vector, b stands for the imposed body force vector, and ρ is the mass density. A superimposed dot indicates the derivative with respect to time t, and the symbols div and ∇ stand for the spatial divergence and gradient operator, respectively. The superscript T indicates the transpose of a tensor, and sym stands for the symmetric part of a tensor. Equation (1) represents balance of linear momentum, Eq.(2) results from balance of angular momentum, Eq.(3) represents Hooke's law extended with respect to actuation stresses S_A, where C is the (fourth order) tensor of elastic constants. Equation (4) is a fundamental linear kinematical relation appropriate for small deformations. The body B under consideration is enclosed by the surface $\partial B = \partial B_U \cup \partial B_S$. On ∂B_U, the displacement is described as $\hat{u}$, while on the complementary part ∂B_S the traction is prescribed as $\hat{s}$, see Eqs. (5) and (6). The unit outer normal vector at ∂B is denoted as n, and Eq. (6) reflects Cauchy's fundamental theorem on the stresses. Equation (7) states inhomogeneous initial conditions, which must be compatible with the boundary conditions in Eq. (5) and (6), r being the initial displacement, and v the initial velocity. We assume the geometry of ∂B and the fields under consideration to be nice enough, such that the subsequent mathematical manipulations of Eqs. (1)-(7) make sense.

Actuation stress In extension to the classical theory of linear elasticity, see Gurtin [15], an actuation stress S_A has been included in Hooke's law, Eq. (3). For the sake of a further clarification, we write

$$S_A = C\left[E_A\right], \tag{8}$$

where E_A is an actuating eigenstrain. The latter notion can be used to characterize various physical sources of stress and strain, which are utilized in smart structure technology and which are different from imposed forces, induced boundary displacements or inhomogeneous initial conditions. A prominent example for eigenstrains is the linear theory of thermoelasticity, where S_A and E_A represent linear mappings of the temperature, see Carlson [17]. Analogously, S_A and E_A represent linear mappings of the electric field vector for the linear theory of piezoelectricity, which is often used in smart structures, see the literature cited in the above Introduction. In the present contribution, we use the notions "actuation" stress S_A and "actuating" eigenstrain E_A, respectively, in order to indicate that we deal with physical eigenstrain-type effects that are utilized in smart materials for the sake of actuation, assuming that S_A can be externally imposed as a function of space and time. Should it be necessary to consider a coupling of E_A to the strain E (e.g. due to the direct piezoelectric effect) or to the strain rate $\dot{E}$ (in case the coupled theory of thermoelasticity must be taken into account), then a further problem has to be solved in order to find the proper distribution of electric or heat sources that produce the corresponding distribution of eigenstrains E_A. The latter problems are beyond the scope of the present contribution, in which we ask for certain desired distributions of S_A only.

Formulation of the stress-tracking problem The following problem is treated in the present contribution: Find an actuation stress S_A, such that the total stress follows a properly prescribed trajectory S_D everywhere within B and for all times $t \geq 0$:

$$S = S_D \tag{9}$$

Subsequently, we shortly call S_D the desired stress, and we talk about the stress tracking problem in connection with Eq.(9).

3 A preliminary result stemming from shape control

In order to provide an introduction into the above stress-tracking problem, we recall a result stemming from the complementary problem of tracking zero displacements, also denoted as shape control, see Refs. [11]-[14]: Assume that

$$\hat{u} = 0 \;, \quad r = 0 \;, \quad v = 0 \tag{10}$$

in Eqs. (5) and (7). If the actuation stress satisfies the following conditions

$$div S_A + b = 0, \tag{11}$$

$$\partial B_S \;:\quad S_A n = \hat{s} \tag{12}$$

then the displacements vanish throughout the body for all times ≥ 0:

$$\Rightarrow u = 0 \tag{13}$$

We shortly may say that the actuation stress S_A must be in quasi-static local equilibrium with the imposed forces b and $\hat{s}$ in order to achieve the goal of shape control, Eq.(13). But, substituting Eq.(13) into Hooke's law, Eq.(3), it follows that

$$S = S_A. \tag{14}$$

Hence, shape control does not only mean to yield zero displacements, Eq.(13), but it can also be interpreted as a tracking of quasi-static stress distributions that satisfy Eqs.(11) and (12), $S_D = S_A$. This method, which is restricted to the class of solutions of Eqs.(11) and (12), has been followed by our group in Ref. [18]. In the present paper, we develop a more general solution for the above stress-tracking problem, Eq.(9), by working directly with stresses, starting from a representation of the above initial value-problem, Eqs. (1)-(7), in terms of stresses dating back to Ignaczak [16].

4 A solution for the stress-tracking problem

Ignaczak [16] layed down the following stress-based re-formulation of Eqs.(1)-(7):

$$sym\nabla\left(\rho^{-1}(divS + b)\right) = K\left[\ddot{S} - \ddot{S}_A\right], \tag{15}$$

$$\partial B_U \ : \quad divS + b = \rho\ddot{\hat{u}}, \tag{16}$$

$$\partial B_S \ : \quad Sn = \hat{s}, \tag{17}$$

$$t = 0 \ : \quad S - S_A = C\left[sym\nabla r\right] \ , \quad \dot{S} - \dot{S}_A = C\left[sym\nabla v\right] \tag{18}$$

Motivated by Ignaczaks considerations on the completeness problem for stress equations of motion in the linear elasticity theory [16], we introduce the following time-dependent integral over the body B:

$$I(t) = \int_B \left(\rho^{-1}div\bar{S} \cdot div\bar{S} + K\left[\dot{\bar{S}}\right] \cdot \dot{\bar{S}}\right) dV \tag{19}$$

with the tensor of elastic compliances $K = C^{-1}$, and where we have introduced the following error stress

$$\bar{S} = \bar{S}^T = S - S_D \tag{20}$$

in order to have a measure for the deviation of the actual stress S from the desired stress S_D. Derivation with respect to time yields

$$\frac{1}{2}\frac{d}{d}I(t) = \int_B \left(\rho^{-1}div\bar{S} \cdot div\dot{\bar{S}} + K\left[\ddot{\bar{S}}\right] \cdot \dot{\bar{S}}\right) dV. \tag{21}$$

For the sake of a re-formulation of Eq. (21), we note the following properties of the tensor of elastic compliances K with respect to any symmetric tensor A and B, see Gurtin [15],

$$K\left[A\right]\cdot B=K\left[B\right]\cdot A\;,\quad K\left[A\right]\cdot A>0\quad for\quad A\neq 0 \tag{22}$$

Moreover, for any vector field a and second order tensor field A and B, there is

$$a\cdot B=div\left(B^{T}a\right)-\left(\nabla a\right)\cdot B. \tag{23}$$

The divergence theorem reads

$$\int_{B}div\left(Ab\right)dV=\int_{\partial B}\left(Ab\right)\cdot ndS=\int_{\partial B}\left(A^{T}n\right)\cdot bdS. \tag{24}$$

Reformulating the boundary conditions, Eqs.(16) and (17), in terms of the error-stress,

$$\partial B_{U}\;\;:\quad div\bar{S}=-b+\rho\ddot{\hat{u}}-divS_{D}, \tag{25}$$

$$\partial B_{S}\;\;:\quad \bar{S}n=\hat{s}-S_{D}n \tag{26}$$

and utilizing Eqs. (22)-(24), after some derivations we arrive at the following re-formulation of Eq.(21):

$$\begin{aligned}\frac{1}{2}\frac{d}{dt}I(t)=&\int_{\partial B_{S}}\left(\dot{\hat{s}}-\dot{S}_{D}n\right)\cdot\left(\rho^{-1}div\bar{S}\right)dS\\&+\int_{\partial B_{U}}\left(\ddot{\hat{u}}-\rho^{-1}\left(b+divS_{D}\right)\right)\cdot\left(\dot{\bar{S}}n\right)dS\\&+\int_{B}\left(\nabla\left(\rho^{-1}\left(divS_{D}+b\right)\right)+K\left[\ddot{S}_{A}-\ddot{S}_{D}\right]\right)\cdot\dot{\bar{S}}dV.\end{aligned} \tag{27}$$

Hence, if we require that each of the first bracketed terms in the products that form the three integrands in Eq.(27) do vanish,

$$\partial B_{S}\;\;:\quad S_{D}n-\hat{s}=0, \tag{28}$$

$$\partial B_{u}\;\;:\quad \ddot{\hat{u}}-\rho^{-1}\left(b+divS_{D}\right)=0, \tag{29}$$

$$\nabla\left(\rho^{-1}\left(divS_{D}+b\right)\right)+K\left[\ddot{S}_{A}-\ddot{S}_{D}\right]=0, \tag{30}$$

then it follows that the integral in Eq.(21) becomes constant and thus equal to its initial value:

$$I(t)=0\quad\Rightarrow\quad I(t)=const.=I(t=0), \tag{31}$$

with

$$I(t=0)=2\int_{B}\left(\rho^{-1}div\bar{S}\cdot div\bar{S}+K\left[\dot{\bar{S}}\right]\cdot\dot{\bar{S}}\right)dV_{t=0}. \tag{32}$$

Thus, vanishing of the initial error stress and initial error stress velocity,

$$t = 0 \ : \quad \bar{S} = 0 \ , \quad \dot{\bar{S}} = 0 \tag{33}$$

does imply the vanishing of the integral in Eq.(21) itself:

$$I(t = 0) = I(t) = 0. \tag{34}$$

But, from the properties of the scalar product and the tensor of elastic compliances, namely that

$$div\bar{S} \neq 0 \quad \Rightarrow \quad div\bar{S} \cdot div\bar{S} > 0, \tag{35}$$

$$\dot{\bar{S}} \neq 0 \quad \Rightarrow \quad K\left[\dot{\bar{S}}\right] \cdot \dot{\bar{S}} > 0, \tag{36}$$

see Eq. (22), it follows that Eq. (34) implies the vanishing of the error stress everywhere in B and for all times $t \geq 0$:

$$\bar{S} = 0 \quad \Rightarrow \quad S = S_D \tag{37}$$

such that the goal of stress tracking, Eq.(9) is reached, see Eq.(20).

Discussion We now summarize the conditions, for which this solution for tracking of transient stresses does hold:

$$\ddot{S}_A = \ddot{S}_D - C\left[\nabla\left(\rho^{-1}\left(divS_D + b\right)\right)\right] \tag{38}$$

$$\partial B_S \ : \quad S_D n = \hat{s}, \tag{39}$$

$$\partial B_U \ : \quad divS_D + b = \rho\ddot{\hat{u}}, \tag{40}$$

$$t = 0 : \quad S_A = S_D - C\left[sym\nabla r\right] \ , \quad \dot{S}_A = \dot{S}_D - C\left[sym\nabla v\right]. \tag{41}$$

Equation (41) follows by substituting the initial conditions, Eq.(18), into the requirement formulated in Eq.(33), Eq.(38) is a re-formulation of the requirement of Eq.(30), and Eqs.(39) and (40) correspond to Eqs.(28) and (29). Equations (39) and (40) mean that the desired stress S_D must be compatible with the boundary conditions, Eqs. (16) and (17), otherwise the goal of stress tracking can not be reached. Eqs.(38) and (41) give a means to construct an actuation stress, in case the desired stress does not satisfy the field equation, Eq.(15), and the initial conditions, Eq.(18), in the absence of an actuation stress. As it was to be expected, Eqs.(38) - (41) follow directly by replacing S in Eqs.(15)-(18) by the desired stress S_D.

Acknowledgements Support of the authors H. Irschik and M. Krommer from the K2 Austrian Center of Competence in Mechatronics (ACCM), and of M. Krommer from the Austrian Science Fund (FWF Translational project L441-N41 *Sensor Systems for Structural and Health Monitoring*) is gratefully acknowledged.

References

1. U. Gabbert and H.S. Tzou (eds.), Proceedings of the IUTAM Symposium on Smart Structures and Structronic Systems, Magdeburg, Germany 2000. Kluwer, 2001.
2. L. Faravelli, B. F. Spencer jr. (eds.), Proceedings of the US Europe (ESF-NSF) Workshop on Sensors and Smart Structures Technology, Como and Somma Lombardo, Italy, 2002. Wiley 2002.
3. F. Casciati (ed.), Proceedings of the Third World Conference on Structural Control, Como, Italy, 2002, 3 Volumes. Wiley 2002.
4. F. Ziegler, K. Watanabe (eds.), Proc. IUTAM Symposium on Dynamics of Advanced Materials and Smart Structures, Yonezawa, Japan, 2002. Kluwer, 2003.
5. R. Flesch, H. Irschik and M. Krommer (eds.), Proceedings of the Third European Conference on Structural Control, Vienna, Austria 2004, 2 Volumes, Schriftenreihe der Technischen Universität Wien, 2005.
6. A. K. Belyaev, D. A. Indeitsev, (eds.), Proceedings of the Fourth European Conference on Structural Control (4ECSC), St.Petersburg, Russia, 2008, 2 Volumes. Russian Academy of Sciences, 2008.
7. R. Shoureshi, (ed.), CD-ROM Proceedings of ESF-NSF Workshop on Advancing Technological Frontiers for Feasibility of Ageless Structures, Strasbourg, France, 2003.
8. Markus Gusenbauer, Hans Irschik, Dynamic Stress Compensation in a Circular Disc by Smart Actuation, in R. Shoureshi, ed., CD-ROM Proceedings of ESF-NSF Workshop on Advancing Technological Frontiers for Feasibility of Ageless Structures, Strasbourg, France, 2003.
9. Gusenbauer, M., Irschik, H., Eberst, C., Stress Suppression by Smart Material Actuation, Proc. Third Europ. Conf. Structural Control, Vienna, Austria 2004, (H.Irschik, R. Flesch, M. Krommer, eds.), Vol. I, p. M2-9-M2-12, Schriftenreihe der Technischen Universität Wien, Vienna 2005.
10. Irschik, H., Gusenbauer, M., Body Force Analogy for Transient Thermal Stresses. Journal of Thermal Stresses, Volume 30, pp. 965-975 (2007).
11. Irschik, H., A review on static and dynamic shape control of structures by piezoelectric actuation, Engineering Structures, Vol. 24, p. 5-11, 2002.
12. Irschik, H., Pichler, U., An extension of Neumanns method for shape control of force-induced elastic vibrations by eigenstrains, International Journal of Solids and Structures, Vol. 41, p. 871-884, 2004.
13. M. Krommer, H. Irschik, Sensor and actuator design for displacement control of continuous systems, Smart Structures and Systems, Vol. 3, p. 147-172, 2007.
14. H. Irschik, M. Krommer, M. Nader, Ch. Zehetner, Mechatronics - The Innovation Request, Advances in Science and Technology, Vol. 56, 1-10, 2008.
15. Gurtin, M. E., The Linear Theory of Elasticity, Encyclopedia of Physics (S. Flügge, Ed.), VIa/2, p. 1-296, Springer-Verlag, Berlin, 1972.
16. Ignaczak, J., A Completeness problem for stress equations of motion in the linear elasticity theory, Arch. Mech. Stos., Vol. 15, p. 225-234, 1963.
17. Carlson, D. E., Linear Thermoelasticity, Encyclopedia of Physics (S. Flügge, Ed.), VIa/2, p. 1-297-345, Springer-Verlag, Berlin, 1972.
18. H. Irschik, M. Gusenbauer, U. Pichler: Dynamic Stress Compensation by Smart Actuation. In: SPIE-Conference on Smart Structures and Materials, San Diego, USA, 2004: Modeling, Signal Processing, and Control (R. C. Smith, Ed.). Proc. SPIE, Vol. 5383, Paper No. 386 (2004).

Non-Linear Dynamic Deformation of a Piezothermoelastic Laminate

Masayuki Ishihara, Yasuhiro Watanabe and Naotake Noda

Abstract This paper presents an analysis on the nonlinear transient behavior of a piezothermoelastic laminate. For the analytical model, a laminated beam is considered to be composed of elastic structural and piezoelectric layers that are subjected to mechanical, thermal, and electrical loads as disturbances or intended control procedures. The deformation of the laminate is analyzed using the classical laminate theory and the von Kármán strain. Equations of motion in terms of the displacements are obtained and analyzed through the Galerkin method. As a result, the dynamic deflection of the laminate is found to be governed by the equation for a polynomial oscillator, and the transient large deformation due to mechanical, thermal, and electrical loads are obtained. Through these results, the characteristics of the transient deformation of the laminate are discussed in detail.

1 Introduction

Piezoelectric materials have been used extensively as sensors and actuators to control structural configuration and to suppress undesired vibration in engineering due to their superior coupling effect between elastic and electric fields. Fiber reinforced plastics (FRP) such as graphite/epoxy are in demand for lightweight structures because they are lighter than general metals and have high specific strength. The structures composed of laminated FRP and piezoelectric materials are called piezothermoelastic laminates and have attracted considerable attention in fields such as aerospace engineering and micro electro mechanical systems. For aerospace applications, structures have to be comparatively large and lightweight. Because of this, they are vulnerable

---

Masayuki Ishihara
Osaka Prefecture University, 1-1 Gakuen, Naka, Sakai, Osaka 599-8531, Japan, e-mail: ishihara@me.osakafu-u.ac.jp

to disturbances such as environmental temperature changes and collisions with space debris. As a result, the deformations caused can be relatively large. Therefore, the large deformations of piezothermoelastic laminates were analyzed by several researchers [1-3].

The studies mentioned above [1-3] dealt with the static behavior of piezothermoelastic laminates. However, aerospace applications of these laminates involve dynamic deformation. Therefore, dynamic problems for large deformations of piezothermoelastic laminates have become a focus of study [4-7].

In these analyses [4-7], dynamic deformation deviating arbitrarily from the equilibrium state was not considered, although it is very important from a practical viewpoint for something such as aerospace applications. Therefore, in a previous study Ishihara and Noda [8] analyzed steady vibration deviating from the equilibrium state and obtained the relationship between the deflection of the laminate and its velocity under various loading conditions, excluding the effect of damping.

In practice, it is important to consider the effect of damping on analyzing the dynamic behavior because damping changes such dynamic characteristics as the transient behavior and natural frequencies. Therefore, an analysis of transient dynamic behavior that takes damping into account is important to estimate dynamic characteristics properly. This paper presents an analysis of nonlinear transient dynamic behavior for a piezothermoelastic laminated beam with the damping effect and dynamic deflections that deviate arbitrarily from the equilibrium state considered. For the analytical model, a laminated beam with both ends simply supported is considered, composed of fiber-reinforced laminate and piezoelectric layers subjected to mechanical, thermal, and electrical loads as disturbances or as intended control procedures. Nonlinear large deformation of the laminate is analyzed based on the von Kármán strain [9] and classical laminate theory. Equations of motion for the laminate are derived using the Galerkin method [10]. As a result, the dynamic deflection of the beam is found to be governed by the equation for a polynomial oscillator [11]. According to the equation, the transient large deformation due to mechanical, thermal, and electrical loads are obtained. Moreover, numerical calculation is performed to investigate the nonlinear transient deformation and how to stabilize it.

2 Theoretical analysis

2.1 Problem

The model considered is a simply supported beam with dimensions $a \times b \times h$ and composed of N layers as shown in Fig. 1. Two of the N layers ($z_{k-1} \leq$

$z \leq z_k$, $z_{k'-1} \leq z \leq z_{k'}$) exhibit piezoelectricity while the other layers do not. The beam is laminated in a symmetrical cross-ply manner. The laminate is subjected to the transverse load $Q(t)$ in the z direction and the temperatures $\theta_0(t)$ and $\theta_N(t)$ on the upper ($z = -h/2$) and the lower ($z = h/2$) surfaces of the laminate respectively as mechanical and thermal disturbances. To control the effects of the disturbances, the laminate is also subjected to the electric potentials $V_k(t)$ and $V_{k'}(t)$ on $z = z_{k-1}$ and $z = z_{k'}$ respectively. The surfaces $z = z_k$ and $z = z_{k'-1}$ are both level surfaces of electric potential.

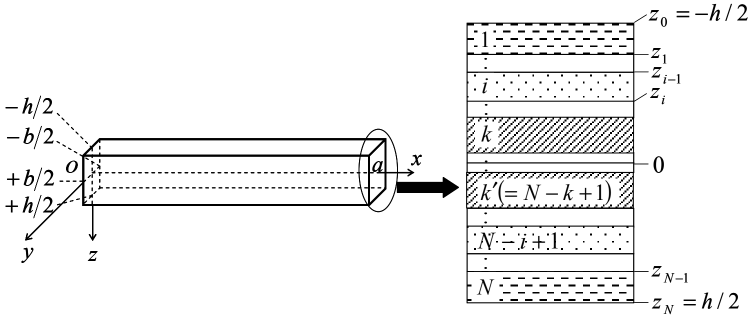

Fig. 1 Analytical model

2.2 *Governing equations*

Based on the classical laminate theory, the von Kármán strain, and the constitutive equation of piezothermoelasticity, the constitutive relations for the laminate are given as follows [8, 12]:

$$N_x = A\left[\frac{\partial u^0}{\partial x} + \frac{1}{2}\left(\frac{\partial w}{\partial x}\right)^2\right] - N_x^T - N_x^E\,, \quad M_x = -D\frac{\partial^2 w}{\partial x^2} - M_x^T - M_x^E \quad (1)$$

where N_x and M_x denote the resultant force and moment respectively, u^0 and w denote the displacement components in the x- and z- directions respectively, A and D denote the extensional and bending rigidities respectively. Moreover, N_x^T, M_x^T, N_x^E, and M_x^E are obtained as follows [8]:

$$N_x^T = \frac{1}{2}\left[\Theta_N(t) + \Theta_0(t)\right]\sum_{i=1}^{N}\lambda_i\left(z_i - z_{i-1}\right),$$

$$M_x^T = \frac{1}{3h}\left[\Theta_N(t) - \Theta_0(t)\right]\sum_{i=1}^{N}\lambda_i\left(z_i^3 - z_{i-1}^3\right),$$

$$N_x^E = e_k\left[V_k(t) - V_{k'}(t)\right]\ , \quad M_x^E = e_k\left[V_k(t) + V_{k'}(t)\right]\frac{z_k + z_{k-1}}{2} \tag{2}$$

where λ_i and e_i denote the stress-temperature coefficient and piezoelectric coefficient respectively for the i-th layer. Equations of motion which integrate the effect of in-plane resultant forces into anti-plane motion are given as follows [8]:

$$\frac{\partial N_x}{\partial x} = 0\ , \quad \rho h\frac{\partial^2 w}{\partial t^2} + c_d\frac{\partial w}{\partial t} = N_x\frac{\partial^2 w}{\partial x^2} + \frac{\partial^2 M_x}{\partial x^2} + Q \tag{3}$$

where ρ and c_d denote the average mass density with respect to z and the damping coefficient. By substituting Eq. (1) into Eq. (3), the equations of motion expressed by the displacements are given as follows:

$$L_1\left(u^0, w\right) = \frac{\partial}{\partial x}\left(N_x^T + N_x^E\right),$$

$$\rho h\frac{\partial^2 w}{\partial t^2} + c_d\frac{\partial w}{\partial t} + L_2(u^0, w) = Q - \frac{\partial^2}{\partial x^2}(M_x^T + M_x^E) - (N_x^T + N_x^E)\frac{\partial^2 w}{\partial x^2} \tag{4}$$

where the definitions of the differentiation operators L_1 and L_2 are given as

$$L_1\left(u^0, w\right) = A\left[\frac{\partial^2 u^0}{\partial x^2} + \frac{\partial w}{\partial x}\frac{\partial^2 w}{\partial x^2}\right],$$

$$L_2\left(u^0, w\right) = -A\left[\frac{\partial u^0}{\partial x} + \frac{1}{2}\left(\frac{\partial w}{\partial x}\right)^2\right]\frac{\partial^2 w}{\partial x^2} + D\frac{\partial^4 w}{\partial x^4}. \tag{5}$$

2.3 Galerkin method

The Galerkin method [10] is used to solve Eq. (4). Trigonometric functions are chosen as the trial functions and the considered displacements are expressed as series:

$$\left\{u^0, w\right\} = \sum_{m=1}^{\infty}\left\{u_m(t), w_m(t)\right\}\sin\alpha_m x \ : \quad \alpha_m = \frac{m\pi}{a} \tag{6}$$

to satisfy the simple support conditions. Then, the Galerkin method is applied to Eq. (4) to obtain

$$\int_0^a\left[L_1\left(u^0, w\right) - \frac{\partial}{\partial x}\left(N_x^T + N_x^E\right)\right]\sin\alpha_{m'} x\,\mathrm{d}x = 0,$$

$$\int_0^a \left[\rho h \frac{\partial^2 w}{\partial t^2} + c_d \frac{\partial w}{\partial t} + L_2\left(u^0, w\right) - Q + \frac{\partial^2\left(M_x^T + M_x^E\right)}{\partial x^2} \right.$$
$$\left. + \left(N_x^T + N_x^E\right)\frac{\partial^2 w}{\partial x^2}\right] \sin\alpha_{m'} x \mathrm{d}x = 0 \ , \quad m' = 1, 2, 3, \ldots, \infty. \tag{7}$$

By substituting Eq. (6) into Eq. (7) and integrating, the simultaneous nonlinear equations with respect to u_m and w_m are obtained. Moreover, by eliminating u_m from the equations, the following simultaneous nonlinear ordinary differential equations with respect to w_m ($m = 1, 2, 3, \ldots, \infty$) are obtained

$$\rho h \frac{\mathrm{d}^2 w_m}{\mathrm{d}t^2} + c_d \frac{\mathrm{d}w_m}{\mathrm{d}t} + k_m^L w_m + \sum_{m'=1}^{\infty}\sum_{i=1}^{\infty}\sum_{k=1}^{\infty} k_{m,m'ik}^N w_{m'} w_i w_k = p_m,$$
$$m = 1, 2, 3, \ldots, \infty \tag{8}$$

where the definitions of k_m^l, $k_{m,m'ik}^N$, and p_m are given as

$$\begin{aligned} k_m^L &= \alpha_m^2\left[D\alpha_m^2 - \left(N_x^T + N_x^E\right)\right], \\ k_{m,m'ik}^N &= \frac{1}{8} A \alpha_{m'}^2 \alpha_i \alpha_k \left(\mathit{\Delta}_{c,ikm'm} - \sum_{l=1}^{\infty} \frac{2\alpha_i}{\alpha_l}\delta_{ikl}\delta_{m'lm}\right), \\ p_m &= Q_m + \alpha_m^2\left(M_{x,m}^T + M_{x,m}^E\right), \end{aligned} \tag{9}$$

and $Q_m(t)$, $M_{x,m}^T(t)$, and $M_{x,m}^E(t)$ denote the Fourier coefficients of Q, M_x^T, and M_x^E respectively and the definitions of δ_{ij} and $\mathit{\Delta}_{c,ijkl}$ are given in the previous paper [8].

2.4 Polynomial Oscillator

To develop the physical characteristics of the dynamic behavior of the laminate, Eq. (8) is simplified. By truncating the infinite series in Eq. (6), therefore, in Eq.(8), up to one term and considering Eq. (8) for $m = 1$, the following nonlinear equation with respect to w_1 is obtained

$$\rho h \frac{\mathrm{d}^2 w_1}{\mathrm{d}t^2} + c_d \frac{\mathrm{d}w_1}{\mathrm{d}t} + k_1^L w_1 + k_{1,111}^N w_1^3 = p_1. \tag{10}$$

Note that, as in Eq. (6), w_1 denotes the deflection at the center of the laminate ($x = a/2$). By introducing non-dimensional variables such as

$$U \equiv \frac{w_{11}}{h},\ \tau \equiv \sqrt{\frac{k^N_{1,111}h}{\rho}}t,\ \lambda \equiv -\frac{k^L_1}{k^N_{1,111}h^2},\ \delta \equiv \frac{c_d}{\sqrt{\rho h k^N_{1,111}h}},\ \alpha \equiv \frac{p_1}{k^N_{1,111}h^3}, \tag{11}$$

Eq. (10) is rewritten in non-dimensional form as

$$\frac{\mathrm{d}^2U}{\mathrm{d}\tau^2} + \delta\frac{\mathrm{d}U}{\mathrm{d}\tau} - \lambda U + U^3 = \alpha \ : \quad \delta \geq 0\,, \quad \alpha \geq 0. \tag{12}$$

2.5 Dynamic Behavior

2.5.1 Static large deflection

First, the static large deflection of the laminate and its stability are examined. The static large deflection is obtained as the equilibrium point U_e of the dynamical system described by Eq. (12). From Eq. (12), U_e is obtained for $\alpha = 0$ as:

$$\begin{aligned} &U_e = 0\,(\equiv U_1)\,, \\ &U_e = \pm\sqrt{\lambda}\,(\equiv U_2) \ : \quad \lambda > 0 \end{aligned} \tag{13}$$

and for $\alpha > 0$ as:

$$\begin{aligned} &U_e = U_3 \ : \quad \lambda < 0, \\ &U_e = U_4 \ : \quad 0 < \lambda < 3\sqrt[3]{(\alpha/2)^2}, \\ &U_e = U_5, U_6, U_7 \ : \quad \lambda > 3\sqrt[3]{(\alpha/2)^2} \end{aligned} \tag{14}$$

where the explicit solutions for U_3 through U_7 are given in the previous paper [8]. The stability of the deflection described by Eqs. (13) and (14) can be examined by considering the small deviation of U in the vicinity of U_e as is usual [11]. The variations of the static large deflection of the laminate with parameter λ are shown graphically in Fig. 2, where solid lines denote stable deflections and broken lines denote unstable ones.

2.5.2 Transient large deflection

The transient large deflection that deviates arbitrarily from the equilibrium state is examined. By introducing new non-dimensional variables such as

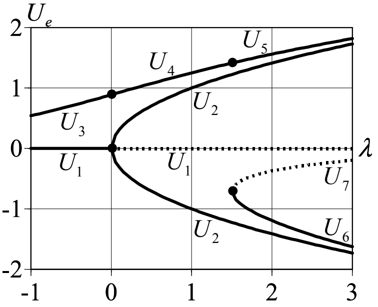

Fig. 2 Variation of static large deflections with parameter λ

$$U' \equiv \frac{U}{\sqrt{|\lambda|}}\ , \quad \tau' \equiv \tau\sqrt{|\lambda|}\ , \quad V' \equiv \frac{dU'}{d\tau'}\ , \quad \alpha' \equiv \frac{\alpha}{|\lambda|\sqrt{|\lambda|}}\ , \quad \delta' \equiv \frac{\delta}{\sqrt{|\lambda|}}, \tag{15}$$

Eq. (12) is rewritten as

$$\frac{\mathrm{d}^2U'}{\mathrm{d}\tau'^2} + \delta' V' - \mathrm{sgn}\,(\lambda)\cdot U' + U'^3 - \alpha' = 0. \tag{16}$$

By solving Eq. (16) for U' through the Runge-Kutta method, the transient behavior of the laminate is analyzed and the results are presented by orbits, that is, the relationship between the deflection U' and velocity V'. From Eqs. (13) and (14), the final state of the transient behavior is found to be classified into three cases depending on parameters λ and α' as:

$$\left.\begin{array}{lll} \text{case(i)}: & \lambda < 0 & \\ \text{case(ii)}: & \lambda > 0 \quad \text{and} & \alpha' > 2\sqrt{3}/9 \\ \text{case(iii)}: & \lambda > 0 \quad \text{and} & 0 \leqslant \alpha' < 2\sqrt{3}/9 \end{array}\right\}. \tag{17}$$

In order to connect the behavior with engineering sense, the following situation is considered:

$$Q = 0\ , \quad \Theta_N = \Theta_0\,(\equiv \Theta)\ , \quad V_k = V_{k'}\,(\equiv V) \tag{18}$$

where Θ and V are assumed as the thermal disturbance and control procedure respectively. Then, from Eqs. (2), (9), (11), (15), and (18):

$$\alpha' = \frac{4\alpha_1^2\,(z_k + z_{k-1})\,e_k V}{\pi\,|\lambda|\,\sqrt{|\lambda|}h^3 k_{1,111}^N},$$

$$\lambda = \frac{\alpha_1^2}{h^2 k_{1,111}^N}\sum_{i=1}^{N}\lambda_i\,(z_i - z_{i-1})\,(\Theta - \Theta_{cr})\ , \quad \Theta_{cr} = \frac{D\alpha_1^2}{\sum\limits_{i=1}^{N}\lambda_i\,(z_i - z_{i-1})} \tag{19}$$

Thus, $\lambda < 0$ and $\lambda > 0$ mean that the laminate is subjected to temperatures that are lower and higher than the buckling temperature respectively, and α'

corresponds to the electric voltage applied to the piezoelectric layers.

Figure 3 shows the transient vibration of the laminate for case (i), where the temperature is lower than the buckling temperature. Figure 4 shows the result for the case (ii), where the temperature is higher than the buckling temperature and the electric voltage is higher than the critical value. From Figs. 3 and 4, the laminate is found to vibrate, decay, and tend to the final deflections U_3' (corresponding to U_3) and U_4' (corresponding to U_4).

Figure 5 shows the transient vibration of the beam for the case (iii), where the temperature is higher than the buckling temperature and the electric voltage is smaller than the critical value. In Fig. 5, the points denoted by U_5', U_6' and U_7' correspond to the equilibrium points U_5, U_6 and U_7 respectively and the dotted line shows the separatrix, or the orbit that passes through the unstable equilibrium point U_7' and disregards the effect of damping ($\delta' = 0$). From Fig. 5, it is found that, when the initial deformation is outside the separatrix, deformation reaches out to a branch of the separatrix and tends to the equilibrium point enclosed by the branch.

Fig. 3 Transient deformation for case (i) ($\lambda < 0$, $\alpha' = 1$, $\delta' = 0.2$)

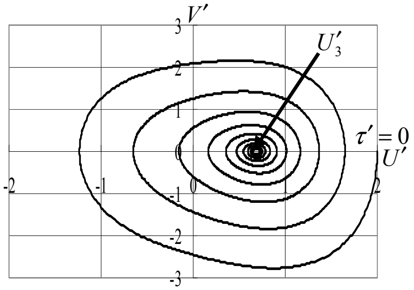

Fig. 4 Transient deformation for case (ii) ($\lambda > 0$, $\alpha' = 1$, $\delta' = 0.2$)

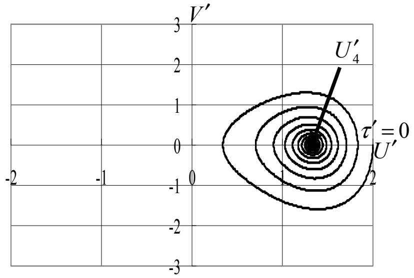

Finally, Fig. 6 shows the effect of the electric voltage on the transient deformation. The desired final deformation is found to be possible to achieve by applying the appropriate electric voltage, which is of great importance in practical viewpoint.

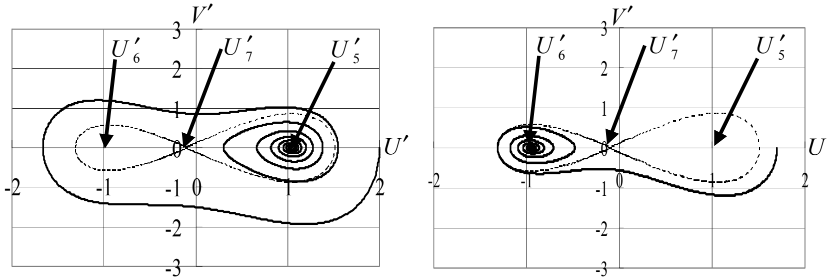

(*a*) $(U', V')|_{\tau'=0} = (2, 0)$ (*b*) $(U', V')|_{\tau'=0} = (1.7, 0)$

Fig. 5 Transient deformation for case (iii) ($\lambda > 0$, $\alpha' = 0.1$, $\delta' = 0.2$)

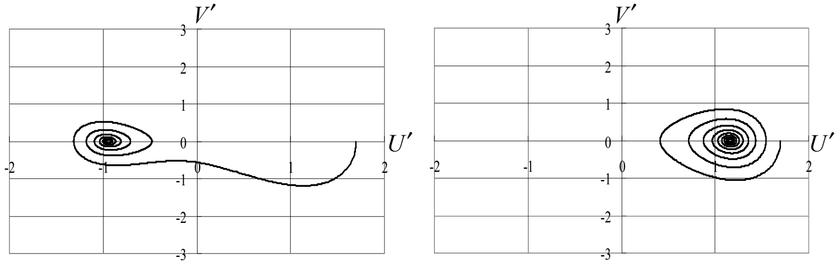

(*a*) $\alpha' = 0.1$ (*b*) $\alpha' = 0.4$

Fig. 6 Transient deformation $\left(\lambda > 0\ ,\ \delta' = 0.2\ ,\ (U', V')|_{\tau'=0} = (1.7, 0)\right)$

3 Conclusion

The nonlinear transient behavior of a piezothermoelastic laminate is analyzed with the damping effect and the dynamic deflection that deviates arbitrarily from the equilibrium state considered. For the analytical model, a rectangular laminated beam with both ends simply supported and composed of fiber-reinforced laminate and piezoelectric layers is considered and subjected to mechanical, thermal, and electrical loads as disturbances or as intended control procedures. Nonlinear large deformations of the laminate are analyzed based on the von Kármán strains and classical laminate theory. As a result, the dynamic deflection of the laminate is found to be governed by the equation for a polynomial oscillator. Using the equation, the transient large deformation with the damping effect considered due to mechanical, thermal, and electrical loads is obtained. From the results for the transient large deformation, it is found that appropriate application of the electric voltage to the piezoelectric layers can govern the final deformation of the beam.

References

1. Mukherjee A, Chaudhuri A S (2002) Piezolaminated beams with large deformations. Int J Solids Struct 39:4567-4582.
2. Shen H S (2001) Postbuckling of Shear Deformable Laminated Plates with Piezoelectric Actuators under Complex Loading Conditions. Int J Solids Struct 38:7703-7721.
3. Shen H S (2002) Postbuckling of Laminated Cylindrical Shells with Piezoelectric Actuators under Combined External Pressure and Heating. Int J Solids Struct 39:4271-4289.
4. Tzou H S, Zhou Y (1995) Dynamics and Control of Nonlinear Circular Plates with Piezoelectric Actuators. J. Sound Vibr 188:189-207.
5. Tzou H S, Zhou Y H (1997) Nonlinear Piezothermoelasticity and Multi-Field Actuations, Part 2, Control of Nonlinear Deflection, Buckling and Dynamics. J. Vibr. Acoust 119:382-389.
6. Ishihara M, Noda N (2003) Non-Linear Dynamic Behavior of a Piezothermoelastic Laminated Plate with Anisotropic Material Properties. Acta Mech 166:103-118.
7. Ishihara M, Noda N (2003) Non-Linear Dynamic Behavior of a Piezothermoelastic Laminate Considering the Effect of Transverse Shear. J Thermal Stresses 26:1093-1112.
8. Ishihara M, Noda N (2005) Non-Linear Dynamic Behaviour of a Piezothermoelastic Laminate. Phil Mag 85:4159-4179.
9. Chia C Y (1980) Nonlinear Analysis of Plates. McGraw-Hill, New York.
10. Fletcher C A J (1984) Computational Galerkin Method. Springer, New York.
11. Wiggins S (1990) Introduction to Applied Nonlinear Dynamical Systems and Chaos. Springer, New York.
12. Ishihara M, Morishita H, Noda N (2007) Control of Dynamic Deformation of a Piezothermoelastic Beam with a Closed-Loop Control System Subjected to Thermal Disturbance. J Thermal Stresses 30:875-888.

Determining Liquid Properties Using Mechanically Vibrating Sensors

Bernhard Jakoby, E.K. Reichel, F. Lucklum, B. Weiss, C. Riesch, F. Keplinger, R. Beigelbeck and W. Hilber

Abstract Miniaturized sensors for physical liquid parameters can be utilized in applications where liquids in industrial processes are monitored in order to maintain the quality of a process or the associated product. Due to the adverse properties commonly associated with chemical interfaces (lacking reversibility, drift, etc.), sensing physical parameters as indicators for the state of the liquid, in particularly density, viscosity (or more general rheological properties), and infrared absorption is an attractive alternative to conventional chemical sensors. The miniaturization of suitable sensor principles on the one hand facilitates the implementation of these devices online. On the other hand, scaling effect have to be taken into account, which, e.g., in case of viscosity sensors, lead to issues when it comes to applications in complex liquids such as suspensions. In our paper we provide an overview on our recent work discussing the device design, the associated modeling, and the application of the devices.

1 Introduction

In this contribution we report on recent research on miniaturized viscosity sensors, which can be used in industrial process control and related appli-

---

Bernhard Jakoby, E.K. Reichel, F. Lucklum and W. Hilber
Institute for Microelectronics and Microsensors, Johannes Kepler University Linz, Altenbergerstr. 69, A-4040 Linz, Austria, e-mail: bernhard.jakoby@jku.at

B. Weiss
Institute of Fluid Mechanics and Heat Transfer, Johannes Kepler University Linz, Linz

C. Riesch and F. Keplinger
Institute of Sensor and Actuator Systems, Vienna University of Technology, Vienna

R. Beigelbeck
Research Unit for Integrated Sensor Systems, Austrian Acad. of Sciences, Wiener Neustadt

cations wherever process liquids and changes in the liquid's condition are of interest (e.g, in food industry and engine oil quality monitoring). Typical applications that we considered recently were the monitoring of transitions in emulsions [1] and the monitoring of zeolite synthesis [2]. The viscosity (more precisely the "shear viscosity") can be defined in terms of a simple experimental arrangement, where the liquid under test is sheared between two laterally moving plates. The viscosity η is then defined as the ratio between the applied shear stress τ (maintaining the movement) and the resulting gradient of the flow velocity v (i.e. the shear rate $\dot{\gamma}$) of the liquid sheared between the plates:

$$\eta = \frac{\tau}{\partial v_x / \partial y} = \frac{\tau}{\dot{\gamma}} \tag{1}$$

The such defined viscosity (as already proposed by Newton) can be measured in a straightforward manner by laboratory instruments, which in some way impress a shear deformation on the liquid and measure the required torque (or vice versa, i.e. impress torque and measure resulting shear deformation). Such devices typically either utilize continuous rotational movements (avoiding extended translational movements required by the simple plate setup) or oscillatory rotational movements. Most often, the viscosity as defined by (1) crucially depends on the used process parameters, e.g., the impressed shear rate. For instance consider a simple schematic arrangement as shown in Fig. 1 for the measurement of viscosity: a pivoted cylinder is immersed in a viscous liquid. By means of some motor, the cylinder can be driven to perform a continuous rotational movement or rotational oscillation.

For the continuous rotation, the ratio between the applied torque and the rotational speed will be related to the viscosity of the liquid. Now for a so-called "Newtonian" liquid, this ratio yielding the viscosity would not depend on the actually applied rotational speed or, in terms of the definition (1), the viscosity would not depend on the shear rate. For real liquids, such a dependence can, however, occur if, e.g., (macro)molecules in the liquid become disentangled by the shear movement, which would be an example for so-called "non-Newtonian" behavior. This behavior is known as shear-thinning behav-

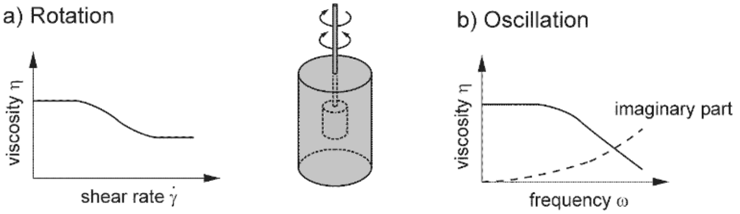

Fig. 1 Basic measurement approaches for viscosity: rotational and vibrational (oscillatory) method.

ior (the viscosity drops with increasing shear rate) and can be reversible or (also partly) non-reversible. This behavior represents a non-linear response, which can be accounted for by describing the viscosity a function of the shear rate. For oscillatory (vibrational) measurements, the cylinder would perform, e.g., sinusoidal oscillations, where, similarly as before, the ratio of the applied torque-amplitude and the amplitude in angular speed could be used as measures for the viscosity. The above-mentioned non-linear behavior here would lead to a dependence of the obtained viscosity on the amplitudes for angular speed and torque. Moreover, another kind of non-Newtonian behavior can appear: the measured viscosity can depend on the applied frequency. More specifically, a phase shift between the torque and the angular speed signals can appear, which represents the onset of elastic behavior. This phenomenon is often referred to as viscoelastic behavior and can be modeled by adopting the common complex notation, where an imaginary part in the viscosity accounts for the elastic part. (This is in analogy to an ohmic resistor supplemented by an additional capacitive part.) In terms of system theory, this kind of non-Newtonian behavior corresponds to a linear distortion in the system response. We note that also the reverse effect can appear at higher frequencies, i.e. dominantly elastic behavior such as the bulk compressibility of a liquid, can show viscous contributions such that the compressibility coefficient shows an imaginary part, which corresponds to the so-called bulk viscosity of a liquid. In contrast to the shear viscosity, the bulk viscosity is difficult to measure and plays a minor role in the analysis of liquid behavior such that it is often neglected.

In general both, linear and non-linear effects can occur, leading to sometimes complicated non-Newtonian behavior of liquids. In rheology, this behavior is a vibrant issue in research (see, e.g., [4] for a thorough account on this).

2 Considered Technologies for Miniaturized Viscosity-Sensors

As discussed above, the measurement of viscosity involves some kind of interaction of moving or vibrating parts with a liquid. In the following we discuss some fundamental principles underlying our work on miniaturized viscosity sensors.

2.1 Thickness Shear Mode Resonators and Related Devices

A very elegant and well defined way to achieve interaction of vibrating bodies with a viscous sample is that of a shear-vibrating plane being in contact with a viscous liquid. For an angular vibration frequency ω, an attenuated shear wave with a characteristic decay length $\delta = \sqrt{2\eta/\rho\omega}$ is excited in the liquid (ρ denotes the density of the liquid). This interaction can be utilized for viscosity sensing. A prominent example is the so-called thickness shear mode resonator, which is most often embodied by piezoelectric disks. The disks (most often quartz) feature electrodes on both faces. By applying an AC voltage, mechanical vibrations can be excited by means of the piezoelectric effect. Choosing an appropriate crystal cut, shear vibrations can be excited. If the disk is immersed in a viscous liquid, an attenuated shear wave as described above is excited at both faces of the disk.

The impedance appearing between the electrodes features a piezoelectrically induced part, which represents the mechanical vibration. Close to the mechanical resonance frequency, this so-called motional arm can be represented as LC-resonance circuit in an equivalent circuit (see, e.g., [6]). A straightforward analysis [6] yields that loading the resonator with a liquid results an additional inductance $L_2$and a loss resistance R_2 in the motional arm of the equivalent circuit. These components can be interpreted as the consequence of the additional mass loading by the entrained liquid layer resulting change in the resonance frequency and the losses associated with the viscous dissipation in the liquid. Both parameters are approximately proportional to the square root of the viscosity-density product of the liquid

$$L_2, R_2 \propto \sqrt{\rho\eta} \tag{2}$$

There are other piezoelectric devices based on shear polarized surface bound modes such as, e.g., Love waves [7] and surface transverse waves [8], which yield similar interaction and sensitivities with respect to the viscosity-density product in terms of the waves damping and wavenumber.

Piezoelectric excitation can be replaced by other excitation mechanisms such as excitation by Lorentz-forces. In [9] the excitation of modes in conducting (e.g., metallic) disks and membranes in terms of induced eddy currents in an external magnetic bias field is described. Here the excitation of dominantly shear-polarized modes is crucially influenced by the geometry of the excitation coil inducing the eddy currents.

Known issues in the design of shear-mode devices include spuriously excited compressional waves [10][11][12], which may lead to disturbing interferences upon reflections from nearby obstacles as, in contrast to shear waves, compressional waves are scarcely damped even in viscous liquids.

In terms of rheology, shear vibrating devices at higher frequencies show a comparatively small penetration depth δ e.g., for water and a frequency of

$6\,MHz$, δ is in the order of $0.2\,microns$. Thus structural effects influencing the viscosity, which are related to microstructures with typical dimensions in the order of δ or above, will not be captured by the sensor. For instance, in emulsions featuring droplets in the dimensions $10\,microns$ or above, the viscosity of the continuous phase rather than that of the entire mixture is sensed. This effect does not occur for microemulsions with droplet sizes below one micron [13]. Similar experiments have been reported with suspensions, see also the discussion for vibrating beams below [14].

Apart from the fact that kind of a "thin film viscosity" is determined, compared to oscillatory lab viscometers, the devices typically feature significantly higher vibration frequencies (some $10\,kHz$ to some $100\,MHz$. At the same time the vibration amplitudes are very small (can be in the nm range). This yield shear rates in the range of $10^7 s^{-1}$ [15], where due to the sinusoidal vibration, we strictly have to speak about an averaged shear rate [16].

Non-Newtonian behavior can be detected in terms of deviations from the relation (2), which holds for Newtonian liquids only. Specifically, based on (2) a linear relation between L_2 and R_2 can be established. If a measured parameter pair yields a deviation from this linear relation this indicates non-Newtonian behavior as will be shown in an example (monitoring of zeolite synthesis) below.

Summarizing, compared to common lab instruments, shear vibrating miniaturized viscosity sensors excite the liquid under test in a significantly different rheological regime, which can be an issue for complex liquids, if the conventional "macroscopic" viscosity values have to be obtained. Still, these sensors can have benefits also for the monitoring of complex non-Newtonian liquids if a proper calibration routine or, more generally, a suitable interpretation scheme for the obtained data is worked out. The latter can be sufficient as in process control, it is often more important to detect changes in the process rather than measure absolute viscosity values. For broad application also in the laboratory, it will be essential, to standardize the method, similarly as it has been done with other novel viscosity measurement methods (e.g., the high-temperature-high-shear or HTHS method in lubrication technology (see, e.g., the standard ASTM D5481-04).

2.2 Vibrating Beam Devices and Membranes

Another simple vibrating structure that can be utilized to determine viscosity and density of liquids is that of a vibrating beam. Even though the structure is simple, its interaction with the liquid is more involved than that of a plane surface performing shear vibrations. However, in comparison to the thickness shear resonators discussed above, the vibrating beams described in the following feature the lower vibration frequencies and larger amplitudes such that the probed rheological regime can be expected to be more comparable to that of conventional lab viscometers, which indeed holds true in the experiment.

In our research, we considered beams implemented in silicon micromachining technology as well as beams implemented by means of thin vibrating polymer foils. The beams are excited by Lorentz forces stemming from an external magnetic field (provided by a permanent magnet) and AC-currents in conductive paths along the beam. For the readout, the induced voltage in a pickup coil (whose windings are partly on the beam and which are thus vibrating in the magnetic field) or an optical readout method can be utilized. Fig. 2 shows basic beam designs. Modeling the interaction of the beam with the liquid is less straightforward. A suitable method considered is the implementation of Euler Bernoulli beam theory by introducing a distributed load along the beam, which represents the interaction with the liquid and thus depends on the transversal motion of the beam given by its lateral displacement $w(x,t)$ [19]. It can be shown [12] that for the calculation of the interaction between beam and liquid, the Navier-Stokes equations can be linearized if the displacement amplitudes in the liquid are sufficiently small. Using complex time-harmonic notation, the distributed load due to interaction with the liquid at some position x along the beam can be linearly related to the displacement amplitude at x by means of a complex-valued coefficient ("mechanical impedance"). In order to determine this coefficient, a 2D approximation can be made if it is assumed that the liquid movements in the direction of the beam axis are negligible. Thus, considering a vibrating cross section of the beam in a 2D model, the ratio between complex resistance force and associated displacement amplitudes can be determined to obtain

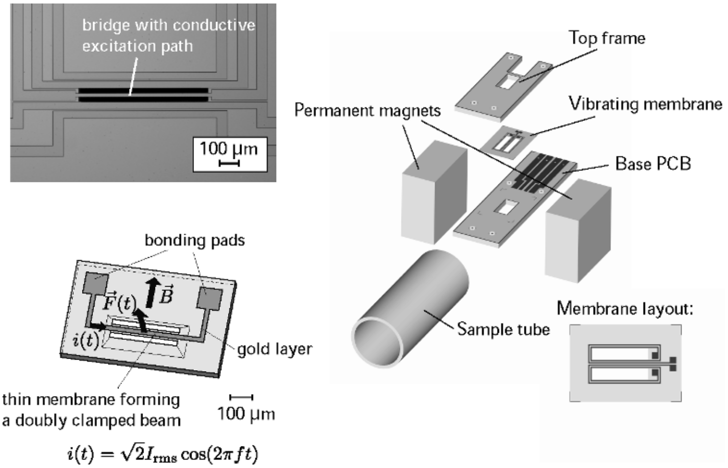

Fig. 2 Clamped-clamped beams in Simicromachining technology (left, [17]) and polymer technology (right, [18]).

said coefficient. In [19] the model involving a spectral domain approach is described. Fig. 3 shows the problem and the plane of computation for the 2D problem as well as an example for the flow field around the vibrating beam cross section computed with the spectral method in 2D. The resulting effect on the beams frequency response is involved but it can be roughly stated that the density mainly affects the resonance frequency while the viscosity dominantly determines the Q-factor (or damping coefficient D) of the resonances.

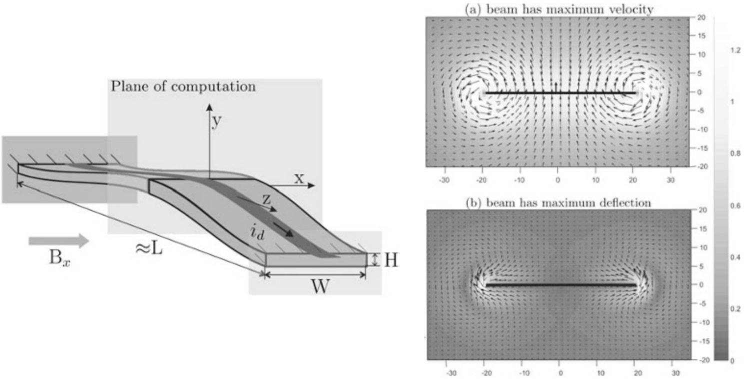

Fig. 3 Beam geometry and associated 2D plane of computation for the fluid resistance force (left) and example for the resulting flow field in the 2D problem (right).

To compare the rheological behavior of beams and TSM resonators, suspensions and Newtonian liquid samples have been characterized with both devices [14]. A glimpse on the results is shown in Fig. 4. These results indicate that a TSM resonator is not suitable for the measurement of viscosity or concentration of the considered SiO2-in-H2O suspensions (Samples 1 to 8), whereas the results for Newtonian liquids (alcohols) follow the expected relation (2). For the vibrating bridge, all these liquids yield a damping coefficient nicely correlating with the liquids viscosity as determined by a lab instrument [14]. We finally note, that the concept of the beam devices is related to the concept of vibrating membranes. In [20] a device is described where the liquid under test is contained in a liquid cell featuring flexible bottom and top walls. Exciting vibrations in these walls, similarly as in the case of the vibrating bridges discussed above, the fluid properties of the liquid will influence the associated resonance properties. This device is suitable for integration in miniaturized fluidic systems. Fig. 5 shows an associated device and typical results illustrating that the relation between the liquid parameters viscosity and density to the device parameters frequency and damping is more complex than for the devices described above (both liquid parameters influence both device parameters) [20]. A mathematical model has been derived to predict the resonance behavior of the sensor cell loaded with a

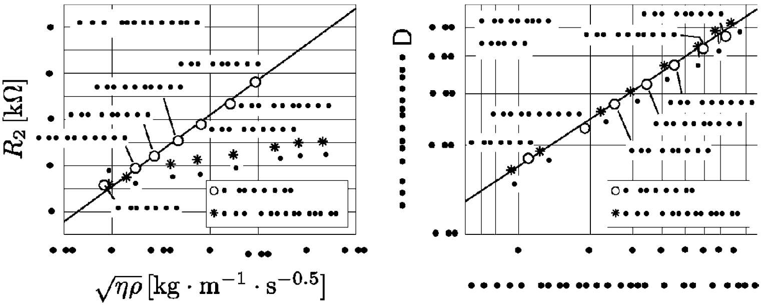

Fig. 4 Viscous loss resistance R2 of a 6 MHz quartz TSM resonator vs. square root of the viscositydensity product (left) showing deviations for non-Newtonian liquid samples. In contrast, the damping factor of a vibrating bridge shows a nice correlation with the viscosity also for complex liquids (right).

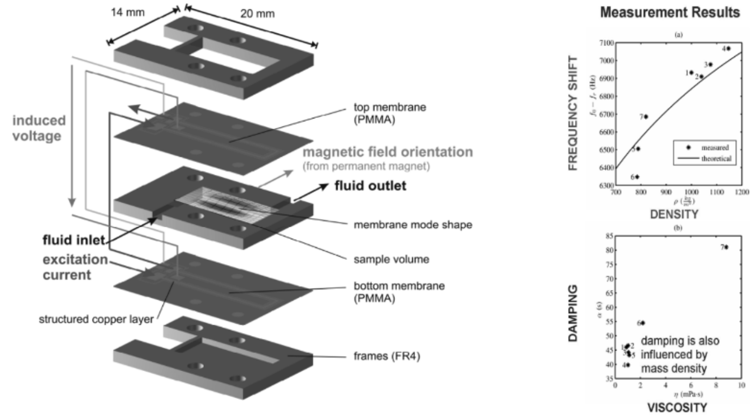

Fig. 5 Double membrane device where the liquid is contained in a cell with vibrating top and bottom walls. Measurements for liquids with various viscosity and density values show that both values influence damping as well as viscosity (right).

liquid [20]. The aim is to calculate the kinetic and potential (elastic) energy terms, and the dissipated power. The modal shape for the vibration of the walls is obtained by applying a Ritz-approach to the fully clamped plate, see Fig. 6. The velocity field in the liquid is then approximately calculated by assuming a potential flow (assuming incompressibility) and adding properly scaled shear-wave solutions at the boundary to fulfill the no-slip condition required for viscous fluid flow. Integration over the fluid volume yields the required energy terms. From these results, the damped resonance frequency and the Q-factor are derived as a function of mass density and viscosity of the fluid [20].

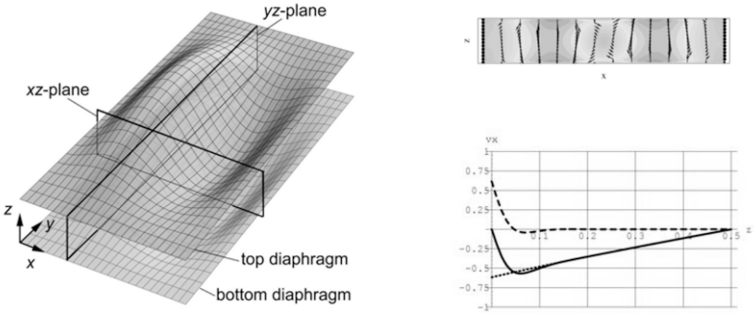

Fig. 6 The modeling of the loaded resonator cell uses the modeshape (left) as the boundary condition for a 2D modeling of the velocity field (top-right) in two orthogonal planes. Based on a potential flow approach (bottom-right, dotted line), a shear wave solution at the boundary (dashed) is added to fulfill the no-slip boundary condition required for viscous flow (solid line).

3 Summary and Conclusions

Microsensor technology facilitates the implementation of sensors for online applications in industrial processes and plants. Devices involving vibrating structures immersed in liquids can be used to determine mechanical and in particular, rheological properties. Due to the associated small vibration amplitudes and high frequencies, the rheological domain can be quite different to that probed by common lab equipment. In particular, this may be an issue for non-Newtonian liquids such as emulsions and suspensions. For the monitoring of changes in the liquid such as phase transitions, the specifically considered rheological domain plays a minor role and the sensor output signals can be subjected to a calibration procedure of some sort.

Acknowledgements The work reported in this paper was partly supported by the Austrian funding agencies FFG (project ASAP-SERMER), FWF (project L103-N07) and the Austrian COMET program supporting the ACCM (Center of Competence for Mechatronics in Linz).

References

1. B. Jakoby, N. Dörr, Monitoring Phase Transitions in Microemulsions Using Impedance and Viscosity Sensors, Proc. IEEE Sensors 2004, p. 627-630.
2. L.R.A. Follens, E.K. Reichel, C. Riesch, J. Vermant, J.A. Martens, C.E.A. Kirschhock, B. Jakoby, Viscosity sensing in heated alkaline zeolite synthesis media, accepted for publication by Physical Chemistry Chemical Physics
3. J. Kuntner, G. Stangl, and B. Jakoby, Characterizing the Rheological Behavior of Oil-Based Liquids: Microacoustic Sensors Versus Rotational Viscometers, IEEE Sens. J.,

vol. 5, no. 5, p. 850-856, Oct. 2005
4. C. Macosko, Rheology: Principles, Measurements and Applications, Wiley/VCH, Poughkeepsie, NY, ISBN: 0-471-18575-2, 1994
5. L.D. Landau and E.M Lifschitz, Lehrbuch der Theoretischen Physik, Band VI, Hydrodynamik, Akadamie Verlag, 1991
6. S.J. Martin, V.E. Granstaff, G.C. Frye, Characterization of a quartz crystal microbalance with simultaneous mass and liquid loading, Anal. Chem. 63 (1981) 2272-2281.
7. B. Jakoby and M. J. Vellekoop, Properties of Love waves: applications in sensors, Smart Mater. Struct., vol. 6, pp. 668-679, 1997.
8. Baer R L, Flory C A, Tom-Moy M and Solomon D S, STW chemical sensors, Proc. IEEE Ultrasonics Symp. (New York: IEEE) pp 293-8, 1992
9. F. Lucklum and B. Jakoby, Novel magnetic-acoustic resonator sensors for remote liquid phase measurement and mass detection, Sensors and Actuators A, vol. 2008, pp. 44-51, July, August 2008.
10. B. A. Martin and H. E. Hager, J. Appl. Phys. 65, 2630, 1989.
11. R. Thalhammer et al., Proceedings of the IEEE International Frequency Control Symposium, IEEE, Orlando, FL, 1997, pp. 105-113.
12. R. Beigelbeck and B. Jakoby, A two-dimensional analysis of spurious compressional wave excitation by thickness-shear-mode resonators, J. Appl. Phys., vol. 95, pp. 4989-4995, May 2004.
13. B. Jakoby, A. Ecker, and M. J. Vellekoop, Monitoring macro- and microemulsions using physical chemosensors, Sensors and Actuators A, vol. 115, no. 2-3, pp. 209-214, 2004.
14. C. Riesch, E.K. Reichel, A. Jachimowicz, F. Keplinger, B. Jakoby, A Micromachined Doubly-Clamped Beam Rheometer for the Measurement of Viscosity and Concentration of Silicon-Dioxide-in-Water Suspensions, Proc. IEEE Sensors Conference 2008, Lecce, Italy, Oct 2629, 2008, pp. 391-394.
15. F. Krispel, C. Reiter, J. Neubig, F. Lenzenhuber, P. W. Krempl, W. Wallnfer and P. M. Worsch, Viscosity sensor based on a symmetric dual quartz thickness shear resonator, Proc. 2003 IEEE International Frequency Control Symposium, Tampa, USA, 5-8 May 2003, p. 1048-1054
16. Personal communication with R. Schnitzer, M. Grschl, E. Benes, and S. Radel
17. C. Riesch, E.K. Reichel, A. Jachimowicz, F. Keplinger, B. Jakoby, A Novel Sensor System for Liquid Properties Based on a Micromachined Beam and a Low-Cost Optical Readout, IEEE Sensors 2007 Proceedings, p. 872-875.
18. E.K. Reichel, C. Riesch, B. Weiss, B. Jakoby, A Vibrating Membrane Rheometer Utilizing Electromagnetic Excitation, Sensors and Actuators A: Physical, 7/8-2008, Vol. 145-146, p. 349-353.
19. B. Weiss, E. K. Reichel, B. Jakoby, "Modeling of a clampedclamped beam vibrating in a fluid for viscosity and density sensing regarding compressibility", Sensors and Actuators A: Physical, Vol 143, Iss 2, 16 May 2008, p. 293-301
20. E.K. Reichel, C. Riesch, F. Keplinger, B. Jakoby, Resonant Measurement of Liquid Properties in a Fluidic Sensor Cell, Proc. Eurosensor XXII 2008, Dresden, VDI, p. 540-543

Mathematical Analysis of Flexural Vibration for a Functionally Graded Material Plate and Vibration Suppression by Flexural Wave Control

Ryuusuke Kawamura, Hiroshi Fujita, Kenichiro Heguri
and Yoshinobu Tanigawa

Abstract In this paper, flexural vibrations of rectangular plates and beams which are consisted of functionally inhomogeneous materials due to cyclic loadings of external force and temperature change are analyzed mathematically. Interference between the flexural vibration due to cyclic loading and that due to cyclic heating is discussed. The amplification effect by loading frequency is also discussed for the deflection and stresses of the beam and the plate. Furthermore, a control problem of the flexural vibration of the FGM beam by the method of wave control is considered. In order to remove progressive wave in flexural waves excited by cyclic loading, intensity and phase lag of control force are derived on the basis of the active sink method. Then, the validity of wave control for the flexural vibration suppression of the FGM beam is discussed.

1 Introduction

Research and development of functionally inhomogeneous materials, such as functionally graded materials, contribute to make performances and functions of structural materials high. The reduction of thermal stresses is one

---

Ryuusuke Kawamura
Faculty of Engineering, University of Miyazaki, Miyazaki 889-2192, Japan,
e-mail: rkawamura@cc.miyazaki-u.ac.jp

Hiroshi Fujita
Graduate School of Engineering, Osaka Prefecture University, Osaka 599-8531, Japan

Kenichiro Heguri
Osaka Prefecture University, Osaka 599-8531, Japan

Yoshinobu Tanigawa
Professor Emeritus, Osaka Prefecture University, Japan,
e-mail: tanigawayoshinobu20070424@zeus.eonet.ne.jp

of important subjects, in order to secure the material strength and to improve the heat resistance. Assuming applications of FGMs to the field of aerospace, structural members become lightweight and thin-walled. Many thin-walled structural members with high aspect ratio are frequently used. Weight saving in the members often results in decrease of stiffness and natural frequency. Hence, to analyze dynamic responses, such as the vibration of structural members due to cyclic loading and heating, is one of important subjects from a viewpoint of structural strength. In our previous works, effects of material inhomogeneity on flexural vibrations were discussed for the FGM beam [1] and rectangular plate [2,3], which were subjected to the cyclic loading and heating. When the loading frequency is close to a natural frequency of the plate, the vibration due to the cyclic loading and that due to the cyclic heating offset each other. However, flexural responses for the vibrating FGM plate with high aspect ratio due to cyclic loadings are not fully made clear.

A number of low dumping natural modes exist in flexible long and large structures such as large space structures. Approaches to their vibration control can be broadly classified into two categories. One is the vibration modal control method. This is effective to treat the problem of comparatively less vibration modes. However, it is impossible to apply the method to the problem in which structures have a number of vibration modes such as large space structures. Instead, an approach to use the control of propagating waves has been studied for problems of dynamic analysis and applied to the control of vibration for structures. This approach proposed by Tanaka and Kikushima [4,5] is one of wave controls and is referred as the active sink method. This method is regarded as promising, since it enables to make vibration modes asleep in the structures. The study which treats a vibration control problem of the structure composed of FGMs from a viewpoint of waves has not been seen yet.

In this paper, we study an effect of plate aspect ratio on interference between flexural vibrations due to the cyclic loading and heating applying to a FGM plate. We discuss a difference in the deflection amplification between the FGM plate with high aspect ratio and a FGM beam. Then, we attempt to treat a control problem of the flexural vibration of the FGM beam by the method of wave control.

2 Flexural Vibrations for FGM Beam and Rectangular Plate

2.1 Analytical Development

We consider a plate of thickness h as shown in Fig. 1. The plate initially at zero temperature is bounded by planes $z' = 0$ and $z' = h$. The surface $z' = h$ is kept perfectly insulated while the surface $z' = 0$ is exposed, for time $t > 0$, to a prescribed temperature which varies sinusoidally in time with amplitude T_0 and angular frequency ω. The corresponding one-dimensional boundary-value problem for temperature change $T = T(z', t)$ is:

Fig. 1 Inhomogeneous plate.

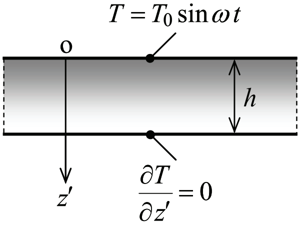

$$c(z')\rho(z')\frac{\partial T}{\partial t} = \frac{\partial}{\partial z'}\left\{\lambda(z')\frac{\partial T}{\partial z'}\right\}, \tag{1}$$

$$T = 0 \text{ at } t = 0, \tag{2}$$

$$T = T_0 \sin \omega t \text{ at } z' = 0, \tag{3}$$

$$\frac{\partial T}{\partial z'} = 0 \text{ at } z' = h. \tag{4}$$

It is assumed that the specific heat capacity $c\rho$ and the thermal conductivity λ are independently given in a form of power of thickness coordinate z',

$$c(z')\rho(z') = c_0\rho_0\left(1 + \frac{z'}{h}\right)^k, \quad \lambda(z') = \lambda_0\left(1 + \frac{z'}{h}\right)^l, \tag{5}$$

where constants, c_0,$\rho_0$and λ_0, are typical quantities of the specific heat, the mass density, and the thermal conductivity; and exponents k and l are parameters representing the inhomogeneity in the specific heat capacity and the thermal conductivity, respectively.

The solution of Eqs. (1)-(5) may be written in a dimensionless form as follows:

$$\bar{T}(\zeta, \tau) = \sum_{j=1}^{\infty} D_{1j}(\zeta)\, e^{-q_j^2\tau} + D_2(\zeta)\cos\bar{\omega}\tau + D_3(\zeta)\sin\bar{\omega}\tau, \tag{6}$$

where the variables ζ,τ and $\bar{\omega}$ denote the dimensionless quantities of coordinate z', time t, and angular frequency ω, whereas the descriptions in detail of eigenvalue q_j and functions $D_{1j}(\zeta)$,$D_2(\zeta)$,$D_3(\zeta)$ are omitted due to limitations of space.

We assume a beam and a rectangular plate which are subjected to a distributed transverse load p and are exposed to a temperature change T from the stress-free state shown as Fig. 2. If the origin of the coordinate in the thickness direction is appropriately chosen in the cross-section of the inhomogeneous beam and plate in which Young's modulus has an arbitrary inhomogeneity in the thickness direction, thermal bending in the inhomogeneous beam and plate can be treated easily. Thus, the coordinate in the thickness direction z whose position of the origin is located at $z' = \eta$ from the top surface $z' = 0$ of the plate is defined as

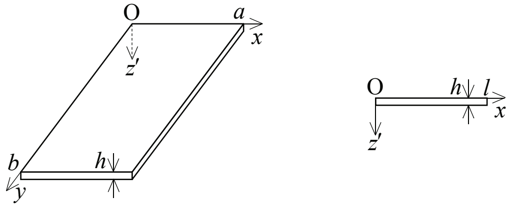

(a) Rectangular plate (b) Beam

Fig. 2 Inhomogeneous rectangular plate and beam.

$$z = z' - \eta. \tag{7}$$

The position η of the origin of the coordinate z is defined as

$$\eta = \int_0^h E(z')z'\,dz' \bigg/ \int_0^h E(z')\,dz'. \tag{8}$$

The equations of motion for the flexural vibration of the inhomogeneous beam and plate are written as

$$\frac{\partial^4 w}{\partial x^4} + \frac{\mu_b}{c_b}\frac{\partial^2 w}{\partial t^2} = \frac{1}{c_b}\left(p - \frac{\partial^2 M_T}{\partial x^2}\right), \tag{9}$$

$$\left(\frac{\partial^2}{\partial x^2} + \frac{\partial^2}{\partial y^2}\right)^2 w + \frac{\mu_p}{c_p}\frac{\partial^2 w}{\partial t^2} = \frac{1}{c_p}\left[p - \frac{1}{1-\nu}\left(\frac{\partial^2}{\partial x^2} + \frac{\partial^2}{\partial y^2}\right) M_T\right], \tag{10}$$

where ν is Poisson's ratio; c_b and c_p are flexural rigidities; μ_b and μ_p are mass per unit length and width; M_T is thermal resultant moment.

We assume that the following cyclic transverse load p applies to the plate.

$$p = p_0 + p_1 \sin \omega_1 t, \tag{11}$$

where p_0 is reference load; p_1 is load amplitude; ω_1 is angular frequency.

The thermal resultant moment M_T is defined as

$$M_T = \int_0^h E(z')\alpha(z')T(z',t)(z'-\eta)\,dz'. \tag{12}$$

It is assumed that Young's modulus E, the coefficient of linear thermal expansion α, the mass density ρ are independently given by a power of z' as

$$E(z') = E_0 \left(1+\frac{z'}{h}\right)^m, \quad \alpha(z') = \alpha_0 \left(1+\frac{z'}{h}\right)^n, \quad \rho(z') = \rho_0 \left(1+\frac{z'}{h}\right)^\gamma, \tag{13}$$

where constants E_0 and α_0 are typical quantities of Young's modulus and the coefficient of linear thermal expansion; and exponents, m,n and γ, are parameters representing the inhomogeneity of Young's modulus, the coefficient of linear thermal expansion, and the mass density, respectively.

The thermo-elastic analysis of the flexural vibration for the inhomogeneous plate is outlined below. Because of the linearity of the problem, the solution of Eq. (10) for the out-of-plane deflection w with simple supports may be written in a dimensionless form as the sum of two deflections due to cyclic loading w_1 and to cyclic heating w_2 as

$$\bar{w} = \bar{w}_1 + \bar{w}_2, \tag{14}$$

$$\begin{aligned} \bar{w}_1 = \frac{1}{\bar{\mu}_p}\frac{16}{\pi^2}\sum_{m=odd}^{\infty}\sum_{n=odd}^{\infty}\frac{1}{mn}\Bigg\{ & \frac{\bar{p}_0}{\varOmega_{mn}^2}(1-\cos\varOmega_{mn}\tau) \\ & - \frac{\bar{p}_1}{\varOmega_{mn}^2-\bar{\omega}_1^2}\left(\sin\bar{\omega}_1\tau - \frac{\bar{\omega}_1}{\varOmega_{mn}}\sin\varOmega_{mn}\tau\right)\Bigg\}\sin\alpha_m\bar{x}\sin\beta_n\bar{y}, \end{aligned} \tag{15}$$

$$\begin{aligned} \bar{w}_2 = \frac{16\bar{h}^2}{(1-\nu)\bar{\mu}_p\pi^2}\sum_{k=odd}^{\infty}\sum_{l=odd}^{\infty}\frac{\alpha_k^2+\beta_l^2}{kl}\Bigg\{ & \sum_{j=1}^{\infty}\frac{1}{\varOmega_{kl}^2+q_j^4} \\ \times\left(e^{-q_j^2\tau} - \cos\varOmega_{kl}\tau + \frac{q_j^2}{\varOmega_{kl}}\sin\varOmega_{kl}\tau\right) & \int_1^2 D_{1j}(\zeta)\zeta^{m+n}(\zeta-1-\bar{\eta})\,d\zeta \\ + \frac{1}{\varOmega_{kl}^2-\bar{\omega}^2}\left(\sin\bar{\omega}\tau - \frac{\bar{\omega}}{\varOmega_{kl}}\cos\varOmega_{kl}\tau\right) & \int_1^2 D_3(\zeta)\zeta^{m+n}(\zeta-1-\bar{\eta})\,d\zeta \\ + \frac{1}{\varOmega_{kl}^2-\bar{\omega}^2}(\cos\bar{\omega}\tau - \cos\varOmega_{kl}\tau) & \int_1^2 D_2(\zeta)\zeta^{m+n}(\zeta-1-\bar{\eta})\,d\zeta\Bigg\}\sin\alpha_k\bar{x}\sin\beta_l\bar{y}, \end{aligned} \tag{16}$$

where the dimensionless natural angular frequency $\mathit{\Omega}_{kl}$ for the flexural vibration of the plate is given by

$$\mathit{\Omega}_{kl} = \sqrt{\frac{\bar{c}_3 \bar{h}^4}{\bar{\mu}_p}} \left(\alpha_k^2 + \beta_l^2 \right), \quad \alpha_k = k\pi, \quad \beta_l = \frac{l\pi}{\bar{b}}. \tag{17}$$

The associated stress is also given as the sum of a solution to cyclic loading and that to cyclic heating. It is illustrated that the stress σ_{yy} may be written in a dimensionless form as the sum of the stress due to cyclic loading σ_{yy1} and that due to cyclic heating σ_{yy2},

$$\bar{\sigma}_{yy} = \bar{\sigma}_{yy1} + \bar{\sigma}_{yy2}, \tag{18}$$

$$\bar{\sigma}_{yy\,1} = -\frac{1}{1-\nu^2} \zeta^m (\zeta - 1 - \bar{\eta}) \bar{h}^2 \left(\nu \frac{\partial^2 \bar{w}_1}{\partial \bar{x}^2} + \frac{\partial^2 \bar{w}_1}{\partial \bar{y}^2} \right), \tag{19}$$

$$\bar{\sigma}_{yy2} = -\frac{1}{1-\nu^2} \zeta^m \left\{ (\zeta - 1 - \bar{\eta}) \bar{h}^2 \left(\nu \frac{\partial^2 \bar{w}_2}{\partial \bar{x}^2} + \frac{\partial^2 \bar{w}_2}{\partial \bar{y}^2} \right) + (1+\nu) \zeta^n \bar{T} \right\}. \tag{20}$$

2.2 Numerical Results and Discussion

Interference between the flexural vibration due to cyclic loading and that due to cyclic heating is examined numerically. The amplification effect by the loading frequency is also examined for the deflection and stresses of the beam and the plate.

Typical material properties are chosen from a mild steel. Thickness h, length a, aspect ratio $\bar{b}(= b/a)$ for a plate and thickness h, length l for a beam are given as

$$h = 2 \times 10^{-3}[\mathrm{m}]\,; \quad a = 1.00[\mathrm{m}]\ , \quad \bar{b} = 9.0 \text{ for plate}, \tag{21}$$

$$h = 2 \times 10^{-3}[\mathrm{m}]\,; \quad l = 1.00[\mathrm{m}] \text{ for beam}. \tag{22}$$

So that the maximum deflection amplitude due to cyclic loading is made closely equal to that due to cyclic heating, reference load p_0 and load amplitude p_1 are given as

$$p_0 = 0[\mathrm{kPa}]\ , \quad p_1 = 1[\mathrm{kPa}]. \tag{23}$$

Angular frequencies in cyclic loading and heating $\bar{\omega}_1$, $\bar{\omega}$ are given as

$$\bar{\omega}_1 = \varepsilon_1 \mathit{\Omega}_{11}^{(h)}, \quad \bar{\omega} = \varepsilon\, \mathit{\Omega}_{11}^{(h)}, \tag{24}$$

where ε_1 and ε are parameters, $\Omega_{11}^{(h)}$ is a fundamental natural angular frequency of the flexural vibration of a homogeneous square plate. Setting $\varepsilon_1 = \varepsilon$, the interference in dynamic responses due to cyclic loading and heating is examined, here. Figures 3 and 4 illustrate the time evolution of out-of-plane deflection $\bar{w}$ at the central point $\bar{x} = \bar{y}/\bar{b} = 0.5$ and that of the stress $\bar{\sigma}_{yy}$ in the plate with aspect ratio $\bar{b} = 9$. When the angular frequencies of cyclic loading and heating are closer to the natural angular frequency of the plate, the deflection due to cyclic loading w_1 and that due to cyclic heating w_2 offset each other regardless of aspect ratio. The same result can be observed in the stress σ_{yy} shown in Fig. 4.

Fig. 3 Time evolution of out-of-plane deflection $\bar{w}$ at the central point $\bar{x} = \bar{y}/\bar{b} = 0.5$ of a FGM plate with aspect ratio $\bar{b} = 9.0$.

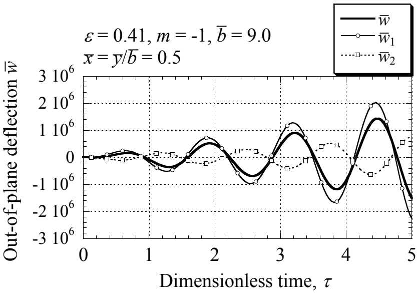

Fig. 4 Time evolution of stress $\bar{\sigma}_{yy}$ at the central point $\bar{x} = \bar{y}/\bar{b} = 0.5$ on the surface $\zeta = 1.0$ in a FGM plate with aspect ratio $\bar{b} = 9.0$.

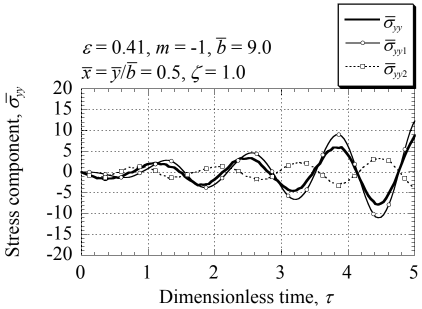

Figure 5 shows the time evolutions of dynamic out-of-plane deflections for the plate with aspect ratio $\bar{b} = 9.0$ and for a beam, respectively. The time evolution of the out-of-plane deflection for the plate with high aspect ratio approaches that for a beam gradually.

Figure 6 shows the variation of deflection amplifications with a parameter in cyclic loadings ε. Here, a deflection amplification is defined as the ratio of the maximum dynamic deflection $\bar{w}_{\max}$ to the maximum quasi-static deflection $\bar{w}_{st\ \max}$. The amplification factors for the plate and the beam increase with an increase of the parameter ε. Furthermore, the amplification factor for the plate approaches that for the beam gradually with increase of the parameter ε.

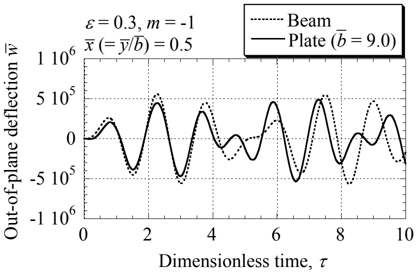

Fig. 5 Time evolution of out-of-plane deflections for a rectangular plate with aspect ratio $\bar{b} = 9.0$ and for a beam.

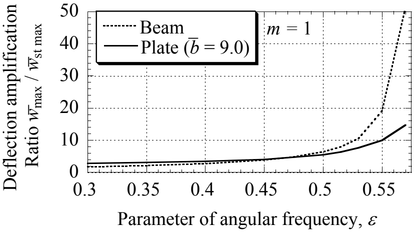

Fig. 6 Variation of deflection amplifications with parameter of angular frequency ε for a rectangular plate and a beam.

3 Vibration Suppression of FGM Beam by Active Sink Method

The concept of wave control for a homogeneous flexible beam has been proposed by Tanaka and Kikushima [4,5]. When energy of an external force is input into structural member, the energy is carried as progressive waves. When the progressive waves arrive at the boundary, reflected waves are exited. Synchronization of interference of these travelling waves causes vibration modes in the structural members. The basic concept of the vibration suppression in the active sink method is to remove reflected waves from structures and to make vibration modes asleep.

We formulate equations for the FGM beam and derive wave vectors by the transfer matrix method. We assume that the beam is subjected to cyclic loading $F_{in} = f_{in} \sin \omega\tau$ at the right boundary edge $\bar{x} = 1.0$ of the beam and control force $F_d = f_d \sin(\omega t + \varphi)$ at the left boundary one $\bar{x} = 0.0$, simultaneously as shown in Fig. 7. The mechanical conditions for the beam are free at both edges. According to the active sink method, we obtain the intensity f_d and the phase lag φ in the control force F_d so as to null the reflected wave in the wave vector. Figures 8 and 9 show an effect of the control force on the out-of-plane deflection of the beam. The intensity of the cyclic loading is assumed as $f_{in} = 0.05$[N] and the angular frequency ω is set as 0.999 times of third natural angular frequency Ω_3. When the control force is applied to the beam, the maximum amplitude of deflection is decreased about less than 2% of one without the control force.

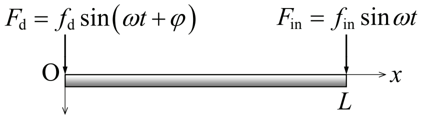

Fig. 7 Vibration suppression of a FGM beam by the active sink method.

Figure 10 shows the difference in the time evolution of deflection at the right boundary edge. The amplitude of the flexural vibration of the beam without control force increases with time. On the other hand, the amplitude of the beam vibration with control remains small with elapse of time. Thus, we can confirm the validity of the active sink method for the vibration suppression of the FGM beam.

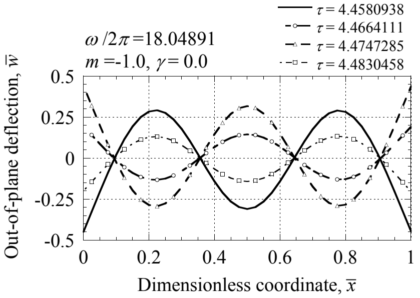

Fig. 8 Longitudinal distribution of out-of-deflection $\bar{w}$ of a FGM beam due to cyclic loading F_{in} without control force.

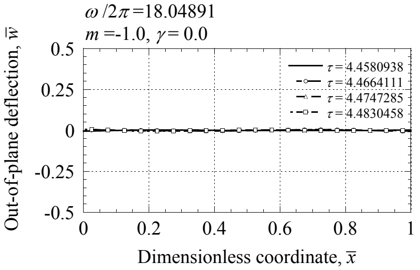

Fig. 9 Longitudinal distribution of out-of-deflection $\bar{w}$ of a FGM beam due to cyclic loading F_{in} with control force F_d.

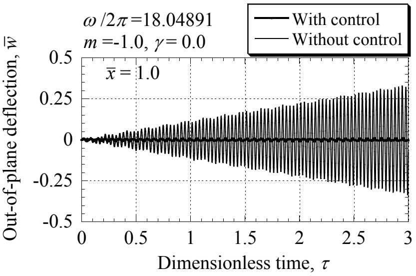

Fig. 10 Effect of addition of control force on the time evolution of out-of-plane deflections at the right boundary edge $\bar{x} = 1.0$ of a FGM beam.

4 Conclusion

Analytical solutions for the FGM beam and plate which are subjected to the cyclic loading and heating are derived. Interference between the flexural vibration due to the cyclic loading and that due to the cyclic heating is discussed numerically. The amplification effect by loading frequency is also discussed for the deflection and stresses of the beam and the plate. A comparison is made for transient flexural responses of the beam and of the plate with high aspect ratio. Furthermore, a vibration suppression of the FGM beam is discussed by applying the active sink method and is illustrated numerically.

Acknowledgements The authors would like to express their gratitude to Professor Hans Irschik and Professor Kazumi Watanabe and organizing committees at the Johannes Kepler University Linz, Austria for their considered efforts to hold this workshop.

References

1. Kawamura R, Tanigawa Y, Hetnarski RB (2003) Thermally induced vibration of an inhomogeneous beam due to a cyclic heating. 177-186 In: Watanabe K, Ziegler F (eds) *IUTAM Symposium on Advanced Materials and Smart Structures*, Solid mechanics and its applications Vol. 106, Kluwer, Dordrecht.
2. Kawamura R, Kusuki S, Matsumoto N (2008) Fundamental thermo-elasticity equations for thermally induced flexural vibration problems for inhomogeneous plates and thermo-elastic dynamical responses to a sinusoidally varying surface temperature. *Journal of Engineering Mathematics*, Vol. 61, No. 2-4, 143-160.
3. Kawamura R, Tanigawa Y, Matsumoto N (2008) Thermally induced vibration of inhomogeneous material rectangular plate due to cyclic variation of thermal and mechanical loads. AIP conference proceedings, Vol. 973, 694-699.
4. Tanaka N, Kikushima Y (1990) Flexural wave control of a flexible beam –Proposition of the active sink method. *Transactions of the Japan Society of Mechanical Engineers* Series C, Vol. 56, No. 522, 351-359 (in Japanese).
5. Tanaka N, Kikushima Y (1990) Flexural wave control of flexible beam –Fundamental characteristics of an active sink system and its verification. *Transactions of the Japan Society of Mechanical Engineers* Series C, Vol. 56, No. 530, 2575-2582 (in Japanese).

Monitoring and control of multi-storey frame structures by strain-type actuators and sensors

Michael Krommer and Markus Zellhofer

Abstract In the present paper we study monitoring and control of multi-storey frame structures. In particular, we consider strain-type sensors and actuators for that purpose. In the first part the concept of collocated continuously distributed strain-type sensors and actuators is introduced. Then we discuss the design of continuously distributed sensors in detail, in order to introduce the concept of strain-type sensor networks afterwards. Here, we focuss on the optimal design of such networks to approximate continuously distributed sensors. Finally, two case studies for a three-storey frame structure are presented. (1) Structural health monitoring for the detection of joints appearing at the connection of floors and sidewalls, and (2) active control of the third floor displacement by PD-controllers.

1 Introduction

Smart structure technology has become a key technology in the design of modern, so-called intelligent, civil, mechanical and aerospace structures. Similar to human beings, these intelligent or smart systems are capable to react to disturbances exerted upon them by the environment they are operating in. For reviews see [1] and [2] and for future challenges and opportunities see [3]. Practical applications of smart structures are e.g. in the fields of active structural vibration control [4] as well as active noise control [5]. One key aspect for a successful design of a smart structure is the communication be-

---

Michael Krommer
Institute for Technical Mechanics, Johannes Kepler University Linz, Altenbergerstr. 69, A-4040 Linz, Austria, e-mail: michael.krommer@jku.at

Markus Zellhofer
Linz Center of Mechatronics GmbH, Altenbergerstr. 69, A-4040 Linz, Austria, e-mail: markus.zellhofer@jku.at

tween structure and controller, the so-called control-structure interaction [6]. Sensors and actuators are responsible for the functioning of this communication. In typical continuous systems a crucial point is the spatial distribution of sensors and actuators to obtain proper information as well as to perform distributed control of continua [6].

In the present paper we concentrate in particular on this latter topic; especially, on the application of strain-type sensors and actuators for multi-storey frame structures with flexible sidewalls.

2 Monitoring and active control of multi-storey frame structures

2.1 Closed loop control strategy

For a multi-storey frame structure the power theorem of mechanics (see [7]) is

$$\frac{d}{dt}T = L^{(e)} + L^{(i)}, \tag{1}$$

in which T is the kinetic energy, $L^{(e)}$ is the power of the external forces and $L^{(i)}$ is the power of the internal forces. Here, we are in particular interested in the power of the internal forces. We assume the sidewalls of the multi-storey frame structure to be modelled as thin beams; then, the bending moment for one sidewall (exemplarily we consider the left sidewall of the i-th storey) is related to the linearized curvature and to some strain-type actuation by means of

$$M_{yiL} = -D_{iL}\frac{\partial^2 w_{iL}}{\partial x_{iL}^2} - M_{iL}^{(a)}. \tag{2}$$

In Eq. (2) M_{yiL} is the bending moment; D_{iL} the bending stiffness, w_{iL} the deflection, x_{iL} the local storey axial beam coordinate and $M_{iL}^{(a)}$ the distributed strain-type actuation. The power of the internal forces then becomes (here R refers o the right sidewall)

$$L^{(i)} = -\frac{d}{dt}W + \underbrace{\sum_{i=1}^{n}\left(\int_0^{h_i} M_{iL}^{(a)}\frac{\partial^2 \dot{w}_{iL}}{\partial x_{iL}^2}dx_{iL} + \int_0^{h_i} M_{iR}^{(a)}\frac{\partial^2 \dot{w}_{iR}}{\partial x_{iR}^2}dx_{iR}\right)}_{L^{(a)}}, \tag{3}$$

such that the power theorem can be written as

$$\frac{d}{dt}\left(T + W\right) = L^{(e)} + L^{(a)}. \tag{4}$$

W is the elastic part of the strain energy and $L^{(a)}$ the power of the actuation. We assume the actuation to be seperable in space and time, with only one time variation $u(t)$ and $2i$ spatial functions $S_{i(L,R)}(x_{i(L,R)})$. The power of the actuation then is

$$L^{(a)} = u(t)\frac{d}{dt}\underbrace{\sum_{i=1}^{n}\left(\int_0^{h_i} S_{iL}(x_{iL})\frac{\partial^2 w_{iL}}{\partial x_{iL}^2}dx_{iL} + \int_0^{h_i} S_{iR}(x_{iR})\frac{\partial^2 w_{iR}}{\partial x_{iR}^2}dx_{iR}\right)}_{y(t)}, \quad (5)$$

in which $y(t)$ is the so-called collocated sensor output (see e.g. [8] or [9]). Hence, we end up with a simple form of the power theorem:

$$\frac{d}{dt}(T+W) = L^{(e)} + u(t)\frac{dy(t)}{dt}. \quad (6)$$

The power of the actuation is the product of the time variation of the actuation $u(t)$ with the time derivative of the collocated sensor signal $y(t)$. This is advantegous from a control point of view. Assume a simple PD control law, $u(t) = -Py(t) - D\dot{y}(t)$, then the power theorem can be cast into

$$\frac{d}{dt}\left(T + W + \frac{1}{2}Py(t)^2\right) = -D\dot{y}(t)^2. \quad (7)$$

From Eq. (7) we postulate the stability of the closed loop system.

2.2 Sensor design

The collocated sensor signal of a distributed strain-type sensor for the multistorey frame structure has been introduced in Eq. (5); such a sensor measures a spatially weighted integral of the linearized curvatures of all sidewalls. The weighing functions (also called shape functions) $S_{iL}(x_{iL})$ and $S_{iR}(x_{iR})$ are yet to be computed. Hence, the problem we are seeking to solve in this section is the following:

Find S_{iL} and S_{iR} for all sidewalls such that the combined sensor output measures a desired structural (kinematical) entity of the multi-storey frame structure.

For details of the design of such sensors see [10]. The solution to this problem is found by applying the principle of virtual work to an auxiliary quasi-static frame, which is choosen identical to the original frame structure. The principle of virtual work reads $\delta W^{(i)} + \delta W^{(e)} = 0$, with the virtual work of the internal forces as

Fig. 1 Measurement of the relative floor displacement of a two-storey frame structure with two storeys

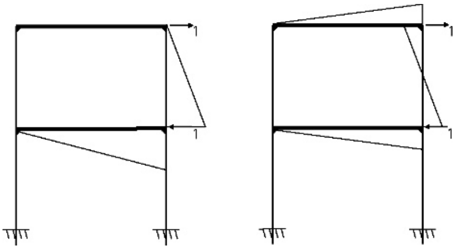

$$\delta W^{(i)} = -\sum_{i=1}^{n} \left(\int_0^{h_i} M_{iL}^{(qs)}(x_{iL}) \frac{\partial^2 \delta w_{iL}}{\partial x_{iL}^2} dx_{iL} + \int_0^{h_i} M_{iR}^{(qs)}(x_{iR}) \frac{\partial^2 \delta w_{iR}}{\partial x_{iR}^2} dx_{iR} \right). \tag{8}$$

In Eq. (8) $M_{i(L,R)}^{(qs)}$ is any statically admissible bending moment and $\delta w_{i(L,R)}$ is any kinematically admissible deflection. We choose the virtual deflection as the deflection of our original frame structure, which is kinematically admissible, $\delta w_{i(L,R)} = w_{i(L,R)}(x_{i(L,R)}, t)$, and the shape function for the sensors are choosen as the statically admissible bending moments of the auxiliary problem $S_{i(L,R)}(x_{i(L,R)}) = M_{i(L,R)}^{(qs)}(x_{i(L,R)})$. Then, the distributed strain-type sensor measures the work of the external forces applied to the quasi-static frame with respect to the original deflection:

$$y(t) = \delta W^{(e)} \Big|_{\delta w_{i(L,R)} = w_{i(L,R)}(x_{i(L,R)}, t)} \tag{9}$$

As an example, we consider a two-storey frame structure. We seek to measure the relative displacement between the first and the second floor. Hence, we apply single unit forces at the two floors in opposite direction in the quasi-static auxiliary problem and calculate any statically admissible bending moment distribution. Two possible distributions for this redundant structure are shown in Figure 1. Shape functions, which represent the deviation of the different statically admissible bending moment distributions are denoted as nilpotent in the literature (see [11]), because their signal is trivial.

3 Optimal design of sensor networks

One of the major problems of using distributed sensors is their practicality. In general, it is more feasible to work with a network of sensor patches; e.g. made of piezoelectric material. In order to study the design of such a network we consider a single-storey of the multi-storey frame structure, which we model as a single-span beam clamped at its lower end and with an end mass at its other end; the latter has a zero slope and can only move horizontally, see Figure 2. The lower end is assumed to be allowed to move horizontally

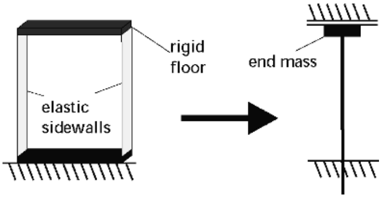

Fig. 2 One-storey frame structure modelled as a beam with an end mass

as well. As strain-type sensors are sensitive to strain only, it is sufficient to study only one storey for the design of the sensor network, and to conclude from it on the design for the multi-storey frame structure.

The span of the beam is subdivided into n sub-sections, $x_i \leq x \leq x_i + \Delta x$, $i = 1, ..., n$, with $x_1 = 0$ and $x_n + \Delta x = L$. Within each sub-section a strain-type sensor patch is located; all of them with a constant width. The sections of the patches are: $\bar{x}_i \leq x \leq \bar{x}_i + \Delta\bar{x}$, $i = 1, ..., n$. To each patch we assign an intensity S_i such that the sensor output of the network is:

$$\bar{y}(t) = \sum_{i=1}^{n} \int_{\bar{x}_i}^{\bar{x}_i+\Delta\bar{x}} S_i w''(x,t)dx \tag{10}$$

In a redundant beam a distributed sensor to measure a specific entity is characterized by a shape function $S(x)$, which depends on q arbitrary constants χ_k, with $k = 1, ...q$, which represent the nilpotent sensor shape functions present in redundant structures. Hence, the signal of the distributed sensor is:

$$y(t) = \int_0^L S(x, \chi_1, ..., \chi_q) w''(x,t)dx. \tag{11}$$

Next, we introduce the error signal $e(t)$ as the difference between the signal of the continuous sensor and the sensor network; $e(t) = y(t) - \bar{y}(t)$. An optimal design of the sensor network requires to minimize the error signal $e(t)$. Based on our previous work [12], we suggest to locate the individual sensor patches and to assign static weights to them according to $(i = 1, ...n)$:

$$S_i = \frac{1}{\Delta\bar{x}} \int_{x_i}^{x_i+\Delta x} S(x)dx \ , \quad \bar{x}_i + \frac{1}{2}\Delta\bar{x} = \left(\int_{x_i}^{x_i+\Delta x} S(x)dx \right)^{-1} \int_{x_i}^{x_i+\Delta x} S(x)xdx. \tag{12}$$

These so-called equal area rule and area center rule render $2n$ linear equations for $2n + q$ unknowns. We obtain q more equations from

$$0 = \int_0^L S(x, \chi_1, ..., \chi_q) w_k''(x)dx - \sum_{i=1}^{n} \int_{\bar{x}_i}^{\bar{x}_i+\Delta\bar{x}} S_i w_k''(x)dx, \tag{13}$$

in which the $k = 1, ..., q$ curvatures are the curvatures due to linear independent static transverse force loadings. In order to be able to use one sensor network for more than one purpose, we consider the location of the sensor patches a priori fixed; hence, we can only choose the weights S_i. In this latter case of a multi-purpose sensor network, we have $n + q$ unknowns, but still $2n + q$ equations. Here, we use a simple least square algorithm in the form

$$\mathbf{A}\mathbf{x} = \mathbf{b} \quad \rightarrow \quad \mathbf{x} = (\mathbf{A}^T\mathbf{A})^{-1}\mathbf{A}^T\mathbf{b} \tag{14}$$

to compute the unknowns $\mathbf{x}$.

As a simple example, we consider the one-storey frame structure of Figure 2 with 8 sensor patches of identical size $\Delta\bar{x} = 1/24$ (a non-dimensional formulation is used), located along the height of the side-walls in an equidistant manner, for which we seek to measure the relative floor displacement. From Eq. (14) we find the solution for the weights to be assigned to the sensor patches for the multi-purpose sensor network. The continuous shape function for the sensor can be deduced from Figure 1; as the floor is assumed rigid only the distribution for the sidewall (combination of a constant and a linear distribution) needs to be considered. In this example, we have a structure with one statically indeterminate constant χ; therefore, we have used a static loading corresponding to the weight of the frame in order to compute the required curvature in Eq. (13). Figure 3(a) shows the dynamic magnification factor for the sensor network for a harmonic ground excitation. The results for the sensor network with 8 patches are good in the lower frequency regime, yet for higher frequencies they are not satisfying. Therefore, we must further refine the assigned weights for dynamic problems.

We assume the patch locations are fixed (multi-purpose network). Then, we extend the intensities as follows

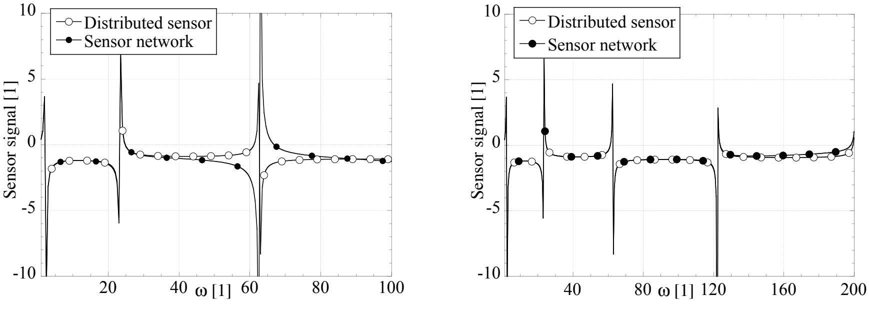

(a) (b)

Fig. 3 Measurement of relative horizontal floor displacement: (a) static sensor network; (b) dynamically refined sensor network

$$\bar{S}_i = S_i + \sum_{j=1}^{m} C_j S_{ji}. \tag{15}$$

Here, the S_{ji} are computed from $j = 1, ..., m$ additional shape function $S_j(x)$ by using the equal area rule, see the first relation in Eq. (12). Finally, the constants C_j are computed from $(k = 1, ...m)$:

$$0 = \int_{0}^{L} S(x, \chi_1, ..., \chi_q) w_k''(x) dx - \sum_{i=1}^{n} \int_{\bar{x}_i}^{\bar{x}_i + \Delta\bar{x}} \left(S_i + \sum_{j=1}^{m} C_j S_{ji} \right) w_k''(x) dx. \tag{16}$$

This dynamic weight refinement strongly depends on a proper choice of the $j = 1, ..., m$ additional shape functions $S_j(x)$ as well as the $k = 1, ..., m$ deflections $w_k(x)$. In the example problem we use the first m eigenmodes for the $w_k(x)$ and the bending moments corresponding to these eigenmodes as the additional shape functions $S_j(x)$. The results are shown in Figure 3(b). One can see that we have a much better accuracy over a much larger frequency range than without the dynamic weight refinement.

4 Case study: three-storey frame structure

In this section we will present two case studies for a three-storey frame structure; first, the structural health monitoring by means of nilpotent sensors, and second the active control of the relative floor displacements by displacement sensors and corresponding collocated actuators.

In both cases we use three patch sensors (actuators) along the height of each of the 6 sidewalls; the sensor length is $30mm$, the width is $108mm$ and their location along the height h of one sidewall are $\bar{x}_i + \Delta\bar{x}/2 = (2i-1)h/6$. The grade of redundancy of this frame structure is $q = 9$, the dimensions are $1476mm \times 344mm \times 108mm$ (total height × sidewall distance × sidewall width), the thickness of the flexible sidewalls (aluminum) is $2mm$ and the mass of each rigid floor (plexiglass) $m = 0.629kg$. The first four natural frequencies are: $2.2Hz$, $6.37Hz$, $9.5Hz$ and $44.35Hz$. As an excitation we consider a ground excitation.

4.1 Structural health monitoring with nilpotent sensors

As the grade of reduncancy is 9, we can compute 9 nilpotent sensor distributions for the three-storey structure. One of them is shown in Figure 4(a). Our goal is to use the nilpotent sensors to monitor possible additional hinges appearing at the interconnection of floors with sidewalls. Figure 4(b) shows a possible damage scenario at floor 1. In order to test our sensor design, we approximate all 9 nilpotent sensors by the sensor network with 18 patches (no contribution from the rigid floors needs to be considered!). Two simulation models are used: one for the undamged structure and one for the structure with the presented damage scenario. A harmonic ground excitation with a frequency $\omega = 15Hz$ is used and at time $t = 0.1s$ we switch from the first simulation model to the second one (with the simulated damage). Four nilpotent sensors start to measure non trivial signals; examplarily we show in Figure 5 the one resulting from the nilpotent sensor of Figure 4(a). One can see that the measured signal coincides very well with the slope at location of the assumed additional hinge at the left sidewall; note, the distributed nilpotent sensor measures the latter slope exactly. Hence, we are not only able to conclude from measurements on the appearance of damage, but also on the location (only four nilpotent sensors start to measure) as well as quantify the damage (the slope is measured!).

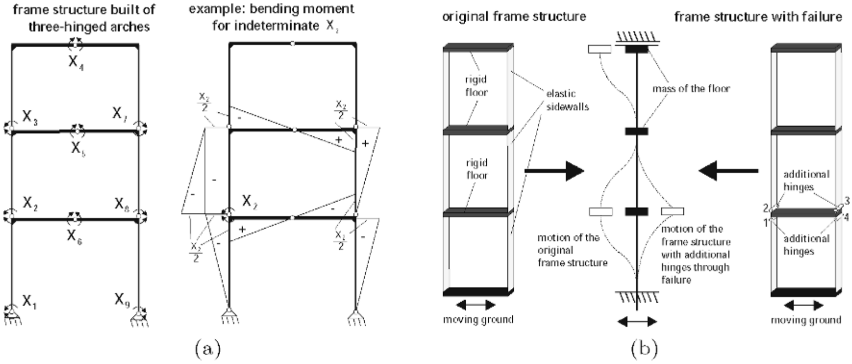

Fig. 4 Three-storey frame structure: (a) nilpotent sensors; (b) damage scenario

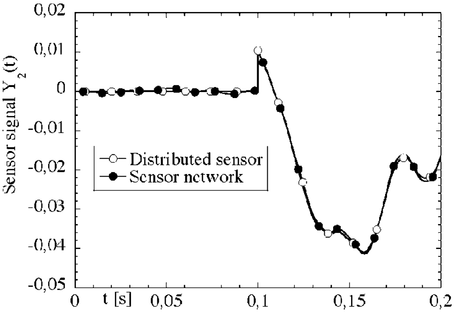

Fig. 5 Three-storey frame structure: nontrivial nilpotent sensor signal $Y_2(t)$ for simulated damage

4.2 Active control of third floor displacement

As a second example we use the sensor network to measure the relative floor displacements. For that sake we only need to approximate the continuous sensors by the 9 patch sensors at the three sidewalls of the right side of the frame. This follows directly from the right figure in Figure 1 by neglecting the contribution from the rigid floors. This results into three independent sensor networks. For active control we use three collocated actuator networks and simple PD-controllers. Figure 6 shows the simulation results for the relative (with respect to the ground excitation) third floor displacement at an excitation frequency of $5Hz$. For the controlled case the relative floor displacement is sigificantly reduced.

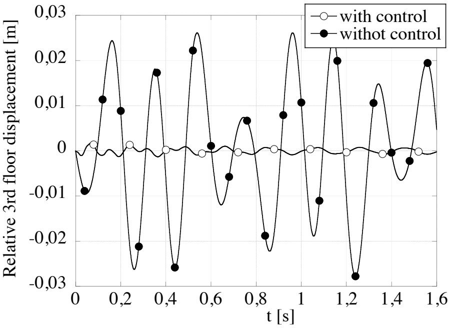

Fig. 6 Three-storey frame structure: Uncontrolled and controlled relative third floor displacement

5 Conclusion

The present paper has presented a general approach for monitoring and control of multi-storey frame structures by means of strain-type sensors and actuators; both, for using continuously distributed sensors and actuators as well as sensor and actuator networks. We have shown that such sensor/actuator systems can be used for structural and health monitoring with a high accuracy, but also for actively controlling the dynamic response of the structure. For the future research will focuss on

- Numerical and experimental validation: Currently, we are working on the analytical and numerical modelling of an existing laboratory three-storey frame structure with attached piezoelectric patches to be used as sensors and actuators, in order to validate our analytical methods.

- Application to other types of structures: The focuss in this direction is on the application of the developed methods for other types of thin-walled structures such as plates and shells.

Acknowledgements Support of the authors from the Austrian Science Fund (FWF Translational project L441-N41 *Sensor Systems for Structural and Health Monitoring*) and of M. Krommer from the Austrian Center of Competence in Mechatronics (ACCM) is gratefully acknowledged.

References

1. E.F. Crawley, Intelligent Structures for Aerospace: A Technology Overview and Assessment. *AIAA Journal*, **32**(8), 1689–1699, 1994.
2. J. Tani, T. Takagi and J. Qiu, Intelligent material systems: application of functional materials. *Applied Mechanics Review*, **51**, 505–521, 1998.
3. S.-C. Liu, M. Tomizuka and G. Ulsoy, Challenges and Opportunities in the Engineering of Intelligent Structures. *Smart Structures and Systems*, **1**(1), 1–12, 2005.
4. R. Alkhatib and M.F. Golnaraghi, Active Structural Vibration Control: A Review. *The Shock and Vibration Digest*, **35**(5), 367–383, 2003.
5. H. Irschik, M. Krommer, M. Nader and U. Pichler, Dynamic piezoelectric shape control applied of shells of revolution with translatory support excitation. L. Faravelli, B.F. Spencer, Jr. eds. *US Europe Workshop on Sensors and Smart Structures Technology*, Como, Italy, April, 2002.
6. U. Gabbert and H.S. Tzou, Preface. U. Gabbert, H.S. Tzou eds. *IUTAM-Symposium on Smart Structures and Structronic Systems*, Magdeburg, Germany, September 2000.
7. F. Ziegler, Mechanics of Solids and Fluids, 2nd corr. ed., Springer, New York, 1998.
8. A. Kugi, Non linear Control Based on Physical Models, Springer, London, 2001.
9. A. Preumont, Vibration Control of Active Strucutres, 2nd ed., Kluwer, Dordrecht, 2004.
10. M. Krommer and H. Irschik, Sensor and Actuator Design for Displacement Control of Continuous Systems. *Smart Structures and Systems* **3**(2), 147–172, 2007.
11. H. Irschik, M. Krommer, A.K. Belyaev and K. Schlacher, Shaping of Piezoelectric Sensors/Actuators for Vibrations of Slender Beams: Coupled Theory and Inappropriate Shape Functions. *Journal of Intelligent Material Systems and Structures*, **9**, 546–554, 1999.
12. M. Krommer, M. Zellhofer and K.-H. Heilbrunner, Strain-type sensor networks for Structural Monitoring of Beam-type Structures. *Journal of Intelligent Material Systems and Structures*, in print.

Transient Piezothermoelastic Problem of a Functionally Graded Thermopiezoelectric Cylindrical Panel

Yoshihiro Ootao

Abstract This paper is concerned with the theoretical treatment of transient piezothermoelastic problem involving a functionally graded thermopiezoelectric cylindrical panel due to nonuniform heat supply in the circumferential direction. The thermal, thermoelastic and piezoelectric constants of the cylindrical panel are expressed as power functions of the radial coordinate variable. We obtained the exact solution for the two-dimensional temperature change in a transient state, and piezothermoelastic response of a simply supported cylindrical panel under the state of plane strain. Some numerical results are shown in figures. Furthermore, the influence of the nonhomogeneity of the material is investigated.

1 Introduction

Piezoelectric materials have coupled effects between the elastic field and the electric field, and have been widely used as the actuators or sensors in smart composite material systems. A new type of piezoelectric materials with material constants varying continuously in the thickness direction, named functionally graded piezoelectric materials (FGPMs), has been developed. It is possible to produce large displacements and reduce the stresses when the FGPMs are used as an actuator. Therefore, the piezoelectric or piezothermoelastic problems for the FGPMs become important, and there are several analytical studies concerned with these problems.

As piezothermoelastic problems, Wang and Noda [1] analyzed a smart FGPM structures by using finite element method. Wu at al. [2] obtained an

---

Yoshihiro Ootao
Department of Mechanical Engineering, Graduate School of Engineering, Osaka Prefecture University, 1-1 Gakuen-cho, Nakaku, Sakai, 599-8531, Japan, e-mail: ootao@me.osakafu-u.ac.jp

exact solution for a FGPM cylinder shell subjected to axisymmetric thermal or mechanical loading. Ying and Zhifei [3] obtained the exact solution of FGPM cantilevers whose material properties change linearly in the thickness direction. Zhong and Shang [4] obtained the exact solution of the simply supported FGPM plates. These papers, however, treated only the piezothermoelastic problems under the uniform heating or the steady temperature distribution. It is well-known that thermal stress distributions in a transient state can show large values compared with the one in a steady state. Therefore, the transient piezothermoelastic problems become important. Ootao and Tanigawa [5] obtained the two-dimensional solution for transient piezothermoelasticity of a FGPM strip. The one-dimensional solutions for transient piezothermoelasticity of a FGPM hollow sphere [6] and a FGPM hollow cylinder [7] were obtained. To the author's knowledge, however, the exact analysis for a transient piezothermoelastic problem of a functionally graded thermopiezoelectric cylindrical panel under two-dimensional temperature distribution has not been reported.

In the present article, we analyzed exactly the transient piezothermoelasticity involving a functionally graded thermopiezoelectric cylindrical panel due to nonuniform heat supply in the circumferential direction as a plane strain problem.

2 Analysis

We consider an infinitely long, functionally graded thermopiezoelectric cylindrical panel that has nonhomogeneous thermal, mechanical and electric properties in the radial direction, the span angle of which is denoted by θ_0. The panel's inner and outer radii are designated r_a and r_b, respectively.

2.1 Heat Conduction Problem

We assume that the cylindrical panel is initially at zero temperature and is heated from the inner and outer surfaces by surrounding media with relative heat transfer coefficients (heat transfer coefficient/thermal conductivity) h_a and h_b. We denote the temperatures of the surrounding media by the functions $T_a f_a(\theta)$ and $T_b f_b(\theta)$, and assume its end surfaces ($\theta = 0, \theta_0$) are held zero temperature. Then the temperature distribution shows a two-dimensional distribution in $r - \theta$ plane. The thermal conductivity λ_r and λ_θ and the heat capacity per unit volume are assumed to take the following form

$$\lambda_r(r) = \lambda_{r0} \left(r/r_b\right)^m , \quad \lambda_\theta(r) = \lambda_{\theta 0} \left(r/r_b\right)^m , \quad c(r)\rho(r) = c_0\rho_0 \left(r/r_b\right)^k \quad (1)$$

where m and k are nonhomogeneous parameters. Using the Eq. (1), the transient heat conduction equation in dimensionless form is

$$\bar{T}_{,\tau} = (m+1)\bar{r}^{m-k-1}\bar{T}_{,\bar{r}} + \bar{r}^{m-k}\bar{T}_{,\bar{r}\bar{r}} + \bar{\lambda}_{\theta 0}\bar{r}^{m-k-2}\bar{T}_{,\theta\theta} \tag{2}$$

where a comma denotes partial differentiation with respect to the variable that follows. The initial and thermal boundary conditions in dimensionless form are

$$\tau = 0;\ \bar{T} = 0 \tag{3}$$

$$\bar{r} = \bar{r}_a;\ \bar{T}_{,\bar{r}} - H_a\bar{T} = -H_a\bar{T}_a f_a(\theta)\ , \quad \bar{r} = 1;\ \bar{T}_{,\bar{r}} + H_b\bar{T} = H_b\bar{T}_b f_b(\theta) \tag{4}$$

$$\theta = 0,\ \theta_0;\ \bar{T} = 0 \tag{5}$$

In Eqs.(2)-(5), we have introduced the following dimensionless values:

$$\left.\begin{array}{c} (\bar{T}, \bar{T}_a, \bar{T}_b) = (T, T_a, T_b)/T_0,\ (\bar{r}, \bar{r}_a) = (r, r_a)/r_b,\ (H_a, H_b) = (h_a, h_b)r_b \\ \bar{\lambda}_{\theta 0} = \lambda_{\theta 0}/\lambda_{r0}, \kappa_0 = \lambda_{r0}/(c_0\rho_0),\ \tau = \kappa_0 t/r_b^2 \end{array}\right\} \tag{6}$$

where T is the temperature change; t is time; and T_0 and κ_0 are typical values of temperature and thermal diffusivity, respectively. Introducing the finite sine transformation with respect to the variable θ and the Laplace transformation with respect to the variable τ, the solution of Eq. (2) can be obtained so as to satisfy conditions (3)-(5). This solution is shown as follows:

$$\bar{T} = \sum_{K=1}^{\infty} \bar{T}_K(\bar{r}, \tau)\sin q_K\theta \tag{7}$$

where

$$\begin{array}{l} \bar{T}_K(\bar{r}, \tau) = \frac{2}{\theta_0}\{\frac{1}{F}(\bar{A}'\bar{r}^{\beta_1} + \bar{B}'\bar{r}^{\beta_2}) \\ + \sum\limits_{j=1}^{\infty} \frac{2\bar{r}^{-m/2}e^{-(2-m+k)^2\mu_j^2\tau/4}}{\mu_j\Delta'(\mu_j)}[\bar{A}J_\gamma(\mu_j\bar{r}^{(2-m+k)/2}) + \bar{B}Y_\gamma(\mu_j\bar{r}^{(2-m+k)/2})]\} \end{array} \tag{8}$$

where $J_\gamma(\ )$ and $Y_\gamma(\ )$ are the Bessel function of the first and second kind of order γ, respectively; Δ and F are the determinants of 2×2 matrix $[a_{kl}]$ and $[e_{kl}]$, respectively; the coefficients $\bar{A}$ and $\bar{B}$ are defined as the determinant of the matrix similar to the coefficient matrix $[a_{kl}]$, in which the first column or second column is replaced by the constant vector $\{c_k\}$, respectively; similarly, the coefficients $\bar{A}'$ and $\bar{B}'$ are defined as the determinant of the matrix similar to the coefficient matrix $[e_{kl}]$, in which the first column or second column is replaced by the constant vector $\{c_k\}$, respectively. The elements a_{kl}, e_{kl} and c_k are obtained from Eq. (4). Furthermore, in Eqs. (7) and (8), β_i, γ, $\Delta'(\mu_j)$ and q_K are

$$\left.\begin{array}{c}\beta_1 = (-m + \sqrt{m^2 + 4q_K^2 \bar{\lambda}_{\theta 0}})/2,\ \beta_2 = -(m + \sqrt{m^2 + 4q_K^2 \bar{\lambda}_{\theta 0}})/2 \\ \gamma = \frac{\sqrt{m^2 + 4q_K^2 \bar{\lambda}_{\theta 0}}}{|2-m+k|},\ \varDelta'(\mu_j) = \left.\frac{d\varDelta}{d\mu}\right|_{\mu=\mu_j},\ q_K = \frac{K\pi}{\theta_0}\end{array}\right\} \tag{9}$$

and μ_j represent the jth positive roots of the following transcendental equation

$$\varDelta(\mu) = 0 \tag{10}$$

2.2 Piezothermoelastic Problem

Let analyze the transient piezothermoelasticity of a functionally graded thermopiezoelectric cylindrical panel with simply supported edges as a plane strain problem. For the thermopiezoelectric material of crystal class mm2, the constitutive relations are expressed in dimensionless form as follows:

$$\left.\begin{array}{c}\bar{\sigma}_{rr} = \bar{C}_{11}\bar{\varepsilon}_{rr} + \bar{C}_{12}\bar{\varepsilon}_{\theta\theta} - \bar{e}_1\bar{E}_r - \bar{\beta}_r\bar{T} \\ \bar{\sigma}_{\theta\theta} = \bar{C}_{12}\bar{\varepsilon}_{rr} + \bar{C}_{22}\bar{\varepsilon}_{\theta\theta} - \bar{e}_2\bar{E}_r - \bar{\beta}_\theta\bar{T} \\ \bar{\sigma}_{zz} = \bar{C}_{13}\bar{\varepsilon}_{rr} + \bar{C}_{23}\bar{\varepsilon}_{\theta\theta} - \bar{e}_3\bar{E}_r - \bar{\beta}_z\bar{T},\ \bar{\sigma}_{r\theta} = \bar{C}_{66}\bar{\gamma}_{r\theta} - \bar{e}_6\bar{E}_\theta\end{array}\right\} \tag{11}$$

where

$$\left.\begin{array}{c}\bar{\beta}_r = \bar{C}_{11}\bar{\alpha}_r + \bar{C}_{12}\bar{\alpha}_\theta + \bar{C}_{13}\bar{\alpha}_z,\ \bar{\beta}_\theta = \bar{C}_{12}\bar{\alpha}_r + \bar{C}_{22}\bar{\alpha}_\theta + \bar{C}_{23}\bar{\alpha}_z \\ \bar{\beta}_z = \bar{C}_{13}\bar{\alpha}_r + \bar{C}_{23}\bar{\alpha}_\theta + \bar{C}_{33}\bar{\alpha}_z\end{array}\right\} \tag{12}$$

The constitutive equation for the electric field in dimensionless form is given as

$$\bar{D}_r = \bar{e}_1\bar{\varepsilon}_{rr} + \bar{e}_2\bar{\varepsilon}_{\theta\theta} + \bar{\eta}_1\bar{E}_r + \bar{p}_1\bar{T},\ \ \bar{D}_\theta = \bar{e}_6\bar{\gamma}_{r\theta} + \bar{\eta}_2\bar{E}_\theta \tag{13}$$

The relations between the electric field intensities and the electric potential ϕ in dimensionless form are defined by

$$\bar{E}_r = -\bar{\phi},_{\bar{r}}\ ,\ \bar{E}_\theta = -\bar{r}^{-1}\bar{\phi},_\theta \tag{14}$$

If the electric charge density is absent, the equation of electrostatics is expressed in dimensionless form as follows:

$$\bar{D}_r,_{\bar{r}} + \bar{r}^{-1}(\bar{D}_r + \bar{D}_\theta,_\theta) = 0 \tag{15}$$

The elastic stiffness constants C_{kl}, the piezoelectric coefficients e_k, the dielectric constants η_k, the coefficients of linear thermal expansion α_k and the pyroelectric constant p_1 in dimensionless form are assumed to take the following forms

$$(\bar{C}_{kl}, \bar{e}_k, \bar{\eta}_k) = (\bar{C}^0_{kl}, \bar{e}^0_k, \bar{\eta}^0_k)\bar{r}^l,\ \bar{\alpha}_k = \bar{\alpha}^0_k\bar{r}^b,\ \bar{p}_1 = \bar{p}^0_1\bar{r}^{l+b} \tag{16}$$

where l and b are arbitrary constants. In Eqs. (11)-(16), the following dimensionless values are introduced:

$$\left.\begin{array}{c}\bar{\sigma}_{kl} = \frac{\sigma_{kl}}{\alpha_0 Y_0 T_0},\ (\bar{\varepsilon}_{kl}, \bar{\gamma}_{kl}) = \frac{(\varepsilon_{kl}, \gamma_{kl})}{\alpha_0 T_0},\ (\bar{u}_r, \bar{u}_\theta) = \frac{(u_r, u_\theta)}{\alpha_0 T_0 r_b} \\ (\bar{C}_{kl}, \bar{C}^0_{kl}) = \frac{(C_{kl}, C^0_{kl})}{Y_0} \\ (\bar{\alpha}_k, \bar{\alpha}^0_k) = \frac{(\alpha_k, \alpha^0_k)}{\alpha_0},\ (\bar{e}_k, \bar{e}^0_k) = \frac{(e_k, e^0_k)}{Y_0 |d_0|},\ (\bar{\eta}_k, \bar{\eta}^0_k) = \frac{(\eta_k, \eta^0_k)}{Y_0 |d_0|^2} \\ (\bar{p}_1, \bar{p}^0_1) = \frac{(p_1, p^0_1)}{\alpha_0 Y_0 |d_0|},\ \bar{D}_k = \frac{D_k}{\alpha_0 Y_0 T_0 |d_0|},\ \bar{\phi} = \frac{\phi |d_0|}{\alpha_0 T_0 r_b},\ \bar{E}_k = \frac{E_k |d_0|}{\alpha_0 T_0}\end{array}\right\} \tag{17}$$

where σ_{kl} are the stress components, ε_{kl} are the normal strain components, $\gamma_{r\theta}$ is the engineering shear strain component, (u_r, u_θ) are the displacement components, D_k are the electric displacement components, and α_0, Y_0 and d_0 are typical values of the coefficient of linear thermal expansion, Young's modulus and piezoelectric modulus, respectively.

Substituting the displacement-strain relations, Eqs. (14) and (16), into Eqs. (11) and (13), and later into Eq. (15) and the equilibrium equations, the governing equations of the displacements and the electric potential in dimensionless form are written as

$$\left.\begin{array}{c}\bar{C}^0_{11}[\bar{u}_{r,\bar{r}\bar{r}} + (l+1)\bar{r}^{-1}\bar{u}_{r,\bar{r}}] + \bar{r}^{-2}(\bar{C}^0_{12} l - \bar{C}^0_{22})\bar{u}_r + \bar{r}^{-2}\bar{C}^0_{66}\bar{u}_{r,\theta\theta} \\ + (\bar{C}^0_{12} + \bar{C}^0_{66})\bar{r}^{-1}\bar{u}_{\theta,\bar{r}\theta} + (\bar{C}^0_{12} l - \bar{C}^0_{22} - \bar{C}^0_{66})\bar{r}^{-2}\bar{u}_{\theta,\theta} + \bar{e}^0_1\bar{\phi}_{,\bar{r}\bar{r}} \\ + [\bar{e}^0_1(l+1) - \bar{e}^0_2]\bar{r}^{-1}\bar{\phi}_{,\bar{r}} + \bar{e}^0_6\bar{r}^{-2}\bar{\phi}_{,\theta\theta} = [\bar{\beta}^0_r(l+b+1) - \bar{\beta}^0_\theta]\bar{r}^{b-1}\bar{T} + \bar{\beta}^0_r\bar{r}^b\bar{T}_{,\bar{r}}\end{array}\right\} \tag{18}$$

$$\left.\begin{array}{c}(\bar{C}^0_{66} + \bar{C}^0_{12})\bar{r}^{-1}\bar{u}_{r,\bar{r}\theta} + [\bar{C}^0_{66}(l+1) + \bar{C}^0_{22}]\bar{r}^{-2}\bar{u}_{r,\theta} \\ + \bar{C}^0_{66}[(l+1)(\bar{r}^{-1}\bar{u}_{\theta,\bar{r}} - \bar{r}^{-2}\bar{u}_\theta) + \bar{u}_{\theta,\bar{r}\bar{r}}] \\ + \bar{C}^0_{22}\bar{r}^{-2}\bar{u}_{\theta,\theta\theta} + \bar{e}^0_6(l+1)\bar{r}^{-2}\bar{\phi}_{,\theta} + (\bar{e}^0_6 + \bar{e}^0_2)\bar{r}^{-1}\bar{\phi}_{,\bar{r}\theta} = \bar{\beta}^0_\theta\bar{r}^{b-1}\bar{T}_{,\theta}\end{array}\right\} \tag{19}$$

$$\left.\begin{array}{c}\bar{e}^0_1\bar{u}_{r,\bar{r}\bar{r}} + [\bar{e}^0_1(l+1) + \bar{e}^0_2]\bar{r}^{-1}\bar{u}_{r,\bar{r}} + \bar{e}^0_6\bar{r}^{-2}\bar{u}_{r,\theta\theta} + \bar{e}^0_2 l\bar{r}^{-2}\bar{u}_r \\ + (\bar{e}^0_2 + \bar{e}^0_6)\bar{r}^{-1}\bar{u}_{\theta,\bar{r}\theta} + (\bar{e}^0_2 l - \bar{e}^0_6)\bar{r}^{-2}\bar{u}_{\theta,\theta} - \bar{\eta}^0_1[\bar{\phi}_{,\bar{r}\bar{r}} + (l+1)\bar{\phi}_{,\bar{r}}] - \bar{\eta}^0_2\bar{r}^{-2}\bar{\phi}_{,\theta\theta} \\ = -\bar{p}^0_1\bar{r}^b[\bar{T}_{,\bar{r}} + (l+b+1)\bar{r}^{-1}\bar{T}]\end{array}\right\} \tag{20}$$

The boundary conditions of inner and outer surfaces can be represented as follows:

$$\bar{r} = \bar{r}_a, 1;\ \bar{\sigma}_{rr} = 0,\ \bar{\sigma}_{r\theta} = 0,\ \bar{D}_r = 0 \tag{21}$$

We now consider the case of a simply supported cylindrical panel and assume that the edges are electrically grounded. The boundary conditions of edges are represented by the following relations:

$$\theta = 0, \theta_0;\ \bar{\sigma}_{\theta\theta} = 0,\ \bar{u}_r = 0,\ \bar{\phi} = 0 \tag{22}$$

We assume the solutions of Eqs. (18)-(20) in order to satisfy Eq. (22) in the following form.

$$\left.\begin{aligned}\bar{u}_r &= \sum_{K=1}^{\infty}[U_{rcK}(\bar{r})+U_{rpK}(\bar{r})]\sin q_K\theta\\ \bar{u}_\theta &= \sum_{K=1}^{\infty}[U_{\theta cK}(\bar{r})+U_{\theta pK}(\bar{r})]cosq_K\theta\\ \bar{\phi} &= \sum_{K=1}^{\infty}[\Phi_{cK}(\bar{r})+\Phi_{pK}(\bar{r})]\sin q_K\theta\end{aligned}\right\} \tag{23}$$

In Eq. (23), the first term on the right side gives the homogeneous solution and the second term of the right side gives the particular solution. We now consider the homogeneous solution. Substituting the first term on the right side of Eq. (23) into the homogeneous expression of the governing equation of Eqs. (18)-(20), and later changing a variable with the use of $\bar{r} = \exp(s)$, we obtained the simultaneous ordinary different equations of U_{rcK}, $U_{\theta cK}$ and Φ_{cK}. We show U_{rcK}, $U_{\theta cK}$ and Φ_{cK} as follows:

$$(U_{rcK}, U_{\theta cK}, \Phi_{cK}) = (U^0_{rcK}, U^0_{\theta cK}, \Phi^0_{cK})\exp(\lambda s) \tag{24}$$

Substituting Eq. (24) into the simultaneous ordinary different equations, the condition that a non-trivial solutions of $(U^0_{rcK}, U^0_{\theta cK}, \Phi^0_{cK})$ exist leads to the following equation.

$$\lambda^6 + A_1\lambda^5 + A_2\lambda^4 + A_3\lambda^3 + A_4\lambda^2 + A_5\lambda + A_6 = 0 \tag{25}$$

where expressions for the coefficients $A_1 - A_6$ are omitted here. From Eq. (25), there might be six real roots, four real roots and one pair of conjugate complex roots, two real roots and two pair of conjugate complex roots, or three pairs of conjugate complex roots.

Given J_R real toots for λ, $U_{rcK}(\bar{r})$, $U_{\theta cK}(\bar{r})$ and $\Phi_{cK}(\bar{r})$ are given by the following expressions:

$$\left.\begin{gathered}U_{rcK}(\bar{r}) = \sum_{J=1}^{J_R} F_{KJ}\bar{r}^{\lambda_J}\ , \quad U_{\theta cK}(\bar{r}) = \sum_{J=1}^{J_R} M_{KJ}(\lambda_J)F_{KJ}\bar{r}^{\lambda_J}\\ \Phi_{cK}(\bar{r}) = \sum_{J=1}^{J_R} N_{KJ}(\lambda_J)F_{KJ}\bar{r}^{\lambda_J}\end{gathered}\right\} \tag{26}$$

If the complex root for λ is expressed by $\lambda_J = \alpha_J \pm i\beta_J$, and given J_I pairs complex roots for λ, $U_{rcK}(\bar{r})$, $U_{\theta cK}(\bar{r})$ and $\Phi_{cK}(\bar{r})$ are given by the following expressions:

$$\left.\begin{aligned}U_{rcK}(\bar{r}) &= \sum_{J=1}^{J_I}\left[C_{1J}\bar{r}^{\alpha_J}\cos(\beta_J\ln\bar{r}) + C_{2J}\bar{r}^{\alpha_J}sin(\beta_J\ln\bar{r})\right]\\ U_{\theta cK}(\bar{r}) &= \sum_{J=1}^{J_I}\{C_{1J}\,\bar{r}^{\alpha_J}[\varGamma_{1J}\cos(\beta_J\ln\bar{r}) - \varOmega_{1J}\sin(\beta_J\ln\bar{r})]\\ &\quad + C_{2J}\bar{r}^{\alpha_J}\left[\varOmega_{1J}cos(\beta_J\ln\bar{r}) + \varGamma_{1J}sin(\beta_J\ln\bar{r})\right]\}\\ \varPhi_{ck}(\bar{r}) &= \sum_{J=1}^{J_I}\{C_{1J}\,\bar{r}^{\alpha_J}[\varGamma_{2J}\cos(\beta_J\ln\bar{r}) - \varOmega_{2J}\sin(\beta_J\ln\bar{r})]\\ &\quad + C_{2J}\bar{r}^{\alpha_J}\left[\varOmega_{2J}cos(\beta_J\ln\bar{r}) + \varGamma_{2J}sin(\beta_J\ln\bar{r})\right]\}\end{aligned}\right\} \tag{27}$$

In Eqs. (26) and (27), F_{kJ}, C_{1J} and C_{2J} are unknown constants.

In order to obtain the particular solution, we use the series expansions of the Bessel functions. Since the order γ of the Bessel function in Eq. (8) is not integer in general, Eq. (8) can be written as the following expression.

$$\bar{T}_K(\bar{r},\tau) = a_0'\bar{r}^{\beta_1} + b_0'\bar{r}^{\beta_2} + \sum_{n=0}^{\infty}\left[a_n(\tau)\bar{r}^{\omega_1} + b_n(\tau)\bar{r}^{\omega_2}\right] \tag{28}$$

where

$$\omega_1 = [(2-m+k)(2n+\gamma)-m]/2,\ \omega_2 = [(2-m+k)(2n-\gamma)-m]/2 \tag{29}$$

$U_{rpK}(\bar{r})$, $U_{\theta pK}(\bar{r})$ and $\varPhi_{pK}(\bar{r})$ of the particular solutions are obtained the function systems like Eq. (28). Then, the stress components and the electric displacements can be evaluated from the displacement components and the electric potential. The unknown constants in the homogeneous solutions such as Eqs. (26) and (27) are determined so as to satisfy the boundary condition (21).

3 Numerical results

Numerical parameters of heat conduction and shape are presented as follows:

$$\left.\begin{aligned}H_b = 1.0,\ H_a = H_b/\bar{r}_a^m,\ \bar{T}_a = 0,\ \bar{T}_b = 1,\ \theta_0 = 90^\circ,\ \ \bar{r}_a = 0.7\\ f_b(\theta) = \left(1-\theta'^2/\theta_b^2\right)H\left(\theta_b - |\theta'|\right),\ \theta_b = 15^\circ,\ \theta' = \theta - \theta_0/2\end{aligned}\right\} \tag{30}$$

where $H(x)$ is Heaviside's function. The typical values of material constants are taken with reference to cadmium selenide. The nonhomogeneous parameters adopted for the numerical calculations are shown in Table 1. Figures 1-5 show the results for Case 1. The variations of temperature change, thermal stresses $\bar{\sigma}_{\theta\theta}$, $\bar{\sigma}_{rr}$ and electric potential in the radial direction at the midpoint of the cylindrical panel ($\theta = \theta_0/2$) are shown in Figures 1, 2, 3 and 5, respectively. The variation of the shearing stress $\bar{\sigma}_{r\theta}$ in the radial direction at the edge ($\theta = 30^\circ$) of the heating region is shown in Figure 4. Figures 6

	m	k	b	l
Case 1	$-1, 0, 1$	0	0	0.01
Case 2	0	0	$1, 0, -1$	0.01
Case 3	0	0	0	$-1, 0.01, 1$

Table 1 Nonhomogeneous parameters

and 7 show the variations of thermal stress $\bar{\sigma}_{rr}$ in the radial direction at the midpoint of the cylindrical panel for Cases 2 and 3, respectively.

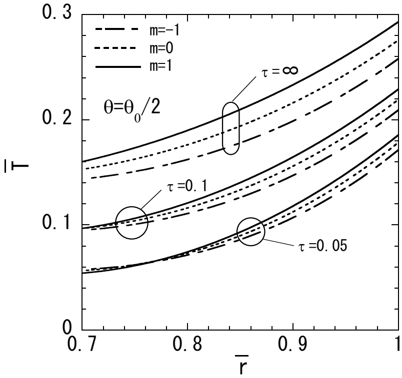

Fig. 1 Variation of temperature change in the radial direction (Case 1, $\theta = \theta_0/2$).

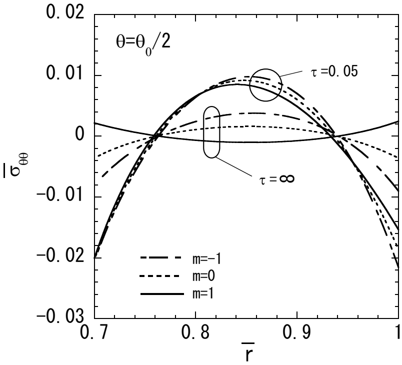

Fig. 2 Variation of thermal stress $\bar{\sigma}_{\theta\theta}$ in the radial direction (Case 1, $\theta = \theta_0/2$).

4 Conclusion

We have analyzed the transient piezothermoelastic problem involving a functionally graded thermopiezoelectric cylindrical panel that has nonhomoge-

Fig. 3 Variation of thermal stress $\bar{\sigma}_{rr}$ in the radial direction (Case 1, $\theta = \theta_0/2$).

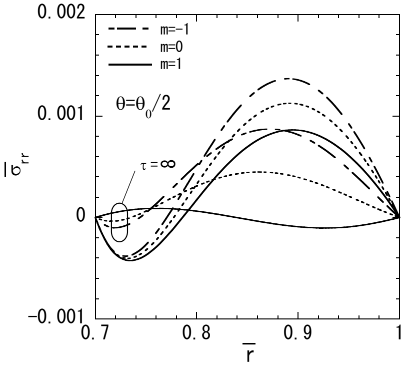

Fig. 4 Variation of thermal stress $\bar{\sigma}_{r\theta}$ in the radial direction (Case 1, $\theta = 30°$).

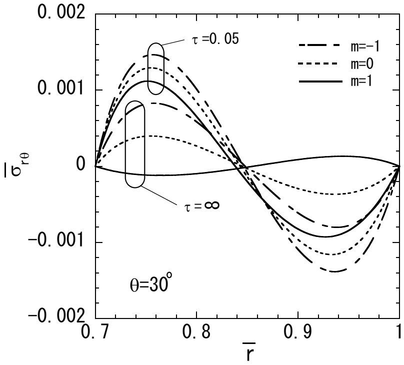

Fig. 5 Variation of electric potential in the radial direction (Case 1, $\theta = \theta_0/2$).

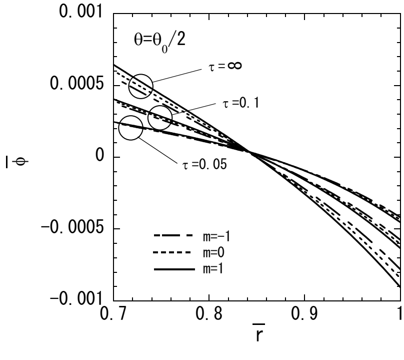

neous thermal, thermoelastic and piezoelectric properties in the radial direction. We obtained the exact solution for the temperature and piezothermoelastic response of a functionally graded thermopiezoelectric cylindrical panel with simply supported edges due to a nonuniform heat supply in the circumferential direction under the plane strain condition. We conclude that we can evaluate not only the normal stress in the radial direction and transverse shearing stress, but also the electric field in a transient state.

Fig. 6 Variation of thermal stress $\bar{\sigma}_{rr}$ in the radial direction (Case 2, $\theta = \theta_0/2$).

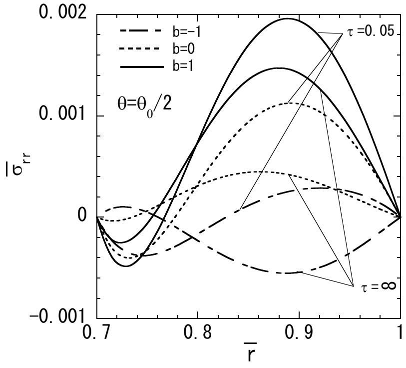

Fig. 7 Variation of thermal stress $\bar{\sigma}_{rr}$ in the radial direction (Case 3, $\theta = \theta_0/2$).

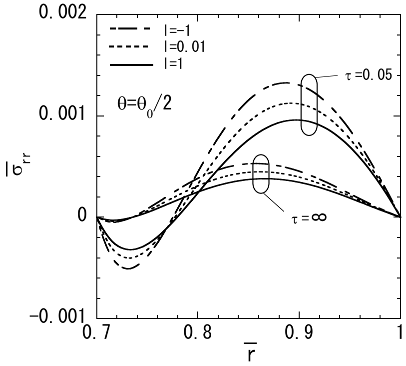

References

1. B.L. Wang, N. Noda, Design of a Smart Functionally Graded Thermopiezoelectric Composite Structures, *Smart Materials and Structures,* Vol.10, pp.189-193, 2001.
2. X.H. Wu, Y.P. Shen, C. Chen, An Exact Solution for Functionally Graded Piezothermoelastic Cylindrical Shell as Sensors or Actuator, *Material Letters,* Vol.57, pp.3532-3542, 2003.
3. C. Ying, S. Zhifei, Exact Solution of Functionally Gradient Piezothermoelastic Cantilevers and Parameter Identification, *Journal of Intelligent Material Systems and Structures,* Vol.16, pp.531-539, 2005.
4. Z. Zhong, E. Shang, Exact Analysis of Simply Supported Functionally Graded Piezothermoelectric Plates, *Journal of Intelligent Material Systems and Structures,* Vol.16, pp.643-651, 2005.
5. Y. Ootao, Y. Tanigawa, The Transient Piezothermoelastic Problem of a Thick Functionally Graded Thermopiezoelectric Strip due to Nonuniform Heat Supply, *Archive of Applied Mechanics,* Vol.74, pp.449-465, 2005.
6. Y. Ootao, Y. Tanigawa, Transient Piezothermoelastic Analysis for a Functionally Graded Thermopiezoelectric Hollow Sphere, *Composite Structures,* Vol.81, pp.540-549, 2007.
7. Y. Ootao, T. Akai, Y. Tanigawa, Transient Piezothermoelastic Analysis for a Functionally Graded Thermopiezoelectric Hollow Cylinder, *Journal of Thermal Stresses,* Vol.31, pp.935-955, 2008.

Control of an Electronic Throttle Valve for Drive-by-Wire Applications

Markus Reichhartinger, Martin Horn and Anton Hofer

Abstract Electrically actuated control devices for regulating the amount of air entering gasoline engines play an essential role in drive-by-wire applications. In this paper an approach to the control of so-called electronic throttle valves is outlined. First a standard sliding-mode controller is presented. It is shown that the performance of the feedback loop can be improved significantly by incorporating time-variable boundary layers.

1 Introduction

The continuously stringent emission and fuel economy regulation implemented by governments motivates the development of drive-by-wire systems in automobiles with combustion engines. Besides modern cars often are equipped with driver-assistance systems such as cruise control, collision warning systems or driver impairment monitoring. Many of them are based upon drive-by-wire concepts as well. A major component of these systems is the so-called electronic throttle valve which eliminates the mechanical link between the accelerator pedal and the throttle valve (see Fig. 1). In electronic

---

Markus Reichhartinger
Control and Measurement Systems Group, Institute of Smart System-Technologies, University of Klagenfurt, Universitaetsstr. 65-67, 9020 Klagenfurt, Austria, e-mail: markus.reichhartinger@uni-klu.ac.at

Martin Horn
Control and Measurement Systems Group, Institute of Smart System-Technologies, University of Klagenfurt, Universitaetsstr. 65-67, 9020 Klagenfurt, Austria, e-mail: martin.horn@uni-klu.ac.at

Anton Hofer
Institute of Automation and Control, Graz University of Technology, Kopernikusgasse 24/2, 8010 Graz, Austria, e-mail: anton.hofer@tugraz.at

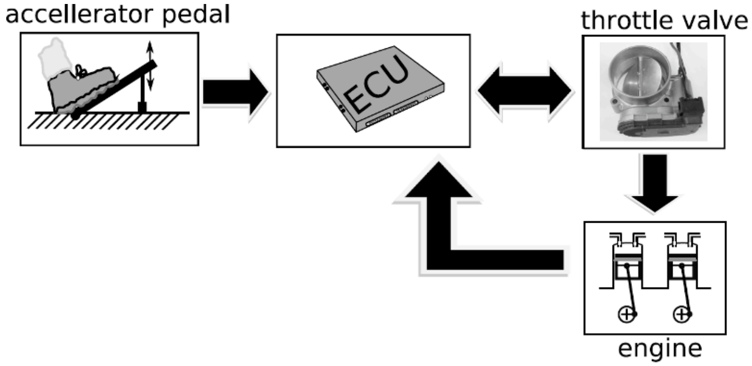

Fig. 1 Principle of a drive-by-wire system.

throttle valves the valve-plate is actuated by a dc-drive via a gear unit. A resistive position sensor measuring the opening angle φ of the valve is integrated into the gear unit. The computation of a suitable reference angle φ^* is managed by the engine control unit (ECU) which is provided with relevant engine data. In the case of an electronic failure two counteracting springs reposition the valve-plate into the so-called limp-home angle φ_0 so that an emergency operation is gururanteed.

In the recent years a number of publications has been dedicated to the modeling, simulation and control of electronic throttle valves. In [1] and [2] a detailed mathematical model of a throttle valve is presented. Experimental procedures to identify unknown model parameters are described as well. In [3] a dynamic friction model and approaches to compensate for fricition phenomena are proposed and practically demonstrated. In [4] an output feedback LQR for a throttle valve and a wastegate system is designed. Due to its undesirable high order the controller is reduced to a classical PI-structure. A control scheme consisting of two LQG based approaches is presented in [5]. A drive-by-wire throttle control in combination with a sliding-mode concept is studied in [6]. The proposed anticipatory band method is compared to conventional bang-bang and PI strategies. A classical sliding-mode technique including a full-state observer is outlined in [7], in [8] a discrete-time version of the control law can be found. In [9] the sliding-mode controller is based on a feedback linearized model of the throttle valve. The application of second order sliding-mode strategies to a throttle valve is presented in [11].

The paper is organized as follows: In Section 2 a mathematical model for the throttle valve system is presented. Section 3 outlines the principles of the proposed control strategy. Section 4 shows simulation results whereas Section 5 is dedicated to experimental findings. Section 6 concludes the work.

2 Mathematical Model

The model used in this work is sufficiently precise to describe the motion of the valve-plate [11] and serves as a basis for the controller design task. The dynamic behaviour of the opening angle φ can be modeled by the differential equation

$$\frac{d^2\,\varphi}{d\,t^2} = -f_{sp} - f_{fr} + f_{mot} \tag{1}$$

where the right-hand side functions

$$f_{sp} = c_0 + c_1\,(\varphi - \varphi_0)\,, \tag{2}$$

$$f_{fr} = k_v\,\frac{d\,\varphi}{d\,t} + k_c\,sign\left(\frac{d\,\varphi}{d\,t}\right) \qquad \text{and} \tag{3}$$

$$f_{mot} = k_m\,u - k_t\frac{d\,\varphi}{d\,t} \tag{4}$$

represent the nonlinear spring characteristic, the friction phenomena and the impact of the dc-motor respectively. The parameters c_0, c_1, k_v, k_c, k_m and k_t are positive constants. The control signal u is a pulse-width modulated signal. Note that in the model made up by equations (1), (2), (3) and (4) phenomena like static friction, gear-backlash as well as the dc-motor dynamics are neglected.

The task of the controller design is to make the opening angle φ track a reference angle φ^* which is generated by the ECU. This motivates the introduction of the tracking error ϵ_1 and its time derivative ϵ_2 as

$$\epsilon_1 := \varphi - \varphi^* \quad \text{and} \quad \epsilon_2 := \frac{d\,\epsilon_1}{d\,t}. \tag{5}$$

The representation of system (1) using the variables defined in (5) is given by the two first order differential equations

$$\begin{aligned}
\frac{d\,\epsilon_1}{d\,t} &= \epsilon_2 \\
\frac{d\,\epsilon_2}{d\,t} &= -c_0 - c_1\,(\epsilon_1 + \varphi^* - \varphi_0) - k\left(\epsilon_2 + \frac{d\,\varphi^*}{d\,t}\right) - \\
&\quad - k_c\,sign\left(\epsilon_2 + \frac{d\,\varphi^*}{d\,t}\right) - \frac{d^2\,\varphi^*}{d\,t^2} + k_m\,u,
\end{aligned} \tag{6}$$

where $k = k_v + k_t$. The parameters of model (6) can easily be identified by experiments described in [2]. The nominal values as well as the bounds of the parameters are summarized in Table 1. Due to its discontinuous right-hand side, uncertain model parameters and imperfections in modelling the control of the throttle valve system is a challenging task. A promising approach to

Table 1 Estimated plant parameters for system (6) with bounds and nominal value.

parameter	value		
	minimal	nominal	maximal
c_0	110	150	195
c_1	70	80	90
k	90	100	110
k_c	33	66	104
k_m	110	120	130
φ_0	0.095	0.095	0.095

address the control problem is the application of a variable structured control law, often referred to as sliding-mode control.

3 Control

The desired dynamic of the tracking error [12, 13] is specified by the differential equation

$$\frac{d\,\epsilon_1}{d\,t} = -\lambda\epsilon_1 \quad \text{with} \quad \lambda > 0. \tag{7}$$

The structure of model (6) motivates the choice of the so-called switching function

$$\sigma(t) := \epsilon_2 + \lambda\epsilon_1. \tag{8}$$

It is the task of the controller to steer an arbitrary initial value $\sigma_0 := \sigma(0)$ to $\sigma = 0$ within *finite* time. The stabilization of $\sigma = 0$ is solved with the help of the so-called equivalent control method [14]. Thereby it is assumed that the surface $\sigma(t) = 0$ has already been reached. To remain there the required control signal u_{eq} for system (6), parametrized with nominal plant parameters, can be calculated from

$$\frac{d\,\sigma}{d\,t} \overset{!}{=} 0. \tag{9}$$

The resulting equivalent control signal is expressed as

$$u_{eq} = \frac{1}{k_m}\left[c_0 + c_1\left(\varphi - \varphi_0\right) + k\frac{d\,\varphi}{d\,t} + k_c\, sign\left(\frac{d\,\varphi}{d\,t}\right) + \frac{d^2\,\varphi^*}{d\,t^2} - \lambda\epsilon_2\right]. \tag{10}$$

A discontinuous part u_{disc} is added to the above control law, i.e.

$$u = u_{eq} + u_{disc} = u_{eq} - \frac{\kappa}{k_m}\, sign\,(\sigma) \qquad \text{with } \kappa > 0 \tag{11}$$

to guarantee finite time convergence of σ. The parameter κ is chosen sufficiently large to reach $\sigma = 0$ even in the case of uncertain parameters. An implementation of control law (11) requires high switching frequency in the control signal u. This evokes the so-called chattering phenomenon [12]. A well known countermeasure is to approximate the discontinuity by a saturation function [15], see Fig. 2. Thereby a so-called boundary layer of width Φ is introduced around $\sigma = 0$.

Fig. 2 The discontinuous *sign*-function is approximated by a *sat*-function.

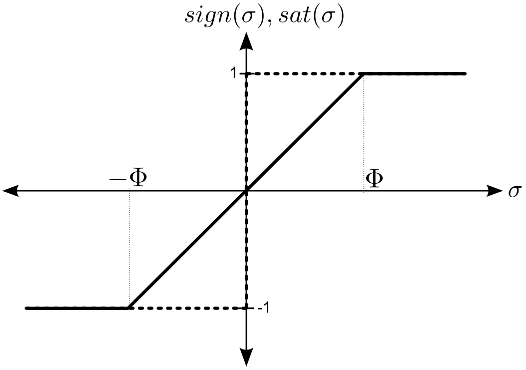

4 Numerical Simulation

The control law (11) is realized in Matlab/Simulink. The simulations are based on a detailed mathematical model, which includes gear-backlash, static friction, mechanical stops and as well the dc-motor dynamics. The simulations are carried out with the reference signal φ^* shown in Fig. 3. The reference signal covers almost the whole range of operation and comprises angles above and below the limp home angle φ_0. Also high angular velocities and discontinuities are covered. The initial controller parameters satisfying sufficient conditions for robust stability [13] were tuned online. A simulation result for the parameters $\kappa = 600$, $\lambda = 55$ and $\Phi = 0.3$ is depicted in Fig. 4. The feedback loop shows excellent steady state behaviour. The absolute value of the tracking error remains below 1° during the entire simulation which is very satisfactory. At time instants of high angular velocities in the reference signal the control signal contains undesired high frequency components which induce mechanical vibrations. The challenge of the experimental parameter tuning is to obtain a closed loop behaviour with satisfactory tracking performance and a chatter-free control signal u.

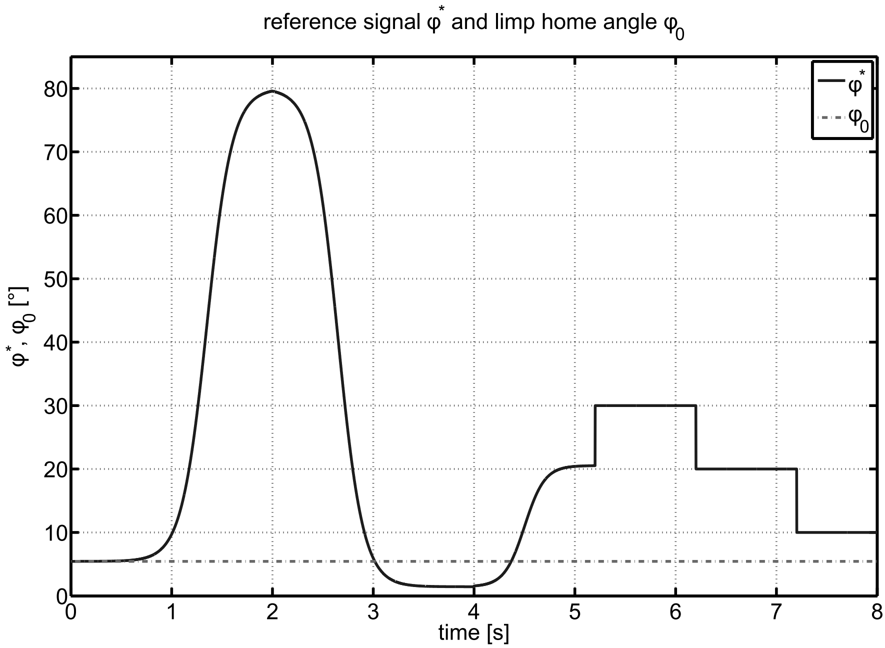

Fig. 3 The reference signal φ^* consists of a smooth and a non-smooth part.

5 Experiment

The experimental hardware consists of a dSpace Microautobox, a H-Bridge power amplification circuit and the electronic throttle valve system. The present control law is executed with a sampling time of $T_s = 1ms$. The implementation of control law (11) is straight forward. The second time derivative of the reference signal φ^* is computed with the help of a DT_2-element. Fig. 5 shows experimental results achieved with controller parameters obtained from simulation. Solely the width Φ of the boundary layer was modified to $\Phi = 0.5$. The feedback loop shows satisfactory tracking performance. The control signal u reveals the undesired chattering-effect. A way to minimize the chattering-effect is to increase the width of the boundary layer. In Fig. 6 results for $\Phi = 1.5$ are depicted. The control signal u shows a negligible chattering-effect at the cost of an unacceptable steady state error. These results motivate the choice of a time varying boundary layer [15]. As observed, the chattering-effect is proportional to the angular velocity of the valve-plate. This fact suggests the choice [10]

$$\Phi = \Phi_0 + \left|\frac{d\varphi}{dt}\right| \quad \text{with} \quad \Phi_0 > 0 \tag{12}$$

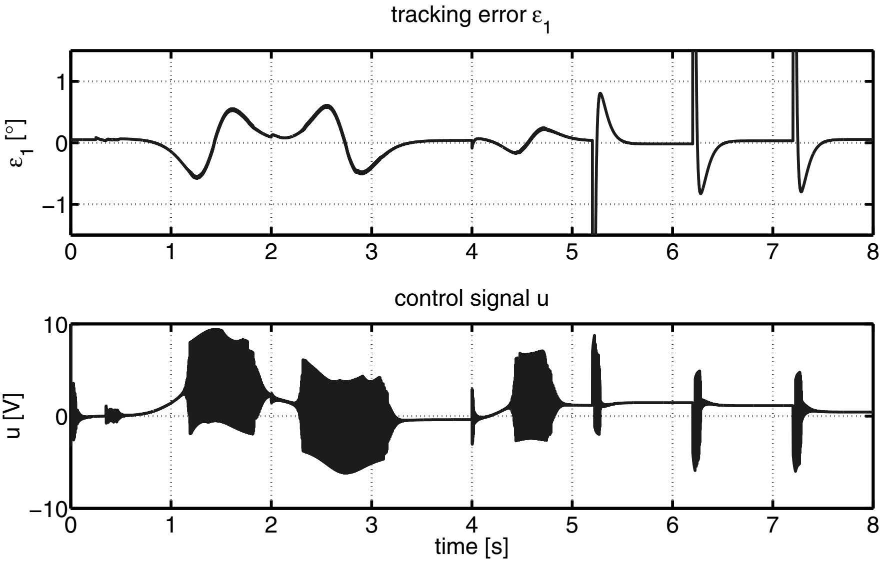

Fig. 4 Simulation results for $\kappa = 600$, $\lambda = 55$ and $\Phi = 0.3$.

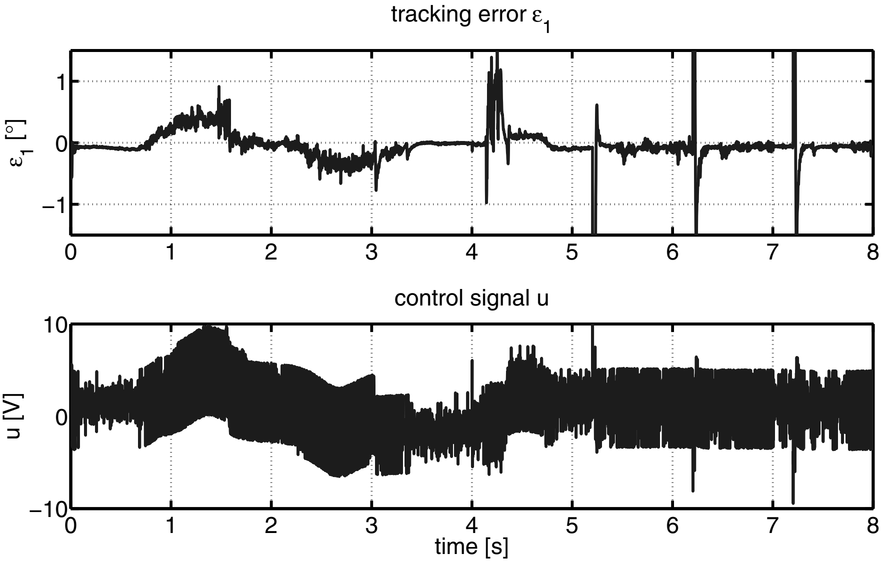

Fig. 5 Experiment: Constant boundary layer width of $\Phi = 0.5$.

for the boundary layer. As a consequence of the above definition the conditions for robust stability have to be adapted appropriately [15]. Results of an experiment with $\Phi_0 = 0.3$ are plottet in Fig. 7. The steady state behaviour is excellent and the chattering-effect in the control signal u is sufficently

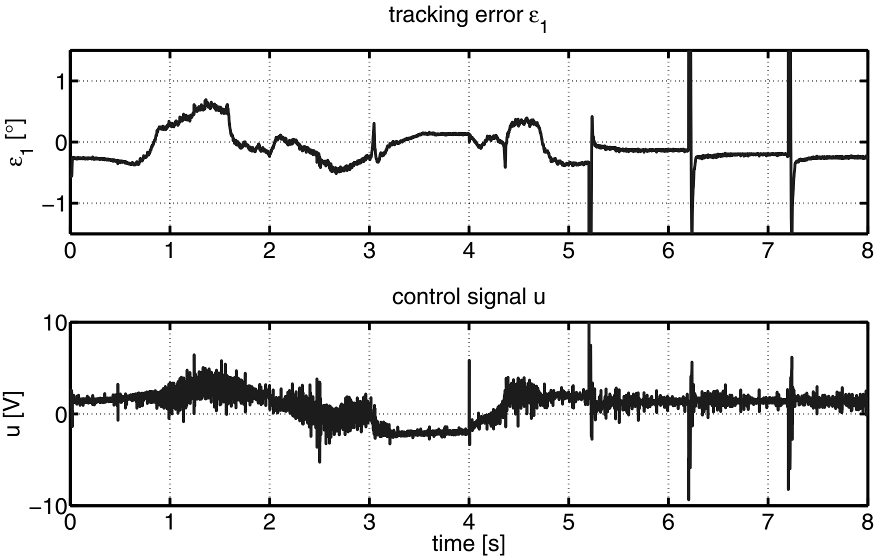

Fig. 6 Experiment: Constant boundary layer width of $\Phi = 1.5$.

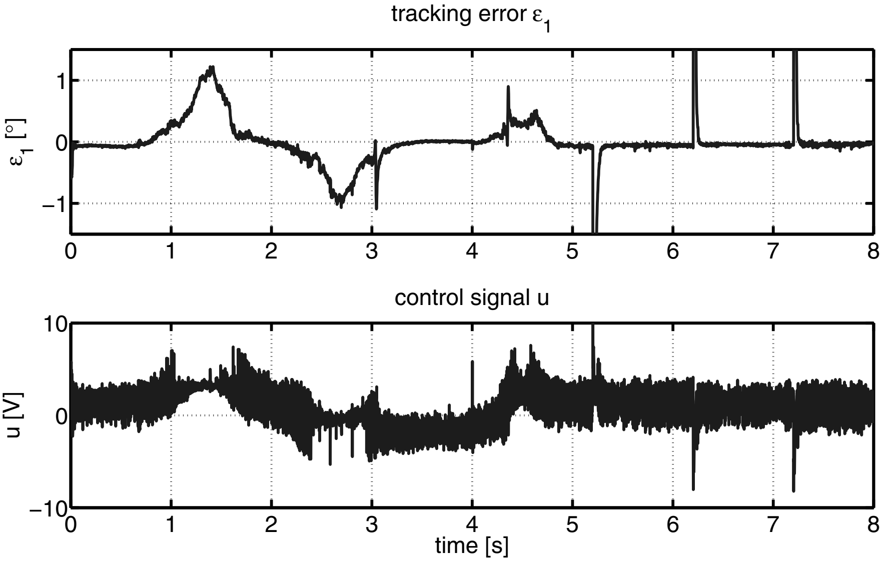

Fig. 7 Experiment: time varying boundary-layer

reduced. The corresponding width Φ of the boundary layer during the experiment is outlined in Fig. 8.

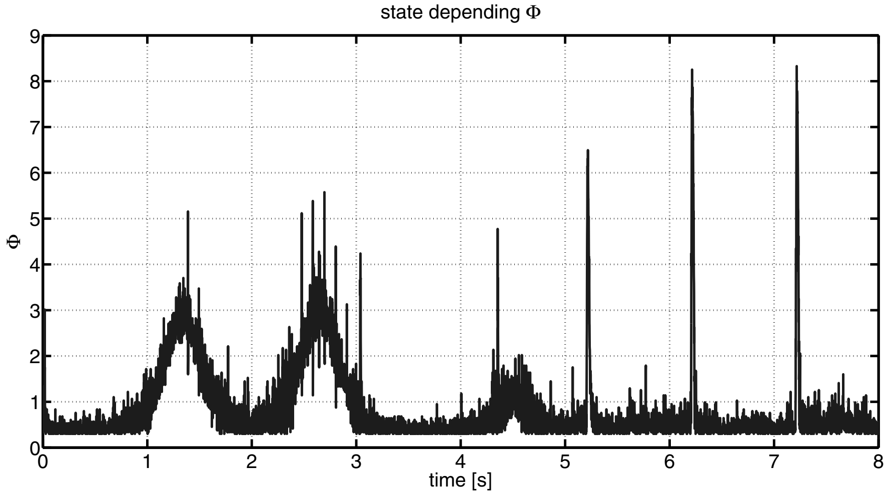

Fig. 8 The thickness of the boundary-layer is varying during the experiment.

6 Conclusion

The scope of the paper is the evolution of a control strategy for electronic throttle valves based on the concepts of variable structure systems. Based upon a standard sliding-mode controller an improved strategy is derived by employing time-variable boundary layers. It is demonstrated that the resulting feedback loop shows excellent tracking performance in simulation and experiment. The implementation of the control law is straight forward and hence suitable for a realization in the engine control unit.

References

1. Scattolini, R. and Sivierob, C. and Mazzuccoa, M. and Riccia, S. and Poggiob, L. and C. Rossi: Modeling and identification of an electromechanical internal combustion engine throttle body. Control Engineering Practice 5, 1253-1259, 1997.
2. Pavković, D. and Deur, J. and Jansz, M. and Perić, N.: Experimental Identification of an Electronic Throttle Body. Proceedings of 10th European Conference on Power Electronics and Applications, 2003.
3. Deur, J. and Pavković, D. and Perić, N. and Jansz, M. and Hrovat, D.: An Electronic Throttle Control Strategy Including Compensation of Friction and Limp-Home Effects. IEEE Transactions on Industry Applications 40, 821-834, 2004.
4. Yigeng Huangfu and Weiguo Liu and Ruiqing Ma: Permanent magnet synchronous motor fault detection and isolation using second order sliding mode observer. Proc. 3rd IEEE Conference on Industrial Electronics and Applications ICIEA 2008, 639.644, 2008.

5. A. Kitahara and A. Sato and M. Hoshino and N. Kurihara and S. Shin: LQG Based Electronic Throttle Control with a Two Degree of Freedom Structure. Conference on Decision and Control, 1996.
6. B. Lee and Y. Kim and D. Cho: Engine Throttle Control Using Anticipatory Band in the Sliding Phase Plane. IEEE Transactions on Control Systems Technology 1, 280-284, 1933.
7. Pan, Y. and Ozguner, U. and Dagci, O. H.: Variable-Structure Control of Electronic Throttle Valve. IEEE Transactions on Industrial Electronics, 55(11), 3899-3907, 2008.
8. Ozguner, U. and Hong, Sulgi and Pan, Yaodong: Discrete-time sliding mode control of electronic throttle valve. Proc. 40th IEEE Conference on Decision and Control, Vol.2, 1819-1824, 2001.
9. Dagzi, O. and Pan, Y. and Ozguner, U.: Sliding Mode Control of Electronic Throttle Valve. Proceedings of the American Control Conference, 1996-2001, 2002.
10. Horn, M. and Reichhartinger, M.: Sliding-Mode Regelung von elektrischen Drosselklappen. International Journal Automation Austria, Vol. 2, 83-96, 2008.
11. Horn, M. and Reichhartinger, M.: Second-order sliding mode control of electronic throttle valves. Proc. International Workshop on Variable Structure Systems VSS '08, 280-284, 2008.
12. V. I. Utkin: Sliding Modes in Control and Optimization. Springer 1992.
13. Edwards, C. and Spurgeon, S. K.: Sliding Mode Control, Theory and Applications. Taylor and Francis Ltd. 1998.
14. Utkin, V. and Guldner, J. and J. Shi: Sliding Mode Control in Electromechanical Systems. Taylor and Francis Ltd. 1999.
15. Slotine, J. and Li, W.: Applied Nonlinear Control. Prentice Hall 1991.

Output Regulation of Smart Structures, Theory and Practice

Thomas Rittenschober and Kurt Schlacher

Abstract Self sensing and actuation of piezoelectric devices make it possible to give mechanical structures new features. Under the assumption of linear piezoelasticity and Kirchhoff plate theory a mathematical model is derived, which is used for the controller design such that harmonic disturbance with either known or unknown disturbance frequency are asymptotically eliminated. Both simulations and laboratory experiments show the performance of the proposed approach.

1 Introduction

Self sensing actuation of function materials enables the collocation of actuator and sensor in a natural manner. But in the case of piezoelectric actuators, self sensing requires a robust separation of the time derivative of the applied voltage from the measured electric current in order to obtain a signal which is proportional to the curvature rate integrated over the piezoelectric patch area. Because of the unfavorable ratio of these two signals, the design of an observer for the electric current due to the direct piezoelectric effect seems most appropriate. But the design of observers relies on accurate modelling of the underlying piezoelastic structure which in our case is chosen to be a rectangular plate equipped with two piezoelectric actuators and two opposite edges either clamped or free. The special mathematical structure of the model facilitates controller synthesis which is shown for the case of har-

---

Thomas Rittenschober
Profactor Production Research Steyr, Austria, e-mail: thomas.rittenschober@profactor.at

Kurt Schlacher
Institute of Automatic Control and Control Systems Technology, Johannes Kepler University Linz, Austria, e-mail: kurt.schlacher@jku.at

monic disturbance suppression with either known or unknown disturbance frequency.

2 The Mathematical Model

The plate structure under investigation along with its geometric properties is depicted in Figure 1. Geometric parameters and material properties are given by $a = 0.45m$, $b = 0.35m$, $c = 0.1m$, $d = 0.1525m$, $e = 0.045m$, $f = 0.01m$, h_b (thickness of plate) $= 0.001m$, h_p (thickness of patch) $= 0.001m$, $k = 0.05m$, $l = 0.55m$, ρ (mass density of plate) $= 7500kg/m^3$, E_b (Young's modulus plate)$= 2 \cdot 10^{11} N/m^2$, E_p (Young's modulus patch)$= 6 \cdot 10^{10} N/m^2$, ν_b (Poisson's ratio of plate) $= 0.33$, ν_p (Poisson's ratio of patch) $= 0.25$, G^{113} (piezoel. coupling const.) $= 6.62 C/m^2$ and F^{33} (relative permittivity) $=$ 1.21e-8F/m.

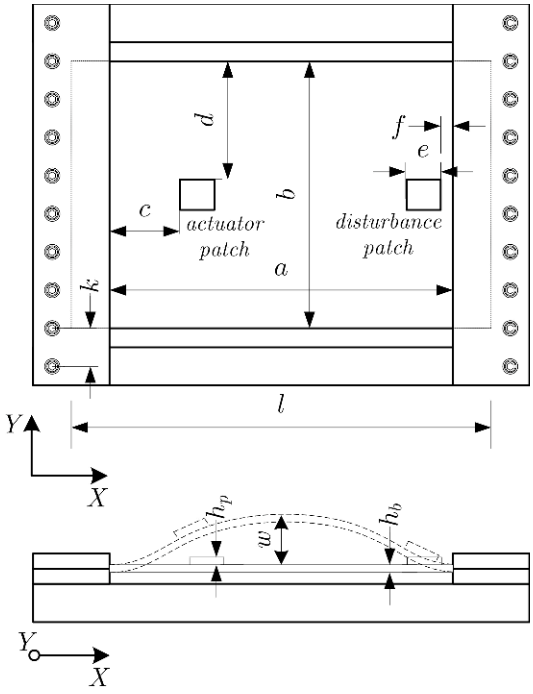

Fig. 1 Geometric configuration of the piezoelastic structure.

Under the assumption of linearized piezoelasticity and the strain displacement relations as introduced by Kirchhoff, the piezoelastic plate-like structure under consideration can be modelled according to the partial differential equation, see [1],

$$\mu\tfrac{\partial^2}{\partial t^2}w + \bar{D}\left(\tfrac{\partial^4}{\partial X^4} + \tfrac{2\partial^4}{\partial X^2\partial Y^2} + \tfrac{\partial^4}{\partial Y^4}\right)(w) \\ = cU\left(\tfrac{\partial^2}{\partial X^2} + \tfrac{\partial^2}{\partial Y^2}\right)(\lambda) - Bd \qquad (1)$$

where the coordinate t represents time, X, Y, Z are local coordinates for the body $\mathcal{B} \subseteq \mathbb{R}^3$, $w = w(t, X, Y)$ is the transverse displacement of the plate's neutral fibre, $\mu = \rho h_b$ is the mass area density of the respective material, $\bar{D}$ is the flexural rigidity of the plate and computes as $\bar{D} = E_b h_b^3 / \left(12\left(1 - \nu_b^2\right)\right)$. We denote by E_b and h_b Young's modulus and the thickness of the support structure, respectively, and ν_b is Poisson's ratio. The associated material and geometric properties of the piezoelectric layer are denoted by a subscript p. Assuming a typical property of transversely isotropic piezoelectric material that the coupling constants G^{113} and G^{223} appearing in the constitutive equations [5]

$$\sigma = C\varepsilon - GE, \\ D = G\varepsilon + FE \qquad (2)$$

are identical, the constant c then computes as $c = G^{113}h_p(h_p + 2h)/4$ and, hence, incorporates piezoelectric and geometric properties. The constant h describes the distance between the neutral fibre and the interface between the piezoelectric layer and the support structure. We denote by σ, ε, C, F, G, E and D in (2) the stress, strain, elasticity, relative permittivity, coupling, electric field and electric flux density tensors, respectively. $U = U(t)$ is the electric potential at the upper electrode of the piezoelectric layer, the shape function $\lambda = \lambda(X, Y)$ describes the weighted spatial distribution of the electric potential U at the upper electrode and $B = B(X, Y)$ is the spatial distribution of the body force acting on the structure. The tensorial components appearing in the constitutive equations (2) are, in general, functions of the spatial coordinates and will be set piecewise constant in our case.

The solution technique applied to the partial differential equation from (1) under the appropriate kinematic and dynamic boundary and initial conditions makes use of separation of variables, i.e. $w(t, X, Y) = \sum_{i=1}^{\infty}\sum_{j=1}^{\infty} q_{ij}(t)\,\phi_{ij}(X, Y)$, the orthogonality property of the eigenfunctions ϕ_{ij} and the Laplace transform. The transfer functions of the system $G_a\left(s, X^1, X^2\right)$ due to piezoelectric actuation may be then written as

$$G_a(s, X, Y) = \frac{\hat{w}(s, X, Y)}{\hat{U}(s)} \\ = \sum_{i=1}^{\infty}\sum_{j=1}^{\infty} \phi_{ij} P_{a,ij} \frac{1}{\frac{s^2}{\omega_{ij}^2} + 1} \qquad (3)$$

with

$$P_{a,ij} = \frac{c}{\omega_{ij}^2} \int_{\mathcal{D}} \phi_{ij} \left(\frac{\partial^2}{\partial X^2} + \frac{\partial^2}{\partial Y^2} \right) (\lambda) \, \Omega$$

where $\mathcal{D}$ denotes the corresponding domain of integration, $\Omega = \mathrm{d}X \mathrm{d}Y$ is the corresponding volume form and $P_{a,ij}$ are the modal gains of mode ij of the transfer function due to piezoelectric actuation. The natural frequencies ω_{ij} for the C-F-C-F configuration are computed according to [4].

Considering the linear constitutive relations from (2), respecting conservation of charge and Kirchhoff's assumptions on the relations of strain and displacement and $G^{123} = G^{213} = 0$, we get $D^3 = -G^{113} Z \frac{\partial^2}{\partial X^2} w - G^{223} Z \frac{\partial^2}{\partial Y^2} w + F^{33} E_3$. Accounting for $G^{113} = G^{223}$, the charge Q at the electrode of the piezoelectric actuator computes as

$$\begin{aligned} Q &= \int_{\mathcal{D}} D^3 \Omega \\ &= \frac{F^{33} e^2}{h_p} U - \frac{1}{2} G^{113} \left(2h + h_p \right) \int_{\mathcal{D}} \left(\frac{\partial^2}{\partial X^2} + \frac{\partial^2}{\partial Y^2} \right) (w) \, \Omega \; . \end{aligned}$$

The constant $C_p = F^{33} e^2 / h_p$ is the capacitance of the piezoelectric patch which in our case is 24.5 nF according to the given geometric and material parameters.

Alternatively, if the electric current $I = I_{indirect} + I_{direct} = \frac{\mathrm{d}}{\mathrm{d}t} Q$, i.e.

$$I = \underbrace{\frac{F^{33} e^2}{h_p} \frac{\mathrm{d}}{\mathrm{d}t} U}_{indirect\ part} - \underbrace{\frac{1}{2} G^{113} \left(2h + h_p \right) \int_{\mathcal{D}} \left(\frac{\partial^3}{\partial t \partial X^2} + \frac{\partial^3}{\partial t \partial Y^2} \right) (w) \, \Omega}_{direct\ part}$$

is at our disposal, we only need to robustly separate the time derivative of actuation voltage from it in order to obtain a signal which is proportional to the curvature rate integrated over the patch area. Due to the unfavorable ratio of these two signals, the design of an observer for the direct part of the electric current seems most appropriate. The corresponding transfer function of such a model is given by

$$\begin{aligned} \bar{G}_a (s) &= \frac{\hat{I} (s)}{\hat{U} (s)} \\ &= \frac{C_p s}{\frac{s^2}{\omega_C^2} + 2\xi_C \frac{s}{\omega_C} + 1} + \sum_{i=1}^{\infty} \sum_{j=1}^{\infty} \frac{2 h_p P_{a,ij}^2 s}{\frac{s^2}{\omega_{ij}^2} + 2\xi_{ij} \frac{s}{\omega_{ij}} + 1} \; . \end{aligned} \tag{4}$$

where we assume proportional damping of the system and take losses and inductance of the patch into account. The PCHD representation of (4) is presented in [6].

In equation (4), we have extended the dynamics due to the indirect piezoelectric effect by taking resistance R_p and inductance L_p of the piezoelectric patch into account, where $\omega_C = 1/\sqrt{L_p C_p}$, $\xi_C = \frac{1}{2} R_p \sqrt{C_p/L_p}$. The transfer function (4), hence, describes the indirect and direct piezoelectric effect by means of a parallel connection of an RLC oscillator and an infinite series of damped spring mass oscillators, respectively.

3 Control Design for Harmonic Disturbance Suppression

A preliminary step in designing a feedback controller for vibration suppression requires the estimation of the current due to the direct piezoelectric effect denoted by $\hat{e} \in \mathbb{R}$. Since the system (4) is infinite dimensional, one cannot construct a realizable observer for (4), but one can construct a finite dimensional approximation [6]. We close the loop with controller, which injects damping, for the robust suppression of harmonic vibrations where the underlying theory is described in [3] and [6].

The proposed controller for the robust suppression of harmonic vibrations exhibits the structure

$$\begin{aligned} \dot{\xi}_1 &= \Phi \xi_1 + \Theta \hat{e}, \\ u_1 &= \Gamma \xi_1 + u_2 \end{aligned} \tag{5}$$

and the memoryless stabilizer

$$\begin{aligned} u_2 &= K_2 \hat{e}, \\ K_2 &> 0. \end{aligned} \tag{6}$$

with the state $\xi_1 \in \mathbb{R}^2$, $\Phi \in \mathbb{R}^{2\times 2}$, $\Theta_1 \in \mathbb{R}^{2\times 1}$, $\Gamma \in \mathbb{R}^{1\times 2}$, the controller outputs $u_1, u_2 \in \mathbb{R}$ and

$$\Phi = \begin{pmatrix} 0 & 1 \\ -\omega_d^2 & 0 \end{pmatrix}, \; \Theta_1 = \begin{pmatrix} 0 \\ K \end{pmatrix}, \; \Gamma = \begin{pmatrix} 0 & 1 \end{pmatrix}, \tag{7}$$

The controller is driven by the observed direct part of the electric current $\hat{e}$.

Remark 1. As far as the proof of stability is concerned, it is required to show that the finite dimensional closed loop system is stable in the context of finite gain $\mathcal{L}_2$ stability and exponential stability of the origin using a passivity based approach, see [2]. The proof, that the regulated variable $\hat{e}$ tends to zero as time goes to infinity in the presence of a harmonic disturbance with a known frequency, involves a change of coordinates and the unique solution of a Sylvester equation, see [3]. The infinite dimensional part of the plant to be controlled is subsequently treated as an additive plant uncertainty and we can hence apply the small gain theorem in order to show that the trajectories of the infinite dimensional closed loop system are bounded in the context of finite gain $\mathcal{L}$ stability, see [2].

If the disturbance frequency is unknown, we may be well advised to extend the proposed controller (5) by some sort of adaptive control. In fact, the update law

$$\dot{\varepsilon} = -\gamma_3 \hat{e} \xi_1^1, \ \gamma_3 > 0$$

ensures that $\lim_{t\to\infty} \hat{e}\,(t) = 0$ where $\varepsilon = \hat{\omega}_d^2 - \omega_d^2$ denotes the difference between the squared estimated and actual disturbance frequency.

Remark 2. The corresponding proof of stability requires changes of coordinates and a Lyapunov stability argument, see [3]. We, thus, ensure that the invariant subspace on which the regulated variable $\hat{e}$ is zero is attractive in the presence of the harmonic disturbance with unknown frequency. The application of the small gain theorem in conjunction with the Hamilton-Jacobi inequality ensures stability of the infinite dimensional closed loop system in the context of finite gain $\mathcal{L}$ stability, see [2].

4 Measurement Results

The actual implementation of the proposed observer and control algorithms are carried out on dSpace RTI 1104 rapid prototyping hardware. The power amplification for the piezoelectric patches is supplied by a Trek PZD 350 dual channel piezo driver which is equipped with a current monitor. The piezoelectric actuator at the boundary injects a harmonic disturbance at $\omega_d = 2\pi 259\ rad/s$. The corresponding sensor and control signals are shown

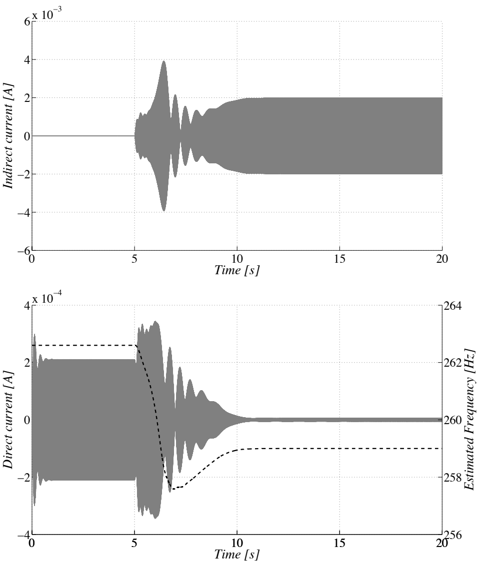

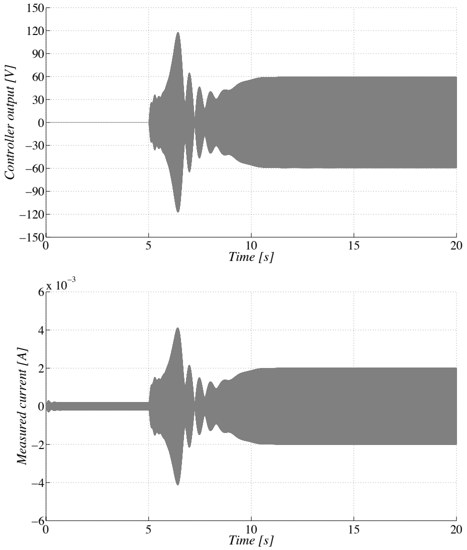

Fig. 2 Time signals for direct part of the measured current, indirect part of measured current, controller output, actually measured current and estimated disturbance frequency when plate structure is excited at $\omega_d = 2\pi 259 \ rad/s$ with frequency estimator initialized at $\omega_d\,(0) = 2\pi 262.6 \ rad/s$.

and in figure 2 with control switched on after five seconds. The update law is initialized with a value of $\omega_d\,(0) = 2\pi 262.6 \ rad/s$ and the estimated frequency progressively converges to the actual disturbance frequency of $2\pi 259 \ rad/s$.

5 Summary

This contribution was concerned with compensation of harmonic vibrations in mechanical structures using the self sensing capability of piezoelectric actuators. The special mathematical structure of the underlying piezoelastic structure facilitates controller synthesis for harmonic disturbance suppression with either known or unknown disturbance frequency.

References

1. C.R. Fuller, S.J. Elliott, P.A. Nelson: Active Control of Vibration, Academic Press, 1993, London.
2. H.K. Khalil: Nonlinear Systems, Prentice Hall Inc., 1996, New Jersey.

3. A. Isidori, L. Marconi, A. Serrani: Robust Autonomous Guidance - an Internal Model Approach, Springer, 2003, London.
4. A.W. Leissa: Vibration of Plates, Scientific and Technical Information Division, National Aeronautics and Space Administration, 1969, Washington D.C.
5. W. Nowacki: Dynamic Problems of Thermoelasticity, Noordhoff International Publishing, 1975, Amsterdam.
6. K. Schlacher, M. Schöberl, T. Rittenschober: Model Based Control of Structures and Machines, a dissipative and internal model based approach, Proc. of the 4^{th} European Conference on Structural Control, St. Petersburg, 2008.

Analysis of Weld Induced Plasticity by BFM

Akihide Saimoto

Abstract A method of analysis for the occurrence of localized thermoplastic strain, in a material under plane strain constraint, is studied based on the Body Force Method (BFM). BFM is an indirect boundary type method for elastic stress analysis based on the principle of superposition. Any inelastic strain can be expressed by the embedded force doublets in BFM. That is, in the analysis, a continuously embedded force doublets into the elastic body are used to express the presence of plastic strain. A simplified model of welding-induced plasticity is treated as a numerical example of the present method.

1 Introduction

In order to evaluate a degree of plastic deformation and residual stresses in the body, employment of the commercial finite element code that examines automated elastic-plastic calculation becomes very popular in recent years. The use of commercial code, however, often brings ineffectiveness from the view point of computational efficiency since most of mechanical and structural components are designed for elastic use, and therefore, the size of the plastic zones, even if they may happen due to the localized stress concentration, would be considerably small or restricted. In order to treat problems including limited plasticity efficiently, Blomerus and Hills proposed a dislocation based technique[1]. In their method, edge dislocations which correspond to the occurrence of plastic flow are introduced into the direction of maximum shear. The magnitude of the Burgers vector at the each dislocation point where the plastic flow occurred are determined through the iterative procedure considering the yield criterion. Since the magnitude of Burgers vector

---

Akihide Saimoto
Department of Mechanical Systems Engineering, Faculty of Engineering, Nagasaki University, 1-14 Bunkyo-machi, Nagasaki 8528521, Japan, e-mail: s-aki@nagasaki-u.ac.jp

at each material point can be determined incrementally, the stress redistribution due to the occurrence of yielding can be simulated reasonably. On the other hand, the dislocation approach sometimes exhibits a convergence problem in which the direction of maximum shear stress varied frequently due to the fluctuation of the magnitude of Burgers vector at each material point.

Chen and Nisitani proposed the other approach to treat the limited plasticity based on the BFM. They employed a force doublet embedded in an elastic continuum in order to express the inelastic strain[2, 3]. Although their method is useful for wide range of limited plasticity, it seems difficult to apply the method to special class of plane strain problems in which the plastic strain in the thickness direction becomes the major component. Since its development in 1967, the BFM has been applied for elastic problems of practical importance. The original BFM is a boundary type method for elastic stress analysis, whose base is the principle of superposition. That is, in BFM any elastic problem is expressed in terms of the superposition of fundamental stress fields. As the fundamental solution, stress field due to an isolated point force acting in an infinite elastic body (usually referred as *Kelvin solution*) is preferably employed due to its simplicity. In fact, based on the principle of the BFM, stress components at an arbitrary point P, $\sigma_{ij}(P)$, in an elastic medium can be written as,

$$\sigma_{ij}(P) = \sigma^{0}_{ij}(P) + \int_{\mathit{\Gamma}} \phi^{k}(Q)\sigma^{k}_{ij}(P,Q)d\mathit{\Gamma}(Q), \tag{1}$$

where $P \in R$ is an arbitrary point in the reference region R which is surrounded by the imaginary boundary $\mathit{\Gamma}$. $Q \in \mathit{\Gamma}$ is a source point which moves along $\mathit{\Gamma}$. $\sigma^{k}_{ij}(P,Q)$ is a fundamental stress solution (stress component σ_{ij} at point P caused by a unit magnitude of point force acting into k_{th}-direction at source point Q) and $\phi^{k}(Q)$ is a density function of the body force which has to be determined so that the given boundary conditions are satisfied.

As discussed in [2, 3], the plastic strain at a point can be replaced by an equivalent force doublet embedded in an perfect elastic solid whose yield stress is infinite. So far, numerical solutions of elastic-plastic problems solved by BFM have been limited to two-dimensional where the plastic strain in the out-of-plain direction can be ignored or almost no influence. However, there exist some important class of problems in which the presence of the out-of-plane plastic strain has to be carefully treated even under the two-dimensional situation. In the present study, the treatment of out-of-plane plastic strain by two-dimensional BFM is discussed in detail. Then the weld-induced plasticity problem is discussed under the assumption that the material is an elastic-perfect-plastic body that obeys Von Mises yield criterion.

2 Solution of Two-Dimensional Elastic Problem by BFM

Before going to further, it would be useful to remind how pure elastic problem is solved by BFM briefly. Consider an infinite sheet with a circular hole of diameter $2a$, subjected to external tensile stresses as illustrated in Fig.1. In this example, the reference region R is an infinite plate excluding the circular disk, therefore, the imaginary boundary Γ is a circular ring of diameter $2a$. The stress component at point P can then be expressed according to Eq.(1) as,

$$\sigma_{xx}(P) = \sigma_{xx}^0 + \int_\Gamma \{\phi^x(Q)\sigma_{xx}^x(P,Q) + \phi^y(Q)\sigma_{xx}^y(P,Q)\}d\Gamma(Q), \tag{2}$$

$$\sigma_{yy}(P) = \sigma_{yy}^0 + \int_\Gamma \{\phi^x(Q)\sigma_{yy}^x(P,Q) + \phi^y(Q)\sigma_{yy}^y(P,Q)\}d\Gamma(Q), \tag{3}$$

$$\sigma_{xy}(P) = \int_\Gamma \{\phi^x(Q)\sigma_{xy}^x(P,Q) + \phi^y(Q)\sigma_{xy}^y(P,Q)\}d\Gamma(Q) \tag{4}$$

in which $\sigma_{ij}^x(P,Q)$ and $\sigma_{ij}^y(P,Q)$ are stress component at reference point $P(x,y)$ due to a unit magnitude of point force acting in the x and y direction at source point $Q(\xi,\eta)$, in an infinite sheet without any hole. σ_{xx}^0 and σ_{yy}^0 are the uniform tensile stresses at infinity. $\phi^x(Q)$ and $\phi^y(Q)$ are the unknown densities of body forces which define the magnitude of body forces at point Q per unit length of an imaginary boundary as,

$$dF_x(Q) = \phi^x(Q)d\Gamma,\ dF_y(Q) = \phi^y(Q)d\Gamma. \tag{5}$$

In numerical analysis, the imaginary boundary Γ is divided into several segments and the density of body forces at each segment is assumed to be constant, linear or quadrateral function of the local coordinates as in a same manner in boundary element methods. That is, the unknown densities of body forces are determined through boundary condition defined from the limiting procedure that the reference point $P \in R$ is approached to the boundary point P^Γ from inside of the region R. When the problem is rather simple,

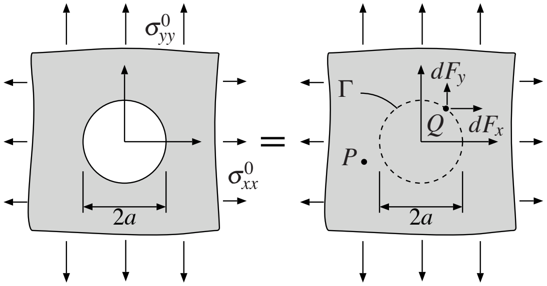

Fig. 1 Analysis of an elastic sheet having a circular hole of diameter $2a$, subjected to external tensile stresses σ_{xx}^0 and σ_{yy}^0 at infinity

the unknown density of body forces have closed form solution and can be determined theoretically. In fact, the situation illustrated in Fig.1 is one of a such case.

It is well known that two-dimensional elasticity problem can be expressed in terms of two complex potentials $\Omega(z)$ and $\omega(z)$ such that,

$$\sigma_{xx} + \sigma_{yy} = 2\big\{\Omega'(z) + \overline{\Omega'(z)}\big\}, \tag{6}$$

$$\sigma_{yy} - \sigma_{xx} + 2i\sigma_{xy} = 2\big\{\overline{z}\Omega''(z) + \omega'(z)\big\} \tag{7}$$

where z is a complex variable that represents the reference point $z = x + iy$. The Kelvin solution (stress field due to a point force of magnitudes F_x and F_y acting at a point $\zeta = \xi + i\eta$ in an infinite elastic sheet) can be expressed in the form of complex potentials as,

$$\Omega(z) = -\frac{F_x + iF_y}{2\pi(\kappa+1)} \log(z-\zeta), \tag{8}$$

$$\omega(z) = \frac{\kappa(F_x - iF_y)}{2\pi(\kappa+1)} \log(z-\zeta) + \frac{F_x + iF_y}{2\pi(\kappa+1)} \frac{\overline{\zeta}}{z-\zeta}, \tag{9}$$

where κ is a constant relating to Poisson's ratio ν as $\kappa = (3-\nu)/(1+\nu)$ for plane stress and $\kappa = 3 - 4\nu$ for plane strain. i is an imaginary unit and the over-bar denotes the complex conjugate. Using the complex potentials, the elastic fields of Fig.1 can be expressed as,

$$\Omega(z) = \frac{\sigma^0_{xx} + \sigma^0_{yy}}{4} z - \frac{1}{2\pi(\kappa+1)} \oint_\Gamma \log(z - ae^{i\theta})\{\phi^x(\theta) + i\phi^y(\theta)\} a d\theta, \tag{10}$$

$$\begin{aligned} \omega(z) = {} & \frac{\sigma^0_{yy} - \sigma^0_{xx}}{2} z + \frac{\kappa}{2\pi(\kappa+1)} \oint_\Gamma \log(z - ae^{i\theta})\{\phi^x(\theta) - i\phi^y(\theta)\} a d\theta \\ & + \frac{1}{2\pi(\kappa+1)} \oint_\Gamma \frac{ae^{-i\theta}}{z - ae^{i\theta}}\{\phi^x(\theta) + i\phi^y(\theta)\} a d\theta, \end{aligned} \tag{11}$$

since the source point ζ is on the circle of radius a which can be expressed as $\zeta = ae^{i\theta}$. The density functions $\phi^x(\theta)$ and $\phi^y(\theta)$ have closed form solution;

$$\phi^x(\theta) = \underbrace{\frac{\kappa+1}{2(\kappa-1)} \big\{\kappa\sigma^0_{xx} - (\kappa-2)\sigma^0_{yy}\big\}}_{=\rho_x = const.} = \rho_x \cos\theta, \tag{12}$$

$$\phi^y(\theta) = \underbrace{\frac{\kappa+1}{2(\kappa-1)} \big\{\kappa\sigma^0_{yy} - (\kappa-2)\sigma^0_{xx}\big\}}_{=\rho_y = const.} = \rho_y \sin\theta. \tag{13}$$

In fact, substituting Eqs.(12), (13) into Eqs.(10), (11) and by examining the contour integral considering $|z| > a$ using the Cauchy's integral theorem, the exact expressions of complex potentials for Fig.1 are obtained as,

$$\Omega(z) = \frac{\sigma_{xx}^0 + \sigma_{yy}^0}{4} z + \frac{\sigma_{xx}^0 - \sigma_{yy}^0}{2} \frac{a^2}{z}, \tag{14}$$

$$\omega(z) = \frac{\sigma_{yy}^0 - \sigma_{xx}^0}{2} z - \frac{\sigma_{xx}^0 + \sigma_{yy}^0}{2} \frac{a^2}{z} + \frac{\sigma_{xx}^0 - \sigma_{yy}^0}{2} \frac{a^4}{z^3}. \tag{15}$$

It is readily found that the density functions of the body force in Eqs.(12) and (13) are given by the product of some constant and the components of unit normal $(\cos\theta, \sin\theta)$ at a point Q on the imaginary boundary Γ. Therefore, the expression of boundary integral in Eqs.(10) and (11) can be transformed into a form of area integral by using the Green's theorem as,

$$\Omega(z) = \frac{\sigma_{xx}^0 + \sigma_{yy}^0}{4} z + \frac{1}{2\pi(\kappa+1)} \iint_{\overline{R}} \frac{\rho_x - \rho_y}{z - \zeta} d\xi d\eta, \tag{16}$$

$$\begin{aligned} \omega(z) = {} & \frac{\sigma_{yy}^0 - \sigma_{xx}^0}{2} z - \frac{\kappa - 1}{2\pi(\kappa+1)} \iint_{\overline{R}} \frac{\rho_x + \rho_y}{z - \zeta} d\xi d\eta \\ & + \frac{1}{2\pi(\kappa+1)} \iint_{\overline{R}} (\rho_x - \rho_y) \frac{\overline{\zeta}}{(z - \zeta)^2} d\xi d\eta, \end{aligned} \tag{17}$$

in which $\overline{R}$ is a region inside of the imaginary boundary Γ, usually referred as an *auxiliary region*. Equivalence of Eqs.(10), (11) and Eqs.(16), (17) directly implies that the influence of the body force applied along the imaginary boundary is equivalent to that of due to embedded force doublets into the auxiliary region. The physical meaning of the force doublet is an embedded eigen strain at the point where it is applied. In the problem that includes any inelastic strain as in plastic strain, therefore, the force doublet is used to express its influence.

In the next section, the line weld model and its thermoelastic solution is discussed. Then the procedure for treating a thermoplastic strain is described

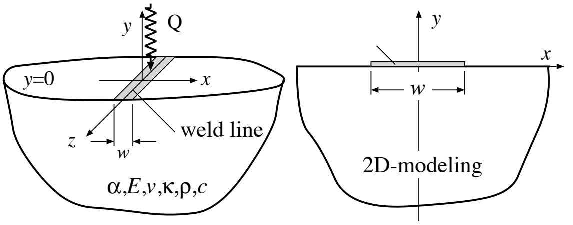

Fig. 2 Simple welding model for stainless steel (Yield stress:$\sigma_Y = 800$MPa, Heat flux:$Q = 11.2$MW/m^2, Linear expansion coefficient:$\alpha = 1.2 \times 10^{-5}$, Young's modulus: $E = 200.2$GPa, Density:$\rho = 7833$kg/m^3, Specific heat:$c = 586$J/kgK, Poisson's ratio:$\nu = 0.3$, Thermal diffusivity: $\kappa = 1.133 \times 10^{-5}$m^2/s and Thermal conductivity:$\lambda = 52$W/mK)

under the assumption that the material follows Prandtl-Reuss flow rule for an elastic-perfect-plastic body under plain strain condition.

3 Simplified Model of Line Welding

Fig.2 shows a simplified weld model treated in this monograph. A uniform strength of transient line heater of width “w” is applied to a surface of a semi-infinite medium for a short duration of time with a strength chosen so that the heat flux delivered from the heater resembles to that of expected under actual welding of stainless steel. In a physical sense, the problem is essentially two dimensional which should simplify the analysis, however, an occurrence of plastic flow in the out-of-plane (z) direction make the problem somewhat cumbersome. The resulted thermoelastic field such as temperature rise $\tau(x,y,t)$ and elastic stress components $\sigma_{ij}(x,y,t)$ due to continuous heating of the duration t, can be written under the assumption of plane strain ($\varepsilon_{zz}=0$) that,

$$\tau(x,y,t) = \frac{Q}{2\pi\kappa\rho c}\int_{-\frac{w}{2}}^{\frac{w}{2}} E_1(S)\,d\xi, \tag{18}$$

$$\begin{aligned}\frac{\sigma_{xx}(x,y,t)}{\overline{\sigma}} &= \int_{-\frac{w}{2}}^{\frac{w}{2}}\left\{\left(2\frac{y^2}{R^2}-1\right)\frac{1-e^{-S}}{S}-E_1(S)\right\}d\xi\\ &\quad-\frac{2y}{\pi}\int_{-\infty}^{\infty}\frac{(x-\xi)^2}{R^4}f(\xi,t)d\xi,\end{aligned} \tag{19}$$

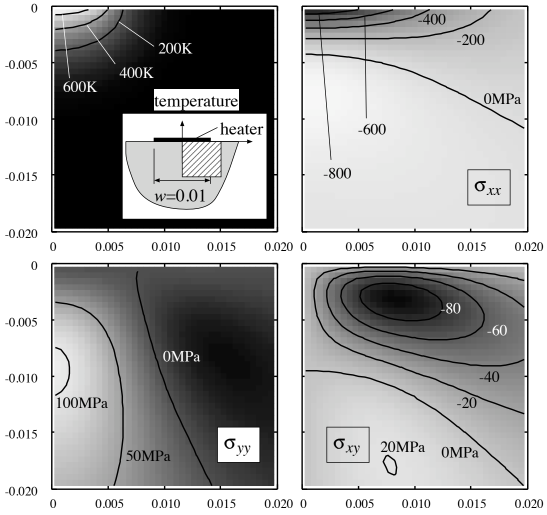

Fig. 3 Temperature and thermoelastic stresses after 1s heating

$$\frac{\sigma_{yy}(x,y,t)}{\overline{\sigma}} = \int_{-\frac{w}{2}}^{\frac{w}{2}} \left\{ \left(1 - 2\frac{y^2}{R^2}\right) \frac{1-e^{-S}}{S} - E_1(S) \right\} d\xi - \frac{2y^3}{\pi} \int_{-\infty}^{\infty} \frac{f(\xi,t)}{R^4} d\xi, \tag{20}$$

$$\frac{\sigma_{xy}(x,y,t)}{\overline{\sigma}} = 2y \int_{-\frac{w}{2}}^{\frac{w}{2}} \frac{x-\xi}{R^2} \frac{1-e^{-S}}{S} d\xi - \frac{2y^2}{\pi} \int_{-\infty}^{\infty} \frac{x-\xi}{R^4} f(\xi,t) d\xi, \tag{21}$$

$$\frac{\sigma_{zz}(x,y,t)}{2\overline{\sigma}} = -\int_{-\frac{w}{2}}^{\frac{w}{2}} E_1(S) d\xi - \nu \frac{y}{\pi} \int_{-\infty}^{\infty} \frac{f(\xi,t)}{R^2} d\xi, \tag{22}$$

where R^2 is a square of distance between reference and source points $R^2 = (x-\xi)^2 + y^2$, (x,y) is a coordinate of reference point, $(\xi,0)$ is a coordinate of source point, $\overline{\sigma}$ is a constant defined by $\overline{\sigma} = \alpha EQ/4\pi\kappa\rho c(1-\nu)$ in which ρ is a mass density, κ is a thermal diffusivity, c is a specific heat, α is a coefficient of linear expansion, E is a Young's modulus, ν is a Poisson's ratio (the concrete values of those material properties used were shown in the caption of Fig.2). S is a non-dimensional parameter defined by $S = R^2/4\kappa t$, $E_1(x)$ is a integral exponential function defined by $E_1(x) = \displaystyle\int_x^{\infty} \frac{e^{-u}}{u} du$ and $f(\xi,t)$ is a function defined as

$$f(\xi,t) = 2\sqrt{\kappa t} \times \left[\frac{1}{p}(1-e^{-p^2}) + pE_1(p^2) \right]_{\frac{\xi+w/2}{2\sqrt{\kappa t}}}^{\frac{\xi-w/2}{2\sqrt{\kappa t}}}. \tag{23}$$

4 Expression of Plastic Strain by Force Doublets

As already mentioned, the most fundamental concept for the treatment of plastic strain in BFM is to replace the distribution of plastic strain by force doublets. Consider an elastic-plastic body whose elasticity constants are E for Young's modulus and ν for Poisson's ratio. The plastic part in the region is noted R^p which is surrounded by an elastic foundation R^e. Next, consider an infinitesimally small plastic element $\omega^p \in R^p$ which has stress components $\sigma_{ij}(P)$ and strain components $\varepsilon_{ij}(P) = \varepsilon^e_{ij}(P) + \varepsilon^p_{ij}(P)$ at point $P \in \omega^p$ where $\varepsilon^e_{ij}(P)$ and $\varepsilon^p_{ij}(P)$ are the elastic and plastic components of the strain at point P, respectively. ω^p can be extracted without affecting the stress field if traction $t_i(P) = \sigma_{ij}(P)n_j(P)$ is applied to the outer surface of ω^p, and at the same time, traction $-t_i$ is applied to the inner surface of the cavity which is made by the extraction of ω^p from R^p where $n_j(P)$ is a component of unit normal at P. Then the plastic element ω^p is transposed into an *ideal elastic* element ω^e which has the same elastic properties (E,ν) with region R^e but its yield stress is infinite so that no yielding takes place. Owing to this transposition, stress state is unchanged but the strain state is decreased by the amount of plastic strain $\varepsilon^p_{ij}(P)$. Therefore, if ω^e is embedded into the cavity of the region R^p, some clearances due to shrinkage of the element would be observed. In order to compensate this strain decrease and to embed an ideal element without any gap, an additive stress $T_{ij}(P)$ have to be applied to ω^e. If such procedure is continued until all the plastic element are transposed to an ideal elastic one. After the completion of such transposition, the stress field at an arbitrary point P may be expressed as follows.

$$\sigma_{ij}(P) = \sigma_{ij}^{\text{therm}}(P) - T_{ij}(P) + \iint_{R^p} \frac{\partial \sigma^k_{ij}(P,Q)}{\partial \xi_\ell} T_{k\ell}(Q) dR^p(Q), \tag{24}$$

where $\sigma_{ij}^{\text{therm}}(P)$ is component of thermoelastic stresses at point P which is shown from Eqs.(19) $\sim$ (22), $T_{ij}(Q)$ is a magnitude of force doublet embedded at point Q, which compensate the strain decrease during the process of transposition from plastic element ω^p to elastic one ω^e. Because of the incremental nature of plasticity, not the total stress but an incremental stress is used to evaluated a present stress state. Then Eq.(24) is replaced by an incremental form as

$$d\sigma_{ij}(P) = d\sigma_{ij}^{\text{therm}}(P) - dT_{ij}(P) + \iint_{R^p} \frac{\partial \sigma^k_{ij}(P,Q)}{\partial \xi_\ell} dT_{k\ell}(Q) dR^p(Q), \tag{25}$$

in which $dT_{ij}(Q)$ is an increment of the magnitude of force doublet, which is related to the increment of plastic strain at point Q. The total stress can be calculated by a sum of stress increments such that $\sigma_{ij}(P) = \sum d\sigma_{ij}(P)$. When Prandtl-Reuss flow rule is employed, each component of plastic strain increment is assumed to be proportional to the component of deviatoric stress S_{ij} with unknown proportionality constant λ. Therefore, the increment of the magnitude of point force doublet can be expressed as

$$dT_{ij}(Q) = D_{ijk\ell} d\varepsilon^p_{k\ell}(Q) = D_{ijk\ell} \left(\sigma_{k\ell}(Q) - \delta_{k\ell} \frac{\sigma_{mm}(Q)}{3} \right) \lambda(Q), \tag{26}$$

where $D_{ijk\ell}$ is an elastic modulus tensor and δ_{ij} is Kronecker delta. It should be noted that the term "$-dT_{ij}(P)$" in Eq.(25) is indispensable with no relation to the value of $\partial \sigma^k_{ij}(P,Q)/\partial \xi_\ell$. In fact, stress components due to point force doublet which acts in the z direction $\partial \sigma^z_{ij}(P,Q)/\partial z$ results no influence at any point P under plane strain condition. However, even when $\partial \sigma^k_{ij}(P,Q)/\partial \xi_\ell = 0$, the term $-dT_{ij}(P)$ still gives a non-zero influence at point P. In a practical analysis, the proportional constant $\lambda(Q)$ in Eq.(26) is the unknown parameter to be determined through numerical analysis. Since $\lambda(Q)$ is not only a function of the position Q but also the function of time t, it is required to determine the value of $\lambda(Q)$ step-wisely, considering the yield criterion. For example, when Von Mises criterion for elastic-perfect-plastic body is supposed, the following relation must hold at a point $P \in R^p$ that

$$\sigma_{eq} = \sqrt{(\sigma_{xx}-\sigma_{yy})^2+(\sigma_{yy}-\sigma_{zz})^2+(\sigma_{zz}-\sigma_{xx})^2+6\sigma_{xy}^2} = \sigma_Y. \quad (27)$$

5 Numerical Procedure and Discussion

For the numerical estimation of residual strain, the time domain is divided into N equally division as $t = n\Delta t, (n = 1, 2, \cdots, N)$ where Δt is a time increment. A space domain is also divided into number of square areas (0.25mm×0.25mm) in which the magnitude of plastic strain (and therefore the magnitude of force doublet) is assumed to be constant over a region and a given time. As a result, the total stress component at the reference time $t = n\Delta t$,$\sigma_{ij}(P)|_n$ can be evaluated as

$$\begin{aligned}\sigma_{ij}(P)|_n = &\sum_{k=1}^{n-1} d\sigma_{ij}(P)|_k + d\sigma_{ij}^{\text{therm}}(P)|_n - dT_{ij}(P)|_n \\ &+ \int_{\Omega} \frac{\partial}{\partial \xi_\ell}\Big\{\sigma_{ij}^k(P,Q)\Big\} dT_{k\ell}(Q)|_n d\Omega^p(Q), \quad (28)\end{aligned}$$

where $dT_{ij}(P)|_n$ is an increment of the magnitude of force doublet at time $t = n\Delta t$. As seen Eq.(26), $dT_{ij}(P)|_n$ is related to the total stress state at $t = n\Delta t$ but it could be reasonable to evaluate its value from the value of

Fig. 4 Residual stress distribution along y axis after complete cool down

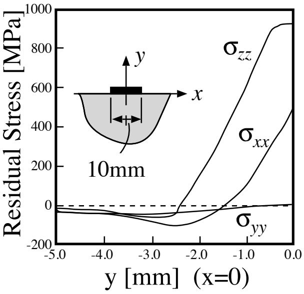

Fig. 5 Residual stress distribution along x axis after complete cool down

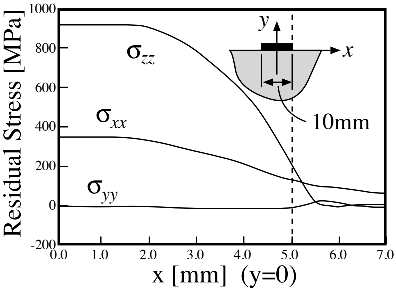

total stress at one time step $\varDelta t$ before. That is, $dT_{ij}(P)|_n$ is approximated by

$$dT_{ij}(P)|_n \approx D_{ijk\ell}\left(\sigma_{k\ell}(P)|_{n-1} - \delta_{k\ell}\frac{\sigma_{mm}(P)|_{n-1}}{3}\right)\lambda(P)|_n \tag{29}$$

in which $\lambda(P)|_n$ is unknown parameter yet not determined. Substitution of Eq.(29) into Eq.(28) gives stress components at arbitrary point P at reference time $t = n\varDelta t$, if parameter $\lambda(P)|_n$ is provided. In order to determine $\lambda(P)|_n$, the yield criterion is used. However, substitution of Eq.(28) into Eq.(27) leads nonlinear simultaneous equations for the determination of $\lambda(P)|_n$ at each reference point P. These nonlinear simultaneous equations should be solved carefully under the constraint that $\lambda(P)|_n \geq 0$. When $\lambda(P)|_n$ becomes negative, it means the unloading process during plastic deformation so that the value of $\lambda(P)|_n$ should set to be 0. In Figs.4 and 5 the residual stress distribution along the y and x axes after complete cool down are shown. As seen, the out-of-plane residual stress component σ_{zz} exhibits the largest value and the usual plane strain relation $\sigma_{zz} = \nu(\sigma_{xx} + \sigma_{yy})$ is violated.

6 Conclusion

A treatment of plastic strain in the direction of out-of-plane based on the principle of the body force method was discussed. The material supposed was elastic-perfect-plastic body that follows Von Mises yield criterion. It was found that the residual stress in the out-of-plane direction σ_{zz} can be estimated independently of the in-plane residual stress components σ_{xx} and σ_{yy}. It was also found that the proposed method provides effective and efficient technique for problems that include limited plasticity.

References

1. P.M. Blomerus and D.A. Hills, An efficient procedure for modeling limited plastic flow, Proc. Inst. Mech. Eng. C, **212**, p.731 (1998)
2. D. -H. Chen and H. Nisitani, Extension of Body Force Method to Elastic-Plastic Problems, Transaction of the Japan Society of Mechanical Engineers, Ser. A, **51**-462, p.571, 1985 (in Japanese)
3. H.Nisitani and D.-H. Chen, Elastic-Plastic Analysis of an Infinite Plate with an Elliptic Hole by Body Force Method, Transaction of the Japan Society of Mechanical Engineers, Ser. A, **51**-465, p.1471, 1985 (in Japanese)

Evaluation of Internal Friction of Viscoelastic Composites with Meso-Scale Structures for Vibration Damping of Mechanical Structures

Yotsugi Shibuya

Abstract Viscoelastic analysis of polymer composites is focused to understand effect of meso-scale structure of composite on the internal friction for application of vibration damping in precision instruments. In this paper, the meso-scale structure of the composite is supposed to be periodically clustered hexagonal array of fibers. Internal damping of the composite is evaluated by energy dissipation in cyclic response. Interaction of fibers and viscoelasticity of the matrix cause the energy dissipation in the composite. To evaluate the damping capacity of the composite in details, a homogenization theory with multi-scale asymptotic expansion is used to analyze meso- and macro-scale behavior of the composite.

1 Introduction

Polymer matrix composites provide an advantage of damping capacity to reduce vibration of structures and enhance controllability of precision instrument [1]. It is important to understand effect of meso-scale structures of composites on damping property. As damping property of the polymer composite varies on frequency of vibration, it is necessary to study on the frequency dependency for the property in detail.

Studies on damping properties of composite have been made for particle-reinforced composites with the viscoelastic interpahse [2], Rayleigh damping of laminated composites [3] and computation modeling and experimental comparison [4]. The three phase model [5] and finite element analysis of unit cell [6,7] were used to solve the problems for damping properties of composites. Design of structure of composites for optimal damping [8] was presented

---

Yotsugi Shibuya
Department of Mechanical Engineering, Akita University, 1-1 Tegata Gakuen-machi, Akita, 010-8502, Japan, e-mail: yshibuya@gipc.akita-u.ac.jp

as an application of the method.

In this paper, viscoelastic analysis of fiber-reinforced polymer composites is made to understand effect of frequency of vibration and meso-scale structure of composites on the internal damping. The meso-scale structure of the composite is supposed to be periodically clustered hexagonal array of unidirectional fibers. To evaluate meso- and macro-scale behavior of the composite in details, a homogenization theory with multi-scale asymptotic expansion of displacements in the composite [9]. To solve perturbed displacements at meso-scale level, a boundary integral method of boundary value problems is used for unit cells. The viscoelastic property of polymer matrix is applied as generalized Maxwell model. Internal damping of the composite is evaluated by stress strain relation in cyclic response as a simulation of experimental technique.

Numerical calculation is made in view of periodical boundary conditions. Damping behavior of the composite is calculated by energy dissipation under cyclic loading.

2 Meso-scale structure of fiber composite

Consider a unidirectional fiber composite with periodically clustered hexagonal array of fibers to apply a homogenization theory [9]. The meso-scale model of the composite is presented in Fig. 1(a) with two coordinate systems. A unit cell for the periodic model is shown in Fig. 1(b) in details. Large-scale coordinate $\boldsymbol{x} = (x_1, x_2, x_3)$ with x_3 axis for fiber direction and small-scale coordinate $\boldsymbol{y} = (y_1, y_2, y_3)$ are employed in the analysis for homogenization. The size of the composite is supposed to be sufficiently large in comparison with the size of the unit cell. Meso-scale structure of the composite is modeled by a basic hexagonal cell where a fiber is placed at off-centered position of the hexagon. A periodical unit cell is consists of three basic hexagonal cells in the figure. Distance between fibers in the unit cell is d_f and diameter of inscribed circle on the hexagon is d_c. The radius of the fiber is a. The fiber volume fraction C_f is

$$C_f = \frac{2\pi\, a^2}{\sqrt{3}\, d_c^2} \tag{1}$$

In the viscoelastic analysis on the effective damping properties of the composite, the governing equations in large- and small-scale coordinate systems can be expressed in the Laplace transform as

$$\frac{\partial}{\partial x_i^\lambda} \hat{\sigma}_{ij}^\lambda(\boldsymbol{x}, \boldsymbol{y}, p) + \hat{F}_i(\boldsymbol{x}, p) = 0 \tag{2}$$

$$\hat{\sigma}_{ij}^\lambda(\boldsymbol{x}, \boldsymbol{y}, p) = \hat{C}_{ijkl}(\boldsymbol{y}, p)\, \hat{\varepsilon}_{kl}^\lambda(\boldsymbol{x}, \boldsymbol{y}, p) \tag{3}$$

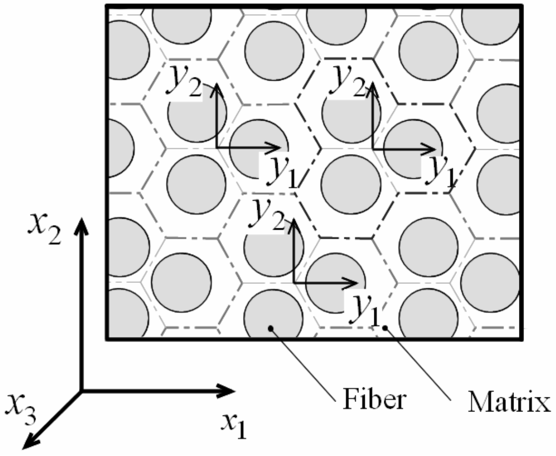

(a) Two-scale coordinate system

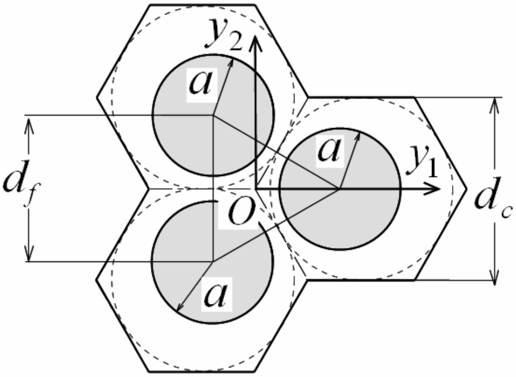

(b) A unit cell model

Fig. 1 Model of the meso-scale structure of unidirectional fiber composite.

$$\hat{\varepsilon}^{\lambda}_{kl}(\boldsymbol{x}, \boldsymbol{y}, p) = \frac{1}{2}\left[\frac{\partial \hat{u}^{\lambda}_{i}(\boldsymbol{x}, \boldsymbol{y}, p)}{\partial x^{\lambda}_{j}} + \frac{\partial \hat{u}^{\lambda}_{j}(\boldsymbol{x}, \boldsymbol{y}, p)}{\partial x^{\lambda}_{i}}\right] \tag{4}$$

where $\hat{}$ indicates the Laplace transform of a function and p is a variable of the Laplace transform. σ_{ij} are the stress components, ε_{ij} are the strain components, F_i are the body forces and u_i are the displacements. C_{ijkl} are the relaxation moduli of the function in $\boldsymbol{y}$.

To derive viscoelastic homogenized equations of the composite, the displacement with two-scale coordinate systems can be expressed by asymptotic expansion with parameter λ as

$$\hat{u}_i^{\lambda}(\boldsymbol{x},\boldsymbol{y},p) = \hat{u}_i^{(0)}(\boldsymbol{x},\boldsymbol{y},p) + \lambda\hat{u}_i^{(1)}(\boldsymbol{x},\boldsymbol{y},p) + \cdots \tag{5}$$

where λ characterizes smallness of the meso-scale structure of the composite. Relation of large scale and small scale coordinate systems and their differential operators are written as

$$\boldsymbol{y} \to \frac{\boldsymbol{x}}{\lambda}\,, \quad \frac{\partial}{\partial x_i^{\lambda}} \to \frac{\partial}{\partial x_i} + \frac{1}{\lambda}\frac{\partial}{\partial y_i} \tag{6}$$

Substituting Eqs. (3)-(5) into the equilibrium equation (2) taking account of Eq. (6), it yields equations of different orders in λ. Then, the equilibrium equations in small-scale coordinate system are written as

$$\frac{\partial}{\partial y_i}\{\hat{C}_{ijkl}(\boldsymbol{y},p)[\hat{\varepsilon}_{kl}^{(1)}(\boldsymbol{y},p) + \hat{\varepsilon}_{kl}^{*}(p)]\} = 0 \tag{7}$$

$$\hat{\varepsilon}_{ij}^{(1)}(\boldsymbol{y},p) = \frac{1}{2}[\frac{\partial\hat{u}_i^{(1)}(\boldsymbol{y},p)}{\partial y_j} + \frac{\partial\hat{u}_j^{(1)}(\boldsymbol{y},p)}{\partial y_i}] \tag{8}$$

where $\hat{\varepsilon}_{kl}^{*}(p)$ is the homogenized strain field in the Laplace transform. The homogenized stress-strain relation and the inverse are written as follows:

$$\begin{aligned}\hat{\sigma}_{ij}^{*}(p) &= \hat{C}_{ijkl}^{*}(p)\hat{\varepsilon}_{kl}^{*}(p)\\ &= \frac{1}{V}\int_V \hat{C}_{ijkl}(\boldsymbol{y},p)[\hat{\varepsilon}_{kl}^{(1)}(\boldsymbol{y},p) + \hat{\varepsilon}_{kl}^{*}(p)]dV(\boldsymbol{y})\end{aligned} \tag{9}$$

where V is the volume of the unit cell and $C_{ijkl}^{*}$is the effective dynamic modulus. Consider a unidirectional carbon-fiber composite with periodic array of fibers.

3 Numerical procedure

The solution of Eq. (7) for the perturbed displacement $\hat{u}_i^{(1)}$is expressed by integral equation form as

$$\begin{aligned}\hat{u}_j^{\beta(1)}(\boldsymbol{y},p) = &\sum_q \int_{\Gamma_{\beta\,q}} [\hat{U}_{ij}^{\beta}(\boldsymbol{y},\boldsymbol{y}',p)\hat{t}_i^{\beta}(\boldsymbol{y}',p) \;-\hat{T}_{ij}^{\beta}(\boldsymbol{y},\boldsymbol{y}',p)\hat{u}_i^{\beta(1)}(\boldsymbol{y}',p)]d\Gamma(\boldsymbol{y}')\\ &-\sum_q \int_{\Omega_{\beta\,q}} \hat{S}_{jkl}^{\beta}(\boldsymbol{y},\boldsymbol{y}',p)\,\hat{\varepsilon}_{kl}^{*}(\boldsymbol{y}',p)\,d\Omega(\boldsymbol{y}')\end{aligned} \tag{10}$$

where symbol β takes m or f, m and f indicate the matrix and fiber phases, respectively. $\Gamma_{\beta q}$ and $\Omega_{\beta q}$ are integral contour along the boundary and integral region, respectively, as shown in Fig. 2. t_i is the surface traction along the boundary Γ, and U_{ij}, T_{ij} and S_{jkl} are fundamental solutions associated to

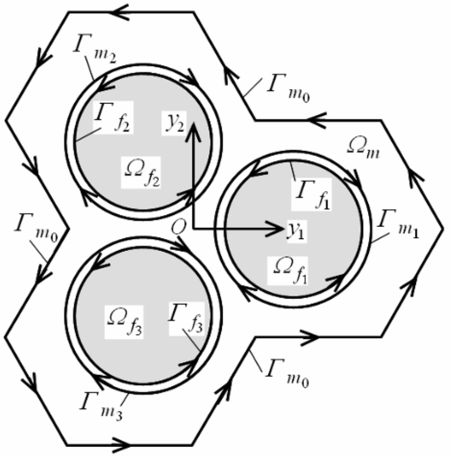

Fig. 2 Contours and domain of integral equation.

displacement, traction and stress, respectively, where an instantaneous point load is subjected to an infinite viscoelestic medium. The solutions are determined from elastic solution by correspondence principle.

Since the perturbed displacement is obtained as solution of boundary integral equations, the it is effective macroscopic stress to reduce to surface integral from Eq. (9) as follows:

$$\begin{aligned}\hat{\sigma}^*_{ij}(p) = \frac{1}{V}\{&\sum_{q=0}^{3}\int_{\Gamma_{mq}}\frac{1}{2}\hat{C}^m_{ijkl}(p)[\hat{u}^{m(1)}_k(\boldsymbol{y},p)\,n_l \\ &+ \hat{u}^{m(1)}_l(\boldsymbol{y},p)\,n_k]\,d\Gamma(\boldsymbol{y}) + \hat{C}^m_{ijkl}(p)\,\hat{\varepsilon}^*_{ij}(p)\,V_m \\ &+ \sum_{q=1}^{3}\int_{\Gamma_{fq}}\frac{1}{2}C^f_{ijkl}[\hat{u}^{f(1)}_k(\boldsymbol{y},p)\,n_l + \hat{u}^{f(1)}_l(\boldsymbol{y},p)\,n_k]\,d\Gamma(\boldsymbol{y}) \\ &+ C^f_{ijkl}\,\hat{\varepsilon}^*_{kl}(p)\,V_f\}\end{aligned} \tag{11}$$

where n_l is the normal vector on the boundary, and V_m and V_f are the volumes of matrix and fiber regions, respectively.

Inverse Laplace transform is obtained by Duhamel integral form. Multiplying both sides of Eqs. (10) and (11) by p and making inverse Laplace transform, we can obtain following equations.

$$\begin{aligned}\frac{\partial u_j^{\beta(1)}(\boldsymbol{y},t)}{\partial t} &= \sum_{q}^{3} \int_{\Gamma_{\beta q}} \int_0^t [U_{ij}^{\beta}(\boldsymbol{y},\boldsymbol{y}',t-\tau)\frac{\partial t_i^{\beta}(\boldsymbol{y}',\tau)}{\partial \tau} \\ &\quad - T_{ij}^{\beta}(\boldsymbol{y},\boldsymbol{y}',t-\tau)\frac{\partial u_i^{\beta(1)}(\boldsymbol{y}',\tau)}{\partial \tau}]\, d\tau\, d\Gamma(\boldsymbol{y}') \\ &\quad - \sum_{q}^{3} \int_{\Omega_{\beta q}} \int_0^t S_{jkl}(\boldsymbol{y},\boldsymbol{y}',t-\tau)\frac{\partial \varepsilon_{kl}^{*}(\boldsymbol{y}',\tau)}{\partial \tau}\, d\tau d\Omega(\boldsymbol{y}') \quad (12)\end{aligned}$$

$$\begin{aligned}\frac{\partial \sigma_{ij}^{*}(t)}{\partial t} &= \frac{1}{V}\{\sum_{q=0}^{3} \int_{\Gamma_{mq}} \int_0^t \frac{1}{2} C_{ijkl}^{m}(t-\tau)[\frac{\partial u_k^{m(1)}(\boldsymbol{y},\tau)}{\partial \tau}\, n_l \\ &\quad + \frac{\partial u_l^{m(1)}(\boldsymbol{y},\tau)}{\partial \tau}\, n_k]\, d\tau\, d\Gamma(\boldsymbol{y}) + V_m \int_0^t C_{ijkl}^{m}(t-\tau)\, \frac{\partial \varepsilon_{ij}^{*}(\tau)}{\partial \tau}\, d\tau \\ &\quad + \sum_{q=1}^{3} \int_{\Gamma_{fq}} \frac{1}{2} C_{ijkl}^{f}[\frac{\partial u_k^{f(1)}(\boldsymbol{y},t)}{\partial t}\, n_l + \frac{\partial u_l^{f(1)}(\boldsymbol{y},t)}{\partial t}\, n_k]\, d\Gamma(\boldsymbol{y}) \\ &\quad + C_{ijkl}^{f}\, \frac{\partial \varepsilon_{kl}^{*}(t)}{\partial t}\, V_f\} \qquad (13)\end{aligned}$$

The boundary equations are solved by taking account of initial conditions and boundary conditions. The initial conditions at $t = 0$ are given as

$$\left.\begin{array}{ll} u_i^{m(1)}(\boldsymbol{y},0) = 0\ , & t_i^{m}(\boldsymbol{y},0) = 0 \\ u_i^{f(1)}(\boldsymbol{y},0) = 0\ , & t_i^{f}(\boldsymbol{y},0) = 0 \\ \varepsilon_{ij}^{*}(0) = 0 & \end{array}\right\} \qquad (14)$$

Boundary conditions for perfect bonding ($r = a$) are assumed. The boundary conditions are written as

$$\left.\begin{array}{ll} u_r^{m(1)} = u_r^{f(1)}\ , & u_\theta^{m(1)} = u_\theta^{f(1)} \\ t_r^{m} = -\, t_r^{f}\ , & t_\theta^{m} = -\, t_\theta^{f} \end{array}\right\} \qquad (15)$$

The response of the composite is obtained from these equations under harmonic load conditions to estimate internal damping effect.

4 Damping properties

A simple shear of the material is considered to evaluate the damping property of materials. The generalized Maxwell model is shown in Fig. 3 to identify the property of the viscoelastic material with frequency dependency. The model consists of spring element with coefficient G_i proportional to strain and dashpot element with coefficient D_i proportional to strain rate. The stress-strain relation described by the generalized Maxwell model is given in the Laplace transform.

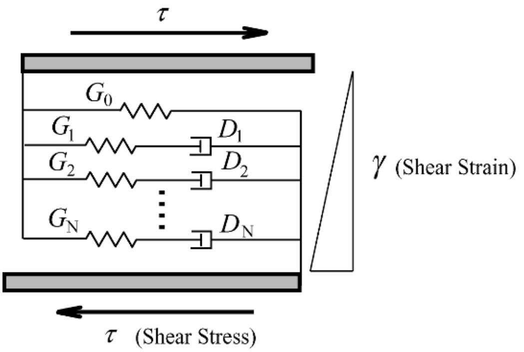

Fig. 3 Generalized Maxwell model.

$$\hat{\tau}(p) = \hat{G}(p)\ \hat{\gamma}(p) \tag{16}$$

where τ is the shear stress and γ is the engineering shear strain. As harmonic shear strain is given and inverse Laplace transform is made, the shear stress is obtained as frequency response.

$$\begin{aligned}\tau(t) &= \bar{G}(\omega)\ \gamma_0 \exp(i\omega t)\\ &= [G'(\omega) + i\ G''(\omega)]\ \gamma_0 \exp(i\omega t)\end{aligned} \tag{17}$$

where γ_0 is the amplitude of the shear strain, ω the angular velocity, t the time and i $(= \sqrt{-1})$ is the imaginary unit. $\bar{G}(\omega)$ corresponds to Fourior transform of the dynamic shear modulus and it is defined as complex modulus. The real part $G'(\omega)$ is storage modulus and imaginary part $G''(\omega)$ is loss modulus. The loss factor is defined as

$$\eta = G''(\omega)/G'(\omega) \tag{18}$$

For the Maxwell model as shown in Fig. 3, the complex modulus can be expressed as

$$\bar{G}(\omega) = [G_0 + \sum_{q=1}^{N} \frac{(\omega D_q)^2 G_q}{G_q^2 + (\omega D_q)^2}] + i\ \sum_{q=1}^{N} \frac{\omega D_q G_q^2}{G_q^2 + (\omega D_q)^2} \tag{19}$$

5 Numerical results and discussion

Numerical calculations are carried out for carbon fiber composite with viscoelastic matrix 3M-467 reinforced by carbon fibers. The carbon fiber is AS-4 and it is treated as an elastic material. The following properties are used from Ref. [10]: $E_L^T = 235\,\mathrm{GPa}$, $E_T^f = 14\,\mathrm{GPa}$, $\nu_{LT}^f = 0.2$, $\nu_T^f = 0.25$, $G_{LT}^f = 28\,\mathrm{GPa}$. The viscoelastic property depending on frequency is taken from Ref. [11]. Fig. 4 shows the complex moduli of the 3M-467 matrix from Ref. [11] and their fitting curves. Solid square symbols indicate the storage modulus and circle symbols are the loss factor. Solid line is the fitting curve of the storage modulus and broken line is of the loss factor. Fig. 5 shows the stress strain relation under harmonic transverse shear loading with variation of fiber volume fraction. As the stiffness of the composite increases with fiber volume fraction, the area of the loop expands widely. The area of the Lissajous curve corresponds to the energy dissipation of the composite for one cycle. The complex moduli are summarized in Table 1. The loss factor is almost same value obtained from these moduli.

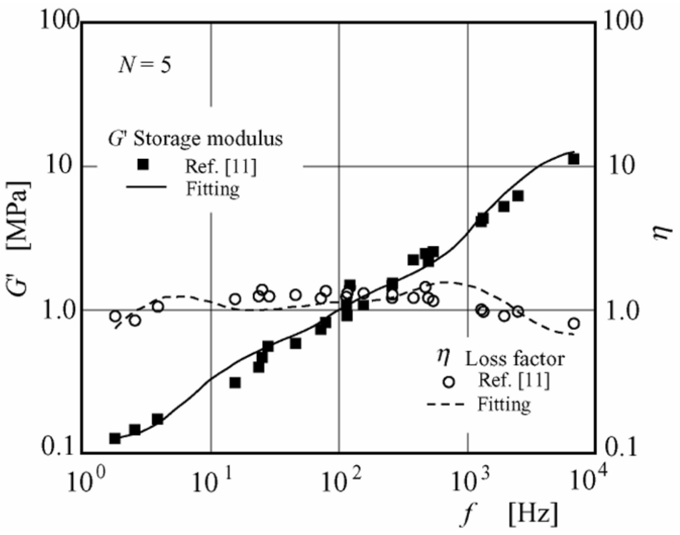

Fig. 4 Fitting of complex moduli with generalized Maxwell model ($N = 5$).

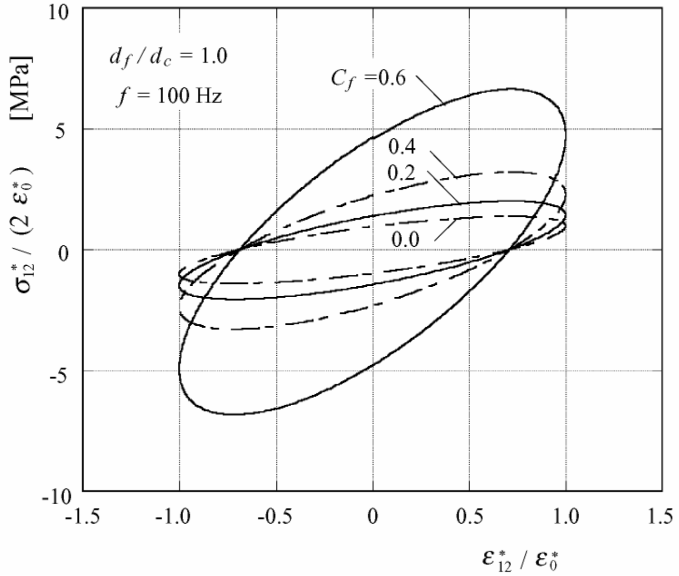

Fig. 5 Effect of fiber volume fraction on stress strain relation.

C_f	$G^{'}$ $[MPa]$	$G^{''}$ $[MPa]$	η
0	0.967	0.969	1.002
0.2	1.415	1.418	1.002
0.4	2.264	2.278	1.002
0.6	4.697	4.697	1.000

Table 1 Complex moduli of the fiber composite

6 Conclusion

Viscoelastic analysis of fiber-reinforced polymer composites is made to understand effect of frequency of vibration and meso-scale structure of composites on the internal damping. The meso-scale structure of the composite is supposed to be periodically clustered hexagonal array of unidirectional fibers.

The viscoelastic property of polymer matrix is applied generalized Maxwell model. Internal damping of the composite is evaluated by energy dissipation in cyclic response as a simulation of experimental technique.

References

1. S. Mori, et al., Damping Effect on Precise Track Following for Nano-Motion Actuator, *IEEE Trans. on Magnetics*, Vol. 41, pp. 842-848, 2005.

2. P.J. Wei and Z.P. Huang, Dynamic Effective Properties of the Particle-Reinforced Composites with the Viscoelastic Interphase, *International Journal of Solids and Structures*, Vol. 41, pp. 6993-7007, 2004.
3. C. Kyriazoglow and F.J. Guild, Finite Element Prediction of Damping of Composite GFRP and CFRP Laminates – a Hybrid Formulation – Vibration damping Experiments and Rayleigh Damping, *Composites Science and Technology,* Vol.67, pp.2643-2654, 2007.
4. A. Agbossou and M. Lagache, Fiber Distribution Effects in Linear Viscoelastic Behavior of Polymer Matrix Composites: Computation Modelling and Experimental Comparison, *Mechanics Research Communications,* Vol.25, pp.105-115, 1998.
5. C. Remillat, Damping Mechanism of Polymers filled with elastic particles, *Mechanics of Materials,* Vol.39, pp.525-537, 2007.
6. M. Koishi, et al., Homogenization Method for Dynamic Viscoelastic Analysis of Composite Materials, *JSME International Journal*, Vol. 40, pp.306-312, 1997.
7. J.L. Tsai and Y.K. Chi, Effect of Fiber Array on Damping Behaviors of Fiber Composites, *International Journal of Solids and Structures,* Vol.37, pp.4791-4810, 2000.
8. Y.M. Yi, et al., Design of Microsrtuctures of Viscoelastic Composites for Optimal Damping Characteristics, *Composites: Part B,* Vol.39, pp.1196-1204, 2008.
9. Y. Shibuya, Evaluation of Creep Compliance of Carbon-Fiber-Reinforced Composites by Homogenization Theory, *JSME International Journal*, Vol. 40, pp. 306-312, 1997.
10. C.P. Carman, et al., Optimization of Fiber Coatings to Minimize Stress Concentrations in Composites Materials, *Journal of Composite Materials*, Vol.27, pp.589-612, 1993.
11. D. Jones, *Handbook of Viscoelastic Vibration Damping*, 2001, Wiley.

An Identification Method of the Time Dependence of the Impact Force by Using Acoustic Response and FEM Analysis

Tomoaki Tsuji, Takafumi Kurimoto and Toshikazu Shibuya

Abstract The radiated sound from the impacted body must have the information with respect to the impact force. We have proposed the method in order to identify the impact force by analyzing the radiated sound from the impacted body. Normally the impact position is unknown and important to measure the impact position. Therefore, in this study, we propose the method to identify the impact position and force by using the radiated sound from the impact body. In the present method, the relationship between the impacted force and sound pressure is obtained by FEM simulation. In order to identify the impact position, the sound pressure, which is measured at the other position, is used. The efficiency of the present method is confirmed by using the many experiments of the plate as the impacted body.

1 Introduction

A lot of studies that identify the impact force have been reported. For instance, Inoue et al. [1-3] identified the impact force by using the strain response caused in the elastic body. In this method, the relation between the known impact force and the strain response is requested, in order to determine the transfer function between the impact force and the strain response. On the other hand, the radiated sound from the impacted body must have

---

Tomoaki Tsuji
Department of Science and Engineering, Chuo University, Bunkyouku , Tokyo, 112-8551, Japan, e-mail: tsuji@mech.chuo-u.ac.jp

Takafumi Kurimoto
Department of Science and Engineering, Chuo University, Bunkyouku , Tokyo, 112-8551, Japan

Toshikazu Shibuya
Department of Mechanical Engineering, Nippon Bunri University, Ooita, 870-03971, Japan

the information with respect to the impact force. If the impact force is identified by measuring the radiated sound, measurement will be made leaving from the impact body, that is non-contact measurement. Author et al. [4, 5] proposed the identify method of the impact force by measuring the radiated sound. In this method, it is necessary to measure the impact force directory before the identification experiment, in order to obtain the transfer function between the impact force and the radiated sound pressure. However, it is difficult to measure the impact force directory. Authors proposed the method to identify the impact force without the preliminary experiment [6]. In this method, the relation between the known impact force and the radiated sound is given by using FEM simulation.

Normally the impact position is unknown, especially in the case of the impact from the flying object. But, it is difficult to investigate the impact position. Therefore, in this study, we propose the method to identify the impact position and force by using the radiated sound from the impact body. In the present method, the relation between the impacted force and sound pressure is obtained by FEM simulation. By this relationship, the time dependence of the radiated sound pressure and impact force can be shown by series form. The unknown coefficient is determined by the least square method using the measured sound pressure. In order to identify the impact position, the sound pressure, which is measured at the other position, is used. The efficiency of the present method is confirmed by using the many experiments of the plate as the impacted body.

2 Experimental set up and measurement

In this study, we propose the method to identify the placement of the impact and the impact force by using the sound pressure measured at different place. Figure 1 shows the outline of the measurement system. The radiated sound from the impacted body is measured by the two microphones, and recorded by the digital oscilloscope. Moreover, the strain data by the strain gauge is recorded. The sound and strain values are transferred into the computer and analyzed. Figure 2 shows the configuration of the impact body as the aluminum bar (ϕ30mm×300mm) and the impacted body as the alu-

Fig. 1 The measuring system of the sound and the strain.

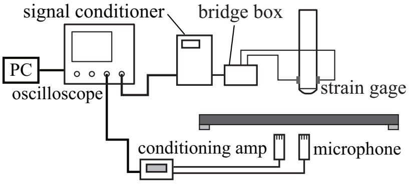

minum plate (201mm×501mm×10mm). The impact bar is freely dropped from height $H$and impacts to the plate at the point x as shown in the figure. Two microphones are in set with the distance 40mm and under the plate with height h. The contact area between the impact bar and the impacted plate approximately the circular rejoin with 10mm diameter. The impacted plate is supported by the silicon rubber seats (20mm×20mm×10mm) under the four corners of the plate. The impact bar falls to the plate through the plastic cylinder of the inside diameter 31mm. The strain gauges are attached on the side of the impact bar at 20mm from the under side of the bar as shown in Fig.2. The impact force can be measured directly by these strain gauges. The radiated sound pressure is measured by the microphone. The Type and the configuration and the performance of this microphone are listed in Table 1. The microphone is calibrated to output the voltage, which is linear to the sound pressure. The actual measurement element of the sound pressure is in the interior from the surface cap of the microphone. By the preliminary experiment, we decided this actual measurement element is in 5mm from the front surface of the microphone.

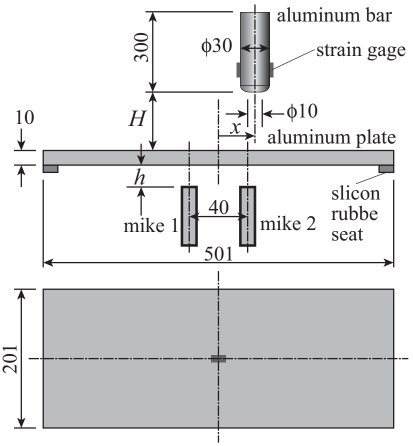

Fig. 2 The configuration of the impact bar and the aluminum plate.

If the stress distribution in the section of the impact bar is assumed as uniform, the time dependence of the impact force $P_{bar}(t)$ at the impact bar can be given by the strain $\varepsilon_{bar}(t)$ at the side of the bar as follow.

Type	4190
configuration	ϕ12.7mm×17.6mm
bandwidth of the frequency	3 ∼ 20kHz
company	*Bruel & Kjaer*

Table 1 The type and the configuration and the performance of the microphone.

$$P_{bar}(t) = E_{bar}\varepsilon_{bar}(t)\frac{\pi}{4}d_{bar}^2, \tag{1}$$

with E_{bar} : the modulus of the longitudinal elasticity and d_{bar}: diameter of the impact bar.

This impact force $P_{bar}(t)$ should equal to the time dependence of the impact force on the plate surface. Thus, we will use these data as the actual measured values of the impact force in order to confirm the identified impact force by the present method.

3 The identification method of the impact force by using the radiated sound and FEM analysis

It is common using the stepwise function as input data, in order to get any response. But, it is difficult to get good accuracy in FEM calculation because of discontinuity. Thus, the following impact force $P_{sim}(t)$ respect with time t is introduced as the input impact force.

$$P_{sim}(t) = P_0\left[\frac{1}{2}\left\{1-\cos(\pi\frac{t}{T})\right\}H(t)H(T-t)+H(t-T)\right], \tag{2}$$

with T : interval time, P_0: magnitude of the impact force and $H(t)$: Heaviside's step function.

The time dependence of the radiated sound pressure $p_{sim}(t)$ for the given impact force$P_{sim}(t)$ can be calculated by FEM analysis. Then, the time dependence of the arbitrary impact force $P(t)$ and sound pressure $p(t)$ can be given by using these functions $p_{sim}(t)$ and $P_{sim}(t)$ as follows.

$$P(t) = \sum_{n=1}^{N} A_n P_{sim}(t+t_n) \quad , \quad p(t) = \sum_{n=1}^{N} A_n p_{sim}(t+t_n), \tag{3}$$

with $t_n = \Delta t \times (n-1)$, Δt: time interval and A_n: unknown coefficient.

The measured sound pressure by the mike 1 is used to identify the impact force $P(t)$, and the one by the mike 2 is used to identify the impact position x. The time dependence of the measured sound pressure is denoted as $p_{exp1}(t)$ and $p_{exp2}(t)$. The square error E_{error1} between the measured values $p_{exp1}(t)$ and the identified values $p(t)$ in Eq.(3) can be shown as follow.

$$E_{error1} = \sum_{i=1}^{N\max}\left\{\sum_{n-1}^{N} A_n p_{sim1}(t_i+t_n) - p_{\exp 1}(t_i)\right\}^2, \tag{4}$$

with t_i(i=1,2... N_{max}): time when the sound pressure is measured and N_{max}: number of values

The unknown coefficient A_n can be given by the least square method as the solution of the following simultaneous linear equations.

$$\sum_{n=1}^{N}\sum_{i=1}^{N\max} A_n p_{sim1}(\tau_i + t_n) p_{sim}(\tau_i + t_m) = \sum_{n=1}^{N} p_{\exp}(\tau_i) p_{sim}(\tau_i + t_m) \qquad (5)$$

If the values of A_n are obtained by Eq.(5), the time dependence of the impact force $P(t)$ for the sound pressure $p_{exp1}(t)$ can be identified by Eq.(3). However, the sound pressure $p\ (t)$ and force $P\ (t)$ are respect with the impact position x, that is the value of x must be known before calculation. Once x is expected as $x = x^*$, the values of A_n can be given by solving Eq.(5). Moreover, the impact force can be given by Eq.(3). For this impact force, we can calculate the sound pressure at the position of the mike 2 by using Eq.(3). The square error of this expected sound pressure $p_{sim2}(t)$ and measured one $p_{exp2}(t)$ can be given as follow.

$$E_{error2} = \sum_{i=1}^{N\max} \left\{ \sum_{n-1}^{N} A_n p_{sim2}(t_i + t_n) - p_{\exp 2}(t_i) \right\}^2 \qquad (6)$$

The impact position x can be decided by minimizing Eq.(6) with respect to the value of x^*. Figure 3 shows the FEM model for the FEM simulation. The mechanical properties of the plate and the air layer are shown in Table 2 and 3. Since the symmetry of the model, the half region should be considered. The boundary conditions for the support are very complicated, since the silicone lubber should be deformed and contacted in any area to the plate. However, within such a short duration, the supporting condition makes no influence [6]. Thus, we use free condition that is no support. The region of air is considered under and beside the plate as shown in Fig.3. The sound wave is reflected at these open boundaries. However, the reflected sound at the open boundary does not reach the position where the sound pressure is measured until time 0.5ms, because the moving distance of the sound wave is 173mm. Thus, the air layer boundary makes no influence to the calculated values at the position where the sound pressure is measured. The mechanical properties and the other conditions for the plate and the air are listed in Table 2 and 3, respectively. The impact force is applied to the circular region with

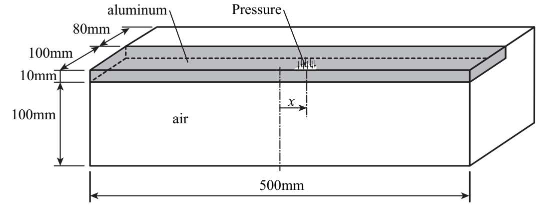

Fig. 3 The simulation model of the plate with the air.

material	Aluminum
configuration	100×500×10 mm
Young's modulus	70 GPa
Poisson's ratio	0.34
density	2700 kg/m^3
N. of element	3705

Table 2 The mechanical properties of the aluminum plate for the FEM analysis.

material	air
configuration	180×500×100 mm
acoustic velocity	346 m/s
density	1.3 kg/m^3
N. of element	24020

Table 3 The mechanical properties of air for the FEM analysis.

diameter $d = 10$mm as the uniformly distributed pressure. The input impact force $P_{sim}(t)$ in Eq.(2) with $T = 0.1$ms and $P_0 = 1$MPa is shown in Fig.4. Time dependent FEM analysis is performed by the commercial FEM code by Ansys inc. The radiated sound pressure at the mike 1, for the impact position $x = 0$ is shown in Fig.5. By substituting this data into Eq.(3), the arbitrary sound pressure can be given.

Fig. 4 The time dependence of the pressure as the input for the FEM simulation ($T = 0.1$ms).

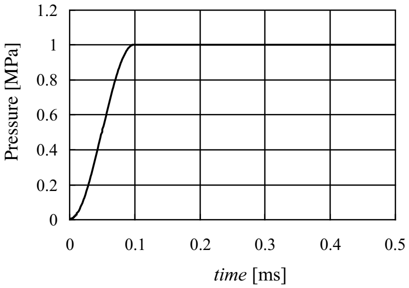

Fig. 5 The time dependence of the sound pressure by FEM simulation at the mike 1 (h= 10mm, x = 0mm).

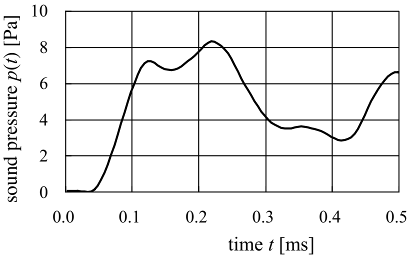

4 The identification of the impact position and impact force

The arbitrary sound pressure and impact force can be given by unknown coefficients A_n. In order to identify the impact force from the radiated sound pressure, the unknown coefficients A_n is determined by minimizing Eq.(4), that is solving Eq.(5). The radiated sound pressure is measured by dropping from height $H = 30$mm to the impact position $x = 0$. The experimental data $p_{exp1}(t_i)$ is obtained through $t = 0$ms to 1ms by dividing $N_{max} = 200$ points. The time interval is $\Delta = 0.005$ms. The calculated sound pressure are satisfactory converged with $N = 40$ to the measured sound pressure. Thus, in the following calculation, the value of $N = 40$ is used.

Figure 6 shows the time dependence of the identified sound pressure at the mike 2 with the values of $x^* =$ -20, 0, 20mm. In the figure the measured sound pressure is shown as gray line. The identified sound pressure at the mike 2 with $x^* = 0$ is in good agreement with the measured one. Thus, the impact position should be $x = 0$. In order to obtain the impact position x, which minimize E_{error2} in Eq.(6), the relationship between x^* and E_{error2} is shown in Fig.7. By this figure, $x^* = 0$ minimizes the E_{error2} that is the impact position is $x = 0$. This position is exactly same as the impact position. Figure 8 shows the time dependence of the identified impact force by using Eq.(3) with the expected impact position $x^* =$ -20, 0, 20mm. The measured impact

Fig. 6 The comparison between the measured and the simulated sound pressure at the mike 2 with the values of $x^* =$ -20, 0, 20mm ($N = 40$).

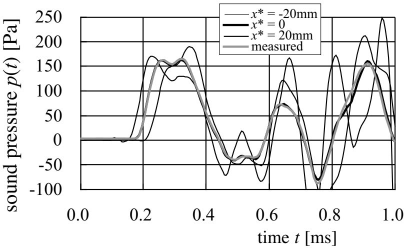

Fig. 7 The relationship between the expected impact position x^* and the least square error of the sound presser by the mike 2 during $t = 0$ to 0.5ms, when the impact position is $x = 0$.

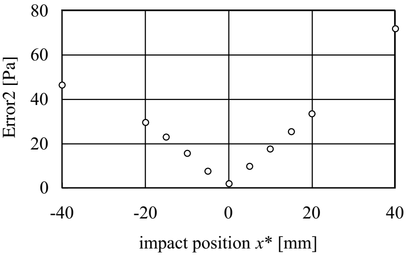

Fig. 8 The time dependence of the impact force with x^* = -20mm, 0, 20mm, when impacted at $x = 0$.

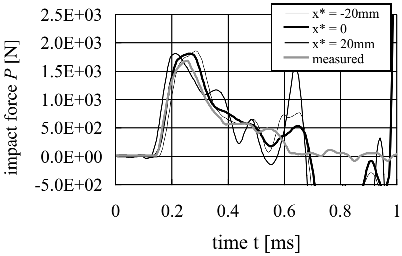

Fig. 9 The relationship between the expected impact position x^* and the square error of the impact force during $t = 0$ to 0.5ms, when the impact position is $x = 0$.

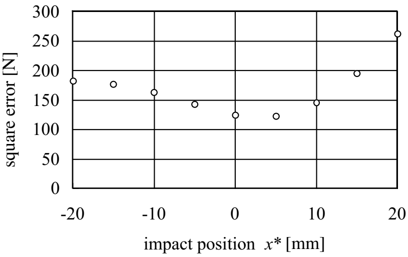

force by the strain gage is shown as gray line. The values with $x^* = 0$ is good agreement with the measured values until time t = 0.5ms. After t= 0.5ms, the identified impact force is not agree with the measured one. It may be caused by the influence of the supporting condition. It is confirmed, that the impact position is identified by the sound pressure of the mike 2 before t = 0.5ms. Figure 9 shows the relationship between the respected impact position x^* and the square error in between the measured and the identified impact force. By this figure, the error takes the minimum value in between $x^* = 0$ to 5mm. Therefore, it is confirmed that the impact position and the impact force can be identified by the sound pressure, which is recorded by the two microphones. In order to confirm the accuracy of the present method, the impact experiments are made with various values of the impact position. Figure 10 shows the relationship between the respect impact position x^* and E_{error2} in Eq.(6) of the mike 2. Increasing the value of x, the graph becomes flatter. Then the determination of the impact position becomes difficult. However,

Fig. 10 The relationship between the expected impact position x^* and the least square error of the sound presser by the mike 2 during $t = 0$ to 0.5ms, with various values of the impact position $x = 0$ to 80mm.

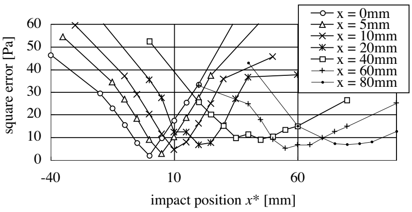

we can obtain the impact position when the impact position is far from the microphone such as $x = 80$mm.

The time dependence of the identified impact force with the impact position $x = 10$, 20 and 40mm are shown in Fig.11. The starting time of impact and the maximum values of impact force are in good agreement with the directly measured ones by the strain gages. In Fig.11(c), the identified impact force is wavering after time $t = 0.3$ms, because the impact position x is leaving from the center of the microphones.

Fig. 11 The comparison between the measured and identified impact force with the impact position $x = 10$, 20, 40mm.

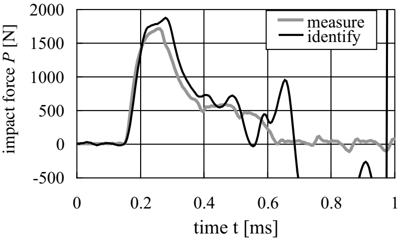

(a) $x = 10$mm

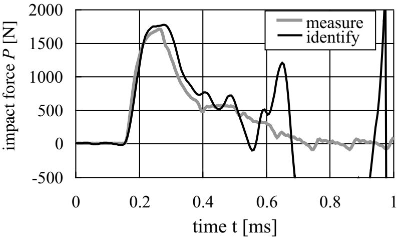

(b) $x = 20$mm

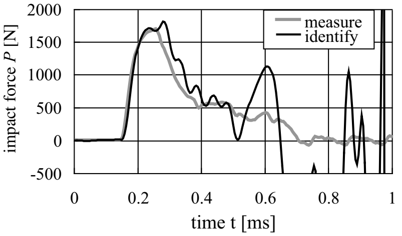

(c) $x = 40$mm

Figure 12 shows the relationship between the impact position x and the square error of the impact force to the measured data during $t = 0$ to 0.5ms. The error is almost same, when the impact position x is smaller than 20mm, that is the impact position is in between the two microphones. The error is increasing with the increment of the impact position, because the impact position is leaving from the center of the microphones.

Fig. 12 The relationship between the impact position x and the square error of the identified impact force respected with the measured one during $t = 0$ to 0.5ms.

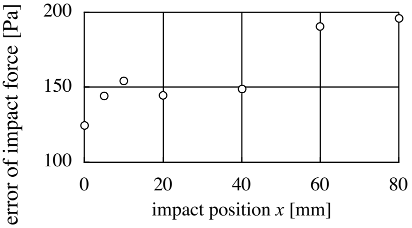

5 Conclusion

In this study, we proposed the method to identify the impact position and the impact force by using the radiated sound pressure with two microphones. By using FEM analysis, the time dependence of the impact force and the impact position can be given without any special experiments before the impact experiment. The present method is confirmed by the many experiments. The results are listed as follows.

1. The impact position and the time dependence of the impact force can be identified by the present method.
2. The impact position can be determined when the impact position far from two microphones.
3. The impact force is satisfactory identified, when the impact position is in between the two microphones.

References

1. Inoue, H., Kishimoto, K., Shibuya, T., Koizumi, T., Estimation of Impact Load by Inverse Analysis : Optimal Transfer Function for Inverse Analysis, Transactions of the Japan Society of Mechanical Engineers, Series A, Vol. 57, No.543 (1991), 2727-2734.
2. Inoue, H. et al., Measurement of Impact Load by Using an Inverse Analysis Technique: Comparison of Methods for Estimating the Transfer Function and its Application to the Instrumented Charpy Impact Test, *Transactions of the Japan Society of Mechanical Engineers*, Series A, Vol. 57, No.534 (1991), pp. 424-429.
3. Inoue, H. et al., Inverse Analysis of the Magnitude and Direction of Impact Force, *Transactions of the Japan Society of Mechanical Engineers*, Series A, Vol. 59, No.559 (1993), pp. 572-579.
4. K. Inoue, T. Tsuji, N. Noda, Impact Force Identification using Radiated Sound from the Impacted Elastic Body, *Experimental & Theoretical Mechanics '93*, (1993), 315-320.
5. Tsuji, T., Kawada, Y., Suzuki, Y., Yamaguchi, T., Noda, N., Identification of an Impact Force by Radiated Sound from the Impacted body : Non-Contact Measuring Experiments of the Identification by the Inverse Analysis, *Transactions of the Japan Society of Mechanical Engineers*, Series A, Vol. 65, No.632 (1999), pp. 701-707.
6. Tsuji, T., Kurimoto, T., Shibuya. T., Determination of the Impact Force at a Plate by using Acoustic Response and FEM Analysis, *Transactions of the Japan Society of Mechanical Engineers*, Series A, Vol. 74, No.742 (2008), pp. 858-863

Infinite Row of Parallel Cracks in a Piezoelectric Material Strip under Mechanical and Transient Thermal Loadings

Sei Ueda

Abstract In this paper, the problem of an infinite row of parallel cracks in a piezoelectric material strip is analyzed under static mechanical and transient thermal loadings. The crack faces are supposed to be completely insulated. By using the Laplace and Fourier transforms, the thermoelectromechanical problem is reduced to a singular integral equation, which is solved numerically. The stress intensity factors for both the embedded and edge cracks are computed. The results for the crack contact problem are also included.

1 Introduction

Due to the rapid growth in application for smart or intelligent systems [1-5], the fracture problems of homogeneous piezoelectric materials under thermal loading conditions have attracted many research activities in recent years [6-12]. Especially, the overshooting phenomena of the stress and electric displacement intensity factors were observed in piezoelectric strips under thermal shock loading condition with a normal crack [6] and a parallel crack [12].

However, in spite of the fact that piezoelectric materials involve multiple cracks, most of the existing contributions are concerned with the fracture behavior of a single crack except for the dynamic interaction between the two coplanar cracks in homogeneous piezoelectric materials under electromechanical loadings [13]. Then, one of the remaining problems that need to be fully understood is that of interaction between cracks in such media subjected to thermal loading, and the present author investigated the thermoelectromechanical interaction of piezoelectric strips under thermoelectric loading with two parallel cracks [14] and with two coplanar cracks [15].

Sei Ueda
Department of Mechanical Engineering, Osaka Institute of Technology, 5-16-1 Omiya, Asahi-ku, Osaka, 535-8585, Japan, e-mail: ueda@med.oit.ac.jp

In this paper, the problem of an infinite row of parallel cracks in a piezoelectric material strip is analyzed under static mechanical and transient thermal loadings. The crack faces are supposed to remain thermally and electrically insulated [16,17]. The superposition technique is used to solve the governing equations. The transient temperature and thermal stress in an uncracked strip are the same as the previous results [18]. This thermal stress is used as the crack surface traction with opposite sign to formulate the mixed boundary value problem. By using the Fourier transform [19,20], the electromechanical problem is reduced to a singular integral equation, which is solved numerically [21]. The stress intensity factors for both the embedded and edge cracks are computed. The results for the crack contact problem are also included.

2 Formulation of the problem

As shown in Fig. 1, suppose a piezoelectric material strip with the thickness h containing an infinite row of parallel cracks of equal length $2c = b - a \quad (0 \leq a < b < h)$ being spaced at equal distance $2d$ perpendicular to the free boundaries. The system of rectangular Cartesian coordinates (x, y, z) is introduced in the material in such a way that one of the crack is located along the z-axis, and the x-axis is parallel to the boundaries. The piezoelectric material is under a mechanical stress σ_0 in the x-direction and is poled in the z-direction. It is assumed that initially the medium is at the uniform temperature T_I (stress free temperature) and is suddenly subjected to a uniform temperature change $T_0 H(t)$ along the bottom surface ($z = 0$), where $H(t)$ is the Heaviside step function and t denotes time. The temperature at the top surface ($z = h$) is maintained at T_I. The crack faces remain thermally and electrically insulated [16,17]. The crack problem may be solved by superposition. In the problem considered here, since the heat conduction is one-dimensional, straight cracks do not obstruct the heat flow in this arrangement, determination of the temperature distribution and the resulting thermal stress would be quite straightforward and the related crack problem would be one of mode

Fig. 1 An infinite row of parallel cracks in a piezoelectric strip.

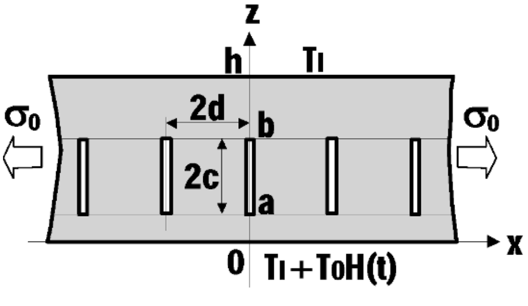

I. The lines of the centers of the cracks $x = \pm(2n+1)d, (n = 0, 1, 2, ...)$ are the axes of symmetry of the configuration and we suppose that each crack is opened under the action of the same distribution of the internal pressure $\sigma_0 + \sigma_0^T(z,t)$ where t is the time, σ_0 is the static mechanical stress and $\sigma_0^T(z,t)$ is the thermal stress induced by the time-dependent temperature change. The thermal stress $\sigma_0^T(z,t)$ has been already obtained in [18]. In the following, the subscripts x, y, z will be used to refer to the direction of coordinates.

The constitutive equations are given by

$$\left.\begin{aligned}
&\sigma_{xx} = c_{11}\frac{\partial u_x}{\partial x} + c_{13}\frac{\partial u_z}{\partial z} + e_{31}\frac{\partial \phi}{\partial z},\ D_x = e_{15}\left(\frac{\partial u_x}{\partial z} + \frac{\partial u_z}{\partial x}\right) - \varepsilon_{11}\frac{\partial \phi}{\partial x}\\
&\sigma_{zz} = c_{13}\frac{\partial u_x}{\partial x} + c_{33}\frac{\partial u_z}{\partial z} + e_{33}\frac{\partial \phi}{\partial z},\ \ D_z = e_{31}\frac{\partial u_x}{\partial x} + e_{33}\frac{\partial u_z}{\partial z} - \varepsilon_{33}\frac{\partial \phi}{\partial z}\\
&\sigma_{zx} = c_{44}\left(\frac{\partial u_x}{\partial z} + \frac{\partial u_z}{\partial x}\right) + e_{15}\frac{\partial \phi}{\partial x}
\end{aligned}\right\} \tag{1}$$

where $\phi(x,z,t)$ is the electric potential, $u_x(x,z,t)$, $u_z(x,z,t)$ are the displacement components, $\sigma_{xx}(x,z,t)$, $\sigma_{zz}(x,z,t)$, $\sigma_{zx}(x,z,t)$ are the stress components and $D_x(x,z,t)$, $D_z(x,z,t)$ are the electric displacement components.

The governing equations for the electromechanical fields may be expressed as follows:

$$\left.\begin{aligned}
&c_{11}\frac{\partial^2 u_x}{\partial x^2} + c_{44}\frac{\partial^2 u_x}{\partial z^2} + (c_{13}+c_{44})\frac{\partial^2 u_z}{\partial x \partial z} + (e_{31}+e_{15})\frac{\partial^2 \phi}{\partial x \partial z} = 0\\
&c_{44}\frac{\partial^2 u_z}{\partial x^2} + c_{33}\frac{\partial^2 u_z}{\partial z^2} + (c_{13}+c_{44})\frac{\partial^2 u_x}{\partial x \partial z} + e_{15}\frac{\partial^2 \phi}{\partial x^2} + e_{33}\frac{\partial^2 \phi}{\partial z^2} = 0\\
&e_{15}\frac{\partial^2 u_z}{\partial x^2} + e_{33}\frac{\partial^2 u_z}{\partial z^2} + (e_{15}+e_{31})\frac{\partial^2 u_x}{\partial x \partial z} - \varepsilon_{11}\frac{\partial^2 \phi}{\partial x^2} - \varepsilon_{33}\frac{\partial^2 \phi}{\partial z^2} = 0
\end{aligned}\right\} \tag{2}$$

From the symmetry conditions it follows that the described problem may be reduced to that of a piezoelectric material rectangle with one crack loaded by the pressure $\sigma_0 + \sigma_0^T(z,t)$. Then the boundary conditions for the rectangular region of $0 \le x \le d$ and $0 \le z \le h$ can be stated as follows:

$$\left.\begin{aligned}
&\sigma_{xx}(0,z,t) = -\sigma_0 - \sigma_0^T(z,t) && (a < z < b)\\
&u_x(0,z,t) = 0 && (0 \le z \le a, b \le z \le h)
\end{aligned}\right\} \tag{3}$$

$$\sigma_{zx}(0,z,t) = 0,\ D_x(0,z,t) = 0 \quad (0 \le z \le h) \tag{4}$$

$$\sigma_{zx}(d,z,t) = 0,\ D_x(d,z,t) = 0,\ \frac{\partial}{\partial z}u_x(d,z,t) = 0 \quad (0 \le z \le h) \tag{5}$$

$$\left.\begin{aligned}
&\sigma_{zx}(x,0,t) = 0,\ \sigma_{zz}(x,0,t) = 0,\ D_z(x,0,t) = 0,\\
&\sigma_{zx}(x,h,t) = 0,\ \sigma_{zz}(x,h,t) = 0,\ D_z(x,h,t) = 0
\end{aligned}\right\} \ (0 \le x \le d) \tag{6}$$

3 Analysis

The general solutions of Eq.(2) are obtained by using the Fourier integral transform techniques [19] :

$$\left.\begin{aligned}
u_x(x,z,t) &= \frac{i}{2\pi}\sum_{j=1}^{6}\int_{-\infty}^{\infty}\frac{|s|}{s}a_{1j}A_{1j}(s,t)\exp(|s|\gamma_{1j}x)\exp(-isz)ds \\
&+\sum_{j=1}^{6}\sum_{n=1}^{\infty}a_{2j}A_{2jn}(t)\exp(\mu_n\gamma_{2j}z)\sin(\mu_n x)+\frac{d-x}{d}F_0(t) \\
u_z(x,z,t) &= \frac{1}{2\pi}\sum_{j=1}^{6}\int_{-\infty}^{\infty}A_{1j}(s,t)\exp(|s|\gamma_{1j}x)\exp(-isz)ds \\
&+\sum_{j=1}^{6}\sum_{n=1}^{\infty}A_{2jn}(t)\exp(\mu_n\gamma_{2j}z)\sin(\mu_n x)+\frac{z}{h}F_1(t) \\
\phi(x,z,t) &= \frac{1}{2\pi}\sum_{j=1}^{6}\int_{-\infty}^{\infty}b_{1j}A_{1j}(s,t)\exp(|s|\gamma_{1j}x)\exp(-isz)ds \\
&+\sum_{j=1}^{6}\sum_{n=1}^{\infty}b_{2j}A_{2jn}(t)\exp(\mu_n\gamma_{2j}z)\sin(\mu_n x)+\frac{z}{h}F_2(t)
\end{aligned}\right\} \tag{7}$$

where $A_{1j}(s,t)$, $A_{2jn}(t)$ $(j = 1,2,...,6, n = 1,2,...)$ and $F_i(t)$ $(i = 1,2,3)$ are the unknown functions to be solved, and $\mu_n = n\pi/d$ $(n = 1,2,...)$. The constants γ_{ij}, a_{ij} and $b_{ij}(i = 1,2, j = 1,2,...,6)$ can be obtained by setting $s \to \infty$ of the functions $\gamma_{1j}(s)$, $a_{1j}(s)$ and $b_{1j}(s)$ $(j = 1,2,...,6)$ in Appendix A of the previous paper [18] and the functions $\gamma_{2j}(s)$, $a_{2j}(s)$ and $b_{2j}(s)$ $(j = 1,2,...,6)$ in Appendix B of the previous paper [22], respectively. Substituting the displacements and electric potential solutions (7) into the constitutive equations (1), one can obtain the stresses and electric displacement components.

The problem may be reduced to a singular integral equation by defining the following new unknown function $G(z,t)$ [20]:

$$G(z,t) = \left\{\begin{array}{cc} \dfrac{\partial}{\partial z}u_x(0,z,t) & (a < z < b) \\ 0 & (0 \le z \le a, b \le z \le h) \end{array}\right\} \tag{8}$$

Making use of the first boundary condition (3) with Eqs.(4)-(6), we have the following singular integral equation for the determination of the unknown function $G(\xi,t)$:

$$\int_b^a G(\xi,t)\left[\frac{1}{\xi-z}+\sum_{i=1}^{4}M_i(\xi,z)+\frac{C}{\Re[Z^\infty]d}\right]d\xi$$
$$=\frac{\pi}{\Re[Z^\infty]}\left[\sigma_0+\sigma_0^T(z,t)\right]\quad(a<z<b)\tag{9}$$

where Z^∞ and $M_i(\xi,z)$ $(i=1,2,3,4)$ are the known constant and kernel functions. The singular integral equation (9) for $a>0.0$ is to be solved with the following subsidiary conditions obtained from the second boundary condition (3).

$$\int_b^a G(\xi,t)d\xi=0\tag{10}$$

For the case of $a=0.0$, the constant C can be determined from the second boundary condition (3) as follows:

$$C=\frac{1}{2}\left[\frac{c_{13}^2\varepsilon_{33}+2c_{13}e_{31}e_{33}-c_{33}e_{31}^2}{c_{33}\varepsilon_{33}+e_{33}^2}-c_{11}\right]\tag{11}$$

To solve the singular integral equation (9) and the additional equation (10) by using the Gauss-Jacobi integration formula [21], we introduce the following function $\Phi(u,t)$:

$$G(\xi,t)=\frac{c\Phi(u,t)}{(1+u)^\alpha(1-u)^{1/2}}\tag{12}$$

where $\alpha=1/2$ for $(a+b)/2>1$ (embedded crack) and $\alpha=-1/2$ for $(a+b)/2=1$ (edge crack), and $u=(2\xi-a-b)/(b-a)\quad(-1<u<1, a<\xi<b)$. The stress intensity factors $K_{Ia}(t)$ at $z=a$ and $K_{Ib}(t)$ at $z=b$ may be defined, and evaluated as

$$\begin{aligned}K_{Ia}(t)&=\lim_{z\to a^-}\{2\pi(z-a)\}^{1/2}\sigma_{xx}(0,z,t)\\&=\left\{\begin{matrix}-\Re[Z^\infty](\pi c)^{1/2}\Phi(-1,t) & (a>0)\\ 0 & (a=0)\end{matrix}\right\}\end{aligned}\tag{13}$$

$$\begin{aligned}K_{Ib}(t)&=\lim_{z\to b^+}\{2\pi(b-z)\}^{1/2}\sigma_{xx}(0,z,t)\\&=\left\{\begin{matrix}\Re[Z^\infty](\pi c)^{1/2}\Phi(1,t) & (a>0)\\ \Re[Z^\infty](2\pi b)^{1/2}\Phi(1,t) & (a=0)\end{matrix}\right\}\end{aligned}\tag{14}$$

4 Numerical results and discussion

To examine the effect of thermoelectroelastic interactions on the stress intensity factors, the solutions of the singular integral equation have been computed numerically. For the numerical calculations, the thermoelectroelastic properties of cadmium selenide are used [4]. Since the values of the coefficients of heat conduction for cadmium selenide could not be found in the literature, the value $\kappa^2 = \kappa_x/\kappa_z = 1/1.5$ is used.

4.1 The Stress Intensity Factors under Pure Mechanical Load

First, we consider the case of $T_0 = 0.0$. In this case, the stress intensity factors are independent of the time t. Fig. 2 shows the effect of $(a+b)/2h$ on $(K_{Ia}, K_{Ib})/\sigma_0(\pi c)^{1/2}$ for various values of d/h with $c/h = 0.1$, respectively. The results for $d/h \to \infty$ are obtained in [18]. As d/h decreases, the values of the stress intensity factors decrease. The stress intensity factors of the crack tips near the free boundary ($(a+b)/2h \to 0.1$ or 0.9) become very large. The influence of the crack location on the stress intensity factors decreases with decreasing d/h.

Fig. 2 The effect of the crack location on the stress intensity factors K_{Ia} and K_{Ib} of the embedded crack under pure mechanical load.

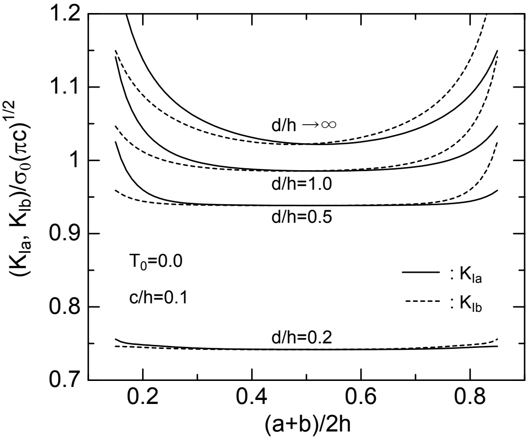

Fig. 3 displays $K_{Ib}/\sigma_0(\pi b)^{1/2}$ of the edge crack versus b/h for various values of d/h. Different from the cases for $d/h \to \infty$, in which $K_{Ib}/\sigma_0(\pi b)^{1/2}$ increases monotonically with increasing b/h, $K_{Ib}/\sigma_0(\pi b)^{1/2}$ for $d/h = 2.0$ initially increases and then gradually decreases with increasing b/h and $K_{Ib}/\sigma_0(\pi b)^{1/2}$ for $d/h \leq 1.0$ decreases monotonically with increasing b/h.

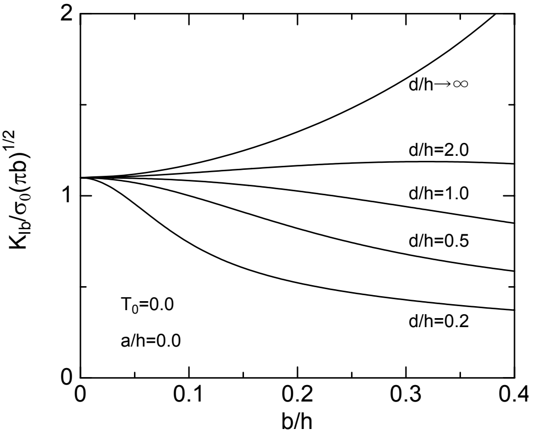

Fig. 3 The effect of the crack length on the stress intensity factor K_{Ib} of the edge crack under pure mechanical load.

4.2 The Stress Intensity Factors of the Embedded Crack under Pure Thermal Load

Next, we consider the case of $\sigma_0 = 0.0$. Assume the bottom surface of the strip is suddenly heated from initial temperature T_I to $T_I + T_0(T_0 > 0.0)$, the calculated normalized stress intensity factors $(K_{Ia}, K_{Ib})/\lambda_{11}|T_0|(\pi c)^{1/2}$ versus time for $c/h = 0.1$, $(a+b)/2h = 0.3$ and $d/h = 0.2$ are shown in Fig. 4. In the figure, the time t is represented through the dimensionless Fourier number defined by

$$F = \frac{\lambda_0 t}{h^2} \tag{15}$$

Since the thermal stress $\sigma_0^T(z,t)$ is statically self-equilibrating, large com-

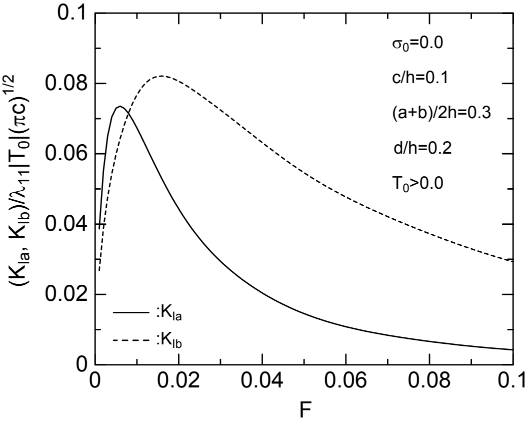

Fig. 4 The transient stress intensity factors K_{Ia} and K_{Ib} of the embedded crack under pure thermal load for $(a+b)/2h = 0.3$ and $d/h = 0.2$.

pressive stress occurs near the surface, and the tensile stress appears inside the strip [18]. Accordingly, the crack will open and the stress intensity factor will be positive. The values of the stress intensity factors increase at first, go through maxima, and then decrease with increasing F. As was expected, the stress intensity factors approach zero when F goes to infinity. The maximum value of $K_{Ia}/\lambda_{11}|T_0|(\pi c)^{1/2}$ is smaller and occurs faster than that of $K_{Ib}/\lambda_{11}|T_0|(\pi c)^{1/2}$.

4.3 The Stress Intensity Factor of the Edge Crack under Pure Thermal Load

Finally, we consider the case of $a/h = 0.0$ (edge crack). As mentioned above, if the strip is heated ($T_0 > 0.0$) suddenly on its bottom surface, large compressive stress will occur near the surface, and the small edge crack will be fully closed and the stress intensity factor will be negative. This is the crack contact problem and this phenomenon would be considered in this section. In this problem it is assumed that the strip contains pre-existing edge cracks of length $b/h = 0.2 \quad (a/h = 0.0)$ and the crack spacing $d/h = 0.1$, and the bottom surface of the strip is cooled ($T_0 < 0.0$) or heated ($T_0 > 0.0$) suddenly. Fig. 5 shows the time dependencies of the normalized stress intensity factor $K_{Ib}/\lambda_{110}|T_0|(\pi c)^{1/2}$ and the value b_0/h indicating the crack contact zone under the cooling process ($T_0 < 0.0$). In this case, because the edge crack is deeper than the tensile zone, the crack tip region ($z = b$) would be subjected to a compressive stress. On the other hand, the part of the crack near the bottom surface $0 \leq z \leq b_0$ would be opened due to the large tensile stress neat the surface, and the stress intensity factor at $z = b$ is equal zero. The unknown crack tip location $z = b_0$ can be obtained from the condition $K_{Ib_0} = 0.0$ at $z = b_0$. Thus the problem may easily be solved by iteration to find b_0 and then compute K_{Ib}. Fig. 6 is the same figures as Fig. 5 under the heating process ($T_0 > 0.0$). Different from the cooling process, the edge crack is deeper than the compressive zone, the crack tip region ($z = b$) would be subjected to a tensile stress and the crack would remain partially open. In other words, the part of the crack, $0 \leq z < a_0$, near the bottom surface would be closed and the stress intensity factor at the crack tip, $z = b$ would remain positive. The unknown crack tip location $z = a_0$ is obtained from the cusp condition $K_{Ia_0} = 0.0$ at $z = a_0$. Thus the problem may easily be solved by iteration to find a_0 and then compute K_{Ib}. The crack contact zone a_0 increases monotonously, and K_{Ib} becomes zero at $F = 0.049$, and the edge crack would be fully closed.

Fig. 5 The transient stress intensity factor K_{Ib} and the crack contact zone b_0 of the edge crack under pure thermal load for $b/h = 0.2$ and $T_0 < 0.0$.

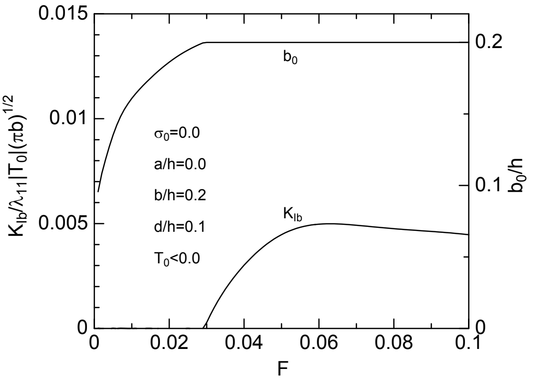

Fig. 6 The transient stress intensity factor K_{Ib} and the crack contact zone a_0 of the edge crack under pure thermal load for $b/h = 0.2$ and $T_0 > 0.0$.

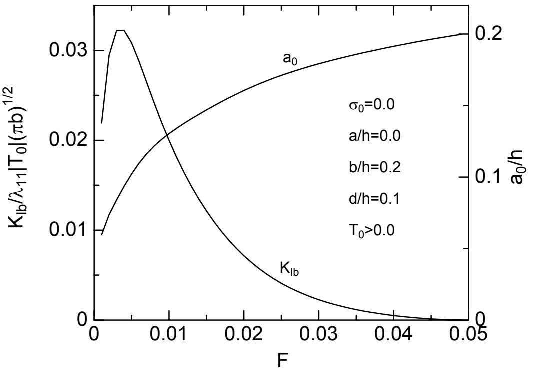

5 Conclusion

The transient fracture problem of an infinite row of parallel cracks in a piezoelectric strip is studied. The effects of the crack spacing, the crack length and the crack location on the fracture behavior are considered. Moreover, taking the crack contact phenomenon into consideration, the transient fracture behavior of a pre-existing edge crack in the strip is considered. The following facts can be found from the numerical results.

1. The stress intensity factors due to both the mechanical and thermal load are lowered by the interaction among cracks, and the influence of it depends on the geometric parameter.
2. In some cases, the stress intensity factors under pure thermal load become negative and the results have no physical meaning. However, when the thermal load is combined with the mechanical load which induces the positive stress intensity factor, those results can be used effectively.
3. Taking the crack contact into consideration, it is found that the edge crack in the strip under the heating process would be fully closed at some time after the thermal shock.

References

1. S.S. Rao, M. Sunar, Piezoelectricity and Its Use in Disturbance Sensing and Control of Flexible Structures: A Survey, *Applied Mechanics Review,* Vol.47, pp.113-123, 1994.
2. T.R. Tauchert, Piezothermoelastic Behavior of a Laminated Plate, *Journal of Thermal Stresses,* Vol.15, pp.25-37, 1992.
3. N. Noda, S. Kimura, Deformation of a Piezothermoelectric Composite Plate Considering the Coupling Effect, *Journal of Thermal Stresses,* Vol.21, pp.359-379, 1998.
4. F. Ashida and T.R. Tauchert, Transient Response of a Piezothermoelastic Circular Disk Under Axisymmetric Heating, *Acta Mechanica,* Vol.128, pp.1-14, 1998.
5. Y. Ootao, Y. Tanigawa, Three-Dimensional Transient Piezothermoelasticity in Functionally Graded Rectangular Plate Bonded to a Piezoelectric Plate, *International Journal of Solids and Structures,* Vol.37, pp.4377-4401, 2000.
6. B.L. Wang and Y.-W. Mai, A Cracked Piezoelectric Material Strip under Transient Thermal Loading, *Transactions of the ASME, Journal of Applied Mechanics,* Vol.69, pp.539-546, 2002.
7. O.P. Niraula and N. Noda, Thermal Stress Analysis in Thermopiezoelastric Strip with an Edge Crack, *Journal of Thermal Stresses,* Vol.25, pp.389-405, 2002.
8. S. Ueda, Thermally Induced Fracture of a Piezoelectric Laminate with a Crack Normal to Interfaces, *Journal of Thermal Stresses,* Vol.26, pp.311-331, 2003.
9. B.L. Wang and N. Noda, The Exact Thermoelectroelasticity Solution for a Penny-Shaped Crack in Piezoelectric Materials, *Journal of Thermal Stresses,* Vol.27, pp.241-251, 2004.
10. S. Ueda, Thermal Stress Intensity Factors for a Normal Crack in a Piezoelectric Strip, *Journal of Thermal Stresses,* Vol.29, pp.1107-1126, 2006.
11. S. Ueda, The Crack Problem in Piezoelectric Strip under Thermoelectric Loading, *Journal of Thermal Stresses,* Vol.29, pp.295-316, 2006.
12. S. Ueda, Transient Response of a Cracked Piezoelectric Strip under Thermoelectric Loading, *Journal of Thermal Stresses,* Vol.29, pp.973-994, 2006.
13. Z.T. Chen and M.J. Worswich, Antiplane Mechanical and Inplane Electric Time-Dependent Load Applied to Two coplanar Cracks in Piezoelectric Ceramic Material, *Theoretical and Applied Fracture Mechanics,* Vol.33, pp.173-184, 2000.
14. S. Ueda and K. Ikawa, Thermoelectromechanical Interaction between Two Parallel Cracks in a Piezoelectric Strip, *Journal of Thermal Stresses,* Vol.31, pp.311-330, 2008.
15. S. Ueda and S. Tani, Thermal Stress Intensity Factors for Two Coplanar Cracks in a Piezoelectric Strip, *Journal of Thermal Stresses,* Vol.31, pp.403-415, 2008.
16. B.L. Wang and Y.W. Mai, Impermeable Crack and Permeable Crack Assumptions, Which One is More Realistic? *Transactions of the ASME, Journal of Applied Mechanics,* Vol.71, pp.575-578, 2004.
17. S. Ueda, Effects of Crack Surface Conductance on Intensity Factors for a Cracked Functionally Graded Piezoelectric Material under Thermal load, *Journal of Thermal Stresses,* Vol.30, pp.731-752, 2007.
18. S. Ueda, A Cracked Functionally Graded Piezoelectric Material Strip Under Transient Thermal Loading, *Acta Mechanica,* Vol.199, pp.53-70, 2008.
19. I.N. Sneddon and M. Lowengrub, *Crack Problems in the Classical Theory of Elasticity,* John Wiley & Sons, Inc., New York, 1969.
20. F. Erdogan and B.H. Wu, Crack Problems in FGM Layers Under Thermal Stresses, *Journal of Thermal Stresses,* Vol.19, pp.237-265, 1996.
21. F. Erdogan, G.D. Gupta and T.S. Cook, *Methods of Analysis and Solution of Crack Problems* (Edited by G.C. Sih), Noordhoff, Leyden, 1972.
22. S. Ueda, Thermal Intensity Factors for a Parallel Crack in a Functionally Graded Piezoelectric Strip, *Journal of Thermal Stresses,* Vol.30, pp.321-342, 2007.

Elastodynamic Doppler Effects by a Moving Interface

Kazumi Watanabe and Naobumi Sumi

Abstract A unified mathematical technique for analyzing a one-dimensional Doppler effects by a moving interface is presented. Exact and closed form expressions for stress waves are obtained. The solution for the stress has no restriction not only for the motion of the interface, but also for the wave nature, impulsive or time-harmonic. As an application example, the Doppler frequency shifts by the uniform and back and forth motions of the interface are discussed for the time-harmonic wave.

1 Introduction

There are two types of the Doppler frequency shift. The one is induced by a moving source and the other by a moving reflector. The latter is named as "scattering" Doppler effects and is called "moving mirror problem" for light and electromagnetic waves. The Doppler frequency shift in electromagnetic and acoustic waves is widely used as the sensing principle, such as laser and ultrasonic velocity meters. The outline of the existing theoretical work for the Doppler effects by the uniformly moving reflector/interface can be found in a relatively updated work by Huang [1]. The Doppler effect by a non-uniformly moving edge of a string has been discussed by Censor[2] and he applied his technique to the Doppler effect for the electromagnetic waves. An approximation technique for the back and forth motion of a mirror has been developed by Van Bladel and De Zutter[3]. In addition to [1], the Doppler

---

Kazumi Watanabe
Department of Mechanical Engineering, Yamagata University, Yonezawa, Yamagata 992-8510 Japan, e-mail: kazy@yz.yamagata-u.ac.jp

Naobumi Sumi
Faculty of Education, Shizuoka University, Shizuoka 422-8529 Japan, e-mail: einsumi@ipc.shizuoka.ac.jp

effects by a uniformly moving electromagnetic interface have also been discussed by Yeh[4], and by Daly and Gruenberg[5] for 2D oblique incident wave. However, the work on the scattering Doppler effects for elastic wave is very scarcely because of its less applicability for solid media. At the present time, the authors can not find any application of the scattering Doppler effects in elastic solid media. But, as the natural extension of academic interest and a hopeful application in the future, the Doppler effect by the moving interface in elastic media is an attractive subject. If the moving interface in the elastic media is considered as a model of the dynamic deformation or phase transformation, the scattering Doppler effects in the solid will play some roles for developing sensing instruments which detect the dynamic deformation.

The present paper develops a unified mathematical technique for analyzing the 1D scattering Doppler effects by the moving interface which separates two dissimilar elastic media. The mathematics developed here is a revised and generalized version of Censors[2]. Our solution is valid for all types of wave form and the interface motion. Applying this general solution to the case of the back and forth motion of the interface, the Doppler effects are discussed for a time-harmonic incident wave.

2 Elastodynamic Scattering Doppler Effect

Let us consider two dissimilar elastic half spaces and take x-axis as shown in Fig. 1. Their interface is moving along the x-axis and is on $x = 0$ at time $t = 0$ and its traveling distance is an arbitrary time function, $l(t)$. We employ the numerical subscripts, 1 and 2, to distinguish two materials and discuss the Doppler effects for the dilatational wave. The 1D dilatational wave field is governed by the equations,

$$\frac{\partial^2 u_x}{\partial x^2} = \frac{1}{c_d^2}\frac{\partial^2 u_x}{\partial t^2} , \quad \sigma_{xx} = (\lambda + 2\mu)\frac{\partial u_x}{\partial x} , \quad c_d = \sqrt{(\lambda + 2\mu)/\rho}, \tag{1}$$

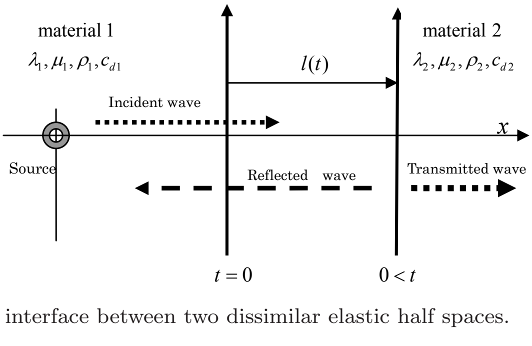

Fig. 1 A moving interface between two dissimilar elastic half spaces.

where u_x and σ_{xx} are the displacement and stress, λ, ν, ρ are Lame's constants and density, and c_d is the velocity of the dilatational wave. Here, we have assumed that *the motion of the interface does not cause any additional disturbances in the wave field* and thus the governing equation (1) holds for all time and the whole region.

We consider an incident wave in the material 1 and it has the arbitrary wave form as

$$u_{x1}^{(i)} = u_0 f\left(t - x/c_{d1}\right)\ , \quad \sigma_{xx1}^{(i)} = -\frac{u_0}{c_{d1}}(\lambda_1 + 2\mu_1) f'\left(t - x/c_{d1}\right), \tag{2}$$

where the arbitrary wave form function $f(z)$ has a single variable z and its derivative is denoted by

$$f'(z) = df(z)/dz \tag{3}$$

In general, as we do not know the frequencies of reflected and transmitted waves in advance, these waves are assumed in the form of Fourier integral with respect to the frequency (This idea is the same as Censors[2]). They are

$$u_{x1}^{(r)} = u_0 \int_{-\infty}^{+\infty} \frac{1}{\varpi} R(\varpi) e^{+i\varpi(t+x/c_{d1})} d\varpi, \tag{4}$$

$$\sigma_{xx1}^{(r)} = \frac{iu_0}{c_{d1}}(\lambda_1 + 2\mu_1) \int_{-\infty}^{+\infty} R(\varpi) e^{+i\varpi(t+x/c_{d1})} d\varpi, \tag{5}$$

for the reflected wave, and

$$u_{x2}^{(t)} = u_0 \int_{-\infty}^{+\infty} \frac{1}{\varpi} T(\varpi) e^{+i\varpi(t-x/c_{d2})} d\varpi, \tag{6}$$

$$\sigma_{xx2}^{(t)} = -\frac{iu_0}{c_{d2}}(\lambda_2 + 2\mu_2) \int_{-\infty}^{+\infty} T(\varpi) e^{+i\varpi(t-x/c_{d2})} d\varpi, \tag{7}$$

for the transmitted wave, where two unknown functions, $R(\varpi)$ and $T(\varpi)$, would be called as the spectrum amplitude.

In order to determine the unknown spectrums, we employ boundary conditions at the moving interface, $x = l(t)$. They are the continuities of the displacement and stress,

$$u_{x1}^{(i)} + u_{x1}^{(r)} = u_{x2}^{(t)}\ , \quad \sigma_{xx1}^{(i)} + \sigma_{xx1}^{(r)} = \sigma_{xx2}^{(t)}\ , \quad x = l(t). \tag{8}$$

Substituting Eqs. (2)-(7) into Eq.(8), we have the coupled integral equations for the spectrum amplitudes,

$$\int_{-\infty}^{+\infty} \frac{1}{\varpi} R(\varpi) e^{+i\varpi\{t+l(t)/c_{d1}\}} d\varpi - \int_{-\infty}^{+\infty} \frac{1}{\varpi} T(\varpi) e^{+i\varpi\{t-l(t)/c_{d2}\}} d\varpi = \\ = -f\left(t - l(t)/c_{d1}\right), \quad (9)$$

$$\int_{-\infty}^{+\infty} R(\varpi) e^{+i\varpi\{t+l(t)/c_{d1}\}} d\varpi + \frac{1}{Z} \int_{-\infty}^{+\infty} T(\varpi) e^{+i\varpi\{t-l(t)/c_{d2}\}} d\varpi = \\ = -if'\left(t - l(t)/c_{d1}\right), \quad (10)$$

where Z is the impedance ratio defined by

$$Z = \frac{\lambda_1 + 2\mu_1}{\lambda_2 + 2\mu_2} \frac{c_{d2}}{c_{d1}} = \sqrt{\frac{(\lambda_1 + 2\mu_1)\rho_1}{(\lambda_2 + 2\mu_2)\rho_2}}. \quad (11)$$

In order to make the same integration form for each spectrum amplitude, we differentiate Eq. (9) with respect to time t,

$$\{1 + M_1(t)\} \int_{-\infty}^{+\infty} R(\varpi) e^{+i\varpi\{t+l(t)/c_{d1}\}} d\varpi - \{1 - M_2(t)\} \times \\ \times \int_{-\infty}^{+\infty} T(\varpi) e^{+i\varpi\{t-l(t)/c_{d2}\}} d\varpi = i\{1 - M_1(t)\} f'\left(t - l(t)/c_{d1}\right), \quad (12)$$

where Mach numbers which are varying with time are defined by

$$M_j(t) = \frac{1}{c_{dj}} \frac{dl(t)}{dt}\ ; \quad j = 1, 2. \quad (13)$$

Then, Eqs. (10) and (12) constitute the algebraic simultaneous equations for the integral of the spectrum amplitude and are solved as

$$\int_{-\infty}^{+\infty} R(\varpi) e^{+i\varpi\{t+l(t)/c_{d1}\}} d\varpi = +i \frac{1 - M_1(t) - Z\{1 - M_2(t)\}}{1 + M_1(t) + Z\{1 - M_2(t)\}} f'\left(t - \frac{l(t)}{c_{d1}}\right), \quad (14)$$

$$\int_{-\infty}^{+\infty} T(\varpi) e^{+i\varpi\{t-l(t)/c_{d2}\}} d\varpi = -i \frac{2Z}{1 + M_1(t) + Z\{1 - M_2(t)\}} f'\left(t - \frac{l(t)}{c_{d1}}\right). \quad (15)$$

The form of the integration in the above equations is very close to that of the Fourier transform, but the exponents of exponential function is slightly different from that of the standard Fourier transform. However, we can find a transform couple for the Fourier transform with non-uniform parameter. That is

$$F(x) = \int_a^b f(\xi) \exp\{+i\xi h(x)\} d\xi \; ; \quad -\infty < x < +\infty$$

$$f(\xi) = \frac{1}{2\pi} \int_{-\infty}^{+\infty} F(x) \exp\{-i\xi h(x)\} h'(x) dx \; ; \quad a < \xi < b \tag{16}$$

where a and b are constants, and $h(x)$ is a monotonically increasing function.

If we assume that the velocity of the moving interface is subsonic for both materials, the two time functions in the argument of the exponential function in Eqs. (14) and (15),

$$T_1(t) = t + l(t)/c_{d1} \; , \quad T_2(t) = t - l(t)/c_{d2}, \tag{17}$$

are monotonically increasing. Then, these functions should be understood as the non-uniform parameter $h(x)$ and apply the transform formula (16) to Eqs. (14) and (15), we have

$$R(\varpi) = \frac{i}{2\pi} \int_{-\infty}^{+\infty} C^{(r)}(t) f'\left(t - l(t)/c_{d1}\right) e^{-i\varpi T_1(t)} T_1'(t) dt \tag{18}$$

$$T(\varpi) = \frac{-i}{2\pi} \int_{-\infty}^{+\infty} C^{(t)}(t) f'\left(t - l(t)/c_{d1}\right) e^{-i\varpi T_2(t)} T_2'(t) dt \tag{19}$$

where $T_j'(t) = dT(t)/dt$, and reflection and transmission coefficients which are not constants are

$$(C^{(r)}(t), C^{(t)}(t)) = \frac{(1 - M_1(t) - Z\{1 - M_2(t)\}, 2Z)}{1 + M_1(t) + Z\{1 - M_2(t)\}}. \tag{20}$$

We have just obtained the spectrum amplitude in the form of Fourier inversion integral. It is no need to evaluate the integral, since this form is preferable for the subsequent treatise. Substituting Eqs. (18) and (19) into the stress wave of Eq. (5) and (7) respectively, and changing the order of integration,

$$-\frac{\sigma_{xx1}^{(r)}}{\lambda_1 + 2\mu_1} = \frac{u_0}{2\pi c_{d1}} \int_{-\infty}^{+\infty} C^{(r)}(\tau) f'\left(\tau - l(\tau)/c_{d1}\right) T_1'(\tau) d\tau \times$$
$$\times \int_{-\infty}^{+\infty} e^{-i\varpi\{T_1(\tau) - (t + x/c_{d1})\}} d\varpi, \tag{21}$$

$$-\frac{\sigma_{xx2}^{(t)}}{\lambda_1+2\mu_1} = \frac{u_0}{2\pi c_{d1}} \int_{-\infty}^{+\infty} C^{(t)}(\tau) f'\left(\tau - l(\tau)/c_{d1}\right) T_2'(\tau) d\tau \times$$

$$\times \int_{-\infty}^{+\infty} e^{-i\varpi\{T_2(\tau)-(t-x/c_{d2})\}} d\varpi. \tag{22}$$

These inner integrals are easily evaluated by applying the integration formula for the Dirac's delta function,

$$\int_{-\infty}^{+\infty} e^{-i\varpi x} d\varpi = 2\pi\delta(x). \tag{23}$$

Eqs. (21) and (22) yield to the form of the single integral,

$$-\frac{\sigma_{xx1}^{(r)}}{\lambda_1+2\mu_1} =$$

$$= \frac{u_0}{c_{d1}} \int_{-\infty}^{+\infty} C^{(r)}(\tau) f'\left(\tau - l(\tau)/c_{d1}\right) T_1'(\tau) \delta\left(T_1(\tau) - (t + x/c_{d1})\right) d\tau, \tag{24}$$

$$-\frac{\sigma_{xx2}^{(t)}}{\lambda_1+2\mu_1} =$$

$$= \frac{u_0}{c_{d1}} \int_{-\infty}^{+\infty} C^{(t)}(\tau) f'\left(\tau - l(\tau)/c_{d1}\right) T_2'(\tau) \delta\left(T_2(\tau) - (t - x/c_{d2})\right) d\tau. \tag{25}$$

Further, we apply the integration formula,

$$\int_{-\infty}^{+\infty} \delta(T(\tau) - x) g(\tau) T'(\tau) d\tau = g(T^{-1}(x)). \tag{26}$$

where $T^{-1}(x)$ is the inverse function of $x = T(\tau)$.

Finally, we have the exact closed form solution for the stress wave,

$$-\frac{\sigma_{xx1}^{(r)}}{\lambda_1+2\mu_1} = \frac{u_0}{c_{d1}} C^{(r)}(t_1) f'\left(t_1 - l(t_1)/c_{d1}\right), \tag{27}$$

$$-\frac{\sigma_{xx2}^{(t)}}{\lambda_1+2\mu_1} = \frac{u_0}{c_{d1}} C^{(t)}(t_2) f'\left(t_2 - l(t_2)/c_{d1}\right), \tag{28}$$

where t_1 and t_2 are inverse functions defined by

$$t_1 = T_1^{-1}(t + x/c_{d1}) \quad \Leftrightarrow \quad t + x/c_{d1} = T_1(t_1),$$
$$t_2 = T_2^{-1}(t - x/c_{d2}) \quad \Leftrightarrow \quad t - x/c_{d2} = T_2(t_2). \tag{29}$$

As for the displacement, Eqs. (18) and (19) are substituted into Eqs. (4) and (6) respectively, and the order of integration is also exchanged. We have

$$\frac{u_{x1}^{(r)}}{u_0} = +\frac{i}{2\pi} \int\limits_{-\infty}^{+\infty} C^{(r)}(\tau) f'\left(\tau - l(\tau)/c_{d1}\right) T_1'(\tau) d\tau \times \\ \times \int\limits_{-\infty}^{+\infty} \frac{1}{\varpi} e^{-i\varpi\{T_1(\tau)-(t+x/c_{d1})\}} d\varpi, \tag{30}$$

$$\frac{u_{x2}^{(t)}}{u_0} = -\frac{i}{2\pi} \int\limits_{-\infty}^{+\infty} C^{(t)}(\tau) f'\left(\tau - l(\tau)/c_{d1}\right) T_2'(\tau) d\tau \times \\ \times \int\limits_{-\infty}^{+\infty} \frac{1}{\varpi} e^{-i\varpi\{T_2(\tau)-(t-x/c_{d2})\}} d\varpi. \tag{31}$$

The integration formula,

$$\int\limits_{-\infty}^{+\infty} \frac{1}{\varpi} e^{-i\varpi x} d\varpi = \begin{cases} -\pi i\,; & x > 0, \\ +\pi i\,; & x < 0, \end{cases} \tag{32}$$

is applied to Eqs. (30) and (31). Then, the displacement wave is given in the form of integral,

$$\frac{u_{x1}^{(r)}}{u_0} = +\frac{1}{2} \int\limits_{\tau=T_1^{-1}(t+x/c_{d1})}^{+\infty} C^{(r)}(\tau) f'\left(\tau - l(\tau)/c_{d1}\right) T_1'(\tau) d\tau - \\ -\frac{1}{2} \int\limits_{-\infty}^{\tau=T_1^{-1}(t+x/c_{d1})} C^{(r)}(\tau) f'\left(\tau - l(\tau)/c_{d1}\right) T_1'(\tau) d\tau, \tag{33}$$

$$\frac{u_{x2}^{(t)}}{u_0} = -\frac{1}{2}\int_{\tau=T_2^{-1}(t-x/c_{d2})}^{+\infty} C^{(t)}(\tau) f'\left(\tau - l(\tau)/c_{d1}\right) T_2'(\tau)d\tau + \\ +\frac{1}{2}\int_{-\infty}^{\tau=T_2^{-1}(t-x/c_{d2})} C^{(t)}(\tau) f'\left(\tau - l(\tau)/c_{d1}\right) T_2'(\tau)d\tau. \tag{34}$$

Consequently, the reflected and transmitted stress waves are obtained exactly. However, it is little bit regrettable that the displacement wave is in the form of integral, not in the closed form. Some applications of this exact solution are shown and the Doppler effects are also discussed in the subsequent sections.

3 Time-Harmonic Wave

When the incident wave is sinusoidal with frequency ω,

$$f(z) = \cos(\omega z)\ , \quad f'(z) = -\omega\sin(\omega z) \tag{35}$$

the stress wave for any motion of the interface is given by

$$\frac{\sigma_{xx1}^{(i)}}{\lambda_1 + 2\mu_1} = \frac{\omega u_0}{c_{d1}}\sin\left\{\omega(t - x/c_{d1})\right\}, \tag{36}$$

$$\frac{\sigma_{xx1}^{(r)}}{\lambda_1 + 2\mu_1} = \frac{\omega u_0}{c_{d1}} C^{(r)}(t_1)\sin\left[\omega\left\{t_1 - l(t_1)/c_{d1}\right\}\right]\ , t_1 = T_1^{-1}(t + x/c_{d1}), \tag{37}$$

$$\frac{\sigma_{xx2}^{(t)}}{\lambda_1 + 2\mu_1} = \frac{\omega u_0}{c_{d1}} C^{(t)}(t_2)\sin\left[\omega\left\{t_2 - l(t_2)/c_{d1}\right\}\right]\ , t_2 = T_2^{-1}(t - x/c_{d2}). \tag{38}$$

Here, the displacement wave is left to the integral form of Eqs. (33) and (34), since the interface motion $l(t)$ is not specified.

Fortunately, the exact expression for the stress gives us a good chance to discuss the Doppler effects. The arguments, so called phase, in the reflection and transmission waves are time-dependent,

$$\Theta_r(t,x) = \omega\left\{t_1 - l(t_1)/c_{d1}\right\}\ , \quad \Theta_t(t,x) = \omega\left\{t_2 - l(t_2)/c_{d1}\right\}. \tag{39}$$

We define the instantaneous frequency for each wave. Differentiating Eq. (39) with respect to time and with aids of the nature of the inverse function defined by Eq. (29), the instantaneous frequency is derived as

$$\omega_r(t,x) = \frac{\partial\Theta_r(t,x)}{\partial t} = \frac{1 - M_1(t_1)}{1 + M_1(t_1)}\omega, \tag{40}$$

for the reflected wave, and

$$\omega_t(t,x) = \frac{\partial \Theta_t(t,x)}{\partial t} = \frac{1 - M_1(t_2)}{1 - M_2(t_2)}\omega, \tag{41}$$

for the transmitted wave, where the non-uniform Mach numbers are defined by Eq. (13). The Doppler frequency shifts, which are thus time-dependent, are

$$\frac{\Delta\omega_r}{\omega} = \frac{\omega_r(t,x) - \omega}{\omega} = -\frac{2M_1(t_1)}{1 + M_1(t_1)}, \tag{42}$$

$$\frac{\Delta\omega_t}{\omega} = \frac{\omega_t(t,x) - \omega}{\omega} = -\frac{M_1(t_2) - M_2(t_2)}{1 - M_2(t_2)}. \tag{43}$$

Then, we readily learn that the Doppler frequency shifts depend only on the Mach numbers and their equation forms are unchanged for any motion of the interface. This guarantees the approximation method [3].

3.1 Uniform motion

When the interface moves uniformly with velocity V,

$$l(t) = Vt, \tag{44}$$

$$M_j = V/c_{dj}\ , \quad j = 1, 2, \tag{45}$$

the coefficients of reflection and transmission are constant,

$$C_r \equiv C^{(r)}(t) = \frac{1 - M_1 - Z(1 - M_2)}{1 + M_1 + Z(1 - M_2)}\ ,\ C_t \equiv C^{(t)}(t) = \frac{2Z}{1 + M_1 + Z(1 - M_2)}, \tag{46}$$

and two inverse functions are expressed exactly,

$$t_1 = T_1^{-1}(\tau) = \frac{\tau}{1 + M_1}\ , \quad t_2 = T_2^{-1}(\tau) = \frac{\tau}{1 - M_2}. \tag{47}$$

Then, the stress wave yields

$$\frac{\sigma_{xx1}^{(i)}}{\lambda_1 + 2\mu_1} = \frac{\omega u_0}{c_{d1}} \sin\left\{\omega(t - x/c_{d1})\right\}, \tag{48}$$

$$\frac{\sigma_{xx1}^{(r)}}{\lambda_1 + 2\mu_1} = \frac{\omega u_0}{c_{d1}} \frac{1 - M_1 - Z(1 - M_2)}{1 + M_1 + Z(1 - M_2)} \sin\left\{\frac{1 - M_1}{1 + M_1}\omega(t + x/c_{d1})\right\}, \tag{49}$$

$$\frac{\sigma_{xx2}^{(t)}}{\lambda_1 + 2\mu_1} = \frac{\omega u_0}{c_{d1}} \frac{2}{1 + M_1 + Z(1 - M_2)} \sin\left\{\frac{1 - M_1}{1 - M_2}\omega(t - x/c_{d2})\right\}, \tag{50}$$

and the Doppler frequency shifts are

$$\omega^{(r)} = \frac{1-M_1}{1+M_1}\omega\ , \quad \frac{\varDelta\omega^{(r)}}{\omega} = \frac{\omega^{(r)}-\omega}{\omega} = -\frac{2M_1}{1+M_1}, \tag{51}$$

for the reflected wave, and

$$\omega^{(t)} = \frac{1-M_1}{1-M_2}\omega\ , \quad \frac{\varDelta\omega^{(t)}}{\omega} = \frac{\omega^{(t)}-\omega}{\omega} = -\frac{M_1-M_2}{1-M_2}, \tag{52}$$

for the transmitted wave.

3.2 Back and forth motion

When the motion of the interface is back and forth, and its maximum velocity is subsonic for both materials,

$$l(t) = l_0\sin(\lambda t)\ , \quad M_j^* = \lambda l_0/c_{dj} < 1\ , \quad j = 1,2. \tag{53}$$

Then Mach numbers are periodic functions of time,

$$M_j(t) = M_j^*\cos(\lambda t)\ , \quad j = 1,2. \tag{54}$$

and the reflection and transmission coefficients, defined by Eq. (20), are also periodic. In this case, two inverse functions $t_j = T_j^{-1}(\cdot)$ have no explicit expressions and we have to obtain t_j numerically, based on their definitions,

$$\begin{aligned} t + x/c_{d1} &= T_1(t_1) = t_1 + (l_0/c_{d1})\sin(\lambda t_1),\\ t - x/c_{d2} &= T_2(t_2) = t_2 - (l_0/c_{d2})\sin(\lambda t_2). \end{aligned} \tag{55}$$

After getting t_j numerically, the periodic Doppler frequency shift and amplitude modulation are given by

$$\frac{\varDelta\omega_r}{\omega} = -\frac{2M_1^*\cos(\lambda t_1)}{1+M_1^*\cos(\lambda t_1)}, \tag{56}$$

$$C^{(r)}(t_1) = \frac{1-M_1(t_1)-Z\{1-M_2(t_1)\}}{1+M_1(t_1)+Z\{1-M_2(t_1)\}}, \tag{57}$$

for the reflected wave, and

$$\frac{\varDelta\omega^{(t)}}{\omega} = -\frac{M_1^*-M_2^*}{1-M_2^*\cos(\lambda t_2)}\cos(\lambda t_2), \tag{58}$$

$$C^{(t)}(t_2) = \frac{2Z}{1+M_1(t_2)+Z\{1-M_2(t_2)\}}. \tag{59}$$

for the transmitted wave.

In the practical use, it is not convenient to obtain the inverse, $t_j = T_j^{-1}(\cdot)$, numerically. But, fortunately, if the Mach numbers are sufficient small, $|M_j| \ll 1$, the inverse functions can be approximated as

$$\begin{aligned} t_1 &= T_1^{-1}(t + x/c_{d1}) \approx t + x/c_{d1}, \\ t_2 &= T_2^{-1}(t - x/c_{d2}) \approx t - x/c_{d2}. \end{aligned} \tag{60}$$

Then, we will have exact expressions for frequency shifts and the stress response.

Figure 2 shows a typical time-response of the reflected stress wave for three impedance ratios. The computations are carried out based on the numerical inversion for the inverse function. The amplitude of the high frequency carrier wave is modulated and its amplitude modulation becomes clearer especially in Fig. 2(c). However, the frequency modulation which is defined by Eq. (56) is less visible, since the Mach number $M_1^* = 0.1$ is so small. The amplitude modulation is caused by the periodic change of the amplitude equation (20) with its frequency λ of the back and forth motion. Thus, this amplitude modulation may be a key signal for detecting the interface motion.

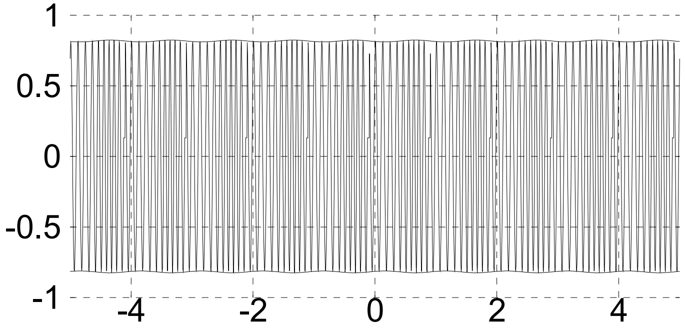

(a) $Z = 10$

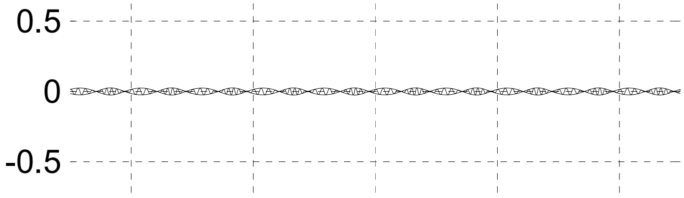

(b) $Z = 1$

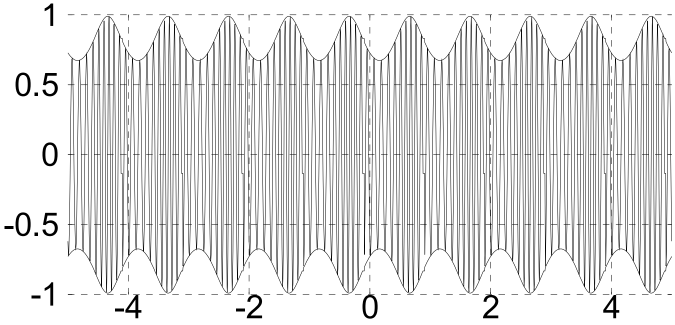

$(c)\ Z = 0.1$

Fig. 2 Typical wave forms for reflected stress wave $(\lambda_1{+}2\nu_1)^{-1}(c_{d1}/\omega u_0)\sigma_{xx1}^{(r)}$. $(l_0\omega/c_{d1} = 1$, $l_0\lambda/c_{d1} = 0.1$, $c_{d1}/c_{d2} = 0.5$, $x/l_0 = -10)$

4 Conclusion

A unified mathematical technique for the 1D elastodynamic Doppler effect by the moving interface has been developed. The exact closed form solution obtained is valid not only for the arbitrary interface motion, but also for every wave form. The solution is applied to the case of the standard uniform motion, and of the back and forth motion. It is shown that the amplitude modulation takes place when the interface motion is periodic, and reflected and transmitted waves include not only the Doppler frequency shit, but also amplitude modulation. The frequency of the amplitude modulation is the same as that of interface motion. These amplitude and frequency modulations may be useful information for developing a motion sensor for detecting the dynamic deformation of solids.

References

1. Y.-X. Huang, Reflection and transmission of electromagnetic waves by a dielectric medium moving in an arbitrary direction, J. Appl. Phys., Vol. 76 (5) (1994), pp. 2575-2581.
2. D. Censor, The generalized Doppler effect and applications, J. Franklin Instit., Vol. 295 (1973), No. 2, pp. 103-116.
3. J. Van Bladel and D. De Zutter, Reflections from linearly vibrating objects: Plane mirror at normal incidence, IEEE trans. Anten. Prop. Vol. AP-29 (1981), No. 4, pp. 629-637.
4. C. Yeh, Reflection and transmission of electromagnetic waves by a moving dielectric medium, J. Appl. Phys., Vo. 36 (1965), No. 11, pp. 3513-3517.
5. P. Daly and H. Gruenberg, Energy relations for plane waves reflected from moving media, J. Appl. Phys., Vol. 38 (1967), No. 11, pp. 4468-4489.

Compensation of flexible vibrations in a two-link robot by piezoelectric actuation

C. Zehetner and J. Gerstmayr

Abstract This paper concerns the active control of flexural vibrations in a two-link robot consisting of two flexible arms with tip masses. Due to inertial forces of distributed and concentrated masses flexural vibrations occur. The robot is moving in a horizontal plane, such that gravity is not considered. In order to compensate the flexible vibrations, piezoelectric actuators are integrated in the arms. In the framework of linear beam theory, the solution of the shape control problem is derived, i.e. the necessary distribution of the piezoelectric actuation strains in order to completely compensate the inertial forces. Assuming that mass distribution, geometrical properties and the link angles are exactly known by appropriate measurements, the flexible vibrations can be fully suppressed. If some parameters are not known exactly, remaining vibrations may occur. Numerical simultions are performed in order to verify the solution of shape control and to study the sensitivity to uncertainties of the parameters.

1 Introduction

The present paper deals with the control of vibrations in flexible multi-body systems using piezoelectric actuation [1]. Exemplarily, a two-link robot consisting of two flexible arms with concentrated tip masses is considered, in which flexible vibrations are caused by inertial forces. In the first step, a solution of the shape control problem is applied, i.e. the distribution of piezo-

---

Christian Zehetner
Linz Center of Mechatronics GmbH, A-4040 Linz, Austria,
e-mail: christian.zehetner@lcm.at

Johannes Gerstmayr
Linz Center of Mechatronics GmbH, A-4040 Linz, Austria
e-mail: johannes.gerstmayr@lcm.at

electric actuation strains is derived in order to compensate the inertial forces. For review on shape control of structures see Irschik [2], applications to elastic structures performing large rigidbody motions have been presented in [3] - [5].

The shape control solution can be considered as a feed-forward control strategy: Assuming that the inertial forces are known by appropriate measurement of the link angles and their time-derivatives, the distributed actuating moment is applied by piezoelectric actuation. It turns out that for each arm at least three spatially distributed actuating moments with different time responses are needed in order to completely compensate the inertial forces.

If there are uncertainties of the parameters, e.g. the mass distribution or geometrical properties of the robot are not exactly known, the vibrations cannot be suppressed completely by means of feed-forward shape control. In order to verify the derived solution of shape control and to study the sensitivity to uncertainties of the parameters, numerical simulations have been implemented within the multibody dynamics simulation code HOTINT [1]. The numerical model includes large deformation beam elements for the robot arms, actuating piezoelectric elements and open loop shape control. The beam elements are based on specific large deformation beam elements, which are available for the Bernoulli Euler case [6] and the shear deformable (Timoshenko) case [7]. Numerical computations are performed with main goal to find an efficient configuration of patches and to test if the system shows the desired behavior.

2 Shape control of a moving cantilever beam

In this section, an initially straight laminated elastic beam is considered which is performing a rigid-body motion in a horizontal plane. Two Cartesian coordinate frames are indroduced: the inertial frame (x_0, y_0, z_0) and the floating frame (x, y, z) which is fixed to the left end B of the beam. The motion is assumed to take place in the plane (x_0, z_0) which is parallel to the plane (x, z). For the notion of a floating frame of reference, see Shabana [8]. The rigid-body motion is determined by the coordinates $x_B^0 = x_B^0(t)$ and $z_B^0 = z_B^0(t)$ of the origin of the floating frame, and its orientation $\varphi = \varphi(t)$ with respect to the inertial frame. The x-axis of the floating system represents the beam axis, with respect to which elastic vibrations take place in the (x, z) plane. The elastic displacement of point P on the beam axis is described by the extension $u = u(x, t)$ and the deflection $w = w(x, t)$. As external excitations, a concentrated tip moment $M_y^e = M_y^e(t)$ and a tip force with the components $F_x^e = F_x^e(t)$ and $F_z^e = F_z^e(t)$ are considered.

In the framework of Bernoulli-Euler beam theory, axial stress is assumed

---

[1] http://tmech.mechatronik.uni-linz.ac.at/staff/gerstmayr/hotint.html

to be predominant, such that the consitututive relations for a laminated beam consisting of passive and actuating layers are given in the additive form

$$\sigma_{xx} = E(\varepsilon_{xx} - \varepsilon^0_{xx}), \qquad \varepsilon^0_{xx} = d_{31} E_z, \tag{1}$$

where σ_{xx} is the axial component of stress, E is an effective Young modulus and ε^0_{xx} is called the axial eigenstrain. In thin piezoelectric layers, the eigenstrains represent the converse piezoelectric effect, with the piezoelectric coefficient d_{31} and the electric field E_z in thickness direction of a layer.

In Zehetner and Irschik [5], the equations of motion for a beam without tip loads have been derived. Considering the latter, yields

$$(A_{11}u')' - \mu(\ddot{u} + 2\dot{w}\dot{\varphi} + w\ddot{\varphi} - u\dot{\varphi}^2) = N'_a - q^e_x, \tag{2}$$

$$-(D_{11}w'')'' - \mu(\ddot{w} + 2\dot{u}\dot{\varphi} - u\ddot{\varphi} - w\dot{\varphi}^2) = M''_a - q^e_z, \tag{3}$$

$$x = 0: \quad u = w = w' = 0, \tag{4}$$

$$x = L: \quad \begin{cases} A_{11}u' = F^e_x + N_a \\ -(D_{11}w'')' = F^e_z + M'_a \\ -D_{11}w'' = M^e_y + M_a \end{cases} \tag{5}$$

with the mass per unit length $\mu = \mu(x) = \int_{A(x)} \rho(x) \mathrm{d}A$. q^e_x and q^e_y are effective distributed forces per unit length caused by inertial forces, $A_{11} = A_{11}(x)$ and $D_{11} = D_{11}(x)$ are effective beam stiffnesses, $N_a = N_a(x,t)$ and $M_a = M_a(x,t)$ represent the actuating force and moment,

$$\begin{aligned} q^e_x &= -\mu(\ddot{x}^0_B \cos\varphi - \ddot{z}^0_B \sin\varphi - x\dot{\varphi}^2), \\ q^e_z &= -\mu(\ddot{x}^0_B \sin\varphi + \ddot{z}^0_B \cos\varphi - x\ddot{\varphi}), \end{aligned} \tag{6}$$

$$\begin{aligned} A_{11} &= \textstyle\int_A E \ \mathrm{d}A, \quad D_{11} = \int_A E z^2 \ \mathrm{d}A, \\ N_a &= \textstyle\int_A E\varepsilon^0_{xx} \ \mathrm{d}A, \quad M_a = \int_A E\varepsilon^0_{xx} z \ \mathrm{d}A. \end{aligned} \tag{7}$$

The initial-boundary value problem formed by equations (2) - (5) is linear with respect to the flexible coordinates u and w, φ, x^0_B and z^0_B are considered as prescribed functions of time. In the following it is assumed that axial vibrations are so small that they can be neglected.

The solution of shape control for transversal beam vibrations is expressed as follows: The effective external excitations are compensated, if the right hand sides of Eqs. (2), (3) and (5) vanish, i.e.

$$M''_a = q^e_z, \qquad x = L: \quad M_a = -M^e_y, \quad M'{}_a = -F^e_z. \tag{8}$$

Integration yields the actuating moment

$$M_a = -M^e_y - F^e_z L(1-\xi) - L^2 \int_\xi^1 (\bar{\xi} - \xi) q_z(\bar{\xi}) \ \mathrm{d}\bar{\xi}, \qquad \xi = \mathrm{x/L}. \tag{9}$$

If the motion starts from rest, i.e. $w(t=0) = \dot{w}(t=0) = 0$, then the elastic displacements vanish, i.e. $w(x,t) = 0$. In the following, the solution of shape control is applied to a two-link robot.

3 Compensation of flexural vibrations in a two-link robot

Figure 1 shows a two-link robot consisting of two flexible arms with lengths L_1, L_2, masses per unit length μ_1, μ_2 and concentrated masses m_1, m_2. The effective loads for the two arms read

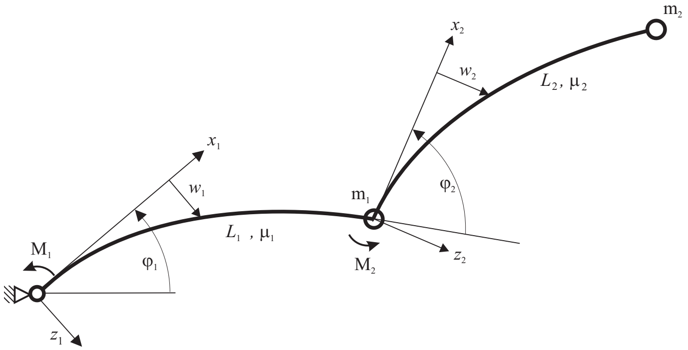

Fig. 1 Two-link robot

$$\begin{aligned}
\text{Arm 1:}\quad & q^e_{z,1} = \mu_1 \xi L_1 \ddot{\varphi}_1, \quad F^e_{z,1} = m_1 L_1 \ddot{\varphi}_1 + m_2 h_{z,1}(t) + \mu_2 L_2 h_{z,2}(t),\\
& M^e_{y,1} = m_2(L_1 g_{z,1}(t) + L_2 \ddot{\varphi}_2) + \mu_2(\frac{1}{2} g_{z,1}(t) L_1 L_2^2 + \frac{1}{3}\ddot{\varphi}_2 L_2^3), \quad (10)\\
\text{Arm 2:}\quad & q^e_{z,2} = \mu_2 L_1 g_{z,1}(t) + \mu_2 \xi L_2 \ddot{\varphi}_2,\\
& F^e_{z,2} = m_2 L_1 g_{z,1}(t) + m_2 L_2 \ddot{\varphi}_2, \quad M^e_{y,2} = 0, \quad (11)
\end{aligned}$$

where $\phi_2 = \varphi_1 + \varphi_2$ has been introduced and $g_{x,1}$, $g_{z,1}$, $g_{x,2}$ and $g_{z,2}$ are functions of time, determined by the rigid-body motion,

$$\begin{aligned}
g_{x,1}(t) &= \ddot{\varphi}_1(\cos\phi_2 \sin\varphi_1 - \sin\phi_2 \cos\varphi_1) + \dot{\varphi}_1^2(\cos\phi_2 cos\varphi_1 + \sin\phi_2 \sin\varphi_1),\\
g_{z,1}(t) &= \ddot{\varphi}_1(\sin\phi_2 \sin\varphi_1 + \cos\phi_2 \cos\varphi_1) + \dot{\varphi}_1^2(\sin\phi_2 cos\varphi_1 - \cos\phi_2 \sin\varphi_1),\\
h_{z,1}(t) &= -(L_1 g_{x,1}(t) + L_2 \dot{\phi}_2^2) \sin\varphi_2 + (L_1 g_{z,1}(t) + L_2 \ddot{\varphi}_2) \cos\varphi_2,\\
h_{z,2}(t) &= -(L_1 g_{x,1}(t) + \tfrac{L_2}{2} \dot{\phi}_2^2 \sin\varphi_2 + (L_1 g_{z,1}(t) + \tfrac{L_2}{2} \ddot{\varphi}_2 \cos\varphi_2. \quad (12)
\end{aligned}$$

Inserting Eqs. (10) and (11) into Eq. (9) yields the actuating moments,

$$\begin{aligned} M_{a,1}(\xi,t) &= \hat{M}_{a,1}^{(0)}(t)S^{(0)}(\xi) + \hat{M}_{a,1}^{(1)}(t)S^{(1)}(\xi) + \hat{M}_{a,1}^{(3)}(t)S^{(3)}(\xi), \\ M_{a,2}(\xi,t) &= \hat{M}_{a,2}^{(1)}(t)S^{(1)}(\xi) + \hat{M}_{a,2}^{(2)}(t)S^{(2)}(\xi) + \hat{M}_{a,2}^{(3)}(t)S^{(3)}(\xi), \end{aligned} \tag{13}$$

with the shape functions

$$\begin{gathered} S^{(0)}(\xi) = 1, \quad S^{(1)}(\xi) = 1 - \xi, \quad S^{(2)}(\xi) = (1-\xi)^2, \\ S^{(3)}(\xi) = \tfrac{1}{2}(1-\xi)^2(\xi+2), \end{gathered} \tag{14}$$

and the time-dependent amplitudes

$$\begin{gathered} \hat{M}_{a,1}^{(0)}(t) = \hat{M}_{a,2}^{(1)}(t) + \hat{M}_{a,2}^{(2)}(t) + \hat{M}_{a,2}^{(3)}(t), \\ \hat{M}_{a,1}^{(1)}(t) = L_1(m_1 L_1 \ddot{\varphi}_1 + m_2 h_{z,1}(t) + \mu_2 L_2 h_{z,2}(t)), \\ \hat{M}_{a,1}^{(3)}(t) = \tfrac{1}{3}\mu_1 L_1^3 \ddot{\varphi}_1, \quad \hat{M}_{a,2}^{(1)}(t) = -m_2(L_1 g_{z,1}(t) + L_2 \ddot{\varphi}_2), \\ \hat{M}_{a,2}^{(2)}(t) = -\tfrac{1}{2} g_{z,1}(t) L_1 \mu_2 L_2^2, \quad \hat{M}_{a,2}^{(3)}(t) = -\tfrac{1}{3}\ddot{\varphi}_2 \mu_2 L_2^3. \end{gathered} \tag{15}$$

Equation 13 shows that for each arm the actuating moment is composed of three parts with different spatial distributions. Spatially distributed actuating moments can be realized e.g. by applying shaped piezoelectric layers on the arms, cf. Zehetner and Irschik [5], i.e. the width of the piezoelectric layer coincides with the spatial distribution of the actuating moment. A more practicable way is to use piezoelectric patches to discretize the distributed actuating moment, cf. Nader et al. [9].

For the following numerical evaluation it is assumed that the actuating moments in Eq. (13) are exactly applied to the arms, since main scope of the numerical simulations is to verify the solution of shape control and to study the sensitivity to uncertainties of parameters.

4 Numerical modeling of the piezo-beam-element

For the numerical simulation of the piezo-electric actuated robot, a fully nonlinear beam finite element is utilized. In the following, the equations of motion of a displacement based finite element, based on the absolute nodal coordinate formulation (ANCF), see Shabana [8], and implemented according to Gerstmayr and Irschik [6], are presented. The beam element has been extended to a formulation based on Reissner's large deformation rod theory, see Gerstmayr et al. [7]. The planar ANCF element, containing eight degrees of freedom, including coupled large bending and axial deformation. According to the Bernoulli-Euler beam theory, the latter finite element considers arbitrary large axial and bending deformation and no shear deformation. The position vector **r** of a point at the beam axis, originally placed at x, see Figure 2, is interpolated by shape functions **S** and element coordinates **q**, which

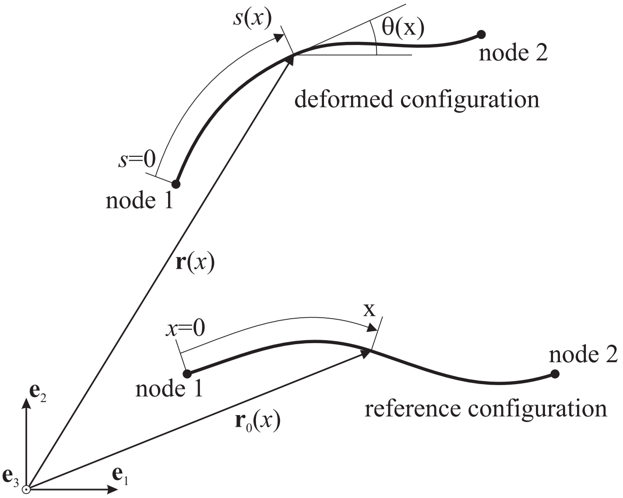

Fig. 2 Planar ANCF element.

follows as

$$\mathbf{r} = \mathbf{S}\,\mathbf{q}, \quad \mathbf{q} = \left[\mathbf{r}^{(1)^T} \quad \mathbf{r}'^{(1)^T} \quad \mathbf{r}^{(2)^T} \quad \mathbf{r}'^{(2)^T}\right]^T \tag{16}$$

with the abbreviation $\mathbf{r}' = \frac{\partial \mathbf{r}}{\partial x}$. Here, $x \in [0,\ L]$ denotes the coordinate of the undeformed beam axis. The shape function matrix $\mathbf{S}_m$ is given as,

$$\mathbf{r} = [S_1\mathbf{I} \quad S_2\mathbf{I} \quad S_3\mathbf{I} \quad S_4\mathbf{I}]\mathbf{q} = \mathbf{S}_m\mathbf{q} \tag{17}$$

where $\mathbf{I}$ is the 2×2 unit matrix. This interpolation allows coupled bending and stretching of the beam axis, while shear is not included. The single shape functions S_i are given by

$$S_1 = 1-3\frac{x^2}{L^2}+2\frac{x^3}{L^3}, \quad S_2 = x-2\frac{x^2}{L}+\frac{x^3}{L^2}, \quad S_3 = 3\frac{x^2}{L^2}-2\frac{x^3}{L^3}, \quad S_4 = -\frac{x^2}{L}+\frac{x^3}{L^2}$$

4.1 Equations of motion

The weak form of the equations of motion is derived from the Lagrange-D'Alembert equation,

$$\delta W_I + \delta W_S - \delta W_E = 0 \tag{18}$$

in which δW_I denotes the virtual work of inertia forces, δW_S is the virtual work of internal (elastic) forces and δW_E is the virtual work of external forces. The mass matrix is determined from the kinetic energy,

$$T = \frac{1}{2}\int_L \rho A \dot{\mathbf{r}}^T \dot{\mathbf{r}}\, dx = \dot{\mathbf{q}}^T \int_0^L \rho A \mathbf{S}_m^T \mathbf{S}_m\, dx\, \dot{\mathbf{q}} = \dot{\mathbf{q}}^T \mathbf{M} \dot{\mathbf{q}} \tag{19}$$

and is defined by $\mathbf{M} = \int_0^L \rho A \mathbf{S}_m^T \mathbf{S}_m\, dx$. Here, A denotes the cross sectional area of the beam element and ρ is the density. The mass matrix is constant and can be stored in sparse form. The virtual work of inertia forces (I) and external forces (E) follow as

$$\delta W_I = \ddot{\mathbf{q}}^T \mathbf{M}\, \delta\mathbf{q} \quad \text{and} \quad \delta W_E^b = \int_L A \mathbf{b}^T \delta\mathbf{r}(x)\, dx \tag{20}$$

The virtual work of elastic forces is defined by

$$\delta W_S = \int_0^L A_{11}(\varepsilon - \varepsilon_0)\delta\varepsilon + D_{11}(K - K_0)\delta K\, dx \tag{21}$$

For details see the paper of Gerstmayr and Irschik [6]. The quantity K, sometimes denoted as the material measure of curvature, is defined by the rate of rotation θ of the cross section,

$$\theta' = \frac{\partial\theta}{\partial s}\frac{\partial s}{\partial x} = \kappa\frac{\partial s}{\partial x} = K = \left(\frac{\mathbf{r}' \times \mathbf{r}''}{|\mathbf{r}'|^2}\right)^T \mathbf{e}_3 \tag{22}$$

The axial strain in the Bernoulli-Euler beam can be split into normal and bending strain, respectively,

$$\varepsilon = |\mathbf{r}'| - 1 \quad \text{and} \quad \varepsilon_{bend} = y\, K \tag{23}$$

Eigenstrains are considered by means of the normal strain ε_0 and the bending strain K_0. The latter two quantities are utilized to include piezo-electric actuation in the large deformation beam element. The terms ε_0 and K_0 are equivalent to initial stretch and initial curvature in a pre-curved beam element. The piezo-electric actuation can be equivalently taken into account by means of actuating normal forces N_a and actuating bending moments M_a,

$$\delta W_S = \int_0^L (A_{11}\varepsilon - N_a)\,\delta\varepsilon + (D_{11}K - M_a)\,\delta K\, dx \tag{24}$$

5 Numerical Examples

In the following we study the motion of a two-link robot, see Figure 3, with tip mass and piezoelectric control. The dimensions of the robot are lengths of the arms $L_1 = L_2 = 0.5$m, a rectangular cross section with height $h = 4.5$mm and width $w = 20$mm, density$\rho = 7850$kg/m^3, Young's modulus $E = 2e11$N/m^2

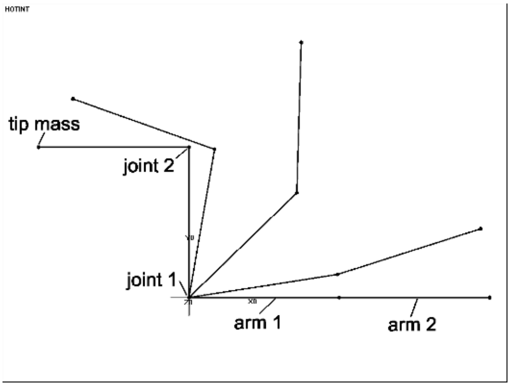

Fig. 3 Two-link robot with tip mass.

and a tip-mass of 1kg. The material is considered to be linear elastic and no gravity is acting upon the robot which is moving in the horizontal plane. The prescribed angles for the two idealized joints are

$$\theta_1 = \theta_2 = 10At^3 - 15At^4 + 6At^5 \quad \text{for} \quad t < 1 \quad \text{else} \quad \theta_1 = \theta_2 = A$$

with the final angular position $A = \pi/2$. Figure 4 shows a comparison of

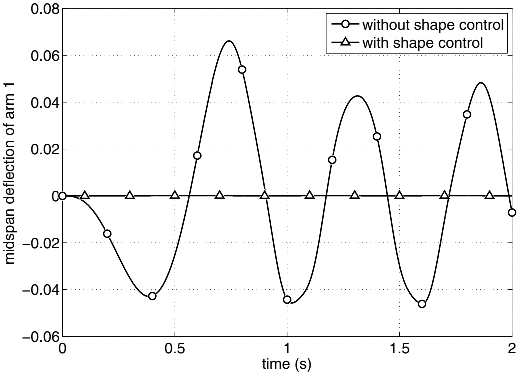

Fig. 4 Comparison of midspan deflection of arm 1 without/with shape control

the robot with and without the idealized piezoelectric control showing the midspan deflection of the first arm in the robot. It is obvious, that by piezoelectric compensation, no deflections occur during the motion of the robot. Not obvious from the very beginning, the compensation model which has been designed for the linearized beam, works for the fully nonlinear simu-

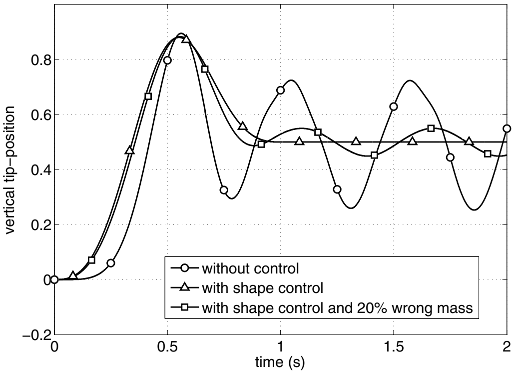

Fig. 5 Sensitivity of shape control to wrong mass-parameter.

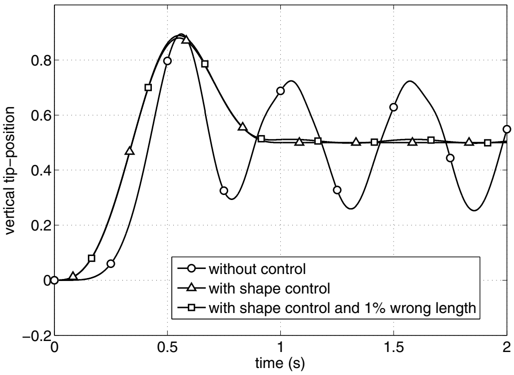

Fig. 6 Sensitivity of shape control to wrong geometrical parameter

lation of the robot. Without control, the robot arm undergoes moderately large deformations which include geometrically nonlinear effects.

In a second test of the feed forward control scheme the case of a disturbed system with an error in the mass is studied. For the comparison of the robot without control, the idealized controlled robot and the controlled robot with wrong mass in the feed forward control, which is 20% of the mass in the dynamical system,, see Figure 5.

In a third test, an error in the length of the first arm is assumed to be of the size 1%. Figure 6 shows the comparison of the robot without control, the idealized controlled robot and the controlled robot with wrong length in the feed forward control.

6 Conclusions

A solution for the shape control problem of an idealized flexible two-link robot has been derived, which fully eliminates the vibrations in the moving robot arms. A numerical model has been set up, which is able to investigate uncertainties of mass distributions or geometrical dimensions. The numerical example shows that it is possible to significantly reduce the flexible vibrations with the help of feed-forward shape control, if the system parameters are well known. It turns out that the proposed solution is moderately sensitive to mass or geometrical uncertainties. With the implemented numerical simulation code parameter studies can be performed in order to find a reasonable configuration for an experimental setup.

Acknowledgements The support of the present work by the Austrian Center of Competence in Mechatronics (ACCM) is gratefully acknowledged.

References

1. Sunar, M. and Rao, S.S.: *Recent advances in sensing and control of flexible structures via piezoelectric materials technology*, Applied Mechanics Reviews, 52 (1999), 1–16.
2. Irschik, H.: *A review on static and dynamic shape control of structures by piezoelectric actuation*, Engineering Structures, 24 (2002), 5–11.
3. Irschik, H., Nader, M., Zehetner, C.: *Exact cancellation of vibrations in elastic structures performing large rigid body motions*: Proceedings of the Tenth International Congress on Sound and Vibration (Stockholm, 2003, ed. Nilsson A and Boden Hans), 7 (2003), 3487–3498.
4. Irschik, H., Pichler, U., Nader, M., Zehetner, C.: *Deformation Compensation in Elastic Solids and Structures Performing Rigid-Body Motions*: Advanced Dynamics and Control of Structures and Machines, (CISM,Udine, ed. H. Irschik and K. Schlacher), CISM Courses and Lectures No. 444 (2004), 53–63.
5. Zehetner, C. and Irschik, H.: *Displacement compensation of beam vibrations caused by rigid-body motions*, Smart Materials and Structures, 14 (2005), 862–868.
6. Gerstmayr, J. and Irschik, H.: *On the correct representation of bending and axial deformation in the absolute nodal coordinate formulation with an elastic line approach*, Journal of Sound and Vibration, 318 (2008), 461–487.
7. Gerstmayr, J., Matikainen, M.K., Mikkola, A.M.: *A geometrically exact beam element based on the absolute nodal coordinate formulation*, Journal of Multibody System Dynamics, 20 (2008), 359–384.
8. Shabana, A. A.: *Dynamics of Multibody Systems* (2nd edition): Cambridge University Press, 1998.
9. Nader, M., Kaltenbacher, M., Krommer, M., von Garssen, H.G., Lerch, R.: *Active vibration control of a slender cantilever using distributed piezoelectric patches*: Proceedings of The Thirteenth International Congress on Sound and Vibration (ICSV13), Vienna (2006).

The basis of optimal active (static and dynamic) shape- and stress-control by means of smart materials

Franz Ziegler

Abstract Vibrations may shorten the lifetime of structures and machines, cause discomfort in many cases (noise radiation) and are totally unwanted in precision engineering. The latter requires also static shape control. The method of unique decomposition of eigenstrains into two constituents, namely in impotent eigenstrains, that do not cause stress and in the complementary nilpotent eigenstrains that do not induce any deformation in the linear elastic solid is considered in detail. These two complete classes of eigenstrains render optimal solutions by keeping shape and stress-control problems well separated. Assuming a common time function of the dynamic load, a novel approach is addressed to annihilate the forced vibrations. This optimal benchmark solution may serve the purpose in practical application to select properly shaped actuator patches and the control current.

1 Introduction

The state-of-the-art of active structural control up to 1990 is available in book form [1], the current one is reflected in [2], with general views collected in [3] and [4]. Haftka and Adelman [5] used transient thermal strains (eigenstrains) imposed on the supporting structure for the first time to minimize deviations of large space structures from their original shape. In [6] an adaptive wing of a fighter plane is considered. Vibration suppression of rotary wings is analyzed in [7]. An early summary is provided in [8]. In [9], reviews with emphasis on piezoelectricity and its application in disturbance sensing and control of flexible structures are provided, however, the sources of eigenstrain are not within the scope of this short paper. Nonlinear optimization routines destroy

---

Franz Ziegler
Vienna University of Technology, Vienna A-1040/E2063, Austria
e-mail: franz.ziegler@tuwien.ac.at

the comfortable settings in the control of linear vibrations. Linear solutions of the inverse problem are presented in [10] with a recent review given in [11]. It is shown that dynamic shape control when based on the annihilation of the quasi-static portion of the force-induced deformations renders the optimal distribution and intensity level of (shaped) actuator patches thereby fully quieting the vibrations. The controlled structure at rest finally carries the quasi-static force-induced stresses only. Such benchmark solutions with unlimited intensity of the actuators understood, serve for the best possible practical design. In [12] the crucial, unique decomposition of an eigenstrain tensor, e.g. of piezoelectric strain, is performed by means of the scalar product measure in Hilbert functional space, rendering its impotent part that does not produce stress, see also [13] and [14], and its complement, the nilpotent eigenstrain that renders stresses but does not produce deformation, see [10], [12] and [15].

2 Suppression of force-induced small vibrations about an equilibrium state

The generalization of static shape control by means of imposed eigenstrains, denoted $\boldsymbol{\varepsilon}^*$, to the dynamic shape control can be based on the dynamic generalization of Maysel's formula, [16], where the dynamic Green's stress dyadic of the structure is applied and a convolution in time must be considered. It is shown below that such a separate solution of the actuator problem is superfluous, see also [17] and [18].

2.1 Force-induced small vibrations about an equilibrium state

The dynamic shape control problem is solved by linear methods in [19], by assigning proper actuator stresses, i.e., transient eigenstresses, assuming the forced vibrations to be known. They elegantly use an extension of Neumann's method in [20], to define directly the properly distributed actuators. The force load must be considered first. Since mass inertia is taken into account, conservation of momentum renders the Euler-Cauchy equation of motion, [21], $\boldsymbol{b}$ is the given transient body force load, if any

$$div\boldsymbol{\sigma} + \boldsymbol{b} = \rho\boldsymbol{a} \,, \quad \boldsymbol{a} = \boldsymbol{u}_{,tt} \tag{1}$$

On part of the boundary, kinematic boundary conditions apply, on the remaining part of the surface, the transient traction of the force load is prescribed,

$$\mathit{\Gamma}_u : \boldsymbol{u} = \boldsymbol{0} \, , \quad \mathit{\Gamma}_\sigma : \boldsymbol{\sigma} \cdot \boldsymbol{n} = \boldsymbol{t}^{(n)} \tag{2}$$

Within the validity of both, linearized geometric relations and Hooke's law, [21],

$$\varepsilon_{ij(F)} = \frac{1}{2}(u_{i,j} + u_{j,i}) \, , \quad \varepsilon_{ij(F)} = C_{ijlm}\sigma_{lm} \tag{3}$$

the solution of the force-displacements $\boldsymbol{u}(\boldsymbol{x}, t) = \boldsymbol{u}^{(F)}$ is determined by Eqs. (1)-(3). It will be shown that dynamic control of these deformations, produced by prescribed body forces and surface traction, is achieved by the control of the much simpler quasi-static solution of the force problem, determined by the successive equilibrium states of the reduced Eq. (1),

$$div\boldsymbol{\sigma}^{(F)}_{(s)} + \boldsymbol{b} = \boldsymbol{0} \tag{4}$$

taking into account the prescribed dynamic boundary condition of Eq. (2). To fully relate the solution to the static shape control, the kinematic boundary condition, see again Eq. (2), is applied as well. With the simplifying assumption for both, body force and traction to be separable in space and time, Eq. (4) has to be solved only once and/or all available static solutions become candidates for dynamic shape control. The directions of the principal strain axes become time invariant! Since it is common practice in structural dynamics and modal analysis, to split the response to the force load into its quasi-static part, already posed by the boundary value problem of Eq. (4),

$$\boldsymbol{u}^{(F)} = \boldsymbol{u}^{(F)}_{(s)} + \boldsymbol{u}^{(F)}_{(d)} \tag{5}$$

the complementary dynamic part in the solution, $\boldsymbol{u}^{(F)}_{(d)}$, is considered further. Subtracting Eq. (4) from Eq. (1) renders the latter in a reduced form. Note both, the "body force" $\boldsymbol{b}^*_{(s)}$, determined by substituting Eq. (5) and, consequently recognized as the inertia force of the quasi-static force solution, and the remaining homogeneous dynamic boundary condition; the kinematic b.c. still holds true,

$$div\boldsymbol{\sigma}^{(F)}_{(d)} + \boldsymbol{b}^*_{(s)} = \rho\boldsymbol{u}^{(F)}_{(d),tt} \, , \quad \boldsymbol{b}^*_{(s)} = -\rho\boldsymbol{u}^{F}_{(s),tt} \, , \quad \mathit{\Gamma}_\sigma : \boldsymbol{\sigma}^{(F)}_{(d)} \cdot \boldsymbol{n} = \boldsymbol{0} \tag{6}$$

2.2 Eigenstrain-induced small vibrations: dynamic shape control

If impotent eigenstrains (with positive sign) equaling the quasi-static force-induced strains $\bar{\varepsilon}^*_{ij(s)}(\boldsymbol{x}) = \varepsilon^{(F)}_{ij(s)}(\boldsymbol{x})$ are imposed, no additional stresses are produced since the eigenstrain is a compatible one, $\boldsymbol{\sigma}^{(\varepsilon)}_{(s)} = \boldsymbol{0}$. That is a trivial solution of the homogeneous Eq. (4) with (ε) substituted for the superscript (F). The remaining dynamic boundary value problem of the eigenstrain load is detemined by (homogeneous dynamic boundary conditions are understood),

$$\begin{aligned} div\boldsymbol{\sigma}^{(\varepsilon)}_{(d)} + \boldsymbol{b}^{*}_{(s)} = \rho\boldsymbol{u}^{(\varepsilon)}_{(d),tt}\,, &\quad \Gamma_{\sigma}:\ \boldsymbol{\sigma}^{(\varepsilon)}_{(d)}\cdot\boldsymbol{n} = \boldsymbol{0}, \\ \boldsymbol{u}^{(\varepsilon)} = \boldsymbol{u}^{(\varepsilon)}_{(s)} + \boldsymbol{u}^{(\varepsilon)}_{(d)}\,, &\quad \boldsymbol{u}^{(\varepsilon)}_{(s)} = \boldsymbol{u}^{(F)}_{(s)} \end{aligned} \tag{7}$$

Since these impotent eigenstrains reproduce one and the same body force distribution $\boldsymbol{b}^{*}_{s}$ as defined in Eq. (6), they render the solution of the dynamic part of the force problem, Eq. (6). Hence, it can be concluded that the quasi-static impotent eigenstrain with reversed sign annihilates also the dynamic part of the force-displacements and, in addition, counteracts the dynamic stress portion of the force problem. The ideal dynamic shape control thus totally suppresses force-induced vibrations (quiet initial conditions have been assumed throughout) and leaves the quasi-static force-produced stresses unchanged. The simple example of the dynamic shape control of a redundant planar smart ideal truss, Fig. 1, by impotent eigenstrains illustrates this solution technique based on the quasi-static force response. The mass is lumped to the nodes, stiffness EA of the member rods is assumed to be constant. Since the load case is prescribed, we can directly calculate the quasi-static strains in the smart member rods, [21], and impose these strains as impotent eigenstrains, thus preserving the quasi-static member forces $\boldsymbol{N}^{(F)}_{(s)}$,

$$\boldsymbol{\varepsilon}^{(F)T}_{(s)} = -\bar{\boldsymbol{\varepsilon}}^{*}_{(s)} = \frac{F(t)}{100EA}\left[-11, 89, -37, 15, -74, -49, 61, 54, -87, -39, -39\right]. \tag{8}$$

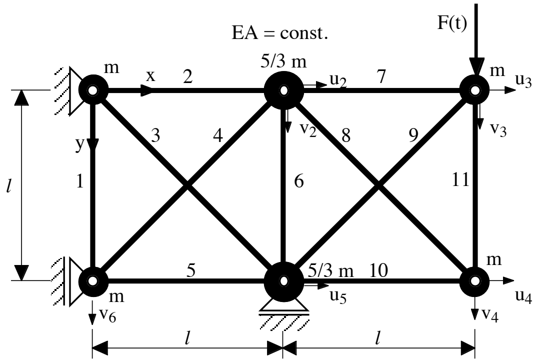

Fig. 1 Smart truss with internal and external redundancy (rank 3)

3 The basis of impotent and nilpotent eigenstrain in Hilbert (energy) space

For a rigorous formulation of the main theorem on eigenstress and eigenstrain, the Hilbert function space H is introduced [12], [14], as the space of second rank symmetric tensors where the components are real functions of spatial coordinates in the function space L_2. Assume, that the eigenstrain tensors are the elements of the Hilbert space. The inner product defines the norm, - of the eigenstrain $\bar{\boldsymbol{\varepsilon}}$,

$$(\boldsymbol{\alpha},\boldsymbol{\beta}) = \int\limits_{\Omega} \boldsymbol{\alpha} \cdot\cdot\, \boldsymbol{C}^{-1} \cdot\cdot\, \boldsymbol{\beta} dV \;, \quad \|\boldsymbol{\alpha}\|_H = \sqrt{(\boldsymbol{\alpha},\boldsymbol{\alpha})} \;, \quad \boldsymbol{\alpha} = \boldsymbol{\beta} = \bar{\boldsymbol{\varepsilon}} \tag{9}$$

Mikhlin [22] and [23] identified the first part of Eq. (9) as twice the strain energy, stored internally in the elastic body if $\boldsymbol{\alpha} = \boldsymbol{\beta} = \bar{\boldsymbol{\varepsilon}}$. Accordingly, the space is thus called energy space. For discretized structures, two mutual orthogonal finite dimensional sub-spaces exist, i. e., any tensor of eigenstrain $\bar{\boldsymbol{\varepsilon}} \in H$ existing in a body can be uniquely decomposed into its impotent $\bar{\boldsymbol{\varepsilon}}^{*}$ and nilpotent $\bar{\boldsymbol{\varepsilon}}^{**}$ constituents, see [12] and [14],

$$\bar{\boldsymbol{\varepsilon}} = \bar{\boldsymbol{\varepsilon}}^{*} + \bar{\boldsymbol{\varepsilon}}^{**} \;, \quad (\bar{\boldsymbol{\varepsilon}}^{*}, \bar{\boldsymbol{\varepsilon}}^{**}) = 0 \;, \quad \boldsymbol{\sigma} = -\boldsymbol{C}^{-1} \cdot\cdot\, \bar{\boldsymbol{\varepsilon}}^{**} \;, \quad \boldsymbol{\varepsilon} = \bar{\boldsymbol{\varepsilon}}^{*} \tag{10}$$

Equation (10) implies: there exists the orthogonal decomposition of the Hilbert (energy) space H into subspaces H_u and H_σ, see [12], $H = H_u \oplus H_\sigma$. Further, the unique decomposition of the space of eigenstrains allows us to establish the significant properties of eigenstress and deformation induced by eigenstrain, see again Eq. (10). Consequently, determination of impotent and nilpotent constituents of eigenstrain imposed on the structure allows in a general manner the determination of eigenstress and deformation caused by eigenstrain without straightforwardly solving the appropriate boundary value problem in linearized elasticity with eigenstrain. Consequently, the static or quasi-static control problems for load stress and deformation (or displacement) are kept apart just by selecting the proper class of eigenstrains. The general solution that may be called the basis of all possible impotent strains in H_u is easily derived by inverting the stiffness matrix, $\boldsymbol{K}^{-1}$ is the flexibility matrix. Each column renders, by means of a proper transformation, [24], a strain distribution in the finite elements or simply in the member rods that constructs such a base vector. For shells and FEM see [25]. Linear shape functions in triangular or tetrahedral finite elements render the candidates of impotent strain tensors constant. In case of higher order elements, a proper mean strain should be determined, see again [24].

3.1 Determination of the dimensions of the subspaces H_u and H_σ of the energy space

The discretized system is composed of N variable types of elements. The number of independent scalar parameters determining the deformation of an element of type "k" is denoted by m_k. The number of elements of type "k" is denoted by n_k. Since $H_\sigma \subset H$, it can be concluded that elastic strain and eigenstrain have the identical approximation in any given element (e.g., given by the shape functions selected for the finite element), thus, it remains valid for deformation and stress as well. The total number of independent scalar parameters defining the deformation of the discrete system thus defines the dimension of space H,

$$dimH = dimH_u + dimH_\sigma = \sum_{k=1}^{N} n_k m_k \tag{11}$$

The determination of $dimH_u$ requires the application of the theorem on eigenstrain, [12]: the eigenstrain in space H belongs to the subspace H_u iff there exist such (fictitious) body forces and surface traction that produce in the same elastic body a deformation that equals the given eigenstrain. Consequently, the number of independent variants of external nodal forces determines the dimension of subspace H_u. It is obvious, that in the case of a three-dimensional discrete system, the dimension of subspace H_u is thus given by: N_n, number of nodes; N_R, number of support reactions ($N_R \geq 6$), cf. with the size of the flexibility matrix,

$$dimH_u = 3N_n - N_R \tag{12}$$

Using Eqs. (11) and (12) renders at once

$$dimH_\sigma = dimH - dimH_u = \sum_{k=1}^{N} n_k m_k + N_R - 3N_n = s \tag{13}$$

equal to the rank of redundancy of the discrete system: The rank of redundancy s is defined by the number of internal and external forces that cannot be determined from the system of nodal equilibrium equations, [21]. Note, for discrete statically determinate structures the dimension of subspace H_σ is zero. Consequently, stress control by eigenstrain can be performed for redundant systems only, [5].

3.2 Construction of the basis of nilpotent eigenstrain

For a given truss it is advisable to use the principle of constraint release rendering forces $\boldsymbol{R}_j$. Then the equilibrium conditions result for arbitrary admissible node displacements $\boldsymbol{w}$ in the generalized form, $S_i^k = S_j^k = S_k$ is the axial member force,

$$\sum_{k=1}^{N_m} S_k \varepsilon_k(\boldsymbol{w}) l_k - \sum_{j=1}^{N_R} \boldsymbol{R_j} \cdot \boldsymbol{w}_j = 0\,, \quad \forall \boldsymbol{w} \in \left(W_2^1(\Omega)\right)^3\,, \quad \boldsymbol{w}_j = \boldsymbol{w}(\boldsymbol{r}_j) \tag{14}$$

With a unit vector $\boldsymbol{e}_k$the strain in a member rod k between nodes numbered i and j becomes $\varepsilon_k(\boldsymbol{w}) = \Delta l_k / l = (1/l_k)(\boldsymbol{w}_j - \boldsymbol{w}_i) \cdot \boldsymbol{e}_k$. Hence, denoting the force acting on the node "m" on the source side of the attached members by $\boldsymbol{F}_m$, Eq. (14) becomes the equilibrium equation in the free-body-diagram,

$$\sum_{m=1}^{N_n} \boldsymbol{F}_m \cdot \boldsymbol{w}_m - \sum_{j=1}^{N_R} \boldsymbol{R}_j \cdot \boldsymbol{w}_j = 0 \tag{15}$$

Therefore, the determination of statically admissible stresses reduces to the solution of the nodal equilibrium equations. Subsequently, the nilpotent eigenstrain can be obtained from the uniaxial Eq. (3). In the course of analysis of the redundant truss, an appropriate basic statically determinate system is selected, [21]. It means that it is necessary to release the redundant supports and member rods. We designate the magnitudes of redundant forces by X_j, $j = 1...s$, where s is the rank of system redundancy. These forces in the selected redundant member rods and supports X_j, $j = 1...s$, form the $(3N_n + s) \times 1$ column matrix: $\boldsymbol{F}^T = \{0...0, X_1...X_s\}$. Thus, constructing the influence function of strain $\varepsilon_i^{X_j} = S_i^{X_j} / E_i A_i$, $i = 1...N_m$, $j = 1...s$, i.e., of eigenstrains due to redundant forces, yields the desired basis of nilpotent eigenstrains.

Considering a simply supported single field of the truss in Fig. 1, $s = 1$, the single nilpotent unit basis is given by

$$\boldsymbol{\phi}_\sigma^{(1)} = \frac{\bar{\boldsymbol{\varepsilon}}^{**}}{\|\bar{\boldsymbol{\varepsilon}}^{**}\|} = \frac{1}{\sqrt{2EAl}\sqrt{1+\sqrt{2}}} \left(\frac{1}{\sqrt{2}}\,,\ -1\,,\ \frac{1}{\sqrt{2}}\,,\ \frac{1}{\sqrt{2}}\,,\ -1\,,\ \frac{1}{\sqrt{2}} \right) \tag{16}$$

4 Conclusion

Vibration annihilation is shown to rely on the quasi-static shape control by imposed impotent eigenstrains. A novel and efficient solution method for modelling and control of static or quasi-static stress and deformation by eigenstrain is ilustrated based on the theorem on decomposition of eigenstrain, [12] and [14]. A straightforward method for the determination of the dimensions in energy space of eigenstrain, subspaces of impotent eigenstrain and nilpotent eigenstrain, for discrete (trusses) or discretized structures (FEM) is discussed.

References

1. Soong T.T. Active structural control: theory and practice. Wiley, 1990
2. Preumont A. Vibration Control of Active Structures. 2ed. Kluwer, 2004
3. Gabbert U. and Tzou H.S. (eds.), Proc. IUTAM Symposium on Smart Structures and Structronic Systems. Kluwer, 2001
4. Watanabe K. and Ziegler F. (eds.), Proc. IUTAM Symposium on Dynamics of Advanced Materials and Smart Structures. Kluwer, 2003
5. Haftka R.T. and Adelman H.M. An analytical investigation of static shape control of large space structures by applied temperature. AIAA-Journal **23**, 450-457 (1985)
6. Austin F., Rossi M.J., Van Nostrad W., Knowles G. and Jameson A. Static shape control of adaptive wings. AIAA-Journal **32**, 1895-1901 (1994)
7. Nitzsche F. and Breitbach E. Vibration control of rotary wings using smart structures. Smart Mat. Struct. **3**, 181-189 (1994)
8. Crawley E.F. Intelligent structures for aerospace: a technology overview and assessment. AIAA-Journal **32**, 1689-1699 (1994)
9. Rao S.F. and Sunar M. Piezoelectricity and its use in disturbance sensing and control of flexible structures. AMR, **47**, 113-123 (1994)
10. Irschik H. and Ziegler F. Eigenstrain without stress and static shape control of structures. AIAA-Journal **39**, 1985-1990 (2001)
11. Irschik H. A review on static and dynamic shape control of structures by piezoelectric actuation. Engring. Struct. **24**, 5-11 (2002)
12. Nyashin Y., Lokhov V. and Ziegler F. Decomposition method in linear elastic problems with eigenstrain. Z. Angew. Math. Mech. **85**(8), 557-570 (2005)
13. Mura T. Micromechanics of Defects in Solids. 2ed. Kluwer, 1991
14. Nyashin Y., Lokhov V. and Ziegler F. Stress-free displacement control of structures. Acta Mechanica **175**(1), 45-56 (2005)
15. H. Irschik and U. Pichler, On eigenstrain without displacements. Acta Mechanica **178**, 111-122 (2005)
16. Irschik H., Fotiu P. and Ziegler F. Extension of Maysel's formula to the dynamic eigenstrain problem. J. Mech. Behaviour of Materials **5**, 59-66 (1993)
17. Ziegler F. Computational aspects of structural shape control. Computers & Struct. **83**, 1191-1204 (2005)
18. Ziegler F. Eigenstrain controlled deformation- and stress-states. Euro. J. Mech. A/Solids, **23**, 1-13 (2004)
19. Irschik H. and Pichler U. Dynamic shape control of solids and structures by thermal expansion strains. J. Thermal Stresses **24**, 565-576 (2001)
20. Irschik H. and Pichler U. An extension of Neumann's method for shape control of force-induced elastic vibrations by eigenstrains. Int. J. Solids Structures **41**, 871-884 (2003)
21. Ziegler F. Mechanics of Solids and Fluids. Repr. 2ed. Springer, 1998
22. Mikhlin S. Variational Methods in Mathematical Physics. Pergamon Press, 1964
23. Lebedev L. and Vorovich I. Functional Analysis in Mechanics. Springer, 2003
24. Zienkiewicz O.C. The Finite Element Method. 3ed., McGraw-Hill, 1977
25. Zallo A. and Gaudenzi P. Finite element models for laminated shells with actuation capability. Computers & Struct. **81**, 1059-1069 (2003)